CORA Cork Open Research Archive
Cartlann Taighde Oscailte Chorcaí

Title	Performance analysis of the parallel acquisition of weak GPS signals
Authors	O'Driscoll, Cillian
Publication date	2007
Original Citation	O'Driscoll, C. 2007. Performance analysis of the parallel acquisition of weak GPS signals. PhD Thesis, University College Cork.
Type of publication	Doctoral thesis
Link to publisher's version	http://library.ucc.ie/record=b1995188
Rights	© 2007, Cillian O'Driscoll. - http://creativecommons.org/licenses/by-nc-nd/3.0/
Download date	2026-11-02 19:06:11
Item downloaded from	https://hdl.handle.net/10468/1373



UCC
University College Cork, Ireland
Coláiste na hOllscoile Corcaigh

Performance Analysis of the Parallel Acquisition of Weak GPS Signals

Cillian O'Driscoll B.E. M.Eng.Sc

January, 2007



A Thesis Submitted to the

National University of Ireland

in Fulfillment of the Requirements for

the Degree of Ph.D.

Supervisor: Dr Colin C. Murphy.
Head of Department: Prof. Patrick J. Murphy.

Department of Electrical and Electronic Engineering,
National University of Ireland, Cork.

Abstract

This thesis provides a comprehensive analysis of the acquisition performance of the mobile-embedded Global Positioning System (GPS) receiver. Particular emphasis is given to the analysis of differentially coherent processing techniques and parallel acquisition strategies. New analytical expressions for the distribution of the decision variable of differentially coherent detectors are derived. In addition, new Gaussian approximations are derived and shown to be more accurate than existing approximations. Using these Gaussian approximations it is demonstrated that the traditional noncoherent combining detector is the best choice when the signal to noise ratio is large, but that differentially coherent combining is a superior choice at low signal to noise ratios.

An analysis of the effects of carrier Doppler, code Doppler and data modulation on detector performance is also conducted. For the noncoherent combining detector, new expressions are obtained for the mean and worst case power attenuation due to the combined effects of carrier Doppler and data modulation. Approximate expressions are also derived for the differentially coherent combining detector.

New expressions are also obtained for the mean and variance of the time to first hit using a Markov chain model and matrix methods. These models permit the use of numerical techniques to determine the optimal choice of receiver parameters for a given performance requirement.

Finally the effect of unknown power levels and multi-access interference (MAI) are considered. A novel technique for detecting MAI, referred to as the power level detector, is introduced and its performance analysed.

All results are verified by Monte Carlo computer simulation using a simplified signal model. The simulations were implemented on a 100 processor computer cluster.

In memory of Harold Collumbell and Finghín O'Driscoll.

Acknowledgements

My sincerest thanks are due to my supervisor, Dr Colin Murphy. His support and encouragement over the duration of this research have been of immeasurable benefit to me. Thank you Colin, for keeping my eye always on the bigger picture.

I would also like to acknowledge the support provided by Prof. Patrick Murphy, who assisted me in many ways and many capacities, not only in making the facilities of the Department available to me, but also in providing me with a home in Teltec. I only hope I didn't outstay my welcome.

Thanks also to Prof. Pat Fitzpatrick of the Boole Centre for Research in Informatics for giving me access to the BCRI computer cluster, without which most of the simulations in this thesis would be running still. Thanks also to Ken Healy for the many patient hours he spent helping me debug my mountains of leaky code.

This work would not have been possible without the financial support of Enterprise Ireland and Ceva Ltd. Thanks to Tony Hadrell, Derek Molyneux, Sue Taylor and Vincent Ashe for their technical support over the years.

A big hearty thanks to all the staff in the Department of Electrical and Electronic Engineering, in particular Kevin, Ralph, Geraldine, Liam, Jer, Mick and Tim. Thanks also to all the staff of the Department of Electronic Engineering, NUI Galway for welcoming me into their midst for the last year.

Particular thanks to Gregor, Olive, Karen, Aoife and Tim for all the discussions, advice, coffees and beers and, more importantly, for showing me that there is an end to all this. To all the others, all I can say is: hang in there!

To my parents and brothers: thanks for everything, for keeping things in perspective and providing me with a safe haven in Kenmare.

Finally, my deepest most heartfelt thanks to my wife, Ruth, who put up with so much and with such patience over the last five years that I don't think I'll ever be able to fully repay the debt.

Contents

Abstract **i**

List of Figures **xi**

List of Tables **xv**

Notation **xvii**

1 Introduction **1**

1.1 Global Positioning System Overview 2

1.2 Thesis Outline 6

2 Acquisition of DS/CDMA Signals: A Review **11**

2.1 Signal Model 11

2.2 Acquisition is an Estimation Problem 15

2.2.1 Estimation Theory and GPS 19

2.2.2 Practical Considerations 24

2.3 Acquisition is a Detection Problem 29

2.3.1 Detection Theory and GPS 35

2.4 The Detector/Estimator 38

2.4.1 Noncoherent Combining 48

2.4.2 Differentially Coherent Combining 53

2.4.3 Differentially Coherent Detection 58

2.4.4 Parallel Detection 61

2.5 The Acquisition Process 75

2.5.1 Acquisition Modes 76

2.5.2 Performance Analysis 83

2.6 Discussion 93

3 The Detector/Estimator I: Signal Effects **95**
3.1 The Maximum Likelihood Form 97
3.1.1 The Effect of a Residual Carrier Frequency Offset 98
3.1.2 The Effect of Data Modulation 99
3.1.3 The Effect of Code Doppler 105
3.2 The Noncoherent Combining Form 112
3.2.1 The Effect of a Residual Carrier Frequency Offset 113
3.2.2 The Effect of Data Modulation 114
3.2.3 The Effect of Code Doppler 122
3.3 The Differentially Coherent Combining Form 125
3.3.1 The Effect of a Residual Carrier Frequency Offset 128
3.3.2 The Effect of Data Modulation 130
3.3.3 The Effect of Code Doppler 136
3.4 The Differentially Coherent Detector 138
3.4.1 The Effect of a Residual Carrier Frequency Offset 139
3.4.2 The Effect of Data Modulation 140
3.4.3 The Effect of Code Doppler 141
3.5 Discussion 143

4 The Detector/Estimator II: Statistical Analysis **147**
4.1 Noise Model 148
4.2 The Noncoherent Combining Detector 151
4.2.1 Approximations and Bounds 152
4.3 Differentially Coherent Signal Processing 155
4.3.1 The Pair-wise Form 160
4.3.2 The Standard Form 167
4.3.3 Gaussian Approximations 172
4.4 Performance Comparisons 182
4.4.1 Deflection Coefficients 184
4.4.2 Receiver Operating Characteristic Curves 186
4.5 Parallel Forms 193
4.5.1 Analysis Issues 198
4.6 Discussion 200

5 The Acquisition Process **203**
5.1 The One H_1 Tile Approximation 204
5.1.1 The Markov Chain Model 204
5.1.2 The Fundamental Matrix 207
5.1.3 Probabilities of Detection and False Alarm 210
5.1.4 First Order Statistics 212
5.1.5 Second Order Statistics 213
5.1.6 Numerical Results 215
5.2 The Effect of Two H_1 Tiles 219
5.2.1 The Markov Chain Model 219
5.2.2 Numerical Results 221
5.3 Optimisation 221
5.4 Discussion 225

6 Multiple Satellites and Unknown Power Levels **233**
6.1 Acquisition in the Presence of MAI 234
6.1.1 Statistics of the Power Level Detector 237
6.2 Acquisition in the Presence of Unknown Power Levels 243
6.3 Discussion 244

7 Conclusions and Future Work **247**
7.1 Conclusions 247
7.2 Future Work 250

A Summation Identities **253**

B Mathematical Derivations **255**
B.1 Derivations from Chapter 3 255
B.1.1 Average Modulation Attenuation when $M \leq D$ 255
B.1.2 Average Modulation Attenuation when $M > D$ 256
B.2 Derivations from Chapter 4 260
B.2.1 Z_I is the Difference of Two Non-Central χ^2 Variates for the Pair Wise Form 260
B.2.2 An Integral Involving the Exponential Function with Trigonometric Functions in the Exponent 262
B.2.3 Derivation of Equation (4.102) 263
B.2.4 Derivation of Equation (4.103) 264

B.2.5 Derivation of $P_{J,N}(\rho)$ by Gaussian Elimination 265
B.2.6 Derivation of the CDF of R for the Standard Form of Differentially Coherent Processing 268
B.2.7 Derivation of Equation (4.140) 269
B.2.8 An Expression for the Probability that one χ^2 Distributed RV Exceeds Another 271
B.3 Derivations from Chapter 5 276
B.3.1 The Fundamental Matrix 276
B.3.2 Probabilities of Detection and False Alarm 279
B.3.3 First Order Statistics 280
B.3.4 Second Order Statistics 281
B.4 Derivations from Chapter 6 283
B.4.1 Mean and Variance of the Power Level Detector 283

C Probability Theory **289**
C.1 Random Events and Random Variables 289
C.2 Expectation and Moments 291
C.3 Transform Domain Techniques 291
C.3.1 The Moment Generating Function 291
C.3.2 The Characteristic Function 292
C.3.3 The Probability Generating Function 293

References **295**

List of Figures

1.1 Principle of Satellite Positioning 3
1.2 Time Delay Between Local and Received Codes 5
1.3 GPS Satellite Constellation 6

2.1 Autocorrelation Function of an m-sequence 14
2.2 GPS Signal Bandwidths, Spread and De-spread 14
2.3 Autocorrelation Function for Gold Codes 15
2.4 The Acquisition Grid for a simulated signal with $C/N_0 = 43.8$ dB-Hz. 26
2.5 Normalised Correlator Output vs Code and Doppler Offsets in the Absence of Noise 27
2.6 Sampling in the Code-Phase Domain 27
2.7 Sampling in the Doppler Domain 28
2.8 Binary Hypothesis Detector Model 29
2.9 Projection of $\boldsymbol{\xi}$ onto Θ 34
2.10 Discretised Two Dimensional Search Space Θ^* for the Acquisition Problem. 36
2.11 The Detector/Estimator covers a subset Γ of the Uncertainty Region 37
2.12 The ML Detector 38
2.13 Distribution of the Decision Statistic for the ML Detector 44
2.14 Data Transition in a Coherent Integration Period of MT_{CA} s. . . . 46
2.15 Noncoherent Combining Detector 48
2.16 Differentially Coherent Combining Detector 53
2.17 Differentially Coherent Detector 59
2.18 Acquisition Grid with Parallel Search Tile 62
2.19 Active Correlator Architecture for Time Domain Parallelism . . . 66
2.20 Structure of the FFT Detector/Estimator 68
2.21 FFT Detector/Estimator Tile in the Uncertainty Region 69

2.22 Tile Coverage in the Uncertainty Region for the FFT Detector/ Estimator using Doppler Rotation 72
2.23 FFT Detector with Post-Correlation Coherent Accumulation . . . 74
2.24 FFT Detector with Pre-Correlation Coherent Accumulation . . . 75
2.25 An Overview of Acquisition Modes 77
2.26 Verification Mode Flow Charts. 80
2.27 Circular State Diagram for the Markov Chain Representation of the Acquisition Process 89

3.1 The ML Detector 97
3.2 Data Transition in a Coherent Integration Period 99
3.3 Power Attenuation Due to Data Modulation in the ML Detector . 101
3.4 Power Attenuation Due to Combined Carrier Doppler and Average Case Data Modulation for the ML Detector 104
3.5 Power Attenuation Due to Combined Carrier Doppler and Worst Case Data Modulation for the ML Detector 105
3.6 Effect of a Residual Code Phase Offset at a Chip Transition. . . . 109
3.7 Power Attenuation Due to Code Doppler in the ML Detector and an Approximation. 111
3.8 Noncoherent Combining Detector 113
3.9 Model of Data Effects in the Noncoherent Combining Detector . . 114
3.10 a) Synchronous Receiver. b) Asynchronous Receiver. 116
3.11 All Possible Bit Boundary Locations for the Synchronous Receiver. 117
3.12 Comparison of Mean Power Attenuation Due to Data Modulation for Synchronous and Asynchronous Forms of the NCD Detector. . 119
3.13 Power Attenuation Due to Combined Carrier Doppler and Worst Case Data Modulation for the NCCD Detector 121
3.14 Power Attenuation Due to Mean Data Modulation vs Code Phase Offset for the NCCD Detector 123
3.15 Power Attenuation due To Residual Code Phase Offset 124
3.16 The Maximum Decision Statistic Occurs when the Code Phase Offset is Zero at the Midpoint of the Observation Interval 124
3.17 Power Attenuation Due to Code Doppler in the NCCD and an Approximation. 126
3.18 Differentially Coherent Combining Detector 126
3.19 The Effect of Carrier Frequency Offset on the DCCD. 129

3.20 Model of Data Effects in the Differentially Coherent Combining Detector 131
3.21 Code Doppler Effect on Summand of the DCCD. 136
3.22 Power Attenuation Due to Code Doppler in the DCCD and an Approximation. 137
3.23 Differentially Coherent Detector 138
3.24 Power Attenuation Due to Code Doppler in the DCD and an Approximation 143

4.1 Noise Power Spectral Density 148
4.2 Scatter Plot for the Pair Wise Form of the DCCD 178
4.3 PDFs and CDFs of Z_I and $R = \sqrt{Z_I^2 + Z_Q^2}$ for the Pair Wise Form of the DCCD 179
4.4 Scatter Plot for the Standard Form of the DCCD 182
4.5 PDFs and CDFs of Z_I and $R = \sqrt{Z_I^2 + Z_Q^2}$ for the Standard Form of the DCCD 183
4.6 ROC Curve Comparison for NCD and the Two Forms of DCCD . 187
4.7 ROC Curve Demonstrating Limitations of the Gaussian Model. . 188
4.8 Doppler Effect on ROC Curve 190
4.9 Gaussian Model vs Exact Calculation for ROC Curves 190
4.10 Effect of Received Power Level on ROC Curves 192
4.11 Effect of Parallelism on the Distribution of the Decision Statistic . 196
4.12 Error in Gaussian Approximation to the Maximum of $\boldsymbol{D}_k$ under H_0 199
4.13 Comparison of Gaussian Approximation and Exact Results from Mathematica$^{\text{TM}}$ of the PDF of the Maximum of $\boldsymbol{D}_k$ under H_0. . . 200

5.1 Circular State Diagram for the Search Mode Under the One H_1 Tile Approximation 205
5.2 Graphical Representation of $\boldsymbol{N}$ under the One H_1 Approximation 210
5.3 Construction of $\boldsymbol{M}$ 213
5.4 Structure of the matrix $\boldsymbol{M}$ under the One H_1 Approximation . . 214
5.5 P_D, Mean and Standard Deviation of T_{FH} vs K, for $P_{fa_0} = 0.01$. 218
5.6 Circular State Diagram for the Search Mode Under the Two H_1 Tile Approximation 220
5.7 P_D, Mean and Standard Deviation of T_{FH} vs K, for $P_{fa_0} = 0.01$. 222
5.8 Contour Plot of $\overline{T}_{FH}$ vs K and P_{fa_0} 224

5.9 Contour Plot of $\overline{T}_{FH}$ vs K and P_{fa_0} 226
5.10 Contour Plot of $\overline{T}_{FH}$ vs K and P_{fa_0} 226
5.11 Contour Plot of $\overline{T}_{FH}$ vs K and P_{fa_0} 227
5.12 Contour Plot of $\overline{T}_{FH}$ vs K and P_{fa_0} 227
5.13 Comparison of P_D, Mean and Standard Deviation of T_{FH} along the Contour $P_D = 0.9$ ($C/N_0 = 43.8$ dB-Hz) 228
5.14 Comparison of P_D, $\overline{T}_{FH}$ and $\sqrt{\text{Var}\left[T_{FH}\right]}$ along the Contour $P_D = 0.9$229
5.15 Comparison of P_D, $\overline{T}_{FH}$ and $\sqrt{\text{Var}\left[T_{FH}\right]}$ along the Contour $P_D = 0.9$230
5.16 Comparison of P_D, $\overline{T}_{FH}$ and $\sqrt{\text{Var}\left[T_{FH}\right]}$ along the Contour $P_D = 0.9$231
5.17 Comparison of P_D, $\overline{T}_{FH}$ and $\sqrt{\text{Var}\left[T_{FH}\right]}$ along the Contour $P_D = 0.9$232

6.1 Sample Plots of the Decision Vector $\boldsymbol{D_k}$ in the Presence and Absence of MAI. 236
6.2 Parallel Form of the ML Detector/Estimator 237
6.3 Distribution of ν for the Power Level Detector 240
6.4 Parallel Form of the DCCD Detector/Estimator 241
6.5 Distribution of ν for the Power Level Detector 242
6.6 Three Dimensional Markov Chain Model 244

B.1 The Marcum Q-function as a contour integral on the Riemann sphere. 272

List of Tables

2.1 The Four Possible Outcomes of a Binary Hypothesis Test 30

3.1 List of Symbols for the Estimation Process 96

4.1 Derivatives of the Determinant of the Matrix $\boldsymbol{P}$ at $\omega = 0$, $\nu = 0$. . 175

5.1 Parameters for Minimum $\overline{T}_{FH}$. 225

Notation

This thesis contains many acronyms, symbols and mathematical functions. There follows a brief desciption of the most important of these, followed by a reference to the page on which they are first introduced. Some symbols are re-used, though it should be clear from the context which meaning is intended.

For both the acronyms and mathematical functions we have endeavoured to use the standard conventions in the literature. The regularised Gamma functions, $\widetilde{\gamma}_K(z)$ and $\widetilde{\Gamma}_K(z)$), consititute an exception; the shorthand we introduce here is not widely used, but we feel it is quite intuitive.

For the symbols used in this thesis we follow some simple conventions. Constant integers are most commonly denoted by capital roman letters, *e.g.* $L = 1023$. Vectors are designated by bold face lower-case roman letters, *e.g.* $\boldsymbol{v}$, whilst matrices are written in bold face upper-case, *e.g.* $\boldsymbol{M}$.

Some common mathematical conventions used in this thesis include: $\Re\{z\}$ and $\Im\{z\}$ denote the real and imaginary parts of the complex number z respectively; $a \triangleq b$ indicates that a is *defined* by b; $\lfloor x \rfloor$ denotes the "floor" function, *i.e.* the largest integer less than or equal to x; $\lceil x \rceil$ denotes the "ceiling" function, *i.e.* the smallest integer greater than or equal to x; $\mathrm{nint}(x)$ denotes the "round" function, which evaluates to the nearest integer to x (note that this definition is ambiguous for half-integers, a common work-around is to round half-integers to the nearest even number, thus $\mathrm{nint}(1.5) = 2$, $\mathrm{nint}(2.5) = 2$, etc.); the determinant of the matrix $\boldsymbol{M}$ is denoted either $|\boldsymbol{M}|$ or $\det \boldsymbol{M}$; $|z|$ denotes the magnitude of the complex number z, thus the absolute value of a matrix determinant is denoted $|\det \boldsymbol{M}|$; z^* denotes the complex conjugate of z; $\boldsymbol{M}^{\mathrm{T}}$ denotes the transpose of the matrix $\boldsymbol{M}$; $\boldsymbol{M}^{\mathrm{H}}$ denotes the joint operation of transposition and complex conjugation of the complex matrix $\boldsymbol{M}$, sometimes called the Hermitian transpose of $\boldsymbol{M}$.

Acronyms and Abbreviations

A-GPS	Assisted GPS	1
AWGN	additive white Gaussian noise	12
BPSK	binary phase shift keying	15
C/A	Coarse/Acquisition	13
CDF	cumulative distribution function	8
CDMA	code division multi-access	2
CHF	characteristic function	92
CZT	Chirp-Z Transform	69
DCCD	differentially coherent combining detector	7
DCD	differentially coherent detector	7
DFT	Discrete Fourier Transform	67
DS/CDMA	direct-sequence code division multi-access	11
DS/SS	direct-sequence spread-spectrum	4
E112	Enhanced 112	1
E911	Enhanced 911	1
FCC	Federal Communications Commission	1
FFT	Fast Fourier Transform	26
FSSD	fixed sample-size detector	32
GLRT	generalised likelihood ratio test	35
GNSS	Global Navigation Satellite System	2
GPS	Global Positioning System	i
IF	intermediate frequency	70
LRT	likelihood ratio test	31
m-sequence	maximal-length sequence	14
MAI	multi-access interference	i
MAP	maximum *a posteriori*	17
MGF	moment generating function	163
ML	maximum likelihood	7
MMSE	minimum mean square error	17
NCCD	noncoherent combining detector	7

PDF	probability density function	8
PGF	probability generating function	87
PMF	probability mass function	87
PN	pseudo-noise	12
PSD	power spectral density	14
RF	radio frequency	4
ROC	receiver operating characteristic	186
rv	random variable	17
SCD	single cell detector	37
SNR	signal-to-noise ratio	22
SPRT	sequential probability ratio test	32
SVN	space vehicle number	16
TDRSS	Tracking and Data Relay Satellite System	65
U-TDOA	uplink time difference of arrival	1
UMP	uniformly most powerful	34

Mathematical Functions

$\Gamma(x)$	Gamma function	41
$\Gamma_K(x)$	upper incomplete Gamma function	49
$\widetilde{\Gamma}_K(x)$	regularised upper incomplete Gamma function	49
$\widetilde{\gamma}_K(x)$	regularised lower incomplete Gamma function	152
$\Phi_X(j\omega)$	Characteristic function of the rv X	292
$\Psi_X(s)$	Moment generating function of the rv X	291
$E_X[x]$	Mathematical expectation of x with respect to the rv X	291
$\mathrm{erf}(z)$	Error function	55
${}_2F_1(a,b;c;z)$	Gauss' hypergeometric function	163
$I_\nu(x)$	modified Bessel function of the first kind of order ν	41
$J_\nu(z)$	Bessel function of the first kind of order ν	158
$K_\nu(z)$	modified Bessel function of the second kind of order ν	54
$\mathbf{\Lambda}(\boldsymbol{r})$	Likelihood ratio	31
$\mathbf{\Lambda_g}(\boldsymbol{r})$	Generalised likelihood ratio	35
$\mathrm{P_X}(z)$	probability generating function of the discrete rv X	293
$(x)_k$	Pochhammer's function	163
$Q_K(a,b)$	Marcum Q-function of order K	41
$\mathrm{Var}[X]$	Variance of the rv X	291

Symbols

$*$	Convolution operator	91
$\odot$	Term-by-term vector product	67
$\otimes$	Discrete convolution operator	91
$\boldsymbol{A}$	Absorbing state probability transition matrix of a Markov Chain	85
α_D	Effective power attenuation due to the residual Doppler offset of the received signal	27
α_m	Effective power attenuation due to modulation of the received signal	47
$\overline{\alpha}_m$	Average effective power attenuation due to modulation of the received signal	47
α_s	Effective power attenuation due to the residual code phase offset of the received signal	43
$\overline{\alpha}_s$	Average effective power attenuation due to the residual code phase offset of the received signal	217
β	Half the carrier phase shift due to Doppler offset during a coherent observation interval	102
B	Number of data-bit boundaries in the observation interval	114
B_{IF}	The IF filter bandwidth	39
$\boldsymbol{C}$	Covariance matrix of a multi-variate distribution	20
C	Total number of cells in the uncertainty region	35
C/N_0	Carrier power to noise power spectral density ratio	8
C_{T}	Number of cells per tile	37
$\widetilde{\boldsymbol{\gamma}}$	Column vector in the $\boldsymbol{M}$ matrix under the two H_1 tile approximation	281
$\widetilde{\boldsymbol{c}}$	Column vector in the fundamental matrix under the two H_1 tile approximation	278
D_0	The decision that the null hypothesis is true	29
D_1	The decision that the alternate hypothesis is true	29
$D_?$	The decision that we do not know which hypothesis is true, more data is needed	32
D	Decision statistic	21

D	The duration of a data bit in code periods	51
d	Detector deflection coefficient, also known as the detection index	184
$\delta\eta$	Residual time dilation coefficient due to the Doppler effect	46
ΔF	Total Doppler uncertainty	45
$\delta\omega_d$	Residual Doppler frequency offset	26
$\Delta\zeta$	Drift in code phase in one coherent observation interval due to code Doppler effects	107
$\delta\zeta$	Residual code phase offset between local and received codes	26
$\boldsymbol{e}$	The all ones vector	207
η	Doppler dilation coefficient	12
$f_{\boldsymbol{r}\|\boldsymbol{\theta}}(\boldsymbol{r} \mid \boldsymbol{\theta})$	likelihood function of the observation vector $\boldsymbol{r}$ given the parameter vector $\boldsymbol{\theta}$	16
f_s	Sampling frequency	39
$f_{\boldsymbol{\theta}\|\boldsymbol{r}}(\boldsymbol{\theta} \mid \boldsymbol{r})$	*a posteriori* PDF of the parameter vector $\boldsymbol{\theta}$ given the observation vector $\boldsymbol{r}$	17
H_0	The null hypothesis, also any state in the Markov chain model where the null hypothesis is true	29
H_{10}	The H_1 state in the Markov chain model adjacent to the H_{11} state	219
H_{11}	The H_1 state in the Markov chain model in which the majority of the signal power resides	219
H_1	The alternate hypothesis, also any state in the Markov chain model where the alternate hypothesis is true	29
H_2	The hypothesis that the decision statistic contains thermal noise and at least one strong interferer	234
H_3	The hypothesis that the decision statistic contains signal, thermal noise and at least one strong interferer	234
$H_{d_{10}}$	Path to the detection state from the H_{10} cell in the circular state diagram of a Markov Chain	220
$H_{d_{11}}$	Path to detection state from the H_{11} cell in the circular state diagram of a Markov Chain	220
H_d	Path to detection state in the circular state diagram of a Markov Chain	88

H_{fa_0}	Path to the False Alarm state from a H_0 state in the circular state diagram of a Markov Chain	205
$H_{fa_{10}}$	Path to the false alarm state from the H_{10} cell in the circular state diagram of a Markov Chain	220
$H_{fa_{11}}$	Path to the false alarm state from the H_{11} cell in the circular state diagram of a Markov Chain	220
H_{fa_1}	Path to the false alarm state from the H_1 cell in the circular state diagram of a Markov Chain	205
H_{fa}	Path to the false alarm state from a H_0 state for single cell detector acquisition	88
H_{mai}	The hypothesis that the decision statistic contains multi-access interference	235
H_{nmai}	The hypothesis that the decision statistic does not contain multi-access interference	235
H_p	Path from false alarm state back to search state for a non-absorbing Markov chain	88
H_{r_0}	Path to the next state from a H_0 state in the circular state diagram of a Markov Chain	88
$H_{r_{10}}$	Path to the next state from the H_{10} state in the circular state diagram of a Markov Chain	220
$H_{r_{11}}$	Path to the next state from the H_{11} state in the circular state diagram of a Markov Chain	220
H_{r_1}	Path to the next state from the H_1 state in the circular state diagram of a Markov Chain	88
$\boldsymbol{I}$	The identity matrix	20
J	Separation between samples in the differential product of differentially coherent detectors	58
K	Number of coherent accumulator outputs used in noncoherent and differentially coherent combining detectors	48
k_B	Boltzmann's constant (1.381×10^{-23} $\text{WK}^{-1}\text{Hz}^{-1}$)	148
$L1$	The GPS L1 carrier frequency (1.57542 GHz)	12
L	The GPS C/A code length (1023 chips)	43
$\boldsymbol{M}$	The square of the fundamental matrix	213

M	Number of code periods in the coherent correlation time	27
$\widetilde{\boldsymbol{M}}$	Sub matrix of the $\boldsymbol{M}$ matrix under the two H_1 tile approximation	281
N_0	Single sided noise power spectral density	14
$\boldsymbol{N}$	Fundamental matrix for a Markov Chain	85
N	The normal distribution	149
$\overline{\boldsymbol{N}}$	Average fundamental matrix for a Markov Chain under the two H_1 tile approximation	278
$\widetilde{\mathrm{N}}$	The complex normal distribution	149
$\widetilde{\mathbf{N}}$	The multidimensional complex normal distribution	150
N_{CA}	Integer number of full code periods occurring during the signal transit time	13
N_s	Number of samples per code period	27
$\widetilde{\boldsymbol{N}}$	Sub matrix of the fundamental matrix under the two H_1 tile approximation	278
N_{T}	Number of tiles in the uncertainty region	37
P_0	Probability that H_0 is true	30
P_1	Probability that H_1 is true	30
$\boldsymbol{P}$	Complex matrix component of the CHF of the differentially coherent accumulator output	156
$\boldsymbol{P}$	State transition matrix for a Markov chain	84
$\overline{\boldsymbol{P}}$	Average state transition matrix for a Markov Chain under the two H_1 tile approximation	277
$P_{d_{10}}$	Probability of correct detection in the H_{10} tile	220
$P_{d_{11}}$	Probability of correct detection in the H_{11} tile	220
$\overline{P}_{d_1}$	Average value of P_d under the two H_1 tile approximation	220
P_D	Overall detection probability	83
P_d	Probability of detection	30
P_{fa_0}	Probability of false alarm under H_0	63
$P_{fa_{10}}$	Probability of false alarm in the H_{10} tile	220
$P_{fa_{11}}$	Probability of false alarm in the H_{11} tile	220
P_{fa_1}	Probability of false alarm under H_1	63
$\overline{P}_{fa_1}$	Average value of P_{fa_1} under the two H_1 tile approximation	220

P_{FA}	Overall false alarm probability	83
P_{fa}	Probability of false alarm	30
P_H	Overall probability of a hit in one of the acquisition modes	79
P_h	Probability of a hit in one dwell	79
P_L	Probability of making one full sweep of the uncertainty region without making a D_1 decision	209
P_m	Probability of a miss	30
P_{r_0}	Probability of correct rejection under H_0	63
$P_{r_{10}}$	Probability of rejection in the H_{10} tile	220
$P_{r_{11}}$	Probability of rejection in the H_{11} tile	220
P_{r_1}	Probability of rejection under H_1	63
$\overline{P}_{r_1}$	Average value of P_{r_1} under the two H_1 tile approximation	220
P_R	Overall probability of rejection in one of the acquisition modes	81
P_r	Probability of correct rejection	30
$\overline{P}_{rd_1}$	Average probability of a rejection followed by a detection in both of the H_1 tiles under the two H_1 tile approximation	221
$\overline{P}_{rd_1}$	Average probability of a rejection followed by a detection in both of the H_1 tiles under the two H_1 tile approximation	279
Ψ	Nuisance parameter space	33
$\boldsymbol{\psi}$	Vector of nuisance parameters	18
$\boldsymbol{Q}$	Hermitian matrix describing the differentially coherent sum	241
$\boldsymbol{Q_I}$	Hermitian matrix describing the real component of a differentially coherent sum	155
$\boldsymbol{Q_Q}$	Hermitian matrix describing the imaginary component of a differentially coherent sum	156
$\boldsymbol{R}$	Transition matrix for recurrent states of a Markov Chain	84
$\mathbb{R}$	The set of real numbers	59
$\widetilde{\boldsymbol{\rho}}$	Row vector in the $\boldsymbol{M}$ matrix under the two H_1 tile approximation	281
$\widetilde{\boldsymbol{r}}$	Row vector in the fundamental matrix under the two H_1 tile approximation	278
$\boldsymbol{S}$	Circulant matrix formed from the spreading code of the satellite of interest	237

$\mathcal{S}_{sv}$	Set of SV ID's for the satellites in view	12
$\boldsymbol{T}$	Transition matrix for transient states of a Markov Chain	84
τ	Time delay	4
T_{ACQ}	Time to correct acquisition	19
$\overline{T}_{ACQ}$	The mean acquisition time	83
T_{CA}	The GPS C/A code period (1 ms)	13
T_{chip}	The PRN chip period (1/1023 ms)	13
T_{coh}	Coherent integration time	100
τ_D	Dwell time	37
$\overline{\tau}_D$	Mean dwell time	86
T_{FH}	Time to first hit	8
$\overline{T}_{FH}$	Mean time to first hit	85
$\boldsymbol{\Theta}$	Auto-correlation matrix formed from the auto-correlation vector of the resampled spreading code	283
Θ	Desired parameter space	25
$\boldsymbol{\theta}$	Auto-correlation vector of resampled spreading code	239
$\boldsymbol{\theta}$	Vector of parameters to be estimated (the *desired* parameters)	16
T_P	False alarm penalty time	82
T_s	Sample time	19
V_{Th}	Decision threshold	38
ω_d	Doppler frequency offset	13
χ'^2	The non-central χ^2 distribution	153
$\boldsymbol{\xi}$	Vector of all parameters, including both desired and nuisance parameters	32
Ξ	Parameter space	32
$\mathbb{Z}^+$	The set of positive integers	41
$\mathbb{Z}$	The set of integers	273
ζ	Code phase offset between local and received codes	13
z	The unit delay operator	67

Chapter 1

Introduction

The worldwide market for mobile-phone technology is expected to reach 3 billion handsets by 2008 [8]. This surge in mobile phone ownership has placed a heavy burden on the emergency services. In Europe alone, 40 million mobile emergency calls are recorded on a yearly basis. It is estimated that in 2.5 million of these cases emergency services are unable to dispatch rescue teams, due to the lack of sufficient location information [4]. In the United States, federal law requires the provision of location information with every mobile initiated emergency call, the so-called Enhanced 911 (E911) standard [43], and Europe is currently working towards its own standard, Enhanced 112 (E112) [5]. The provision of this information has the potential to save many lives every year.

There are currently two approaches to the E911 application that meet the Federal Communications Commission (FCC) E911 requirements: 1) Network based techniques; and 2) handset based techniques. Currently the only network-based technique that meets the requirements is the uplink time difference of arrival (U-TDOA) measurement technique. This requires measurements to be made at a number of network base-stations within range of the mobile device. Knowledge of the location of these base-stations, in addition to knowledge of the time of arrival of the mobile signal, permits a tri-lateration solution of the location of the mobile device. This technique requires a significant financial investment from the network operators for the installation of specialised hardware at the base-station locations [78]. However, the technique works well in all environments where mobile phones can be expected to work. This technique has been widely adopted for use in GSM networks in the United States.

The only handset based technique to meet the FCC requirements is the As-

sisted GPS (A-GPS) technique. This requires the implementation of a GPS receiver within the mobile handset. GPS is an example of a Global Navigation Satellite System (GNSS). GNSS receivers use information from signals transmitted by satellites orbiting the earth to determine the mobile location. In contrast to the U-TDOA technique, the bulk of the cost in this case is contained in the additional cost of the A-GPS enabled handset (about US$5–10 per handset), and so is passed to the user. The A-GPS technique has been widely adopted for code division multi-access (CDMA) mobile networks in the US. However, the integration of a GPS receiver onto a mobile platform presents serious design challenges. The mobile phone must operate indoors, in cars, in urban environments, etc. where the receiver does not have a clear view of the sky. Reception of satellite signals in these environments is problematic, however, and signal availability is a major issue facing the A-GPS enabled mobile phone.

Current state-of-the-art, mobile-embedded GPS receivers rely on two enabling technologies to function in these harsh environments: 1) assistance information is provided to the handset via the mobile network, which gives initial estimates of the signal parameters and mobile location; 2) massive parallelism, in which large swathes of the uncertainty region are searched at once, this may be implemented in either the time or frequency domains. In addition, recent research suggests that novel, differentially coherent techniques may work well in situations where received power levels are low [40, 112, 113].

This thesis provides a performance analysis of parallel architectures for the acquisition of weak GPS signals. In particular, the performance of the traditional noncoherent combining architecture is compared with newer differentially coherent techniques. New analyses of these differentially coherent architectures are derived to aid in this comparison. In addition, the problem of MAI and acquisition when the power level of the received signal is unknown are also considered. A new technique for the detection of MAI, which we term the *power level detector*, is introduced and modelled.

We begin with a brief overview of the Global Positioning System.

1.1 Global Positioning System Overview

The fundamental principle of operation of the Global Positioning System is well described by Enge and Misra in [41]:

> GPS is based on an idea that is both very simple and quite ancient: one's position ... can be determined given distances to objects whose positions are known.

In GPS the "objects" whose positions are known are, in fact, satellites travelling at speeds in excess of 3 kms^{-1}. The principle of operation is demonstrated in Figure 1.1, which illustrates a simple two-dimensional model of the positioning problem. The user is positioned somewhere on the surface of the earth (repre-

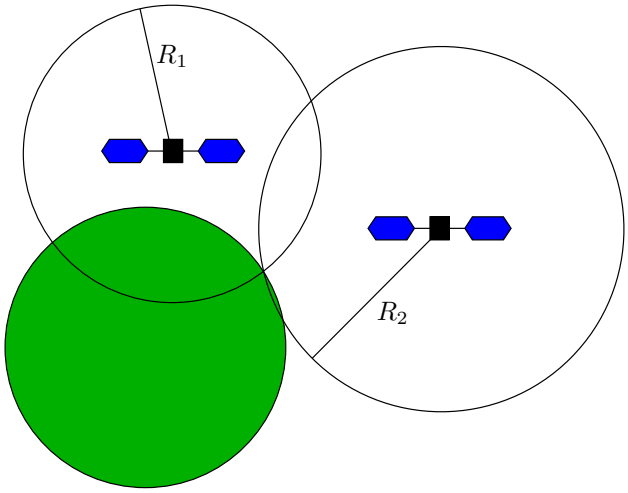


Figure 1.1: Principle of Satellite Positioning

sented by a green disk in the figure), while two satellites orbit overhead. The user is required to have precise knowledge of the location of each of the satellites. To determine the user's location, measurements are made to determine the distance (or range) to each of the satellites, denoted R_1 and R_2. Knowing both the position of the satellites and the range to each satellite, the user position is given by the intersection of two circles, as shown in the figure. Note that this results in two possible positions for the user: one on the surface of the earth, and the other far out in space. Determining the location of the user in two dimensions is, therefore, equivalent to solving the simultaneous equations:

$$|R_1| = \sqrt{(x_1 - x_u)^2 + (y_1 - y_u)^2} \tag{1.1}$$

$$|R_2| = \sqrt{(x_2 - x_u)^2 + (y_2 - y_u)^2}, \tag{1.2}$$

where (x_u, y_u) are the user co-ordinates and $(x_i, y_i),\ i \in \{1, 2\}$ are the co-ordinates of satellite i. In three dimensions, a measurement to a third satellite is re-

quired, which narrows down the possible user locations to the intersection of three spheres. Again, this leads to two possible locations, one of which can usually be readily discarded. If greater positional accuracy is required, then measurements can be made to more satellites.

The principle of operation of GPS is, therefore, quite simple. The complexity arises in the implementation. Two key requirements must be met:

1. The user must have accurate information regarding the location of all the satellites.

2. The user must be able to obtain an accurate measure of the range to each satellite in view (*i.e.* to each satellite from which a signal is received).

In GPS, both of these criteria are met by broadcasting radio frequency (RF) electromagnetic signals from the satellites. This data is broadcast using direct-sequence spread-spectrum (DS/SS) [123] modulation, which consists of two layers. The first consists of a sequence of bits carrying information describing the satellite location, which we refer to as the *data signal*. The second layer consists of a repeating pseudo-random sequence of bits, referred to as the *spreading code*.

The data signal from every satellite contains very precise orbital parameters from which the current position, velocity and acceleration of the satellite can be determined. This information is called *ephemeris information*. In addition, each satellite also transmits coarser (*i.e.* less accurate) orbital parameters for *all* satellites currently in orbit. This data is referred to as *almanac* data. Consequently, a receiver need only demodulate the data from one satellite to obtain reasonably accurate information on the location of all the GPS satellites. To obtain precise location information for a satellite, however, requires demodulating the data signal from that satellite.

The spreading code is a pseudo-random repeating sequence of bits[†], which is synchronised to the satellite clock. In addition, all the satellite clocks are synchronised to GPS time[‡]. Once the signal leaves the transmitter antenna on board the satellite, it takes a finite amount of time, denoted τ, to reach the user's receiver on the surface of the earth. If the receiver is also synchronised

[†]In spread-spectrum terminology the bits of a pseudo-random sequence are usually referred to as *chips*.

[‡]In reality the satellite clocks will be offset from GPS time, but the satellites transmit clock error parameters which can be used at the receiver to determine the offset between satellite time and GPS time.

to GPS time then the user can determine how much time has elapsed between transmission and reception by comparing a locally generated copy of the spreading sequence with the spreading sequence received from the satellite, as illustrated in Figure 1.2. The user knows the speed at which the signal travels (*i.e.* the speed

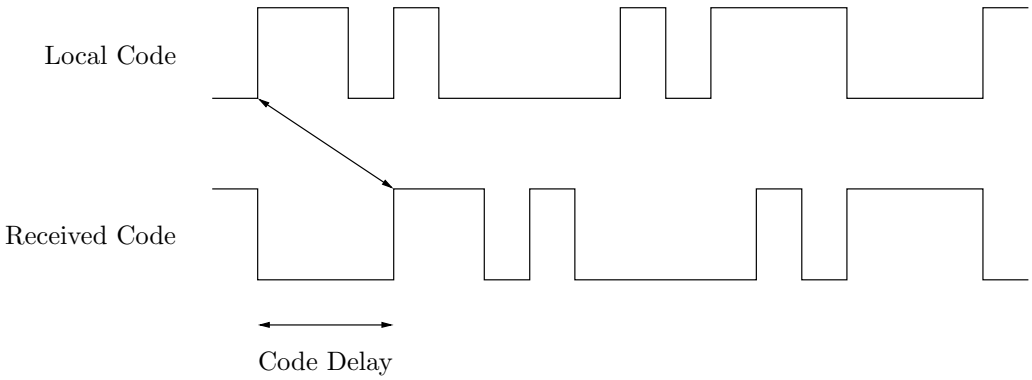


Figure 1.2: Time Delay Between Local and Received Codes

of light in a vacuum: $c \approx 3 \times 10^8$ ms^{-1}) and so can determine the distance to the satellite by the simple equation:

$$R = \tau c. \tag{1.3}$$

Thus, we see that the two requirements for satellite positioning are met by the transmission of the RF signals described above. At any moment in time the user's clock will be in error by an amount referred to as the *clock bias* t_b. This bias affects the range measurement to each satellite identically, the resulting measurement is referred to as a *pseudo-range*, as it is not a true measure of the distance to the satellite. In effect, this introduces another dimension to the positioning problem. By taking measurements to at least four satellites the user receiver can obtain a solution to this four dimensional problem.

The GPS satellite constellation, illustrated in Figure 1.3, has been specifically designed to ensure that at least four satellites are in view from any point on the surface of the earth at any moment in time. The constellation nominally consists of 24 satellites orbiting in six orbital planes equally spaced about the earth, with four satellites per plane. Each plane is inclined at an angle of 55° to the equatorial plane. The satellites orbit at an altitude of approximately 20,000 km, resulting in an orbital period of just under 12 hours. This means that, at any point on the surface of the earth, the pattern of satellites overhead repeats approximately

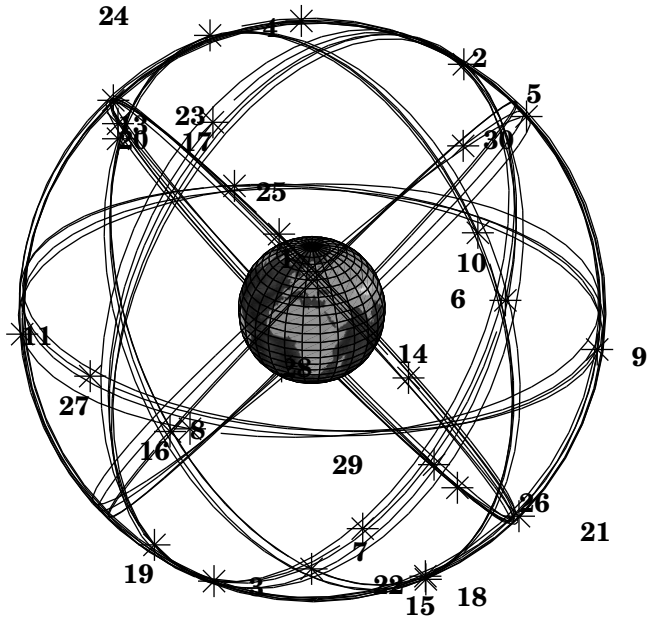


Figure 1.3: GPS Satellite Constellation

every 24 hours.

Much more information on GPS can be found in, for example, [1, 70, 93].

1.2 Thesis Outline

The objective of this thesis is to provide a performance analysis of the acquisition of weak GPS signals. We define any signal received below the stated minimum open air received power of -160 dBW [2] as a weak signal. In particular, efforts are focused on the analysis of parallel architectures for fast acquisition.

In Chapter 2, a comprehensive review of the current state of the art in weak signal acquisition is presented. A detection and estimation theoretic exposition is given and, returning to the original motivations for traditional receiver designs, it becomes apparent why these designs are ineffective when signals are weak and some alternative strategies emerge. In this chapter our model of the acquisition problem is defined. We divide acquisition into two stages:

1. The *detector/estimator*, which is a decision making device returning a decision on whether or not a GPS signal is present at the receiver antenna and, subsequently, estimating the received signal parameters if signal is deemed to be present.

2. The *acquisition process*, which controls the detector/estimator, determining which parameter estimates are to be tested and in what order.

The remainder of the thesis addresses the analysis and modelling of these two components. Four detector/estimator forms are considered in this thesis:

1. The maximum likelihood (ML) detector, which is the optimal detector in the absence of unwanted signal effects, such as data modulation and code Doppler [58].

2. The noncoherent combining detector (NCCD), which is commonly employed in traditional receiver architectures to counteract the deleterious effects of data modulation during acquisition.

3. The differentially coherent combining detector (DCCD), which has recently been examined in the literature due to its seeming superiority over the NCCD when power levels are low (see [15, 40, 112], for example).

4. The differentially coherent detector (DCD), which is another differentially coherent technique, substantially different to the DCCD and also the subject of recent interest [28, 113].

Our treatment begins with an investigation of the detector/estimator. A thorough treatment of the effect of unwanted signal parameters on the detector/estimator is given in Chapter 3. A number of new expressions are derived, particularly in relation to the combined effects of data modulation and Doppler shift on the NCCD and DCCD. A novel treatment of code Doppler effects is also given, and it is demonstrated that the apparent power attenuation due to code Doppler can actually exceed that due to carrier Doppler when dwell times are sufficiently long. The DCD is demonstrated to be particularly robust in the face of data modulation and large Doppler offsets (of the order of 20 kHz).

Having considered the effect of signal on the detector/estimator in Chapter 3, the influence of noise is examined in some detail in Chapter 4. The stochastic nature of the noise necessitates a statistical analysis of acquisition performance. The statistics of the NCCD are well known, the most important results are summarised in Section 4.2. The DCCD and DCD are less well studied, however, and so a novel approach was adopted in the treatment of these differentially coherent techniques under a common framework. The key results include expressions

for the probability density function (PDF) and cumulative distribution function (CDF) of the decision statistic in the absence of signal. It is demonstrated in Section 4.3.1 that the decision statistic follows a distribution commonly referred to as the K-distribution [63]. Unfortunately, no equivalent closed form analytic expression has been found for the signal plus noise case. In this case a new approximation, based on the central limit theorem, is derived and shown to be more accurate than an existing Gaussian approximation.

Utilising the results of the preceding sections, a performance comparison of the various detector/estimator forms is given in Section 4.4.2. It is demonstrated by numerical simulation, that the NCCD is the best choice of detector/estimator when signal power is relatively high ($C/N_0 > 38$ dB-Hz), but that the DCCD displays superior performance in weak signal situations ($C/N_0 \leq -38.8$ dB-Hz). A new union bound on the maximum probability of detection for the parallel form of the NCCD is also derived. In addition, some limitations on the use of Gaussian approximations when analysing parallel architectures are noted.

The final chapters of the thesis treat the acquisition process. In Chapter 5, the performance of the search mode is analysed in terms of the time taken to detect a satellite signal, called the time to first hit, T_{FH}. New expressions for the mean and variance of this quantity are derived using matrix methods for the Markov chain model. These expressions are subsequently used in the numerical optimisation of the receiver parameters. The models developed are quite simple and equally applicable for all forms of detector/estimator discussed in this thesis. Finally, in Chapter 6, the effects of unknown power levels and multiple satellites are considered. A new technique for the detection of MAI, referred to as the power level detector, is introduced and a Gaussian model is developed to predict its performance. The acquisition of GPS signals when the received power level is unknown is considered in Section 6.2. We propose an approach whereby the power level is treated as a signal parameter to be estimated. The range of possible values for the power level defines an uncertainty region, which is subsequently discretised. This adds a third dimension to the signal search process (the first two being the time delay and Doppler frequency offset), which can be analysed in the same manner as was applied to the two dimensional search process of Chapter 5. This approach, used in conjunction with the newly proposed power level detector, permits the fast, reliable acquisition of GPS signals of unknown received power levels in the presence of MAI.

All the results derived in this thesis have been verified by Monte Carlo simulation. The acquisition of weak signals necessitates the use of extended dwell times, which in turn leads to longer simulations. To speed up the simulation process the entire system was modelled on a computer cluster consisting of 100 processors.

Chapter 2

Acquisition of DS/CDMA Signals: A Review

The Global Positioning System (GPS) is a direct-sequence code division multi-access (DS/CDMA) system. In this chapter we present a detailed overview of the existing work on the topic of DS/CDMA signal acquisition. In this manner we introduce the concepts, notations and conventions used throughout this thesis.

An excellent overview of CDMA can be found in [123], including a detailed historical review of the development of the field. For GPS signal processing, [93] is generally considered to be the standard reference, though it is lacking in detail on acquisition aspects. More information can be found in [70], particularly on verification strategies as they apply to the GPS acquisition problem. For a software-based approach [137] is a good source, though it is primarily procedural in its descriptions, focusing on the "hows" rather than the "whys" of GPS signal processing.

The following treatment differs slightly from the more standard introduction to the problem. Here we focus on an estimation-theoretic exposition: beginning with a GPS signal model, we describe signal acquisition as a parameter estimation problem and proceed with the analysis of acquisition strategies using the standard tools of the theories of estimation and detection.

2.1 Signal Model

The GPS signal model adopted in this thesis is simplified in a number of ways, thereby permitting a tractable theoretical analysis. The noise is assumed to

be a zero-mean additive white Gaussian noise (AWGN) process. In reality the noise will be neither Gaussian nor white, however the Gaussian *approximation* is justified by the central limit theorem, and is found to be accurate in practice. In addition we ignore the effect of the front-end filter. In practice the front-end filter limits the bandwidth of both the signal and noise components in the receiver. In addition, the sampled band-limited noise process is not white, as successive noise samples are correlated. Thus, the white noise assumption is an approximation only.

Under the above assumptions, the complex baseband signal model at the input to a GPS receiver can be represented by:

$$r(t) = \sum_{i \in \mathcal{S}_{sv}} \sqrt{\frac{P_i(t)}{2}} d_i\Big(t_i(t)\Big) c_i\Big(t_i(t)\Big) \exp\left(j\left(\omega_0 t_i(t) + \phi_i\right)\right) + n(t), \tag{2.1}$$

where $\mathcal{S}_{sv}$ is the set of all satellites in view, $P_i(t)$ is the received instantaneous signal power from satellite i, $d_i(t)$ is its data signal, $c_i(t)$ is its pseudo-noise (PN) code signal, ϕ_i is its initial carrier phase offset, ω_0 is the $L1$ carrier frequency ($2\pi \times 1575.42$ Mrads^{-1}), $n(t)$ is the noise on the received signal and $t_i(t)$ is a function incorporating time delay and Doppler shift on the signal from satellite i.

In general, $t_i(t)$ is an arbitrary function of t, where t denotes GPS time. However, a simple, first order approximation is given by:

$$t_i(t) = (1 + \eta_i)t - \tau_i, \tag{2.2}$$

where η_i is the time dilation coefficient due to the Doppler effect and τ_i is the time delay due to the transit time between transmitter and receiver. The Doppler effect is essentially a time dilation/contraction effect caused by the relative motion between the transmitter and receiver along the direction of propagation of the radio wave. The Doppler dilation coefficient is defined by [17, Equation (4)]:

$$\eta_i = -\frac{\boldsymbol{u} \cdot (\boldsymbol{v_i} - \boldsymbol{v_u})}{c}, \tag{2.3}$$

where $\boldsymbol{x} \cdot \boldsymbol{y}$ denotes the dot product of the vectors $\boldsymbol{x}$ and $\boldsymbol{y}$, $\boldsymbol{v_i}$ and $\boldsymbol{v_u}$ are the velocity vectors of the i^{th} satellite and the user respectively, $\boldsymbol{u}$ is the unit vector along the line of sight between transmitter and receiver and c is the speed of

light. Thus, if two events in the transmitted signal are separated by T seconds, then they will be separated by $T \times (1 + \eta_i)$ seconds when the signal reaches the receiver. This effect is most commonly associated with a frequency shift on the carrier signal, given by:

$$\exp\left(j\omega_0 t(1+\eta_i)\right) = \exp\left(j\left(\omega_0 + \omega_0\eta_i\right)t\right) = \exp\left(j\left(\omega_0 + \omega_{di}\right)t\right).$$

The Doppler frequency shift between the receiver and satellite i is, therefore, given by $\omega_{di} = \eta_i\ \omega_0$. It is important to remember, however, that the Doppler effect is not limited to this carrier frequency shift: all transmitted signal components which are functions of time are also affected. Thus, the signal may be said to suffer from three Doppler effects; namely carrier Doppler, code Doppler and data Doppler.

The time delay τ_i is given by:

$$\tau_i = N_{CA}T_{\text{CA}} + \zeta T_{\text{chip}} \tag{2.4}$$

where N_{CA} is the integer number of code periods occurring during the signal transit time, T_{CA} is the duration of the Coarse/Acquisition (C/A) code in seconds, T_{chip} is the C/A code chip period in seconds and ζ is the code phase offset measured in code chips and is a real number in the range $[0, 1023)$.

For each satellite the PN code is a pseudo-random sequence of ± 1 values, called *chips*. The purpose of the PN code is two-fold:

1. It is this code that "spreads" the spectrum of the transmitted signal, as the bandwidth of the PN code signal is much greater than that of the data signal. This is what makes the GPS signal a DS/SS signal.

2. The code also introduces a form of multi-access communication known as CDMA.

These codes are carefully chosen to fulfil this dual purpose. Firstly, they must have very good pseudo-randomness properties. This ensures the codes are sufficiently "noise-like" to spread the signal bandwidth effectively. This property is reflected in the autocorrelation function of the PN code. A random noise process has an autocorrelation function that is a delta function. For a PN sequence of a given length L, the optimal approximation to random noise can be shown [46] to

have an autocorrelation function, denoted $R(\tau)$, that is triangular about the zero-delay point, and takes on a constant value of $-1/L$ elsewhere (see Figure 2.1). Such a sequence is called a maximal-length sequence (m-sequence). For the GPS

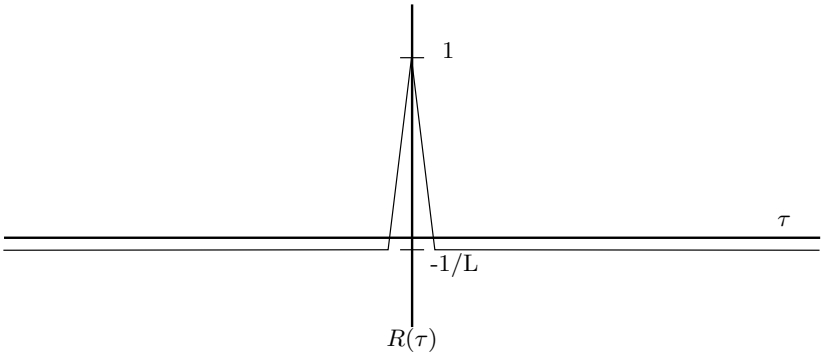


Figure 2.1: Autocorrelation Function of an m-sequence

signal, the bandwidth of the data-signal is approximately 100 Hz, whereas the bandwidth of the spreading code is just over 2 MHz[†]. The power spectral density (PSD) of the resulting spread-spectrum signal is well below the noise-floor, as indicated in Figure 2.2 (note that this figure is not shown to scale).

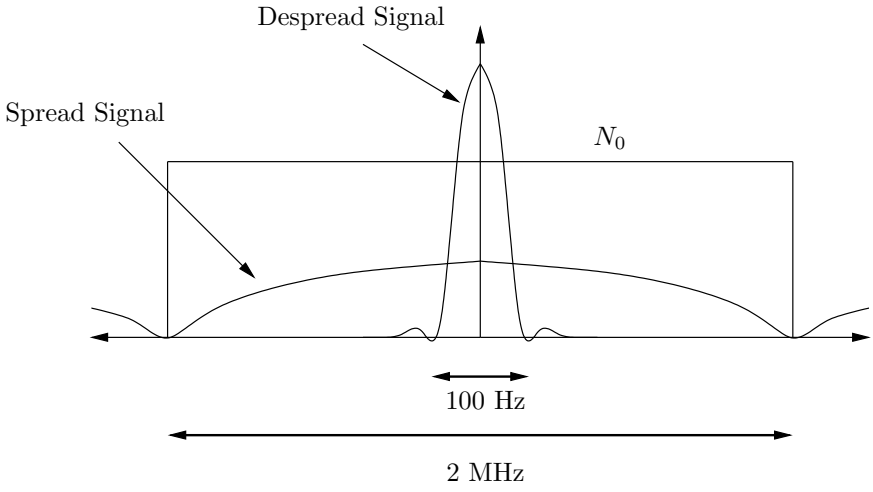


Figure 2.2: GPS Signal Bandwidths, Spread and De-spread

To provide multi-access communications, the PN codes must have very low cross-correlation values. This allows the receiver to correlate the incoming signal

[†]We treat both the data signal and the spreading code as random sequences of ± 1's. The power spectral density in each case is of form $\sin(x)/x$. The bandwidths given above are the *main lobe widths*, or null-to-null bandwidths, as indicated in Figure 2.2.

with a locally-generated copy of the PN code for the satellite of interest: the received signal component from that satellite will be de-spread when the received and local codes are aligned, while those components from other satellites will be, at most, partially de-spread.

For the GPS C/A signal, the codes chosen are length 1023 ($= 2^{10} - 1$) Gold Codes [45], which are a family of sequences providing a guaranteed maximum cross-correlation value at the expense of a slight degradation in the autocorrelation function (relative to an m-sequence). In fact, for the length 1023 Gold codes, the autocorrelation side-lobes and the cross-correlation values are limited to the three values: $63/1023, -1/1023$ and $-65/1023$, as illustrated in Figure 2.3 (not drawn to scale). Finally, the GPS signal is also modulated by a 50 bps data

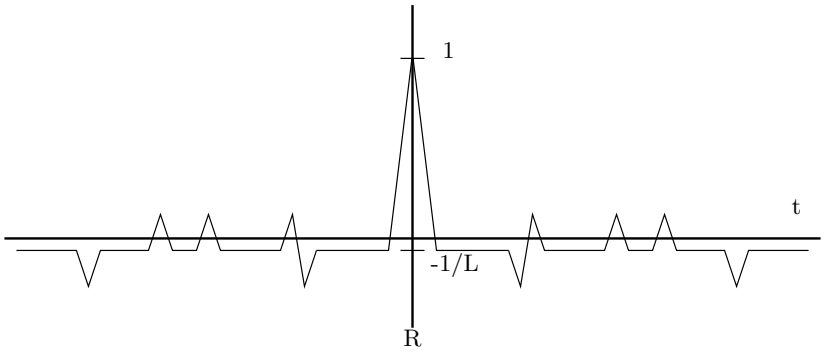


Figure 2.3: Autocorrelation Function for Gold Codes: Note that the cross-correlation function is nearly identical in form, lacking only the main-lobe.

sequence. The modulation scheme is a simple binary phase shift keying (BPSK) scheme, with $D = 20$ code periods per data-bit. The data modulation is synchronous with the spreading code, so data-bit boundaries occur at the start of a PN code sequence. At each data boundary we assume that there is a probability of 0.5 of a bit transition occurring. A bit transition leads to a phase shift of π rad, *i.e.* a change in sign.

2.2 Acquisition is an Estimation Problem

The purpose of the signal processing block of a GPS receiver is to demodulate the data signal of interest, establish the signal transit time and Doppler offset from that satellite and pass all this information to the navigation processing unit where a navigation solution will be produced. From our signal model of Equation (2.1),

and using Equation (2.2) to model the difference in timing between transmitter and receiver, we see that, for a given satellite, the unknown signal parameters are:

1. The satellite space vehicle number (SVN): i.
2. The code phase offset: ζ_i.
3. The Doppler frequency offset: ω_{d_i}.
4. The instantaneous signal power: P_i.
5. The data signal: d_i.
6. The initial phase offset: ϕ_i.

To obtain a position solution the receiver must be able to track the received signal from a number of satellites, for a time duration that is sufficient to ensure that reliable estimates of these parameters can be made. This process requires synchronisation between the transmitter and receiver. This synchronisation is usually achieved in two steps. The first step is a coarse synchronisation, which we call *acquisition*, and the second step is a fine tuning process, usually called *tracking*.

The acquisition problem can be formulated as a parameter estimation problem. Parameter estimation theory is a well-known and much researched topic in the field of probability and statistics (see [54, 66, 111, 142], for example) and defines a number of (goal specific) "optimal" approaches to the solution of the acquisition problem. The approach is similar in each case: a signal is transmitted by a source, with a set of parameters which we denote by the vector $\boldsymbol{\theta}_t$, where the subscript t indicates that this is the "true" parameter vector, the estimator makes a number, denoted N, of observations of the received signal from which is formed the observation vector: $\boldsymbol{r} = \{r_0, r_1, \ldots, r_{N-1}\}$. The parameter point $\widehat{\boldsymbol{\theta}}$ which minimises some suitably chosen cost function is selected as the best estimate of $\boldsymbol{\theta}_t$ given $\boldsymbol{r}$.

All key estimation techniques rely on knowledge of the PDF of the received signal conditioned on the true parameters, which is denoted $f_{\boldsymbol{r}|\boldsymbol{\theta}}(\boldsymbol{r} \mid \boldsymbol{\theta})$. This PDF denotes the *a priori* probability of observing the vector $\boldsymbol{r}$ given that the signal parameters are given by $\boldsymbol{\theta}$. Thus, $f_{\boldsymbol{r}|\boldsymbol{\theta}}(\boldsymbol{r} \mid \boldsymbol{\theta})$ can be viewed as a function of $\boldsymbol{r}$ parameterised by $\boldsymbol{\theta}$. Upon receiving the signal the problem is now inverted: we

now know $\boldsymbol{r}$, but do not know $\boldsymbol{\theta}$. In this case, we consider $f_{\boldsymbol{r}|\boldsymbol{\theta}}(\boldsymbol{r} \mid \boldsymbol{\theta})$ to be a function of $\boldsymbol{\theta}$ parameterised by $\boldsymbol{r}$. We say that $f_{\boldsymbol{r}|\boldsymbol{\theta}}(\boldsymbol{r} \mid \boldsymbol{\theta})$ is a measure of the *likelihood* that the true parameter vector is $\boldsymbol{\theta}$ given that the observation vector is $\boldsymbol{r}$. For this reason, $f_{\boldsymbol{r}|\boldsymbol{\theta}}(\boldsymbol{r} \mid \boldsymbol{\theta})$ is known as the *likelihood function*.

One form of optimal estimator is the minimum mean square error (MMSE) estimator. Letting $\boldsymbol{\varepsilon} = \widehat{\boldsymbol{\theta}} - \boldsymbol{\theta}_t$ denote the error between the estimated and true signal parameters, then the MMSE estimator is that estimator which minimises the mean square error, given by $E\left[\boldsymbol{\varepsilon}^{\mathrm{T}}\boldsymbol{\varepsilon}\right]$, where $E[\boldsymbol{x}]$ denotes the expected value [92] of the random variable (rv) $\boldsymbol{x}$ and $\boldsymbol{x}^{\mathrm{T}}$ denotes the transpose of the vector $\boldsymbol{x}$. This estimator relies on having knowledge of the *a posteriori* distribution of the true parameter vector given the observation vector which we denote $f_{\boldsymbol{\theta}|\boldsymbol{r}}(\boldsymbol{\theta} \mid \boldsymbol{r})$. In fact, it can be shown that the MMSE estimate is given by [111]:

$$\widehat{\boldsymbol{\theta}}_{MMSE} = E[\boldsymbol{\theta} \mid \boldsymbol{r}]. \tag{2.5}$$

The MMSE estimator, therefore, provides, on average, the best estimate in the mean-square sense.

A related estimator is the maximum *a posteriori* (MAP) estimator. The MAP estimate of $\boldsymbol{\theta}$ is that estimate $\widehat{\boldsymbol{\theta}}_{MAP}$ maximising the posterior probability that the estimate is correct, given that the vector $\boldsymbol{r}$ was received. The MAP estimate is, therefore, given by the solution to the equation:

$$\widehat{\boldsymbol{\theta}}_{MAP} = \arg\max_{\boldsymbol{\theta}} f_{\boldsymbol{\theta}|\boldsymbol{r}}(\boldsymbol{\theta} \mid \boldsymbol{r}). \tag{2.6}$$

where $\max_{\boldsymbol{\theta}} f(\boldsymbol{\theta})$ denotes the maximum value of $f(\boldsymbol{\theta})$ as a function of $\boldsymbol{\theta}$ and $\arg\max_{\boldsymbol{\theta}} f(\boldsymbol{\theta})$ denotes the *argument* of the function $f(\boldsymbol{\theta})$ when it takes on its maximum value. The MAP and MMSE estimates of $\boldsymbol{\theta}_t$ coincide if the expected value and the peak of the *a posteriori* PDF coincide. While this will not be the case in general, it does hold for any symmetric, uni-modal distribution, such as the Gaussian. Whilst the MMSE and MAP estimates are derived based on different optimisation criteria, they do coincide for certain types of *a posteriori* distributions.

The difficulty with both MMSE and MAP estimation is the reliance on the availability of $f_{\boldsymbol{\theta}|\boldsymbol{r}}(\boldsymbol{\theta} \mid \boldsymbol{r})$. In practice, we normally have an expression for $f_{\boldsymbol{r}|\boldsymbol{\theta}}(\boldsymbol{r} \mid \boldsymbol{\theta})$,

and these two distributions are related by Bayes' theorem [102, p. 20]:

$$f_{\boldsymbol{\theta}|\boldsymbol{r}}(\boldsymbol{\theta} \mid \boldsymbol{r}) = \frac{f_{\boldsymbol{r}|\boldsymbol{\theta}}(\boldsymbol{r} \mid \boldsymbol{\theta}) f_{\boldsymbol{\theta}}(\boldsymbol{\theta})}{f_{\boldsymbol{r}}(\boldsymbol{r})}. \tag{2.7}$$

However, often we do not have expressions for $f_{\boldsymbol{\theta}}(\boldsymbol{\theta})$ or $f_{\boldsymbol{r}}(\boldsymbol{r})$, and this is indeed the case in GPS signal acquisition. In such cases an alternative estimate, the maximum likelihood (ML) estimate, is commonly used. As we have already seen, the likelihood function of the parameter point $\boldsymbol{\theta}$ is simply the *a priori* probability of the received data signal $\boldsymbol{r}$ given $\boldsymbol{\theta}$. The ML estimate is, therefore, given by the solution to:

$$\widehat{\boldsymbol{\theta}}_{ML} = \arg \max_{\boldsymbol{\theta}} f_{\boldsymbol{r}|\boldsymbol{\theta}}(\boldsymbol{r} \mid \boldsymbol{\theta}). \tag{2.8}$$

It is interesting to note that, under the condition that $f_{\boldsymbol{\theta}}(\boldsymbol{\theta})$ is independent of $\boldsymbol{\theta}$, the ML and MAP estimates are equivalent. Thus, when all the parameters are uniformly distributed, the ML and MAP estimates are identical. Assigning a uniform distribution to $\boldsymbol{\theta}$ is, essentially, equivalent to having zero *a priori* information about $\boldsymbol{\theta}$.

In certain cases we may not be interested in estimating *all* of the unknown parameters. For instance, in GPS signal acquisition, the initial phase offset ϕ is unknown, but no attempt is made to estimate it. Such parameters are referred to as nuisance parameters, and estimators are typically designed to be invariant to the nuisance parameters. This is achieved by specifying the conditional likelihood function, which depends on the nuisance parameters, then defining the likelihood function to be the expectation of the conditional likelihood, with expectation taken over the distribution of the nuisance parameters. Thus, letting $\boldsymbol{\psi}$ denote the vector of nuisance parameters [66]:

$$f_{\boldsymbol{r}|\boldsymbol{\theta}}(\boldsymbol{r} \mid \boldsymbol{\theta}) = E_{\boldsymbol{\psi}}\big[f_{\boldsymbol{r}|\boldsymbol{\theta},\boldsymbol{\psi}}(\boldsymbol{r} \mid \boldsymbol{\theta}, \boldsymbol{\psi})\big],$$

where $E_{\boldsymbol{\psi}}[f(\boldsymbol{\psi})]$ denotes the expected value of $f(\boldsymbol{\psi})$ with respect to the rv $\boldsymbol{\psi}$, and estimation proceeds as normal. We will consider nuisance parameters, and ways to deal with them, in more detail in Section 2.3.

Having given this brief overview of estimation theory, it is worth pointing out that the GPS signal acquisition problem differs from the pure estimation problem in the following important ways:

1. In the acquisition problem we are never totally sure that the signal is actu-

ally present, hence the problem is generally a combined *detection/estimation* problem.

2. The acquisition problem is concerned with obtaining a *coarse* estimate of $\boldsymbol{\theta}_t$. Hence, rather than trying to minimise the mean-square error, it would usually be more appropriate to try to maximise the probability that the error is within some predefined bound. This bound is normally determined by the *pull-in range* [20] of the tracking loops.

3. Of particular importance in the acquisition problem is the *time* taken to acquire the signal, denoted T_{ACQ}. In fact, much of the remainder of this thesis will express the analysis of receiver performance in terms of T_{ACQ}. In the estimation problems discussed earlier no importance was placed on the time taken to make an estimate. T_{ACQ} is, of course, intimately related to N, the number of samples observed and $1/T_s$, the rate at which samples are taken.

2.2.1 Estimation Theory and GPS

For the GPS acquisition problem the likelihood function is known and so an ML estimation approach is taken. Considering Equation (2.1); assuming we are interested in acquiring the signal from satellite k and $k \in \mathcal{S}_{sv}$ (*i.e.* the signal from satellite k is actually present at the receiver antenna), then we can re-write Equation (2.1) as:

$$\begin{aligned} r(t) =& \sqrt{\frac{P_k(t)}{2}} d_k(t_k(t)) c_k(t_k(t)) \exp\left(j\left(\omega_0 t_k(t) + \phi_k\right)\right) \\ &+ \sum_{\substack{i \in \mathcal{S}_{sv} \\ i \neq k}} \sqrt{\frac{P_i(t)}{2}} d_i(t_i(t)) c_i(t_i(t)) \exp\left(j\left(\omega_0 t_i(t) + \phi_i\right)\right) + n(t). \end{aligned} \tag{2.9}$$

Since, in practice, the signal power from each satellite is so low (≤ -160 dBW), and the spectrum so broad (2 MHz null-to-null), then the total signal power received from all satellites is still well below the noise floor[†]. Thus, the sum total contribution from all the satellites that we are not interested in acquiring can be

[†]With 12 satellites in view, all of which are received with a signal power of -160 dBW, the total signal power received is still about 4 dB below the total noise power in a 2 MHz bandwidth, assuming a noise PSD of -203.8 dBW/Hz [140]

modelled as an additional contribution to the Gaussian noise term $n(t)$, resulting in the following approximation to Equation (2.9):

$$r(t) = \sqrt{\frac{P_k(t)}{2}} d_k(t_k(t)) c_k(t_k(t)) \exp\left(j\left(\omega_0 t_k(t) + \phi_k\right)\right) + \widetilde{n}(t) \tag{2.10}$$

$$= s_k(t) + \widetilde{n}(t) \tag{2.11}$$

where $\widetilde{n}(t)$ is a zero mean complex AWGN process with single-sided PSD N_0 W/Hz. The observation vector $\boldsymbol{r}$ is formed by sampling $r(t)$ at N time intervals uniformly separated by T_s seconds such that:

$$\boldsymbol{r} = \left[r(0), r(T_s), r(2T_s), \ldots, r((N-1)T_s)\right]^{\mathrm{T}},$$

and so $\boldsymbol{r}$ has an N-dimensional complex Gaussian distribution. The likelihood function is, therefore, given by† [54, Appendix B]:

$$f_{\boldsymbol{r}|\boldsymbol{\theta}}(\boldsymbol{r} \mid \boldsymbol{\theta}) = \pi^{-N} \left|\boldsymbol{C}\right|^{-1} \exp\left(-(\boldsymbol{r}-\boldsymbol{\mu})^{\mathrm{H}} \boldsymbol{C}^{-1} (\boldsymbol{r}-\boldsymbol{\mu})\right), \tag{2.12}$$

where $\boldsymbol{x}^{\mathrm{H}}$ denotes the combined operation of transposition and complex conjugation on the complex vector $\boldsymbol{x}$ (often called the Hermitian transpose), $\boldsymbol{C}$ is the $N \times N$ covariance matrix of the Gaussian noise samples defined by:

$$\boldsymbol{C} \triangleq E_{\boldsymbol{r}}\left[\boldsymbol{r}\boldsymbol{r}^{\mathrm{H}}\right], \tag{2.13}$$

$|\boldsymbol{C}|$ denotes the determinant of $\boldsymbol{C}$ and $\boldsymbol{\mu}$ is the vector of mean values $\boldsymbol{\mu} = E[\boldsymbol{r}]$. Note that $\boldsymbol{\mu}$ is equal to the vector of signal components $\boldsymbol{s}_k$, defined in Equation (2.11):

$$\boldsymbol{s}_k = \left[s(0), s(T_s), s(2T_s), \ldots, s((N-1)T_s)\right]^{\mathrm{T}}.$$

Note that the variable $\boldsymbol{\mu}$ contains all the information relating to the parameter vector $\boldsymbol{\theta}$: $\boldsymbol{\mu} = \boldsymbol{s}_k(\boldsymbol{\theta})$.

We assume that the noise samples in the I and Q channels are mutually independent with variance σ^2, so that the covariance matrix is given by $\boldsymbol{C} = \sigma^2 \boldsymbol{I}$, where $\boldsymbol{I}$ denotes the $N \times N$ identity matrix. The likelihood function can, therefore,

†This complex distribution should be viewed as a short-hand representation of the joint PDF of the in-phase and quadrature components, rather than as a true PDF. For example, one cannot compute the (meaningless) probability $\Pr\{\boldsymbol{r} < \boldsymbol{w}\}$ by performing a complex integration of Equation (2.12) over the region of N-dimensional complex space for which $\boldsymbol{r} < \boldsymbol{w}$.

be written:

$$f_{\boldsymbol{r}|\boldsymbol{\theta}}(\boldsymbol{r} \mid \boldsymbol{\theta}) = \pi^{-N}\sigma^{-2N} \exp\left(\frac{-1}{\sigma^2}(\boldsymbol{r} - \boldsymbol{s}_k(\boldsymbol{\theta}))^{\mathrm{H}}(\boldsymbol{r} - \boldsymbol{s}_k(\boldsymbol{\theta}))\right) . \tag{2.14}$$

Given that σ^2 is known, maximising the likelihood function is equivalent to maximising (note the presence of the minus sign on the left hand side):

$$-(\boldsymbol{r} - \boldsymbol{s}_k(\boldsymbol{\theta}))^{\mathrm{H}}(\boldsymbol{r} - \boldsymbol{s}_k(\boldsymbol{\theta})) = -|\boldsymbol{r}|^2 - |\boldsymbol{s}_k(\boldsymbol{\theta})|^2 + 2\Re\{\boldsymbol{r} \cdot \boldsymbol{s}_k(\boldsymbol{\theta})\}, \tag{2.15}$$

where $\Re\{z\}$ denotes the real part of the complex number z. The term $|\boldsymbol{r}|^2$ is unaffected by our estimate, and so we can reduce the ML estimation problem to the determination of that vector $\widehat{\boldsymbol{\theta}}$ which maximises the metric[†]:

$$D_k(\boldsymbol{\theta}) = 2\Re\{\boldsymbol{r} \cdot \boldsymbol{s}_k(\boldsymbol{\theta})\} - |\boldsymbol{s}_k(\boldsymbol{\theta})|^2, \tag{2.16}$$

which we refer to as the *decision statistic* for satellite k. In general, we denote by D_k the decision statistic for satellite k, whatever form that decision statistic may take. The metric above consists of two components, the first is given by twice the real part of the correlation between the observation vector and the signal vector, the second is a measure of the energy in the signal vector, and can be viewed as a biasing term. The first component is our first encounter with what we will refer to as a *correlative form*. We will see that, in general, the optimal estimator or detector can be expressed through some metric involving the correlation of the received signal and the known form of the signal to be detected/estimated.

Hurd et al. [58] were perhaps the first to investigate an estimation theoretic approach to the GPS signal, though this work focused on tracking rather than the acquisition problem and was applied to the P-code[‡] rather than the C/A-code. As a result, the authors do not consider the effects of data modulation. The signal parameters are therefore: the code phase offset ζ, the Doppler offset ω_d, the signal power P and the initial carrier phase offset ϕ. The desired parameter space is the two-dimensional space with elements $\boldsymbol{\theta} = [\zeta, \omega_d]$, while the nuisance parameter space is the two-dimensional space with elements $\boldsymbol{\psi} = [P, \phi]$. The ML estimate of the true desired parameter vector, $\boldsymbol{\theta}_t$, is shown in [58] to be given by

[†]This metric is essentially equivalent to a discrete form of [58, Equation (2.10)].

[‡]The P-code is a restricted access military code which is transmitted along with the civilian C/A-code. The P-code has a chip-rate ten times the C/A-code rate, and a period of one week. We do not consider it further in this thesis.

$\widehat{\boldsymbol{\theta}} = \left[\widehat{\zeta}, \widehat{\omega_d}\right]$, such that the expression [58, Equation (2.15)]:

$$\left| \int_0^{NT_s} r(t) c_k(t - \widehat{\zeta} T_{\text{chip}}) \exp\left(-j\widehat{\omega_d} t\right) dt \right|^2$$

is maximised. This result corresponds to an analogue receiver, the discrete-time equivalent is given by the metric:

$$D_k(\boldsymbol{\theta}) = \left| \boldsymbol{r} \cdot \boldsymbol{s}_k(\boldsymbol{\theta}) \right|^2 , \tag{2.17}$$

where, in this case:

$$\boldsymbol{s}_k(\widehat{\boldsymbol{\theta}}) = \left\{ c_k(nT_s - \widehat{\zeta} T_{\text{chip}}) \exp\left(-j\widehat{\omega_d} n T_s\right) \right\}_{n=0,1,\ldots,N-1} .$$

Note that this metric differs from that in Equation (2.16) above. This difference arises due to the averaging over the nuisance parameters (P and ϕ). Note that the metric of Equation (2.17) is independent of the both the received signal power $|\boldsymbol{s}_k|^2$ and the phase of the received signal, ϕ. This metric again exhibits the correlative form, though, in this case, the square magnitude of the correlator output is taken. The maximum likelihood (ML) estimate of $[\zeta_t, \omega_{dt}]$ is obtained by maximising the metric of Equation (2.17), under the conditions that both the Doppler offset and the received signal power are constant over the observation interval. Note that, in the presence of fading or data modulation[†], this estimator is no longer optimal in the maximum likelihood (ML) sense. It is also interesting to note that the metric is independent of the received signal power, P. The same receiver can be used to provide the ML estimate $\widehat{\boldsymbol{\theta}}_{ML}$, irrespective of the received signal-to-noise ratio (SNR). Of course, we would expect that the estimator performance, in terms of the mean square error, will degrade for decreasing SNR. As the SNR decreases the length, N, of the observation vector must be increased to maintain estimator performance. Thus, the acquisition time, T_{ACQ}, will increase as the received signal strength decreases.

In practice, the authors of [58] implement what they term an approximate maximum likelihood estimator (AMLE), in which the function $D_k(\boldsymbol{\theta})$ above is evaluated over a finite grid in the uncertainty space. The AMLE simply chooses

[†]Sudden phase changes due to data bit transitions can be thought of as impulses in the Doppler domain.

that point in the grid for which the metric is a maximum as an approximation to the ML estimate. This is a common approach in the acquisition of DS/SS signals, since, as previously mentioned, a high degree of accuracy is generally not required at this stage.

In [25], Chawla and Sarwate define an optimal estimator of the code-phase offset, ζ, for a general DS/SS system under the assumption that the Doppler offset, ω_d, equals zero and the signal of interest is free of data modulation. The desired parameter space is, therefore, one dimensional, θ_t is a scalar and there are no nuisance parameters. The Chawla/Sarwate optimal estimator is based on the MAP estimator above (see Equation (2.6)) but, rather than maximising the *a posteriori* probability density, the probability that the estimate is within a certain range of θ_t is maximised. In addition, this estimator operates, not directly on the received signal $\boldsymbol{r}$, but rather on the correlation of the received signal and the PN code of the signal of interest. Given that the tracking loop pull-in range is given by Δ[†], the Chawla/Sarwate optimal estimate is given by:

$$\widehat{\theta}_{CS} = \arg \max_{\widehat{\theta}} \int_{\widehat{\theta}-\Delta}^{\widehat{\theta}+\Delta} f_{\theta_t|\boldsymbol{x}}(u \mid \boldsymbol{x}) du, \tag{2.18}$$

where $\boldsymbol{x}$ is the vector of correlator outputs at whole-chip intervals in the code-phase dimension. It is interesting to note that, whereas the correlative form arose naturally in the ML estimator of Hurd et al., Chawla and Sarwate assume the correlative form as a starting point for their estimator.

The Chawla/Sarwate estimator has a number of drawbacks: 1) it is computationally intensive, involving the determination of the local extrema of a polynomial function, followed by the evaluation of terms involving the Gaussian integral at these local extrema to determine the global extremum; 2) it is not readily extensible to the case of unknown Doppler offset, as the *a posteriori* PDF is generally not available in this case. The authors consider a number of simplifications to counter these difficulties. Firstly, the search space is discretised, this is exactly the same approach as taken by Hurd et al. Secondly, the *estimate* is also discretised, thereby effectively transforming the problem from an estimation problem to a detection problem. The probability that the signal resides in each cell is calculated and the cell with the maximum probability is chosen as the true cell.

[†]If the initial code phase offset error is greater than Δ, the tracking loop will not converge on the true code phase offset.

A simplified form of this estimator is implemented by simply choosing that value of l such that the metric $x_l + x_{l+1}$ is maximised, where x_l denotes the l^{th} correlator output. This last approach is called the locally optimum detector.

This approach was expanded on by Srinivasan and Sarwate [129], where a simple approximation to the optimal estimation scheme is considered. In this case the maximum output of the correlator is selected $l^* = \arg\max \boldsymbol{x}$ where, again, $\boldsymbol{x}$ is the vector of correlator outputs, and an improved estimate of the true code-phase offset is obtained by the interpolation formula:

$$\widehat{\zeta} = l^* + \frac{x_{l^*+1} - x_{l^*-1}}{2\left(2x_{l^*} - x_{l^*-1} - x_{l^*+1}\right)}.$$

2.2.2 Practical Considerations

Whilst the DS/SS signal acquisition problem is fundamentally an estimation problem, this approach was adopted at a comparatively late stage in the topic's history. This is primarily due to the excessive hardware and computational requirements of the estimation theoretic approach. In practice, signal acquisition is usually implemented as a signal detection problem. We will discuss detection theory and its application to this problem in the next section. Initially, however, we highlight some of the practical issues which arise in both the detection and estimation approaches.

We have seen (Equation (2.16)) that the correlative form arises in the general problem of ML estimation, and we will see in the next section that this form arises also in the context of the detection problem. In practice, this can be implemented in one of two ways:

1. Correlator receiver: the received signal is cross-correlated with all possible vectors $\boldsymbol{s}_k(\boldsymbol{\theta})$ and the argument of the maximum value is chosen as $\widehat{\theta}_{ML}$.

2. Matched filter receiver: for each possible $\boldsymbol{\theta}_t$ the received signal is passed through a filter matched to $\boldsymbol{s}_k(\boldsymbol{\theta}_t)$, and again the argument of the maximum value is chosen as $\widehat{\theta}_{ML}$.

From an implementation perspective, the correlator receiver is a very simple architecture to implement, requiring very little circuit area. The matched filter approach is more complex, but has a much faster decision rate. The correlator architecture makes one decision for every N samples input, whereas the matched

filter requires N samples to start, but can make a decision at every sample thereafter. Traditionally, matched filtering has not been implemented for GPS receivers, though interest has been increasing of late, particularly in relation to the modernised and military signals [33]. Nonetheless, we focus on the active correlator architecture in the remainder of this thesis.

One major difficulty with the ML receiver architecture is that $\boldsymbol{\theta}_t$ is a continuous variable and, hence, can take on an infinite number of values. The maximum likelihood estimate is made by evaluating the metric $D_k(\boldsymbol{\theta})$ at all possible values of $\boldsymbol{\theta}$ and choosing that value $\widehat{\boldsymbol{\theta}}$ that maximises the metric. If $\boldsymbol{\theta}$ is a continuous variable, this would require evaluating the metric at an infinite number of points. As we have already seen for both the Hurd/Statman/Vilnrotter and Chawla/ Sarwate estimators, this difficulty is easily overcome using the sampling theorem [102]. In practice, a discrete number of correlator (or matched filter) outputs are calculated, usually evenly distributed through the parameter space Θ. By the sampling theorem, the value of the metric $D_k(\boldsymbol{\theta})$ can be reconstructed from these correlator outputs provided that, for every dimension in Θ, the frequency of samples in that dimension is greater than twice the maximum frequency component of $D_k(\boldsymbol{\theta})$ in that dimension. Thus, the outputs of a finite number of correlators can be used to determine the maximum likelihood estimate $\widehat{\theta}_{ML}$.

This discretisation is demonstrated in Figure 2.4, where a two dimensional search grid is shown. The true parameter vector is

$$\boldsymbol{\theta}_t = [\zeta_t = 233\text{chips}, \omega_{dt} = -879\text{Hz}]$$

and the correlation function has been formed over 2ms of samples with 2048 samples[†] per ms. There are a total of 2048 points in the code-phase dimension and 40 points in the Doppler dimension, for a total of $81,920$ correlator outputs. The ML estimator uses information from all these points to determine the optimal estimate of $\boldsymbol{\theta}_t$. Clearly, this represents a significant computational requirement.

A second practical issue is the choice of the spacing of the sample points in the parameter uncertainty space. To determine the distribution of samples of $D_k(\boldsymbol{\theta})$ required to make a reasonable estimate of $\boldsymbol{\theta}_t$, we consider the functional relationship between the correlator outputs and the received signal in the absence

[†]The number of samples has been specifically chosen to be a power of 2 to facilitate the use of the fast Fourier Transform in the computation of the correlation function. This will be discussed in more detail in Section 2.4.4.

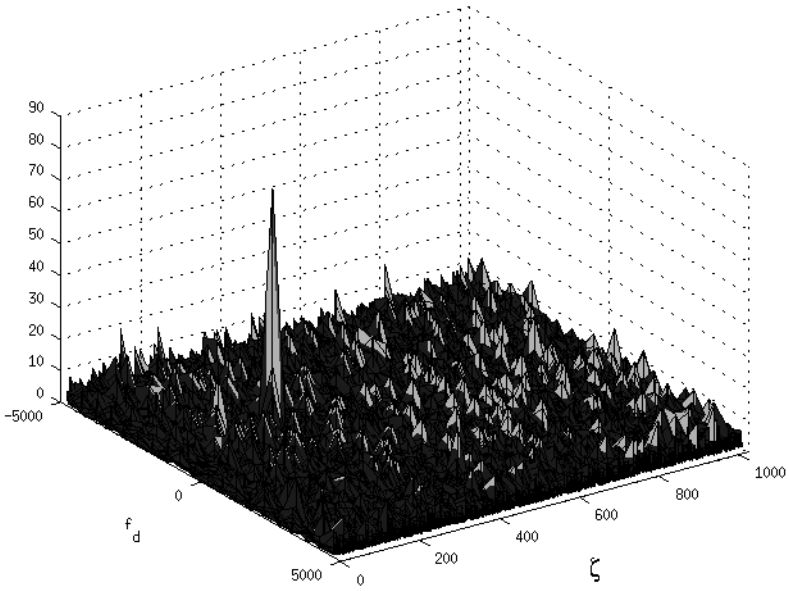


Figure 2.4: The acquisition grid for a simulated signal with $C/N_0 = 43.8$ dB-Hz and 2 ms coherent integration. The true code phase is 233 chips and the true Doppler offset is -879 Hz.

of noise. This relationship is illustrated graphically in Figure 2.5. Again, we consider the two dimensions $[\zeta, \omega_d]$. Since we are primarily interested in having sufficient samples of $D_k(\boldsymbol{\theta})$ in the vicinity of $\boldsymbol{\theta}_t$, we consider the following two cases:

1. Given $\omega_d = 0$, we look at the metric as a function of ζ: $D_k(\zeta \mid \omega_d = 0)$
2. Given $\zeta = 0$, we look at $D_k(\omega_d \mid \zeta = 0)$.

Initially we consider sampling in the code phase domain. Our metric calculates the correlation of the received signal with the local code, and we have seen in Section 2.1 that the auto-correlation function of Gold codes is triangular about the zero delay point. A sample spacing of 0.5 code chips is often chosen, as this ensures the correlation peak is not missed. This is illustrated in Figure 2.6. We denote by $\delta\zeta$ the residual code-phase offset at the sample closest to the true peak. This is a measure of the accuracy of our measurement. The sample spacing may also be chosen for other reasons, for instance in the example of Figure 2.4 we chose a uniform sample spacing with $2,048$ samples per code period. This represents a sample spacing of just under 0.5 chips. The reason for choosing this

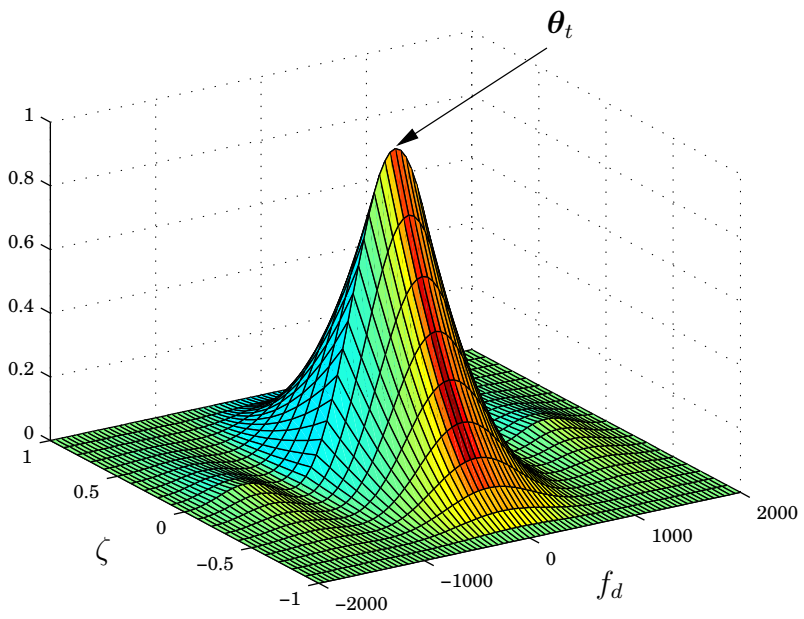


Figure 2.5: Normalised Correlator Output vs Code and Doppler Offsets in the Absence of Noise

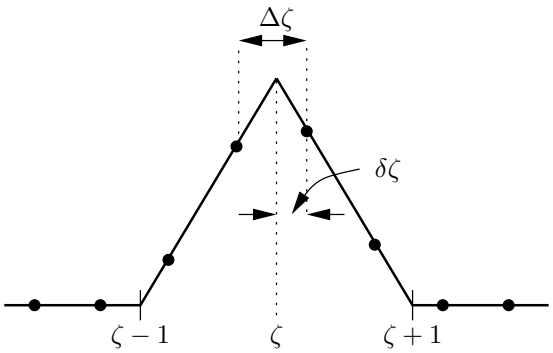


Figure 2.6: Sampling in the Code-Phase Domain: $\Delta\zeta = 0.5$ chips

particular number is that it is an integer power of 2 ($2,048 = 2^{11}$) and, hence, the correlation function can be very efficiently calculated using the Fast Fourier Transform (FFT) (this will be discussed in more detail in Section 2.4.4).

To determine a suitable sampling rate in the Doppler domain we consider the effect of the *residual* Doppler offset, defined by $\delta\omega_d = \omega_d - \widehat{\omega_d}$, on the correlator output under the zero-noise assumption. It can be shown [133] that, in the presence of a residual Doppler offset of $\delta\omega_d$ rad/s, the signal power at the output

of the correlator is multiplied by an attenuation factor, denoted $\alpha_D(\delta\omega_d)$, where:

$$\alpha_D(\delta\omega_d) = \left| \frac{1}{N_s M} \frac{\sin\left(\delta\omega_d M N_s T_s/2\right)}{\sin\left(\delta\omega_d T_s/2\right)} \right|^2 \approx \left|\mathrm{sinc}\left(\delta\omega_d M N_s T_s/2\right)\right|^2 , \qquad (2.19)$$

M is the integer number of code periods in the correlation interval, N_s is the number of samples per code period and $\mathrm{sinc}(x) = \sin(x)/x$[†]. This function is plotted as a function of $f_d = \delta\omega_d/(2\pi)$ in Figure 2.7. Recalling that the C/A code

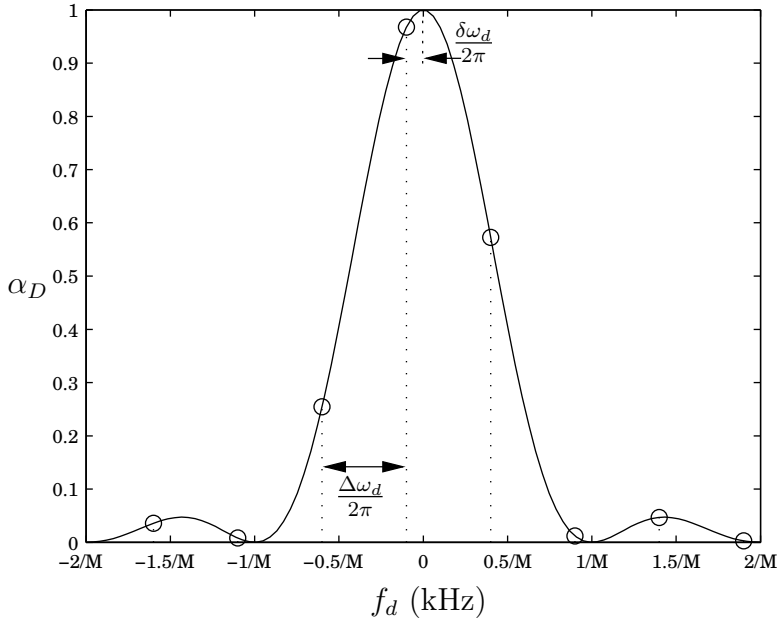


Figure 2.7: Sampling in the Doppler Domain: Samples every $\Delta f_d = \frac{\Delta\omega_d}{2\pi} = \frac{1}{2MT_{\mathrm{CA}}}$ Hz= $\frac{1}{2M}$ kHz.

period is $T_{\mathrm{CA}} = 1$ ms, then suitable choice of $\Delta\omega_d$ is $\frac{1}{MT_{\mathrm{CA}}}$ Hz, which ensures a maximum attenuation of about 4dB due to frequency sampling effects. Note that the sampling is a function of M, and, for example, as the correlation period M increases, the spacing of correlators in the frequency domain must be decreased to compensate. Hence, making longer observations will necessitate the use of more correlators. This relationship is linear; *i.e.* a K-fold increase in the observation interval implies a K-fold increase in the number of correlators required to cover the uncertainty region.

This is a significant problem for weak signal acquisition: to increase the sensitivity of the receiver we increase the number of samples accumulated and, there-

[†]Note that $\mathrm{sinc}(x)$ is often defined as $\sin(\pi x)/(\pi x)$.

fore, we must also increase the number of correlators used to cover the same frequency uncertainty region. Thus, to acquire weak signals requires more time *and* more hardware to maintain system performance levels.

2.3 Acquisition is a Detection Problem

Whereas in the previous section we have identified acquisition as an estimation problem, here we consider acquisition as a *detection* problem. In other words, the purpose of the acquisition unit is to detect whether or not a signal from a given satellite is present at the receiver antenna. In reality, acquisition is a combined detection/estimation problem. We begin with an overview of the basic concepts of detection theory.

Binary Hypothesis Testing

The simplest problem in detection theory is called the binary hypothesis test [54, 66, 111, 142], and is a useful example to illustrate the principle of detection. Consider an information source which can output one of two possible choices, as illustrated in Figure 2.8. In the simplest case, the two possibilities are that the source either produces no signal, or it produces some signal with a known form. This signal is passed through a channel and the result is the input to the decision making device, or *detector*. The purpose of the detector is to determine which of

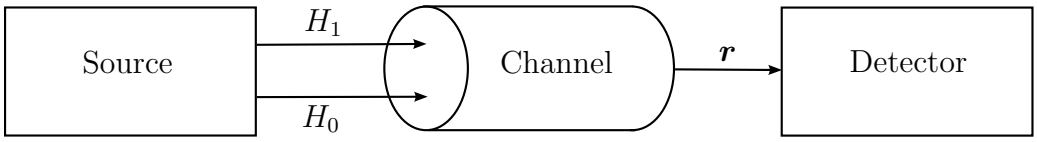


Figure 2.8: Binary Hypothesis Detector Model

the two choices was output by the source. The detector must, therefore, choose between two *hypotheses*: the first hypothesis is called the *null hypothesis* and is denoted H_0, this is usually associated with the hypothesis that the source did not output any signal. The second hypothesis is termed the *alternate hypothesis*, denoted H_1, and is usually associated with the hypothesis that the source did, in fact, output a signal. The detector will, therefore, make one of two *decisions*:

- D_0: The decision that H_0 is true,

- D_1: The decision that H_1 is true.

Thus, there are four possible outcomes to the simple binary hypothesis test, as tabulated in Table 2.1.

Decision	True Hypothesis	
	H_0	H_1
D_0	Correct Rejection	False Dismissal
D_1	False Alarm	Correct Detection

Table 2.1: The Four Possible Outcomes of a Binary Hypothesis Test

To determine the "optimal" detector we assume that the detector receives as input N observations of the received signal which together form the observation vector $\boldsymbol{r}$. The set of all possible vectors $\boldsymbol{r}$ forms an "observation space", denoted $\boldsymbol{R}$. The detector divides the observation space into two distinct regions, $\boldsymbol{R_0}$ and $\boldsymbol{R_1}$, and the decision is made as follows: if $\boldsymbol{r} \in \boldsymbol{R_1}$ then the decision D_1 is made, if $\boldsymbol{r} \in \boldsymbol{R_0}$ then the decision D_0 is made. The detector performance is, therefore, entirely dependent on how the regions $\boldsymbol{R_0}$ and $\boldsymbol{R_1}$ are chosen, and can be measured by four parameters (corresponding to the four outcomes of Table 2.1):

1. P_d: the probability of correct detection.
2. P_{fa}: the probability of false alarm.
3. P_m: the probability of a miss (probability of false dismissal).
4. P_r: the probability of correct rejection.

These probabilities are easily seen to be given by:

$$P_d = \int_{\boldsymbol{R_1}} f_{\boldsymbol{r}|H_1}(\boldsymbol{x} \mid H_1) d\boldsymbol{x} \qquad P_{fa} = \int_{\boldsymbol{R_1}} f_{\boldsymbol{r}|H_0}(\boldsymbol{x} \mid H_0) d\boldsymbol{x}$$
$$P_m = \int_{\boldsymbol{R_0}} f_{\boldsymbol{r}|H_1}(\boldsymbol{x} \mid H_1) d\boldsymbol{x} \qquad P_r = \int_{\boldsymbol{R_0}} f_{\boldsymbol{r}|H_0}(\boldsymbol{x} \mid H_0) d\boldsymbol{x}.$$

Optimisation criteria for the detector problem are determined by the degree of prior knowledge available. We denote by P_0 and P_1 the *a priori* probabilities that H_0 and H_1 are true, respectively. In situations where we have knowledge of P_0 and P_1 it is common to apply Bayes' criterion [142, p. 24] to the optimisation

of the detection problem. Here we assign "costs" to each of the four receiver outcomes: denoting by $C_{i,j}$ the cost of making decision D_i given that hypothesis H_j is true, Bayes' criterion is to minimise the cost function (also called the Bayes' risk):

$$C = C_{0,0}P_0P_r + C_{0,1}P_1P_m + C_{1,0}P_0P_{fa} + C_{1,1}P_1P_d. \tag{2.20}$$

It can be shown [111] that fulfilling Bayes' criterion is equivalent to performing the test:

$$\frac{f_{\boldsymbol{r}|H_1}(\boldsymbol{r} \mid H_1)}{f_{\boldsymbol{r}|H_0}(\boldsymbol{r} \mid H_0)} \underset{D_0}{\overset{D_1}{\gtrless}} \frac{P_0\left(C_{1,0} - C_{0,0}\right)}{P_1\left(C_{0,1} - C_{1,1}\right)}, \tag{2.21}$$

where this notation means: if the left hand side is greater than the right hand side, choose D_1, if the right hand side is greater than or equal to the left hand side choose D_0. The term $f_{\boldsymbol{r}|H_1}(\boldsymbol{r} \mid H_1)/f_{\boldsymbol{r}|H_0}(\boldsymbol{r} \mid H_0)$ is called the *likelihood ratio* of the vector $\boldsymbol{r}$, denoted $\boldsymbol{\Lambda}(\boldsymbol{r})$, and, hence, the test is known as the likelihood ratio test (LRT). In general, the LRT can be expressed as:

$$\boldsymbol{\Lambda}(\boldsymbol{r}) \underset{D_0}{\overset{D_1}{\gtrless}} \eta, \tag{2.22}$$

where η is known as the *threshold* of the test. Note that, even though $\boldsymbol{r}$ is an N-dimensional vector of complex numbers, the optimal decision rule is a simple comparison of two scalar quantities.

In situations where it is not possible to assign meaningful probabilities to P_0 and P_1 the criterion used to optimise the decision is the Neyman-Pearson criterion [142, p. 33]. In this case, the regions R_0 and R_1 are chosen to maximise the probability of detection for a given probability of false alarm. Interestingly, it can be shown that this test can again be expressed as an LRT. In this case, the decision threshold η is chosen to achieve the design point P_{fa}. In fact, given that we require $P_{fa} \leq \alpha$, the Neyman-Pearson threshold, denoted η_{NP}, is given by the solution to:

$$\alpha = \int_{\eta_{NP}}^{\infty} f_{\boldsymbol{\Lambda}(\boldsymbol{r})|H_0}\Big(\boldsymbol{\Lambda}(\boldsymbol{r}) \mid H_0\Big)\, d\,\boldsymbol{\Lambda}(\boldsymbol{r})\,. \tag{2.23}$$

The important thing to note about the Bayes and Neyman-Pearson detectors is that they both result in the comparison of the likelihood ratio (a scalar) with a single threshold. Indeed, it is easy to see that the same criteria can be met

by comparing any monotonic function[†] of the likelihood ratio with a suitably modified threshold. Any such scalar quantity is called a *sufficient statistic* for the problem.

Both the Bayes and Neyman-Pearson detectors operate on the assumption that exactly N observations of the received signal are made. This situation arises frequently, for instance, in bit-decoding where a decision must be made in each bit-interval. Thus, given that there are N samples in each bit-interval, the detector will make its decision based on N observations of the received signal. This type of detector is referred to as a fixed sample-size detector (FSSD). In certain applications the signal observations arrive in a sequential fashion and there is no limit on the observation interval. In this instance an alternate form of detector may be used, known as a *sequential detector*.

The sequential detector makes a decision on the reception of each signal observation and the decision is based on all observations up to that point in time. Thus, on reception of the n^{th} observation r_{n-1}, the detector makes a decision based on the observation vector $\boldsymbol{r_n} = [r_0, r_1, \ldots, r_{n-1}]$. In addition to the two decisions available in the FSSD, the sequential detector adds the third option:

- $D_?$: The decision that we do not have enough data to be sufficiently sure whether H_0 or H_1 is true.

The vector $\boldsymbol{r_n}$ is an element of an n-dimensional space, which we denote $\boldsymbol{R^n}$. The sequential detector divides $\boldsymbol{R^n}$ into three regions: $\boldsymbol{R_0^n}, \boldsymbol{R_1^n}$ and $\boldsymbol{R_?^n}$. As before, the decision is based on which region contains the observed vector. If the detector makes a $D_?$ decision then a new observation sample is taken. This process continues until either a D_0 or a D_1 decision is made.

Wald [144, 145] demonstrated that the sequential likelihood ratio test (which he called the sequential probability ratio test (SPRT)) is optimal in the sense that it requires the least number of samples, *on average*, of any possible detector for a given P_{fa} and P_d. Despite this advantage, the average number of samples required by the SPRT can be shown to be very sensitive to the SNR [96]. This limits its applicability in the acquisition of GPS signals and we therefore consider it no further here.

[†]A monotonic function is a function which is either non-increasing or non-decreasing over its entire range. A monotonic function is most easily identifiable by the property that its first derivative never changes sign.

Composite Hypotheses

Thus far, we have assumed that the signal models under both hypotheses are completely known by the detector. It often happens that the detector may know the general *form* of the signal under each hypothesis, but the signal depends on certain parameters that are unknown to the detector. In this case, the problem is known as a composite hypothesis test, as the detector must decide whether the received signal corresponds to one *family* of possible signals or another.

We denote by $\boldsymbol{\xi}$ the signal parameter vector and by Ξ the total signal parameter space. We assume that the received signal component has parameter vector $\boldsymbol{\xi}_t \in \Xi$. There are two possible approaches to the composite hypothesis test. The first is to attempt to design a test which is independent of $\boldsymbol{\xi}$. This may not always be possible. The second approach is to make an estimate $\widehat{\boldsymbol{\xi}}$ of $\boldsymbol{\xi}$ and design a test that operates under the assumption that $\widehat{\boldsymbol{\xi}} = \boldsymbol{\xi}_t$.

The first approach is only useful if we have no interest in what the actual parameters are. We will, therefore, divide the parameter vector into two components, as we did for the estimation problem. We denote by $\boldsymbol{\theta} \in \Theta$ the vector of parameters that we would like to estimate (the *desired* parameters) and by $\boldsymbol{\psi} \in \Psi$ the vector of nuisance parameters. Further, we assume that $\Xi = \Theta \cup \Psi$. Thus, combining the two approaches mentioned above, the detector will implement a test that relies on an estimate of $\boldsymbol{\theta}$, but is independent of $\boldsymbol{\psi}$.

Considering firstly the design of a test independent of $\boldsymbol{\psi}$, there are a number of possibilities:

- $\boldsymbol{\psi}$ is a rv with a known distribution, $f_{\boldsymbol{\psi}}(\boldsymbol{\psi})$.
- $\boldsymbol{\psi}$ is an rv with an unknown distribution.
- $\boldsymbol{\psi}$ is not an rv.

When $\boldsymbol{\psi}$ is an rv with a known distribution, then the LRT can be used as before, with [142, Equation (296)]:

$$\boldsymbol{\Lambda}(\boldsymbol{r}) = \frac{f_{\boldsymbol{r}|H_1}(\boldsymbol{r} \mid H_1)}{f_{\boldsymbol{r}|H_0}(\boldsymbol{r} \mid H_0)} = \frac{E_{\boldsymbol{\psi}}\big[f_{\boldsymbol{r}|H_1,\boldsymbol{\psi}}(\boldsymbol{r} \mid H_1, \boldsymbol{\psi})\big]}{E_{\boldsymbol{\psi}}\big[f_{\boldsymbol{r}|H_0,\boldsymbol{\psi}}(\boldsymbol{r} \mid H_0, \boldsymbol{\psi})\big]}. \tag{2.24}$$

Unfortunately, it may not be possible to evaluate the expectation operations in closed form and, even if it is possible, the resulting expression will often not be easy to implement [66].

The latter two cases (when $\boldsymbol{\psi}$ is either an rv with unknown distribution or is not an rv) can be treated together. In this instance, efforts to design a test that is independent of $\boldsymbol{\psi}$ proceed on a more *ad hoc* basis. A common approach [111] is to investigate the likelihood ratio (or any sufficient statistic) as a function of $\boldsymbol{\psi}$, and to try to derive a mapping, $f(\boldsymbol{r})$, of the observation vector such that the result is *invariant* to changes in $\boldsymbol{\psi}$, *i.e.*:

$$\nabla_{\boldsymbol{\psi}} \boldsymbol{\Lambda} \left(f(\boldsymbol{r}) \mid \boldsymbol{\psi} \right) = 0.$$

From a signal-space perspective this is equivalent to projecting the true parameter vector $\boldsymbol{\xi}_t$ onto the subspace Θ. The likelihood ratio test then becomes:

$$\boldsymbol{\Lambda} \left(f(\boldsymbol{r}) \right) \underset{D_0}{\overset{D_1}{\gtrless}} \eta(\boldsymbol{\psi}).$$

Note that the left-hand side of this expression is independent of the nuisance parameters. If the mapping f can be chosen such that the threshold $\eta(\boldsymbol{\psi})$ is also independent of the nuisance parameters, then the test is known as a uniformly most powerful (UMP) test [142, Section 2.5]. This nomenclature comes from the original statistical theory of binary hypothesis tests, where the quantity we refer to as P_{fa} was known as the *size* of a test, and P_d was known as the *power* of a test. A UMP test is a test of a given size whose power is greater than or equal to the power of *any* other test of the same, or lesser, size.

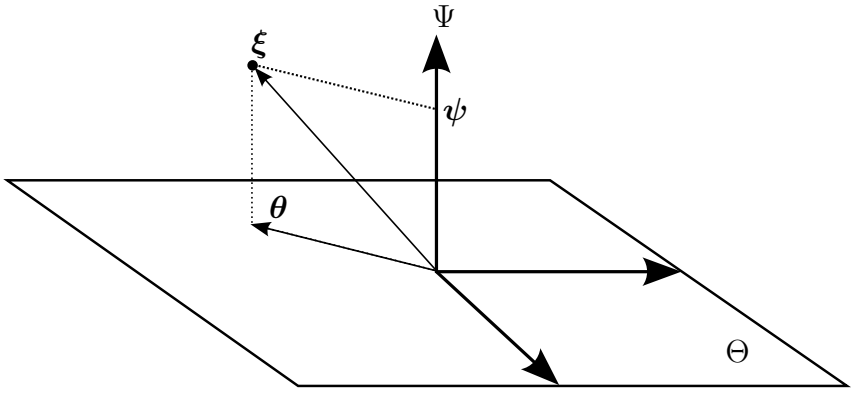


Figure 2.9: Projection of $\boldsymbol{\xi}$ onto Θ

It is not always possible to derive a suitable mapping $f(\boldsymbol{r})$, for instance consider the abstract representation of f depicted in Figure 2.9. In this case, $\boldsymbol{\psi}$ is orthogonal to $\boldsymbol{\theta}$ and, therefore, f is achieved as the projection of $\boldsymbol{\xi}$ onto the plane

Θ. However, in situations where Ψ and Θ are not orthogonal subspaces[†] of Ξ, this projection will not be independent of $\boldsymbol{\psi}$. In such cases one may still choose a mapping such that the dependence of the likelihood function on the nuisance parameters is reduced, rather than completely eliminated. We shall see an example of this approach in Section 2.4.3.

We have discussed a number of mechanisms for dealing with the nuisance parameters $\boldsymbol{\psi}$, but what of the desired parameters $\boldsymbol{\theta}$? This is the point at which the theories of detection and estimation converge. A standard approach in this instance is to *estimate* the desired parameters. If the ML estimator is used then the resulting test is known as a generalised likelihood ratio test (GLRT) [142, p. 92], and may be expressed as:

$$\boldsymbol{\Lambda}_{\mathbf{g}}(\boldsymbol{r}) \triangleq \frac{\max\limits_{\boldsymbol{\theta}} f_{\boldsymbol{r}|H_1,\boldsymbol{\theta}}(\boldsymbol{r} \mid H_1, \boldsymbol{\theta})}{\max\limits_{\boldsymbol{\theta}} f_{\boldsymbol{r}|H_0,\boldsymbol{\theta}}(\boldsymbol{r} \mid H_0, \boldsymbol{\theta})} \underset{D_0}{\overset{D_1}{\gtrless}} \eta, \tag{2.25}$$

where η, as before, is calculated using either the Bayes' or Neyman-Pearson criteria and $\boldsymbol{\Lambda}_{\mathbf{g}}(\boldsymbol{r})$ is called the generalised likelihood ratio. This approach and its variants are those most commonly employed in the acquisition of DS/SS signals.

2.3.1 Detection Theory and GPS

The acquisition of GPS signals can, therefore, be achieved through the formation of a GLRT, as above. It can usually be assumed that, under H_0, the distribution of the received signal vector is dependent only on the noise parameter N_0, which can be estimated independently of the signal parameter vector. The generalised likelihood ratio can, therefore, be written as:

$$\begin{aligned} \boldsymbol{\Lambda}_{\mathbf{g}}(\boldsymbol{r}) &= \max_{\boldsymbol{\theta}} \frac{f_{\boldsymbol{r}|H_1,\boldsymbol{\theta}}(\boldsymbol{r} \mid H_1, \boldsymbol{\theta})}{f_{\boldsymbol{r}|H_0}(\boldsymbol{r} \mid H_0)} && (2.26) \\ &= \max_{\boldsymbol{\theta}} \boldsymbol{\Lambda}(\boldsymbol{r} \mid \boldsymbol{\theta}). && (2.27) \end{aligned}$$

Thus, acquisition consists of two components. Firstly, the likelihood ratio is calculated for all possible parameter points in Θ, and the argument of the largest value is chosen as $\widehat{\boldsymbol{\theta}}$. Secondly, the largest value of $\boldsymbol{\Lambda}(\boldsymbol{r})$ is compared to the threshold η and, based on the result, a decision is made. The first component is

[†]Two vector spaces are orthogonal if every constituent vector of one space is orthogonal to every constituent vector of the other.

an estimation event and the second is a detection event. We, therefore, refer to the fundamental operation of the acquisition process as the *detector/estimator*.

In practice, the search space is discretised which results in a two-dimensional grid, denoted Θ^*, as shown in Figure 2.10. The total code phase uncertainty is denoted T and the total Doppler uncertainty is given by Ω. Each element of the

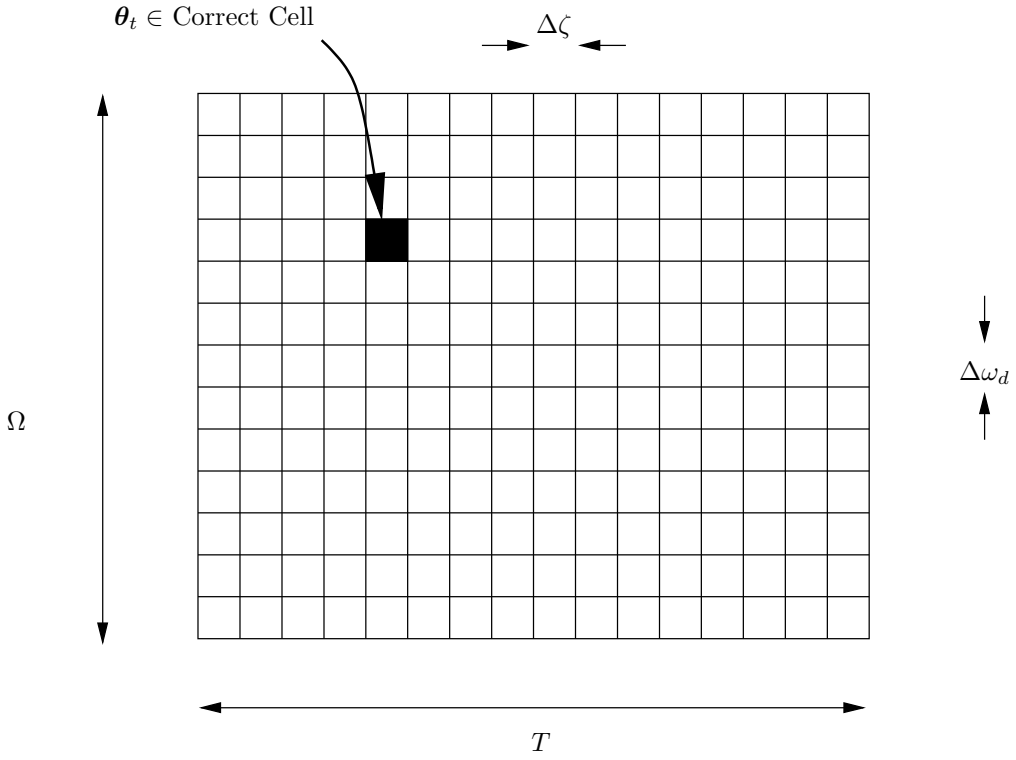


Figure 2.10: Discretised Two Dimensional Search Space Θ^* for the Acquisition Problem.

grid is called a "cell" and there are a total of C cells in the uncertainty region. The likelihood function is evaluated at one sample point per cell (usually the centre point of the cell), and the ML estimate, $\widehat{\boldsymbol{\theta}}_{ML}$, is obtained by finding the argument of the maximum of the reconstructed likelihood function. In reality, a sub-optimal estimate is usually obtained simply by choosing as $\widehat{\boldsymbol{\theta}}$ the co-ordinates of that cell for which the likelihood function is maximum.

To implement the GLRT, therefore, requires one correlator or matched filter for every cell in the uncertainty region. In general, this is infeasible due to the excessive hardware requirements of such an architecture. The standard approach is to approximate the GLRT by serialising the detection process. In this case, rather than calculating all points of the likelihood ratio function at once, it is only

calculated for a subset Γ of Θ^*. A decision is then made on whether or not $\boldsymbol{\theta}_t$ is in Γ and a local approximation to the ML estimate of $\boldsymbol{\theta}_t$ within Γ is returned. The operation of the detector/estimator within Γ can then be described by Equations (2.28) and (2.29):

$$\widehat{\boldsymbol{\theta}} = \arg\max_{\boldsymbol{\theta}\in\Gamma} \; \boldsymbol{\Lambda}\left(\boldsymbol{r} \mid \boldsymbol{\theta}\right) \tag{2.28}$$

$$\boldsymbol{\Lambda}\left(\boldsymbol{r} \mid \widehat{\boldsymbol{\theta}}\right) \underset{D_0}{\overset{D_1}{\gtrless}} \eta \tag{2.29}$$

This is represented graphically in Figure 2.11 below, where we see that the detector/estimator covers a subset of the uncertainty space. We refer to this coverage as a *tile*, and denote by C_{T} the number of cells within a tile. The time spent in each tile is called the dwell time and is denoted τ_D. The C cells of the uncertainty

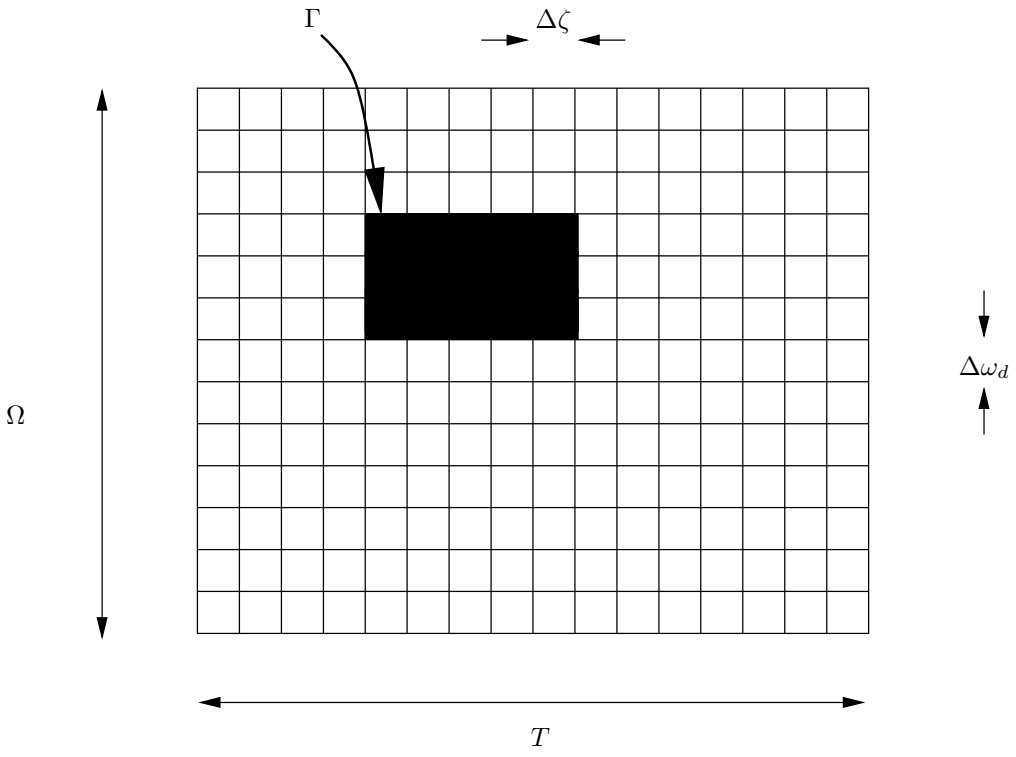


Figure 2.11: The Detector/Estimator covers a subset Γ of the Uncertainty Region

region are thereby subdivided into N_{T} tiles, each containing C_{T} cells. We will generally assume that the tiles are disjoint, so we have $C = C_{\mathrm{T}} \times N_{\mathrm{T}}$.

The serialisation of signal acquisition necessitates the design of a "controller" to guide the detector/estimator through the uncertainty space. We refer to the

operation of this controller as the *acquisition process*. Whereas the design of the detector/estimator determines the dwell time and the probabilities of correct detection, false alarm, etc. within a tile, the acquisition process determines the order in which tiles are searched. We can consider the detector/estimator to be in *motion* through the uncertainty space; the speed of motion is determined by the detector/estimator dwell time, whilst the direction of motion is determined by the acquisition process.

In Section 2.4 we will consider various forms for the detector/estimator, beginning with the simplest form (which we call the single cell detector (SCD)), and extending to various parallel architectures. In Section 2.5 we will look at existing work on the acquisition process.

2.4 The Detector/Estimator

The optimal form of the detector/estimator (in the absence of data modulation) was derived by Hurd et al. [58], and is referred to here as the ML detector. The structure of this detector is illustrated in Figure 2.12. This single cell detector calculates the metric of Equation (2.17) for satellite k and parameter estimate $\widehat{\boldsymbol{\theta}} = \left[\widehat{\zeta}, \widehat{\omega_d}\right]$. The parameters of this detector are: 1) the number of samples per code

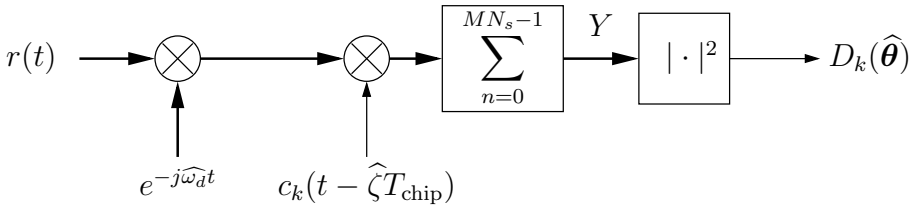


Figure 2.12: The ML Detector

period, which we denote N_s; 2) the number of code-periods coherently combined, which we denote M and 3) the decision threshold, denoted V_{Th}. We have assumed that an integer number of code periods are used in the observation vector $\boldsymbol{r}$, this guarantees that the auto- and cross-correlation properties of the spreading codes are maintained. We have also assumed an integer number of samples per code period. If the detector metric $D_k(\widehat{\boldsymbol{\theta}})$ exceeds the decision threshold V_{Th}, then a "hit" is declared and $\widehat{\boldsymbol{\theta}}$ is chosen as the optimal parameter estimate.

The detector performance is measured by the following three parameters:

- The probability of correct detection P_d. This is the probability that $D_k(\widehat{\boldsymbol{\theta}}) > V_{\text{Th}}$ given that the estimate is sufficiently "close"[†] to the true parameter vector $\boldsymbol{\theta}_t$.
- The probability of false alarm P_{fa}. This is the probability that $D_k(\widehat{\boldsymbol{\theta}}) > V_{\text{Th}}$ given that the estimate is not sufficiently close to $\boldsymbol{\theta}_t$.
- The dwell time τ_D. This is the amount of time taken to make a decision and is given by MT_{CA}.

To determine P_{fa} and P_d requires knowledge of the statistical distribution of $D_k(\boldsymbol{\theta})$ under H_0 and H_1, respectively. Considering initially the distribution under H_0, the input $r(t)$ then consists of AWGN and the PDF of the observation vector is given by (see Equation (2.12)):

$$f_{\boldsymbol{r}|H_0}(\boldsymbol{r} \mid H_0) = \left(\pi\sigma^2\right)^{-MN_s} \exp\left(-\frac{|\boldsymbol{r}|^2}{\sigma^2}\right), \tag{2.30}$$

where $\boldsymbol{r}$ is a length MN_s vector of complex Gaussian random variables with independent real and imaginary components, $\sigma^2 = 0.5N_0B_{\text{IF}}$, N_0 is the single sided noise PSD, and B_{IF} is the two-sided IF filter bandwidth which we will assume to be approximately equal to the sampling frequency $f_s = 1/T_s$. Multiplying $\boldsymbol{r}$ by the complex exponential $\exp\left(-j\widehat{\omega_d}t\right)$ causes a rotation in the components of $\boldsymbol{r}$ but does not affect its PDF[‡]. The combined effect of multiplying by the spreading code and accumulating the result is to filter the observation vector, resulting in a single complex sample Y_k. This sample is formed as the sum of MN_s zero-mean complex random variables and, hence, is itself a zero-mean complex random variable with variance σ_Y^2 where [102]:

$$\sigma_Y^2 = MN_s\sigma^2. \tag{2.31}$$

The decision statistic is then formed via:

$$D_k(\boldsymbol{\theta}) = \Re\left\{Y_k\right\}^2 + \Im\left\{Y_k\right\}^2 \tag{2.32}$$

[†]The estimate must be within the pull-in range of the tracking loops.

[‡]The in-phase and quadrature components are assumed to be independent, hence the PDF of $\boldsymbol{r}$ is circularly symmetric about the origin. Thus, it is invariant to rotation about the origin.

This is the sum of the squares of two independent, zero-mean Gaussian random variables. Thus, $D_k(\boldsymbol{\theta})$ has a central χ^2 distribution with two degrees of freedom [92], and its PDF is given by:

$$f_{D_k(\boldsymbol{\theta})|H_0}(x \mid H_0) = \begin{cases} \dfrac{1}{2\sigma_Y^2} \exp\left(-\dfrac{x}{2\sigma_Y^2}\right) & x \geq 0 \\ 0 & x < 0. \end{cases} \tag{2.33}$$

The probability of false alarm is then given by:

$$\begin{aligned} P_{fa} &= \int_{V_{\text{Th}}}^{\infty} f_{D_k(\boldsymbol{\theta})|H_0}(x \mid H_0) dx \\ &= \exp\left(-\frac{V_{\text{Th}}}{2\sigma_Y^2}\right). \end{aligned} \tag{2.34}$$

Under H_1, $r(t)$ contains both signal and noise components:

$$r(t) = s_k(t) + n(t).$$

The complex observation vector $\boldsymbol{r}$ is, therefore, given by $\boldsymbol{r} = [r_0, r_1, \ldots, r_{MN_s-1}]^{\text{T}}$ and:

$$r_n = s_{k,n} + n_n,$$

where, from Equation (2.10), and ignoring the effect of code Doppler, we have:

$$s_{k,n} = \sqrt{\frac{P_k(nT_s)}{2}} d_k(nT_s) c_k(nT_s - \zeta_t T_{\text{chip}}) \exp\left(j\left[\omega_{dt} nT_s + \phi_k\right]\right). \tag{2.35}$$

The input to the squaring device, Y_k, is then a non-zero mean complex Gaussian random variable whose PDF is given by:

$$f_{Y_k|H_1}(y \mid H_1) = \frac{1}{\pi\sigma_Y^2} \exp\left(-\frac{|y-\mu|^2}{\sigma_Y^2}\right), \tag{2.36}$$

where:

$$\mu = \sum_{n=0}^{MN_s-1} s_{k,n} c_k\left(nT_s - \widehat{\zeta} T_{\text{chip}}\right) \exp\left(-j\widehat{\omega_d} nT_s\right). \tag{2.37}$$

The decision statistic $D_k(\boldsymbol{\theta})$ has a non-central χ^2 distribution with two degrees

of freedom, non-centrality parameter λ:

$$\lambda \triangleq |\mu|^2 \tag{2.38}$$

and PDF [92]:

$$f_{D_k(\boldsymbol{\theta})|H_1}(x \mid H_1) = \begin{cases} \frac{1}{2\sigma_Y^2} \exp\left(-\frac{x+\lambda}{2\sigma_Y^2}\right) I_0\left(\frac{\sqrt{x\lambda}}{\sigma_Y^2}\right) & x \geq 0 \\ 0 & x < 0, \end{cases} \tag{2.39}$$

where $I_\nu(\cdot)$ is the ν^{th} order modified Bessel function of the first kind defined by [9, 13]:

$$I_\nu(x) = \sum_{k=0}^{\infty} \frac{\left(\frac{x}{2}\right)^{\nu+2k}}{k!\,\Gamma(k+\nu+1)}, \tag{2.40}$$

where $\Gamma(K)$ is the gamma function, defined by [13, Equation (11)]:

$$\Gamma(x) = \int_0^\infty \exp(-t)\, t^{x-1} dt, \tag{2.41}$$

which, for $x \in \mathbb{Z}^+$, is related to the factorial function by: $\Gamma(x) = (x-1)!$. The probability of detection, P_d, is given by:

$$\begin{aligned} P_d &= \int_{V_{\text{Th}}}^\infty f_{D_k(\boldsymbol{\theta})|H_1}(x \mid H_1) dx \\ &= Q_1\left(\frac{\sqrt{\lambda}}{\sigma_Y}, \frac{\sqrt{V_{\text{Th}}}}{\sigma_Y}\right), \end{aligned} \tag{2.42}$$

where $Q_K(a,b)$ is the K^{th} order Marcum Q-function, defined by [102]:

$$Q_K(a,b) = \int_b^\infty x \left(\frac{x}{a}\right)^{K-1} \exp\left(-\frac{a^2+x^2}{2}\right) I_{K-1}(ax)\, dx, \tag{2.43}$$

and the positive square roots are taken in Equation (2.42). It is common to consider a normalised form, $\widetilde{D}_k$, of the decision statistic:

$$\widetilde{D}_k(\widehat{\boldsymbol{\theta}}) = \frac{D_k(\widehat{\boldsymbol{\theta}})}{\sigma_Y^2}. \tag{2.44}$$

The probabilities of false alarm and detection can then be written, respectively,

as:

$$P_{fa} = \exp\left(-\frac{{V_{\text{Th}}}'}{2}\right) \tag{2.45}$$

$$P_d = Q_1\left(\sqrt{\gamma}, \sqrt{{V_{\text{Th}}}'}\right), \tag{2.46}$$

where $\gamma = \lambda/\sigma_Y^2$ is the SNR at the input to the squaring device and ${V_{\text{Th}}}' = V_{\text{Th}}/\sigma_Y^2$ is the normalised decision threshold.

Clearly, in this model, the threshold V_{Th} sets P_{fa} and P_d. Increasing the threshold causes both P_{fa} and P_d to decrease. Similarly, decreasing the threshold causes both probabilities to increase. To increase P_d whilst keeping P_{fa} constant requires a longer observation interval, *i.e.* M must be increased. Similarly, as the received signal power level decreases, M must be increased to maintain constant performance (in terms of P_{fa} and P_d).

The performance of this detector is heavily dependent on γ, the pre-detection SNR. To examine the effect of the detector parameters on γ we consider the following cases for the phase of the received signal, under the assumption that the magnitude is constant:

1. The phase offset is constant and unknown.
2. There is a constant Doppler offset, which is also unknown.
3. The signal is subject to random phase reversals due to data modulation.

Phase offset is constant and unknown

In this case, there is no Doppler offset and the signal component of $\boldsymbol{r}$ is given by:

$$s_{k,n} = \sqrt{\frac{P_k}{2}} c_k(nT_s - \zeta_t T_{\text{chip}}) \exp(j\phi_k). \tag{2.47}$$

Assuming the code phase estimate, $\widehat{\zeta}$, is correct, the non-centrality parameter, λ, is then given by:

$$\begin{aligned}\lambda &= \left| \sum_{n=0}^{MN_s-1} \sqrt{\frac{P_k}{2}} \exp(j\phi_k) \right|^2 \\ &= 0.5(MN_s)^2 P_k. \end{aligned} \tag{2.48}$$

The pre-detection SNR is then given by:

$$\gamma = \frac{0.5(MN_s)^2 P_k}{\sigma_Y^2} \tag{2.49}$$

$$= MN_s\gamma_0 \tag{2.50}$$

where $\gamma_0 = \frac{P_k}{2\sigma^2}$ is the SNR at the receiver input. Hence, γ is linearly dependent on the product MN_s, for a given input SNR. A reduction of 10dB in the received signal power requires an increase in MN_s of 10dB for the same performance in terms of P_{fa} and P_d. This can be achieved by increasing either M, N_s or both.

If there is a residual error in the code phase estimate of $\delta\zeta$ chips then the non-centrality parameter is given by:

$$\lambda = \left| \sum_{n=0}^{MN_s-1} \sqrt{\frac{P_k}{2}} c_k(nT_s) c_k(nT_s - \delta\zeta T_{\text{chip}}) \right|^2$$

$$= 0.5(MN_s)^2 R_k(\delta\zeta)^2 P_k, \tag{2.51}$$

where $R_k(\delta\zeta)$ is the auto-correlation function of the spreading code for a code offset of $\delta\zeta$ chips. This latter parameter can be modelled by the following triangular function about the origin:

$$R_k(\delta\zeta) \approx \begin{cases} 1 - |\delta\zeta| & |\delta\zeta| \leq 1 \\ 0 & \text{Otherwise.} \end{cases}$$

The effect of the residual code phase offset can, therefore, be modelled as an attenuation of the received signal power by a factor $\alpha_s(\delta\zeta)$, where:

$$\alpha_s(\delta\zeta) = (1 - |\delta\zeta|)^2 \tag{2.52}$$

Now the maximum value of $\delta\zeta$ depends on the sampling rate in the code phase domain, as discussed earlier. Increasing N_s increases the number of samples per code period and, hence, leads to a reduction in the maximum code phase offset possible, denoted $\delta\zeta_{\max}$, where:

$$\delta\zeta_{\max} = \frac{L}{N_s}, \tag{2.53}$$

where $L = 1023$ is the length of the GPS C/A code in chips. The effect of

increasing N_s is three-fold: 1) the pre-detection SNR is increased, leading to an increase in P_d for a given P_{fa}; 2) the maximum code phase offset in the H_1 cell is decreased, again increasing the post-detection SNR; 3) the number of cells in the code phase uncertainty region is increased. This latter effect leads to an increased computational requirement for acquisition which, in turn, results in either a longer acquisition time, or greater area/power requirements.

Similarly, increasing M leads to increased receiver sensitivity at the cost of an increased dwell time. This is illustrated in Figure 2.13, where the distribution of the normalised decision statistic for the ML detector is shown.

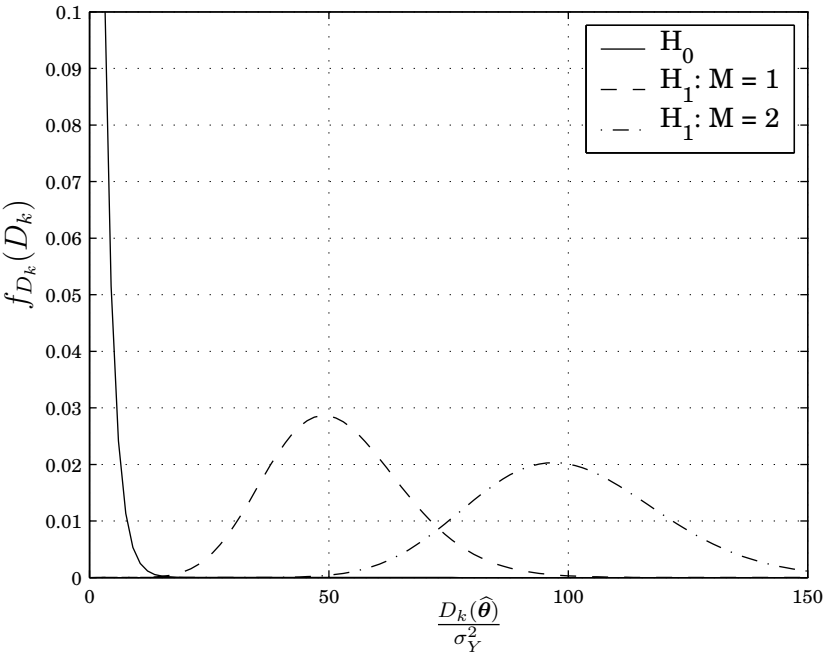


Figure 2.13: Distribution of the Decision Statistic for the ML Detector. The decision statistic has been normalised by the noise variance at the input to the squaring device. A received C/N_0 of 43.8 dB-Hz is assumed.

At low received signal power it is common to increase M and to keep N_s fixed. The increase in acquisition time is, therefore, linearly dependent on the decrease in signal power. Alternatively, use can be made of adjacent samples of the correlation function to generate a better approximation to the correlation peak by interpolation. This approach was suggested, for instance, by Srinivasan and Sarwate [129] for parallel estimation and by Yoon et al. [155] for serial detection.

Constant Doppler offset

In the presence of a constant Doppler offset ω_{dt}, the signal component of $\boldsymbol{r}$ is given by:

$$s_{k,n} = \sqrt{\frac{P_k}{2}} c_k(nT_s - \zeta_t T_{\text{chip}}) \exp\left(j\left[(\omega_{dt} - \widehat{\omega_d})nT_s + \phi_k\right]\right). \tag{2.54}$$

Again, assuming that $\widehat{\zeta}$ is correct, the non-centrality parameter λ is given by:

$$\begin{aligned}\lambda &= \left| \sum_{n=0}^{MN_s-1} \sqrt{2P_k} \exp\left(j\left[(\omega_{dt} - \widehat{\omega_d})nT_s + \phi_k\right]\right) \right|^2 \\ &= 0.5(MN_s)^2 P_k \; \alpha_D\left(\delta\omega_d\right), \end{aligned} \tag{2.55}$$

where $\delta\omega_d = \omega_{dt} - \widehat{\omega_d}$ and $\alpha_D(\delta\omega_d)$ is given in Equation (2.19). The important thing to note about this attenuation factor is that it is primarily dependent on M. Increasing M increases the detector's sensitivity to Doppler offsets, as discussed previously. Increasing M for a fixed Doppler uncertainty increases the number of Doppler bins that must be searched, thereby increasing the overall acquisition time. Recall that, from Equation (2.19), we saw that a suitable choice of frequency domain sampling was one sample every $\frac{1}{MT_{\text{CA}}}$ Hz$\frac{1}{M}$ kHz. Thus, given a total frequency uncertainty of ΔF, there will be $M\Delta F/1000$ Doppler bins to be searched. Thus, increasing M to increase the receiver sensitivity leads to a corresponding (linear) increase in the size of the uncertainty region. We have already seen that, in the absence of Doppler, the best strategy for coping with a decrease in received signal power is to increase M. We now see that, not only does this increase the dwell time per cell, it also increases the number of cells in the uncertainty region. The acquisition time, therefore, increases approximately as the square of the loss in signal power. In the following sections we will consider some common techniques that attempt to alleviate this increase in acquisition time.

In the presence of both code phase and Doppler offsets in the H_1 cell a detailed analysis would require consideration of the effects of code Doppler. The code Doppler effect leads to a difference in chip rates between the local and received codes. This can be partially accounted for by modifying the chip rate of the local code to match the current Doppler frequency estimate $\widehat{\omega_d}$. Consequently,

the local code should be generated as:

$$c_k\left(t \times (1+\widehat{\eta}) - \widehat{\zeta} T_{\text{chip}}\right),$$

where $\widehat{\eta} = \widehat{\omega_d}/\omega_0$ is the estimate of the Doppler dilation coefficient defined in Equation (2.3). A residual code Doppler effect due to error in the estimate of the Doppler dilation coefficient, denoted $\delta\eta$, where:

$$\delta\eta = \eta_t - \widehat{\eta}, \tag{2.56}$$

will remain, however. This effect is usually negligible in comparison to the carrier Doppler attenuation. For instance, if the Doppler bin width is chosen to be $1/M$ kHz, then the maximum residual Doppler offset in the H_1 bin is $1/(2M)$ kHz. The residual Doppler dilation coefficient is then given by $\delta\eta = 500/M \times 1/\omega_0$, where $\omega_0 = 2\pi \times 1.57542 \times 10^9$ rad s^{-1}, and so, in MT_{CA} seconds the code phase will have moved just $\delta\eta LM = 1023 \times 500/(1.57542 \times 10^9) \approx 3 \times 10^{-4}$ chips, which is negligible.

The effect of data modulation

As discussed in Section 2.1, the GPS signal is modulated by a 50 bps BPSK data sequence. This leads to a data bit boundary every $D = 20$ ms. At each data bit boundary there is a probability of 0.5 of a bit transition occurring (assuming equiprobable binary symbols). A bit transition leads to a phase shift of π rad, *i.e.* a change in sign. If a bit transition occurs during the coherent accumulation period then a reduction in the pre-detection SNR will result. This is illustrated in Figure 2.14, where we assume the bit boundary occurs a fraction δ_T of the way through the observation interval (*i.e.* at a time $\delta_T MT_{\text{CA}}$ seconds after the accumulation begins). The non-centrality parameter λ is then given by:

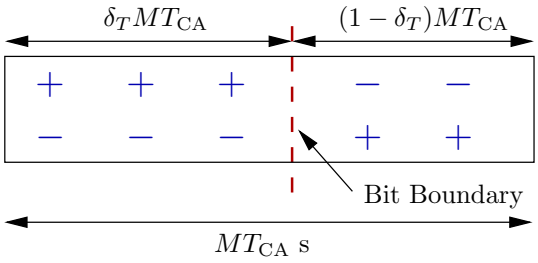


Figure 2.14: Data Transition in a Coherent Integration Period of MT_{CA} s.

$$\lambda = \left| \pm \sum_{n=0}^{\lceil \delta_T M N_s \rceil - 1} \sqrt{\frac{P_k}{2}} \exp\left(j\phi_k\right) \mp \sum_{n=\lceil \delta_T M N_s \rceil}^{M N_s - 1} \sqrt{\frac{P_k}{2}} \exp\left(j\phi_k\right) \right|^2$$
$$\approx 0.5 (M N_s)^2 \left(1 - 2\delta_T\right)^2 P_k, \tag{2.57}$$

where $\lceil x \rceil$ is the nearest integer greater than or equal to x and the approximation in the second step is due to the approximation $\lceil \delta_T M N_s \rceil \approx \delta_T M N_s$. The effect of a data bit transition within the coherent integration period can, therefore, be modelled as an attenuation of the received signal power by a factor $\alpha_m(\delta_T)$, where:

$$\alpha_m\left(\delta_T\right) = \left(1 - 2\delta_T\right)^2. \tag{2.58}$$

The average data attenuation, denoted $\overline{\alpha}_m$, can be found by taking the average probability of a transition occurring within the observation interval (*i.e.* $M/(2D)$) and averaging over $0 \leq \delta_T < 1$, yielding the simple expression in Equation (2.59) below [37, Equation (8-6)]:

$$\overline{\alpha}_m \approx \begin{cases} 1 - \frac{M}{3D} & M < D \\ \frac{D}{M}\left(1 - \frac{D}{3M}\right) & M \geq D. \end{cases} \tag{2.59}$$

From this we see that increasing M causes an increase in the *average* power attenuation due to modulation effects. Note also from Equation (2.58) that the worst case attenuation occurs when $\delta_T = 0.5$, at which point the signal power is completely eliminated. In this case, the detector design must be modified, since signal detection is impossible.

Thus, we must address the following fundamental conundrum for the fast, reliable acquisition of weak DS/CDMA signals: to enhance receiver sensitivity we must increase M, but, in so doing, we suffer the dual effect of both an increase in the size of the uncertainty region (thereby increasing the acquisition time still further) and an increase in the effective power attenuation due to data modulation. In the following sections we summarise the most common techniques to overcome these difficulties with weak signal acquisition, perhaps the most common of which is the use of noncoherent combining.

2.4.1 Noncoherent Combining

Noncoherent combining is a technique for increasing P_d for a given P_{fa} in the presence of a randomly varying phase offset (due, for example, to a carrier Doppler offset, or data modulation effects) at the receiver antenna. This approach dates back to the early days of radar detection theory [83] and the detection of unknown signals in noise [139]. It has found wide application in the acquisition of DS/SS signals in the presence of Doppler offset and data modulation [24, 26, 27, 37, 105, 115, 134] and is also widely used in the acquisition of GPS signals [70, 137, 140].

Fundamentally, the NCCD is an energy detector. It operates by accumulating a number, denoted K, of outputs from the ML detector discussed in the previous section. The detector structure is illustrated in Figure 2.15. The receiver perfor-

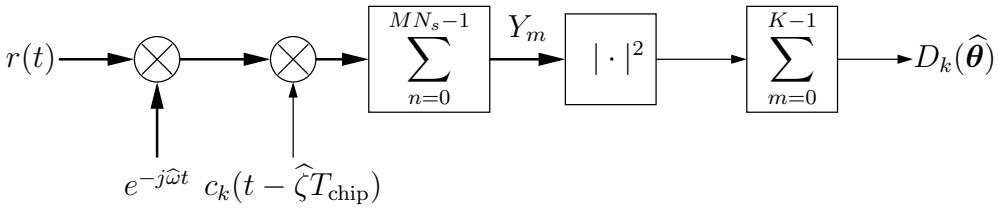


Figure 2.15: Noncoherent Combining Detector

mance parameters are, once again, the dwell time, τ_D, and the probabilities of detection, P_d, and false alarm, P_{fa}, and are easily derived from the performance parameters of the ML detector. The NCCD combines K sequential outputs from the ML detector and so the dwell time is simply K times the dwell time of that detector:

$$\tau_D = KMT_{\mathrm{CA}}. \tag{2.60}$$

Under hypothesis H_0, the output of the ML detector was already seen to be a central χ^2 distributed rv with two degrees of freedom. From [92], we know that the sum of K independent χ^2 rvs with n degrees of freedom is itself a central χ^2 rv, with nK degrees of freedom. The distribution of the decision statistic under H_0 is, therefore, the distribution of a χ^2 rv with $2K$ degrees of freedom and variance of the underlying Gaussian distribution $\sigma_Y^2 = MN_s\sigma^2$, given by:

$$f_{D_k(\boldsymbol{\theta})|H_0}(x \mid H_0) = \begin{cases} \dfrac{1}{2\sigma_Y^2}\dfrac{1}{\Gamma(K)}\left(\dfrac{x}{2\sigma_Y^2}\right)^{K-1}\exp\left(-\dfrac{x}{2\sigma_Y^2}\right) & x \geq 0 \\ 0 & x < 0. \end{cases} \tag{2.61}$$

The probability of false alarm, P_{fa}, is then given by:

$$\begin{aligned} P_{fa} &= \int_{V_{\mathrm{Th}}}^{\infty} f_{D_k(\boldsymbol{\theta})|H_0}(x \mid H_0)dx \\ &= \frac{\Gamma_K\left(\frac{V_{\mathrm{Th}}}{2\sigma_Y^2}\right)}{\Gamma(K)}, \end{aligned} \tag{2.62}$$

where $\Gamma_K(x)$ is the complementary incomplete Gamma function of order K [13, Equation (13)]:

$$\Gamma_K(x) = \int_x^{\infty} \exp(-t)\, t^{K-1} dt. \tag{2.63}$$

For notational convenience we introduce the function:

$$\widetilde{\Gamma}_K(x) \triangleq \frac{\Gamma_K(x)}{\Gamma(K)}, \tag{2.64}$$

which is sometimes called the regularised incomplete gamma function of order K [150]. Therefore, we have $P_{fa} = \widetilde{\Gamma}_K\left(V_{\mathrm{Th}}/(2\sigma_Y^2)\right)$.

Under hypothesis H_1, recall that the output of the ML detector is a non-central χ^2 distributed rv with two degrees of freedom and non-centrality parameter λ. Denoting by λ_m the non-centrality parameter of the m^{th} output of the ML detector, then the metric $D_k\left(\widehat{\boldsymbol{\theta}}\right)$ is a non-central χ^2 distributed rv with $2K$ degrees of freedom and non-centrality parameter (see Equation (2.38) for a definition of λ_m):

$$\lambda = \sum_{m=0}^{K-1} \lambda_m. \tag{2.65}$$

The distribution of $D_k\left(\widehat{\boldsymbol{\theta}}\right)$ is then given by:

$$f_{D_k(\boldsymbol{\theta})|H_1}(x \mid H_1) = \begin{cases} \dfrac{1}{2\sigma_Y^2}\left(\dfrac{x}{\lambda}\right)^{\frac{K-1}{2}} \exp\left(-\dfrac{x+\lambda}{2\sigma_Y^2}\right) I_{K-1}\left(\dfrac{\sqrt{x\lambda}}{\sigma_Y^2}\right) & x \geq 0 \\ 0 & x < 0, \end{cases} \tag{2.66}$$

where $I_K(\cdot)$ is the modified Bessel function of the first kind of order K, as defined by Equation (2.40). The probability of detection is given by:

$$P_d = \int_{V_{\mathrm{Th}}}^{\infty} f_{D_k(\boldsymbol{\theta})|H_1}(x \mid H_1)dx$$

$$= Q_K\left(\frac{\sqrt{\lambda}}{\sigma_Y}, \frac{\sqrt{V_{\mathrm{Th}}}}{\sigma_Y}\right), \tag{2.67}$$

where $Q_K(a, b)$ is the K^{th} order Marcum Q-function, as defined in Equation (2.43).

By increasing K, P_d can be increased for a given P_{fa}, or, equivalently, a lower P_{fa} can be achieved for a given P_d. This comes, of course, at the expense of an increased dwell time. It is worth pointing out that the increase in P_d that can be achieved is much less than that achieved by using a longer dwell time in the ML detector, provided there is no data modulation or residual Doppler offset. To see the advantage of the NCCD it is necessary to consider its behaviour in the presence of data modulation and Doppler effects.

Constant Doppler offset

If there is a constant residual Doppler offset $\delta\omega_d$ present at the input to the coherent accumulator, then the non-centrality parameter of the NCCD will be given by summing Equation (2.55):

$$\begin{aligned}\lambda &= \sum_{m=0}^{K-1} 0.5(MN_s)^2 P_k\ \alpha_D(\delta\omega_d) \\ &= 0.5K(MN_s)^2 P_k\ \alpha_D(\delta\omega_d).\end{aligned} \tag{2.68}$$

Note that the effective power attenuation induced by this offset is identical to that induced for the ML detector. This means that, using the NCCD, we can extend the observation interval without reducing the size of the Doppler bins. This is the primary advantage of the NCCD.

Consider a simple example to illustrate this point: if the received SNR, γ, is -26 dB, and a performance of $P_{fa} = 1 \times 10^{-5}$ and $P_d = 0.9$ is required, then either an ML detector with $M = 8$ or an NCCD with $M = 1$ and $K = 14$ is required[†]. But, with $M = 8$ there will be 8 times as many Doppler bins to be searched, therefore a sweep of the entire uncertainty region would take $64 \times T_U$ seconds, where T_U is the time taken to sweep through the uncertainty region when $M = 1$. The NCCD detector, on the other hand, can sweep through the entire uncertainty region in $14 \times T_U$ seconds. So the NCCD can cover the entire

[†]In fact, these parameters will yield $P_d = 0.93$ for the ML detector, and $P_d = 0.91$ for the NCCD so we are not exactly comparing like with like. The example is, however, illustrative of the advantage of non-coherent combining.

uncertainty region in less than a quarter of the time taken by the ML detector, despite the fact that each individual dwell takes nearly twice as long. Note also, however, that the ML detector will yield a much more accurate estimate of the Doppler offset due to the narrower bin spacing required.

One point that is often overlooked is the effect of code Doppler. We previously saw for the ML detector that code Doppler effects are negligible, due to the inherent limit on the residual Doppler offset as the observation interval increases. For the NCCD there is no such limit: we can increase the observation interval by increasing K, which does not affect the maximum residual Doppler offset in the H_1 cell. Let $\Delta\zeta$ denote the change in code phase offset during the coherent observation interval due to Doppler effects. We have already seen that $\Delta\zeta \approx 3 \times 10^{-4}$ chips, so the drift in ζ in one coherent subinterval is small. However, in accumulating K of these coherent sub-intervals the total change in ζ is given by $K \times \Delta\zeta$. If K is large, say of the order of 10^3 (which is common for very weak signals), then this code Doppler effect becomes significant. Code Doppler effects are considered in [27].

The effect of data modulation

Within the observation interval there will be B data-bit boundaries, where:

$$B = \left\lfloor \frac{MK}{D} \right\rfloor \text{ or } \left\lceil \frac{MK}{D} \right\rceil, \tag{2.69}$$

depending on where the first boundary occurs[†]. In general, $M < D$ and so $B < K$. Thus, in one observation interval, there will be B coherent sub-intervals containing bit boundaries and $K - B$ sub-intervals without bit boundaries. Each sub-interval is of duration MT_{CA} s. Assuming that the i^{th} boundary occurs a fraction $\delta_{T,i}$ of the way through a coherent sub-interval, then the effective power attenuation due to the data modulation is given by [26, Equation 12][‡]:

$$\alpha_m = 1 - \frac{1}{K} \sum_{i=0}^{B-1} t_i \times \left(1 - (1 - 2\delta_{T,i})^2 \right), \tag{2.70}$$

[†]If the first bit boundary occurs within the first $(MK) \mod D$ coherent sub-intervals there will be $\lceil MK/D \rceil$ boundaries in total. Otherwise there will be $\lfloor MK/D \rfloor$ boundaries.

[‡][26, Equation 12] is equivalent to Equation (2.70) under the substitutions: $\alpha_m \to G/J$, $K \to J$, $B \to Q$, $t_i \to c_i$ and $\delta_{T,i} \to 1/2 - \xi_i$.

where t_i equals 1 if a bit transition occurs at the i^{th} boundary (either from $+1$ to -1 or *vice versa*), and equals 0 if no transition occurs.

It can also be shown [37] that the mean effective power loss is, once again, given by Equation (2.59). In other words, the *average* effective power attenuation due to data modulation depends only on M and is independent of K. Another interesting point to note is that the worst case modulation attenuation occurs when: a) there is a transition at every bit boundary, *i.e.* $t_i = 1 \; \forall \; i$, and b) each transition occurs exactly half way through a coherent sub-interval,*i.e.* $\delta_{T,i} = 0.5 \; \forall i$. From Equation (2.70), this leads to the simple lower bound:

$$\alpha_m \geq 1 - \frac{B}{K}. \tag{2.71}$$

So, whereas the worst case modulation attenuation for the ML detector resulted in the complete elimination of the signal from the decision statistic, the NCCD ensures a certain minimum signal power in the decision statistic, even in the presence of worst-case data modulation. This is the second major advantage of the NCCD over the ML detector.

In certain situations, such as weak signal acquisition, even the small modulation loss incurred by the NCCD may by too great a price to pay. In such instances efforts can be made to eliminate the modulation effects entirely. One approach is to use multiple matched filter correlators, each matched to the PN code modulated by a different data pattern [100]. This leads to a significant increase in the hardware requirements of the detector when the observation interval is long. Psiaki [103] considered a similar approach for the GPS acquisition problem, which he called the "Full-Bits Method". In this case twenty detectors are implemented, offset from one another by one code period. The maximum correlator output is chosen as the test statistic. If this corresponds to the true parameter estimate then it will also yield an estimate of the data bit transition time.

Another approach, also suggested in [103], is called the "Half-Bits Method". In this case only two correlators are implemented, offset from one another by ten code periods. Each correlator, in effect, operates as an NCCD with $M = 10$, operating on alternate 10 ms intervals. While this requires twice the amount of time for the same performance as a standard NCCD detector, it has the advantage that one of the correlators is guaranteed not to see any data transitions. The effect of data modulation is, therefore, completely eliminated, at the cost of increased

hardware and increased dwell times. Note also that M is fixed at ten, so the frequency uncertainty region will contain ten times as many cells as for an $M = 1$ detector.

Another approach to the elimination of data modulation effects is to provide information on the data through an alternate communications link. For mobile telephony, a number of standards [3, 7] have been created to enable the provision of assistance information from the base station to the mobile terminal.

2.4.2 Differentially Coherent Combining

The noncoherent combining detector works by ignoring the phase information at the output of the coherent correlator. Thus, signal degradation due to phase errors, such as Doppler offset and data modulation, is reduced. The DCCD operates by maintaining *differential* phase information between successive correlator outputs. The basic principle is that there will be a high degree of correlation between the phases of successive correlator outputs when the signal is present, but they will be essentially independent under the influence of noise alone. Denoting by Y_r the r^{th} output of the coherent correlator, the differentially coherent product is formed as:

$$Z_r = Y_r Y_{r-1}^*, \tag{2.72}$$

where Y^* denotes the complex conjugate of Y. The DCCD forms a decision statistic by accumulating a number (say R) of these differentially coherent products. This is illustrated in Figure 2.16, where the decision statistic has been formed by taking the square magnitude of the accumulator output.

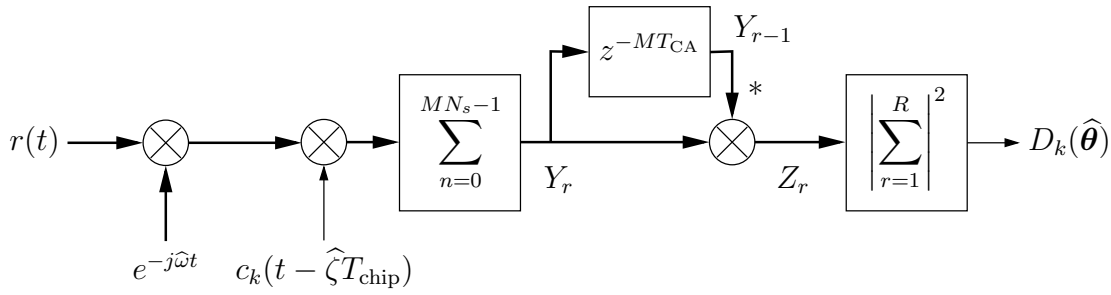


Figure 2.16: Differentially Coherent Combining Detector: z^{-T} denotes a delay of T seconds, * denotes complex conjugation.

This approach was originally suggested by Zarrabizadeh and Sousa [156] for the acquisition of DS/SS signals. In [156] the authors considered a matched-filter

receiver and only the simple case $R = 1$, *i.e.* only two successive samples are differentially combined. In addition, the decision statistic was formed by taking just the real part of Z, rather than the magnitude.

The performance parameters are again given by the dwell time τ_D and the probabilities of false alarm P_{fa} and detection P_d. The dwell time is easily seen to be $2MT_{\mathrm{CA}}$. Under H_0, the output of the coherent correlator Y_r is a zero-mean complex Gaussian rv with variance $\sigma_Y^2 = MN_s\sigma^2$:

$$Y_r = Y_{r,I} + jY_{r,Q},$$

where I and Q denote the in-phase and quadrature components, respectively, and so the decision statistic is given by:

$$D_k\left(\widehat{\boldsymbol{\theta}}\right) = Y_{r,I}Y_{r-1,I} + Y_{r,Q}Y_{r-1,Q}.$$

The distribution of $D_k\left(\widehat{\boldsymbol{\theta}}\right)$ is then given by [156, Equation (20)]:

$$f_{D_k(\boldsymbol{\theta})|H_0}(x \mid H_0) = \frac{1}{2\sigma_Y^2}\exp\left(-\frac{|x|}{\sigma_Y^2}\right). \tag{2.73}$$

The probability of false alarm is then given by:

$$\begin{aligned} P_{fa} &= \int_{V_{\mathrm{Th}}}^{\infty} f_{D_k(\boldsymbol{\theta})|H_0}(x \mid H_0)dx \\ &= \frac{1}{2\sigma_Y^2}\exp\left(-\frac{|V_{\mathrm{Th}}|}{\sigma_Y^2}\right). \end{aligned} \tag{2.74}$$

The derivation of the statistics under the hypothesis H_1 is more involved, but the authors show that [156, Equation (33)]:

$$\begin{aligned} P_d &= \int_{V_{\mathrm{Th}}}^{\infty} f_{D_k(\boldsymbol{\theta})|H_1}(x \mid H_1)dx \\ &= \frac{1}{\pi}\int_{-\infty}^{\infty} K_0\left({V_{\mathrm{Th}}}' - \tau\right)\Psi\left(\tau\right)d\tau, \end{aligned} \tag{2.75}$$

where $K_\nu\left(\cdot\right)$ is the modified Bessel function of the second kind of order ν, defined

by [13, Equation (57)]:

$$K_\nu(z) = \lim_{p \to \nu} \frac{\pi}{2} \frac{I_{-p}(z) - I_p(z)}{\sin p\pi}, \tag{2.76}$$

$I_p(z)$ is the modified Bessel function of the first kind, defined in Equation (2.40), $\Psi(\tau)$ is defined by:

$$\Psi(\tau) = \frac{1 + \operatorname{erf}\left(\frac{m}{\sqrt{2}}\right)}{4} - \frac{1}{\sqrt{8\pi}} \int_0^\infty \exp\left(-\frac{(y-m)^2}{2}\right) \operatorname{erf}\left(\frac{-m + \tau/y}{\sqrt{2}}\right) dy$$

and $\operatorname{erf}(z)$ is the error function, defined by [13, Equation (23)]:

$$\operatorname{erf}(z) = \frac{2}{\sqrt{\pi}} \int_0^z \exp\left(-t^2\right) dt. \tag{2.77}$$

The authors of [156] demonstrate that, in the absence of data modulation and Doppler shift, this detector outperforms the ML detector by up to 4–5 dB, in terms of the mean acquisition time. The greatest improvement in performance is at low SNR.

This approach was further analysed by Iinatti and Pouttu [59, 60]. In [59] the authors study Doppler effects on the DCCD as defined by Zarrabizadeh and Sousa, and also introduce what they term the "differential noncoherent (DNC) detector". This is similar to the detector of Figure 2.16, in that the decision statistic is formed as the square magnitude of the accumulator output. Through simulations, the authors show that the DCCD outperforms the ML detector in the presence of Doppler. In [60], the authors extend their analysis to include the effects of data modulation and jamming. Of particular interest is their approach for mitigating the effects of data modulation. The differential statistic $\Re\{Z\}$ is compared with a threshold, if it falls below that threshold then Z is negated before being passed to the accumulator. The purpose of this approach is to detect data bits after differential processing and to eliminate them prior to accumulation. The authors note that the presence of data modulation degrades the performance of the DCCD, but that it still outperforms the ML detector.

Jeong et al. [65] take a more analytical approach, considering the DCCD in the presence of fading for slot synchronisation in DS/CDMA communications networks. Of primary interest in [65] is the methodology employed. Modelling

the observation vector as a multi-dimensional complex Gaussian rv, the authors use a characteristic function† approach, in conjunction with a result due to Turin [138], to derive expressions for the distribution of the decision statistic under H_0 and H_1. The approach used in [65] provides the mechanism by which we obtain the major result in this thesis in Chapter 4.

Shin and Lee [116] applied the results of [65] to the analysis of a system incorporating a DCCD as the verification stage in a multi-dwell system with a matched filter search stage. The authors demonstrate a modest improvement in mean acquisition time relative to the NCCD detector.

More recently, related approaches have been considered in the context of GPS signal acquisition [15, 16, 40, 112, 113]. It is interesting to note that the first two DCCD-related papers for GPS were published within weeks of each other in autumn 2004.

Elders-Boll and Dettmar [40] consider a parallel architecture for the DCCD with estimation of the frequency offset, and fine code phase estimation based on [25]. The authors then demonstrate that the DCCD outperforms the NCCD in both the presence and absence of data modulation. The performance metric they use is the probability of detection P_d, but they make no reference to thresholds or P_{fa}. It would appear that they only evaluate the performance of the detector within the H_1 Doppler bin, and simply choose the maximum decision statistic as the code phase estimate.

Schmid and Neubauer [112] presented an essentially identical system that same month. This paper consisted of a more formal analysis of the DCCD performance. The accumulator output is modelled as a Gaussian rv, in accordance with the central limit theorem [92]. The decision statistic is then formed as the square magnitude of this rv and, hence, has a χ^2 distribution with two degrees of freedom. Again the authors use P_d as a performance metric, demonstrating an improvement in sensitivity over noncoherent combining, averaging about 1.5 dB, *i.e.* the DCCD requires about 1.5 dB lower SNR to achieve the same (P_{fa}, P_d) as an NCCD using the same dwell time. There is, however, a flaw in the Gaussian approximation made in this paper. The author's assume that the real and imaginary components of the accumulator output can be modelled as independent rvs. In Section 4.3.3 we shall demonstrate that this is not, in fact, the case and derive a new, more accurate Gaussian approximation based on this result.

†See Appendix C.3 for a discussion of the properties of characteristic functions.

Ávila-Rodríguez et al. [15, 16] have recently proposed a similar scheme. In this case, the authors consider the accumulation of every *second* differential product, and use only the real part as the decision statistic:

$$D_k\left(\widehat{\boldsymbol{\theta}}\right) = \Re\left\{\sum_{r=0}^{(R-1)/2} Y_{2r}^{*} Y_{2r+1}\right\}. \tag{2.78}$$

It is shown that the resulting rv can be expressed as the difference of two χ^2 rvs. Under H_0 the decision statistic is distributed as the difference of two *central* χ^2 rvs and hence the probability of false alarm is given by[†]:

$$P_{fa} = \frac{1}{2^{\frac{R-1}{2}}\sqrt{\pi}\Gamma\left(\frac{R}{2}\right)} \int_{V_{\text{Th}}}^{\infty} |x|^{\frac{R-1}{2}} K_{\frac{R-1}{2}}\left(|x|\right) d\, x. \tag{2.79}$$

Under H_1 the authors model the distribution of the decision statistic as the difference of a non-central and a central χ^2 rv. In Section 4.3.1, however, we shall demonstrate that the decision statistic is, in fact, distributed as the difference of two non-central χ^2 rvs. It appears that no closed-form solution is currently known for the distribution of the difference of two non-central χ^2 distributions, but the authors present a numerical technique for calculating P_d based on the Gil-Pelaez inversion theorem [44]. In addition to the theoretical analysis of their system, the authors also present a Monte-Carlo analysis. Whilst this system is shown to outperform the NCCD detector for zero Doppler offset, its performance degrades rapidly in the presence of Doppler shift. This is primarily due the use of only the real part of the differential output in the decision statistic. In the presence of a Doppler frequency offset, some signal power will inevitably move into the imaginary component and, hence, will be lost to this detector. The authors also note that the performance of their proposed detector is slightly less than that predicted by theory, which is interesting in itself (this is due to the error in their model under H_1 discussed above, we will return to this in Section 4.3.1).

In summary, differentially coherent combining is a promising technique which has been demonstrated to yield a 4–5 dB improvement in terms of the mean acquisition time for high SNR [156]. To extend the approach for lower SNR, a large number of coherent correlator outputs can be differentially coherently

[†]This interesting distribution was also discussed by Marcum [83, Equation (145)] in the context of radar detection.

combined. The analysis of such a system is difficult due to the correlation between successive differentially coherent products. A number of approaches have been used to overcome this difficulty. Firstly, Jeong et al. [65] developed an interesting mathematical technique based on some results on quadratic forms in multi-dimensional complex Gaussian rvs. They did not confirm this analysis with simulation, however. Secondly, Schmid and Neubauer [112] invoked the central limit theorem to make a Gaussian approximation to the decision variable. Finally, Ávila-Rodríguez et al. [16] proposed a modified form for which they were able to derive an exact closed-form expression for P_{fa} and a simple numerical routine for the determination of P_d. It is unclear whether this approach may be extended to the analysis of the original form of the DCCD, although it seems unlikely due to the difficulties introduced by the inter-dependence of the Z_r terms.

An interesting point to note is that we can generalise the DCCD to allow for different delay times. In Figure 2.16 the output of the accumulator is delayed by MT_{CA} s, prior to being conjugated and multiplied by the current output. A generalised DCCD detector would use a delay of JMT_{CA} s, where J is a non-negative integer. In this way we can consider both the NCCD ($J = 0$) and DCCD considered above ($J = 1$) to be special cases of a more general detector structure, though we find that there is no benefit (at least in the cases considered in this thesis) in increasing J above 1.

2.4.3 Differentially Coherent Detection

Differentially coherent detection[†] is another technique to counteract the effects of Doppler offset and data-modulation. It is, in many ways, similar to the differentially coherent combining technique discussed above, with the exception that the differential product is taken *prior* to correlation. The general form of the DCD is illustrated in Figure 2.17.

Originally proposed for GPS by Coenen and van Nee in 1992 [29], this approach takes advantage of the "shift-and-add" property of Gold codes [45] which ensures that the sum[‡] of a Gold code and a shifted version of that same Gold

[†]Also called differential decoding, pre-correlation differential detection and differential detection.

[‡]Gold codes are sequences of integers modulo 2 (or, equivalently, sequences of elements of the *Galois Field* GF(2) [140, Appendix B]). Prior to transmission each chip is mapped from the field GF(2) to the field of real numbers $\mathbb{R}$ by the mapping $\{0, 1\} \rightarrow \{+1, -1\}$, such that addition in GF(2) is equivalent to multiplication in $\mathbb{R}$.

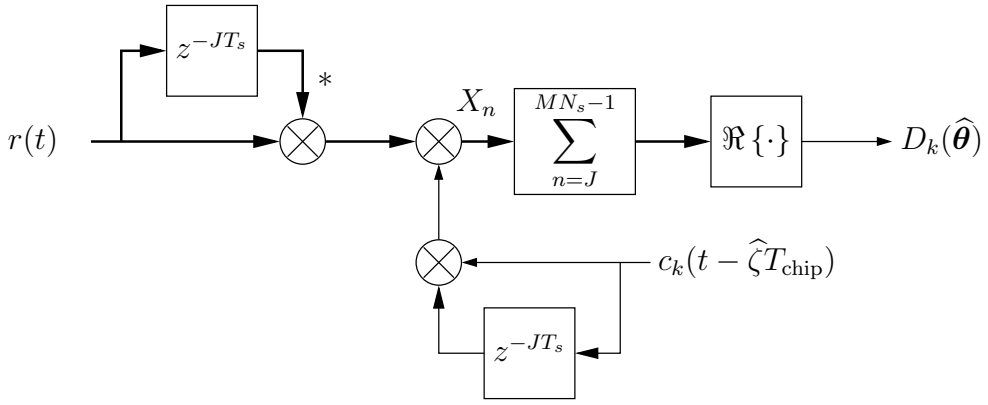


Figure 2.17: Differentially Coherent Detector

code results in another Gold code from the same family. Hence, applying the differential product to the received signal maps all the incoming Gold codes to new Gold codes in the same family, *provided* that the delay is an integer multiple of the chip period T_{chip}. To detect the signal from a given satellite the same differential product must be applied to the locally generated code, as indicated in Figure 2.17.

The advantage of differentially processing the received signal prior to correlation is that the effects of Doppler offset and data-modulation are effectively eliminated, whilst the auto- and cross-correlation properties of the signal are maintained. The major disadvantage is that the noise power is significantly increased *prior* to correlation.

In [29] the authors suggest the use of coherent accumulation to help mitigate the loss in SNR due to differential processing. Their approach is very interesting, relying heavily on the properties of the Gold codes. By storing one complete code period of received data in a shift register, the authors use the shift-and-add property to generate multiple (M) copies of the same Gold code, with the same shift offset relative to the received code, from the same set of received data. These M codes are coherently combined prior to correlation processing. Unfortunately, due to the structure of the Gold codes, the choice of a suitable value for M is limited to the single case $M = 4$, which provides a limited gain in SNR. However, by combining this technique with the type of coherent combining demonstrated in Figure 2.17, the pre-detection SNR can be increased still further. We consider this approach no further in this thesis.

A form of DCD was also proposed by Chung in 1995 [28] for the acquisition of

DS/SS signals in Rayleigh fading [102] channels. Chung considered only DS/SS systems using m-sequences as the spreading codes. The analysis follows a procedure very similar to that used by Schmid and Neubauer [112] for the DCCD, though it predates that work by almost a decade. The decision statistic is formed as the real part of the accumulator output, and is modelled as a Gaussian rv, again by invoking the central limit theorem. This approximation is shown to be accurate for low input SNRs. Simulation results indicate that the DCD significantly outperforms the NCCD in terms of mean acquisition time and that the DCD is significantly less sensitive to Doppler offsets than the NCCD. The system considered by Chung, however, consists of a matched filter (or a bank of parallel matched filters) whereas active correlation is of greater interest in GPS acquisition.

This differentially coherent approach was also considered for the GPS acquisition problem by Lin and Tsui [81, 137], who refer to it as the "Delay and Multiply" approach. The authors appear to have been unaware of the earlier work by Coenen and van Nee, and Chung. This work was developed with the aim of providing new acquisition algorithms for a software-based GPS receiver, and focuses on issues associated with performing the differentially coherent processing when the received data is a stream of real, rather than complex, numbers. In a related work [82] the same authors suggest that, while the delay and multiply method is the fastest acquisition technique in high SNR environments, it is incapable of acquiring weak signals. No formal analysis is presented in any of this work, other than some results from the processing of real data. Also, the authors use arbitrary time delays whereas, strictly speaking, the time delay must be a multiple of the chip time to take advantage of the shift-and-add property of Gold codes.

Finally, in a recent paper by Shanmugam et al. [113], the NCCD, DCCD and DCD schemes are compared using actual "live" GPS signals. Again, considering only the performance of the detector within a single cell, the authors demonstrate that: 1) the DCD is significantly more sensitive to input SNR than either the DCCD or NCCD; 2) the effects of Doppler shift, Doppler drift and data modulation on the DCD are negligible; and 3) the DCCD outperforms the NCCD, though the difference tends to decrease as the coherent accumulation period is increased. The authors suggest that the DCD scheme may be useful for fast acquisition in high SNR environments, or for high dynamic environments (*i.e.*

environments subject to large Doppler offsets, say ≥ 20 kHz).

While the differentially coherent technique discussed above is essentially an *ad hoc* approach to the acquisition problem, it can be thought of as an attempt at a detector *invariant* to the received Doppler offset and data modulation. This invariance was discussed in Section 2.3. In essence, the output of the differentially coherent product in Figure 2.17 is independent of the Doppler offset and data modulation affecting the received signal. The DCD treats both of these effects as nuisance parameters, and provides an estimate of the code phase offset alone. Thus, the desired parameter is the scalar $\theta = \zeta$, and all other signal parameters are considered to be nuisance parameters. For this reason, comparisons between this detector and the two forms of combining detector discussed previously are, in a sense, unfair. Both the noncoherent and differentially coherent combining detectors produce estimates of both the code phase and Doppler offsets of the received signal whilst the DCD produces an estimate of the code phase only. It is also important to note that, if a DCD is to be used in the acquisition stage, then the tracking will have to be achieved in a differentially coherent fashion also, since other tracking loops require some knowledge of the frequency of the received signal to function properly. A differentially coherent code tracking loop has been considered in [42].

2.4.4 Parallel Detection

The detectors examined thus far have all been single cell detectors, generating a single test statistic for a single parameter estimate. A practical implementation might rely on more than one decision statistic prior to making a decision. We consider a vector of decision statistics, $\boldsymbol{D_k}(\boldsymbol{\theta})$, corresponding to a number of points in the uncertainty space. We refer to this collection of points as a *tile* in the uncertainty space, and denote by C_{T} the number of cells in a tile. This situation is illustrated in Figure 2.18. Note that a tile could have any shape, it need not consist of a set of contiguous cells in the uncertainty region, though this will generally be the case. In addition, all C_{T} decision statistics need not be gathered at once but may, in fact, be gathered serially [31]. We refer to any acquisition architecture relying on multiple measurements of the decision statistic as a parallel architecture. A decision is made based on the parallel consideration of a number of parameter points, even though the decision statistics were not necessarily calculated in parallel.

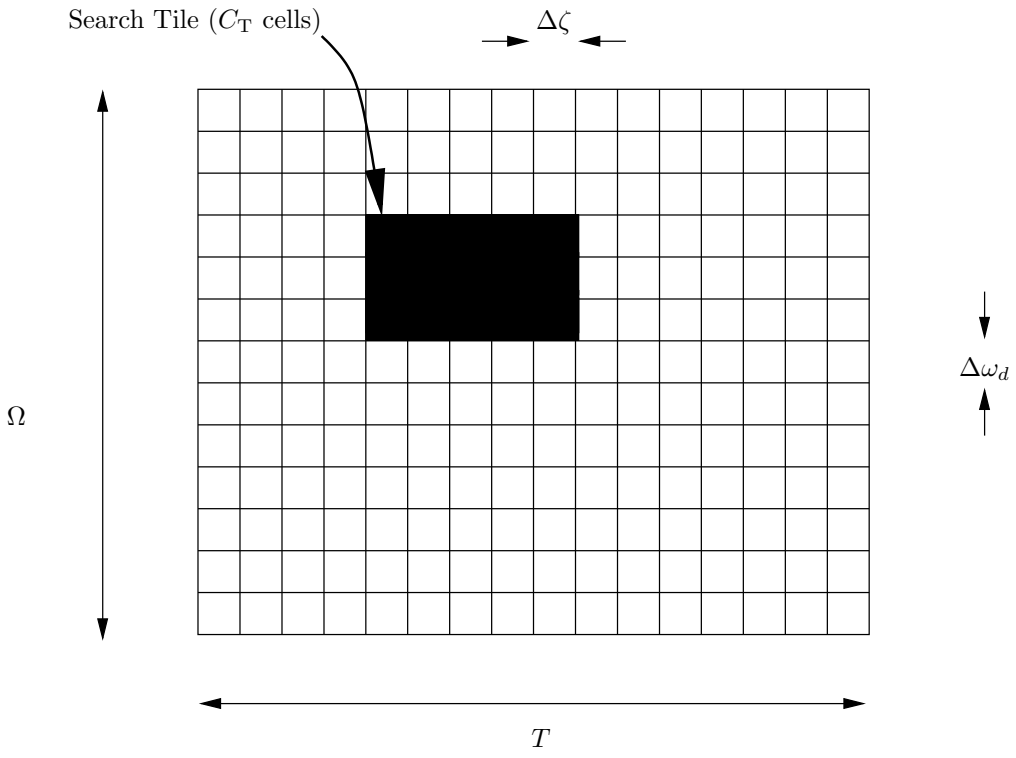


Figure 2.18: Acquisition Grid with Parallel Search Tile

Within a tile the local approximation to the ML estimate is given by the parameter point for which $\boldsymbol{D_k}(\boldsymbol{\theta})$ is a maximum. Corazza [31] refers to this as the *MAX* criterion. If the decision statistic of the ML parameter estimate crosses a predetermined threshold V_{Th} then a "hit" is declared and the signal is deemed to have been detected in that cell. Corazza referred to this as the threshold crossing, or *T/C* criterion. Note that both detection and estimation events occur within each tile.

The performance of the detector/estimator is determined by the dwell time and the statistics of the decision variable. The dwell time is simply the time taken to compute the vector $\boldsymbol{D_k}$, and depends on whether all test statistics within a tile are calculated at once, or whether they are calculated serially. The parallel calculation of all the decision statistics within a tile will be much faster, but will also require more hardware.

The statistics of the detector/estimator are related to the distribution of the largest of a number of rvs. This a well known quantity in probability theory, known as the extreme value distribution [52]. Given N independent rvs

$X_1, X_2, \ldots X_N$, with distributions:

$$f_{X_i}(x) \ : \ 1 \leq i \leq N$$

and CDFs:

$$F_{X_i}(x) \ : \ 1 \leq i \leq N,$$

then the probability that all the X_i are less than some value x is given by:

$$\Pr\{X_i < x \ : \forall i \ 1 \leq i \leq N\} = \prod_{i=1}^{N} F_{X_i}(x).$$

Letting $f_{Y_i}(y)$ denote the probability density of the event: $X_i > X_j \ \forall \ j \neq i$, at the point $X_i = y$, then:

$$f_{Y_i}(y) = f_{X_i}(y) \prod_{\substack{j=1 \\ j \neq i}}^{N} F_{X_j}(y), \tag{2.80}$$

and so the probability that X_i is both greater than all the other rvs and greater than the threshold V_{Th} is given by:

$$1 - F_{Y_i}(V_{\mathrm{Th}}) = \int_{V_{\mathrm{Th}}}^{\infty} f_{X_i}(y) \prod_{\substack{j=1 \\ j \neq i}}^{N} F_{X_j}(y) d\, y. \tag{2.81}$$

During the observation interval there are two possibilities: either the tile under test contains the true signal parameter point $\boldsymbol{\theta}_t$, in which case we refer to the tile as a H_1 tile, or it does not, in which case we have a H_0 tile. The statistics of the detector/estimator are, therefore, given by:

1. P_d: the probability of correctly identifying $\boldsymbol{\theta}_t$ in a H_1 tile.
2. P_{r_1}: the probability of rejecting a H_1 tile. This occurs when all components of $\boldsymbol{D_k} < V_{\mathrm{Th}}$ in a H_1 tile.
3. P_{fa_1}: the probability of false alarm in a H_1 tile. The largest component of $\boldsymbol{D_k}$ is greater than the threshold, and does *not* correspond to $\boldsymbol{\theta}_t$.
4. P_{r_0}: the probability of correctly rejecting a H_0 tile.
5. P_{fa_0}: the probability of false alarm in a H_0 tile.

The simplest model of the detector/estimator assumes that there is only one H_1 cell, all other cells containing only noise. Thus, assuming that there are C_{T} cells per tile, and using Equation (2.81) above, we have [31, 134]:

$$\begin{aligned} P_d &= \int_{V_{\mathrm{Th}}}^{\infty} f_{D_k(\boldsymbol{\theta})|H_1}(y \mid H_1) \left[F_{D_k(\boldsymbol{\theta})|H_0}(y \mid H_0)\right]^{C_{\mathrm{T}}-1} d\,y && (2.82)\\ P_{r_1} &= F_{D_k(\boldsymbol{\theta})|H_1}(V_{\mathrm{Th}} \mid H_1) \left[F_{D_k(\boldsymbol{\theta})|H_0}(V_{\mathrm{Th}} \mid H_0)\right]^{C_{\mathrm{T}}-1} && (2.83)\\ P_{fa_1} &= 1 - P_d - P_{r_1} && (2.84)\\ P_{r_0} &= \left[F_{D_k(\boldsymbol{\theta})|H_0}(V_{\mathrm{Th}} \mid H_0)\right]^{C_{\mathrm{T}}} && (2.85)\\ P_{fa_0} &= 1 - P_{r_0}. && (2.86) \end{aligned}$$

Similar expressions can be derived to model the spread of the influence of $\boldsymbol{\theta}_t$ amongst multiple cells [26] but this is beyond our scope here. Note that Equations (2.82) to (2.86) are valid for all forms of detector discussed previously. The form of the detector determines $f_{D_k(\boldsymbol{\theta})|H_i}(y \mid H_i)$ $i = 0, 1$, as seen in Equations (2.33), (2.39), (2.61), (2.66) and (2.73). The CDF of the decision statistic in each cell is given by:

$$F_{D_k(\boldsymbol{\theta})|H_i}(y \mid H_i) = \int_{-\infty}^{y} f_{D_k(\boldsymbol{\theta})|H_i}(z \mid H_i) dz \quad i = 0, 1.$$

When the signal can be assumed to be present, and the search tile covers the entire uncertainty space, then no detection stage is required: the problem is one of pure estimation. The threshold can, therefore, be set to minus infinity and a simple union bound on P_{fa_1} can be found [25, 85, 108]:

$$P_{fa_1} \leq \sum_{\substack{j=1 \\ j \neq i}}^{C_{\mathrm{T}}} \Pr\left\{D_k(\boldsymbol{\theta_j}) > D_k(\boldsymbol{\theta_i}) \;\mid\; \boldsymbol{\theta}_t = \boldsymbol{\theta_i}\right\}. \tag{2.87}$$

For the ML detector Milstein et al. [85] use a result due to Stein [131] to show that:

$$\Pr\left\{D_k(\boldsymbol{\theta_j} \mid H_0) > D_k(\boldsymbol{\theta_i} \mid H_1)\right\} = \frac{1}{2}\left[1 - Q_1\left(\sqrt{b}, \sqrt{a}\right) + Q_1\left(\sqrt{a}, \sqrt{b}\right)\right], \tag{2.88}$$

where a and b are the SNR in the H_0 and H_1 cells respectively. Equation (2.88) gives the probability that one χ^2 rv with two degrees of freedom is greater than another. In [122, Equation (8)] Simon and Alouini give a similar expression for two χ^2 rvs with $2K$ degrees of freedom which can be applied in the case of the

noncoherent combining detector. Simon and Alouini's expression is considerably more involved than Equation (2.88) above. In a forthcoming paper [89] we present a simplified form of Simon and Alouini's expression.

The above presentation gives us a means to analyse the parallel form of the detector/estimator, but does not consider its implementation. In the following sections we consider two different approaches to the implementation of the parallel detector/estimator. The first, most obvious form, is simply a cascading of multiple single cell detectors. We refer to this approach as *time-domain parallelism* [26, 33, 85, 107, 108, 125, 127, 134]. An alternative approach is to take advantage of the redundancy inherent in the calculation of the generalised likelihood ratio using transform domain techniques. This approach is referred to as *transform-domain parallelism* [10, 11, 29, 30, 34, 141, 153, 154].

Time-Domain Parallelism

The earliest designs for parallel acquisition of DS/CDMA signals focused on architectures for the efficient construction of banks of matched filters [85, 126, 127, 134]. A length T analogue matched filter consists of a tapped-delay line which holds T seconds of the received signal and generates a single output which is a function of that T-second data set. The delay line requires T seconds to fill but provides a continuous output thereafter. A digital matched filter stores, say, M samples of the received input, requires M samples to "fill up" and then generates an output at every sampling instant thereafter. To speed up the acquisition of DS/CDMA signals a bank of N matched filters is implemented, each filter is M samples long, and the total code phase uncertainty is NM samples. Each filter is matched to a different *sub-sequence* of the spreading code of the satellite of interest. Once the matched filters are filled then a total of N possible code phases can be tested every sampling instant. In this architecture there is a fundamental trade-off between the degree of parallelism and performance. The greater the number of filters implemented in parallel the shorter the sub-sequence to which each filter is matched and, hence, the greater the correlation side lobes.

Milstein et al.'s paper [85] appears to be the first on the topic, presenting a theoretical analysis of the architecture in the absence of Doppler effects. This was also the first reported use of the union bound and Equation (2.88). This was followed by Su's treatment [134], who adapted Milstein's approach to include Doppler effects by applying noncoherent combining. Further early work on the

matched filter parallel architecture was conducted by Sourour and Gupta [126, 127] to account for Rayleigh fading effects.

The first parallel active correlator architecture seems to have been the ML estimator for the GPS tracking process by Hurd et al. [58], discussed in Section 2.3.1. In 1988, the parallel active correlator acquisition architecture was suggested independently by Cheng [26] for GPS and Davisson and Flikkema [37] for the Tracking and Data Relay Satellite System (TDRSS). Cheng's analysis is interesting, in that he considers the effects of data modulation and the use of noncoherent combining, but ignores Doppler effects. In a later paper, [27], Cheng extended the work of Hurd et al. to the acquisition problem. In [27], the author considers the effects of both Doppler offset and data modulation, showing that there is an optimum choice for K, the number of subintervals to be noncoherently combined.

The general form of the active correlator based, time-domain, parallel acquisition architecture is given in Figure 2.19. Alternative parallel schemes for the

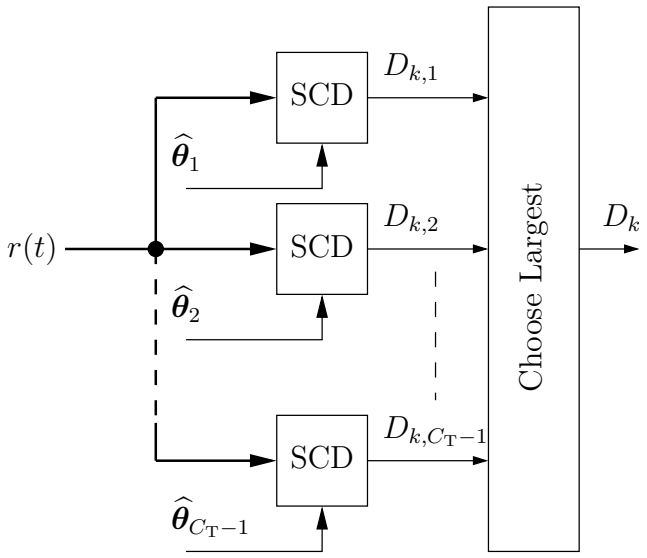


Figure 2.19: Active Correlator Architecture for Time Domain Parallelism. SCD Denotes a Single Cell Detector.

acquisition of DS/CDMA signals in the presence of data modulation have been suggested in [80] and [152].

Transform-Domain Parallelism

Possibly the first mention of transform-domain parallelism in the literature was by Cohn and Lempel in 1977 [30]. In this paper the authors use the fact that generating the cross-correlation function for all possible code offsets can be viewed as a matrix multiplication. Now, if the spreading codes are m-sequences then this matrix is shown to be a permutation of the Walsh-Hadamard matrix [143]. If L is the length of the spreading code then the multiplication of an $L \times 1$ vector by an $L \times L$ matrix requires L^2 operations. However a fast transform method (called the *Walsh Transform* [21]) permits the calculation of the product of a vector by a Walsh-Hadamard matrix in only $L \log_2 L$ operations. The correlation function can then be implemented efficiently by applying a permutation to the input vector (the observation vector for one complete code period), calculating the fast Walsh transform of this vector and then applying the inverse permutation to the result to obtain the cross-correlation of the input vector and the spreading code. Whilst this approach relies on the use of m-sequences, and so is not applicable to the GPS problem, it does demonstrate the use of efficient parallelism to eliminate redundancy in the calculation of the correlation function.

By far the most common form of transform-domain parallelism is frequency-domain parallelism. This appears to have been first suggested by van Nee and Coenen in 1991 [141]. The key observation in this case is that cross correlation in the time domain is equivalent to multiplication by the appropriate complex conjugate in the frequency domain:

$$\mathcal{F}\left\{\int_0^{T_{\mathrm{CA}}} r(\tau)c_k(\tau - t)d\tau\right\} \Longleftrightarrow R(j\omega)C_k^*(j\omega), \tag{2.89}$$

where $\mathcal{F}\{\cdot\}$ denotes the Fourier transform and $R(j\omega)$ and $C_k(j\omega)$ are the Fourier transforms of $r(t)$ and $c_k(t)$ respectively. The discrete equivalent can be written:

$$\begin{aligned} \mathrm{DFT}\{\boldsymbol{r} \cdot z^{\tau}\boldsymbol{c_k}\} &= \left\{\sum_{l=0}^{N-1}\left(\sum_{n=0}^{N-1} r_n c_{k,n-\tau}\right)\exp\left(-j\frac{2\pi\tau}{N}l\right)\right\}_{\tau=0,1,\ldots,N-1} \\ &\Longleftrightarrow \boldsymbol{R} \odot \boldsymbol{C_k^*}, \end{aligned} \tag{2.90}$$

where $\boldsymbol{r} = [r_0, r_1, \ldots, r_{N-1}]$ and $\boldsymbol{c_k} = [c_{k,0}, c_{k,1}, \ldots, c_{k,N_1}]$ are the received signal vector and local code vector respectively, z is the unit delay operator, $\mathrm{DFT}\{\cdot\}$ denotes the Discrete Fourier Transform (DFT), $\boldsymbol{R}$ and $\boldsymbol{C}$ are the DFTs of $\boldsymbol{r}$ and

$\boldsymbol{c}$ respectively, $\boldsymbol{a} \odot \boldsymbol{b}$ is the term-by-term product of the vectors $\boldsymbol{a}$ and $\boldsymbol{b}$ and the indexing $c_{k,n+\tau}$ is cyclic, *i.e.* $c_{k,n+\tau} = c_{k,n+\tau \bmod N}$. Thus, Equation (2.90) calculates the *circular correlation* between the vectors $\boldsymbol{r}$ and $\boldsymbol{c_k}$. Note that this is precisely the correlation function to be determined according to Hurd et al. [58] for the maximum likelihood estimator (see Equation (2.17)).

The general form of the FFT-based detector/estimator is given in Figure 2.20. The output metric $\boldsymbol{D_k}(\widehat{\boldsymbol{\theta}})$ is a length N vector of real numbers. To implement a

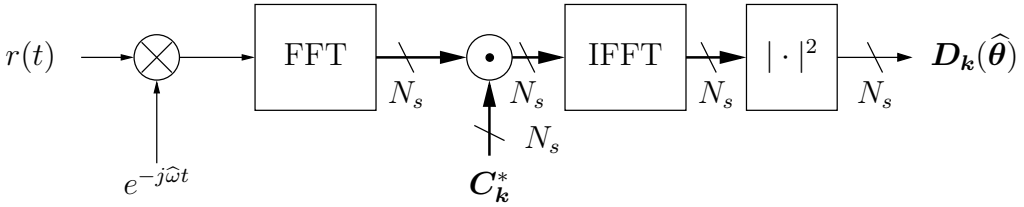


Figure 2.20: Structure of the FFT Detector/Estimator

local GLRT, the location of the maximum value of $\boldsymbol{D_k}$ is chosen as the optimal estimate of the code phase offset, and detection occurs if this value exceeds a threshold. This method covers all possible code phase offsets for a given Doppler estimate $\widehat{\omega_d}$ using a single observation interval. The detector/estimator tile, therefore, occupies one complete Doppler bin, as illustrated in Figure 2.21.

Sampling Schemes

The DFT can be calculated very efficiently using an algorithm known as the Fast Fourier Transform (FFT) [21]. The FFT relies heavily on the factorisation of N, the length of the observation vector. The optimal FFT algorithm occurs when N is a power of 2, in which case the FFT can be calculated in $2N \log_2 N$ operations, compared with $2N^2$ operations by direct evaluation of the DFT.

In [141] the received signal is sampled at twice the chip rate, and so there are $N = 2046$ samples per code period. To enable the use of an efficient FFT this vector is then padded with two zeros to obtain a vector of length $N = 2048 = 2^{11}$. An alternative approach is to sample both the incoming signal and the local code at a rate which directly yields an observation vector whose length is a power of two. For example, in [95] the authors used a sample rate of 4.096 MHz to yield $N = 4096 = 2^{12}$ samples per code period. The problem with these approaches is that, when resampling or zero-padding, the structure of the spreading codes is modified and, hence, the auto- and cross-correlation properties are affected.

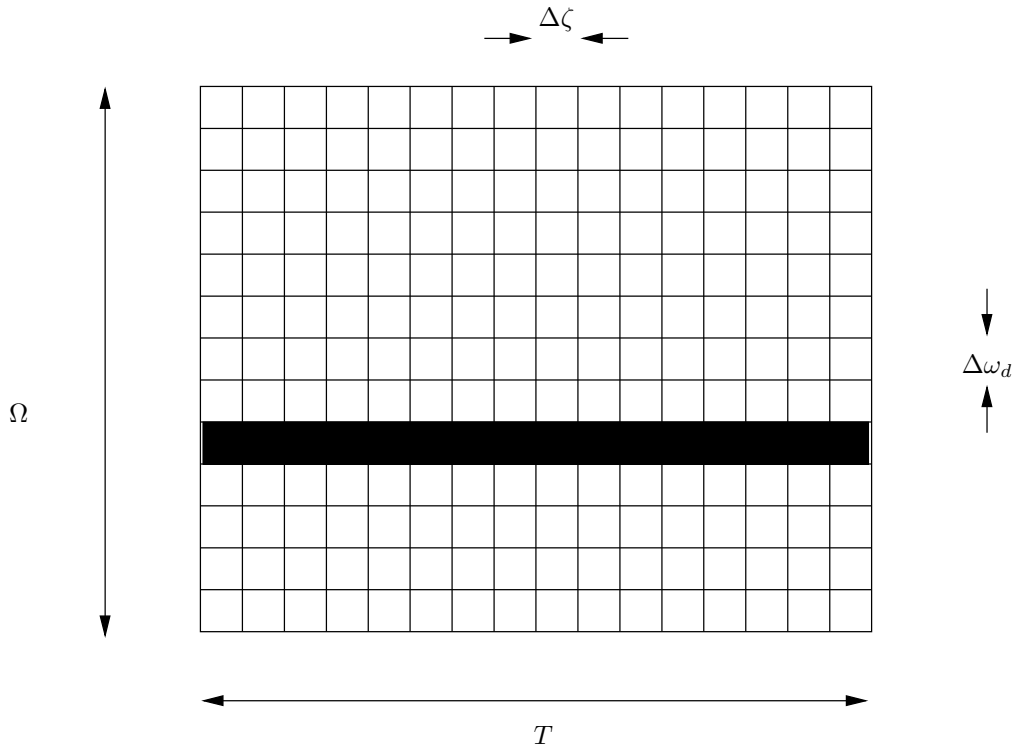


Figure 2.21: FFT Detector/Estimator Tile in the Uncertainty Region

In general, this results in an increase in the cross-correlation sidelobes, and a distortion of the main lobe, which loses its triangular shape. In practice, these effects are small when the modifications are small. For example, padding a vector of 2046 samples with just two extra zeros does not lead to a dramatic increase in cross-correlation values. Various other sampling schemes have been considered in the literature [12, 34, 81, 130, 137, 153], which we now consider briefly.

Davenport [34] considered the use of the Chirp-Z Transform (CZT), in which case the received signal is sampled at a rate commensurate with the chip rate, is then padded with zeros to a length which is a power of two, and then a "chirp" function is applied prior to taking the FFT. The correlation is performed in the frequency domain as above, the inverse FFT is taken, and the result is "de-chirped". The chirp function is a damped (complex) exponential which effectively eliminates the distortion caused by the zero padding. Yang [153] considered a related approach, but the chirp function is effectively pre-calculated and applied only to the local code. In this instance, an arbitrary sampling rate can be applied at the front end, yielding M samples per code period. The observation vector is then extended to a length $2N$ vector, where N is a power of two, by zero-padding.

The local code vector is also increased to a length $2N$ but, in this case, the last M components are simply a repetition of the first M. Although not explicitly stated by Yang, it would appear that this approach is only valid for $N > M$, in which case the modified vector has sufficient "room" for two repetitions of the length M original vector. The remaining components are set to zero. The circular correlation property of the local and received signals is restored by this approach, but it requires a significant increase in the amount of processing required. For example, if the incoming signal is sampled at a rate of two samples per chip then $M = 2046$, which means $N \geq 2048$ and so a minimum of a 4096 point FFT is required. Yang also discusses the advantages of sampling at a rate that is *not* a multiple of the chip rate. The difference in rates between the incoming signal and the local reference allows a greater accuracy in measuring the code phase offset.

Tsui [137] considers the use of the FFT in a software GPS signal processor. His approach relies on direct-downconversion from intermediate frequency (IF) to baseband at a sampling rate of 5MHz, yielding 5000 samples per code period. While the principle of the FFT algorithm can be applied in this case (since 5000 is not a prime number), it is not well suited to hardware implementation. In an effort to overcome this difficulty, Starzyk et al. [12, 130] propose what they refer to as the "Averaging Correlation" approach. The 5000 point observation vector is down-sampled to 5 separate 1024 point vectors, a similar operation is applied to the local code. The local code is then correlated with each of the candidate observation vectors by the frequency domain method, and the maximum peak from amongst the candidate vectors is chosen as the code phase estimate. This approach permits the use of the highly efficient 1024-point FFT, as the authors point out, it is much easier in hardware to implement five 1024-point FFTs than a single 5000-point FFT.

Psiaki [103] also considered Tsui's 5 MHz sampling scheme. Again, a software-based receiver was the focus of this paper, but Psiaki considers a re-sampling scheme whereby the received signal is linearly interpolated up to a sampling rate of 8.192 MHz. This yields $8192 = 2^{13}$ points per code period, thereby permitting the use of a highly efficient FFT.

Apart from the numerical efficiency in calculating the correlation function for all code phase offsets, the frequency-domain approach has a number of other advantages [21]:

1. The frequency shift theorem.

2. The time shift theorem.

3. Linearity.

Each of these is discussed briefly here below.

The Frequency Shift Theorem

The frequency shift theorem states:

$$\mathcal{F}\left\{\exp\left(-j\omega_d t\right) f(t)\right\} \Longleftrightarrow F(j(\omega+\omega_d)), \tag{2.91}$$

where $F(j\omega) = \mathcal{F}\left\{f(t)\right\}$. Thus, the Fourier Transform of the product of a function by a complex exponential is simply a shifted version of the transform of the function. For the DFT the shifting can only be implemented as an integer number of samples. This corresponds to a frequency shift by a multiple of the inverse of the observation interval.

The benefit of this theorem is immediately obvious if we consider Figure 2.20. Note that the received signal is multiplied by $\exp\left(-j\widehat{\omega}t\right)$ prior to the FFT block. This achieves down-conversion by the Doppler frequency estimate for a candidate Doppler bin. By the frequency shift theorem, we see that we can move this down-conversion to the other side of the FFT, and so we only need to perform one FFT operation for *all* Doppler bins. This represents a significant saving when the frequency uncertainty is large (*i.e.* when there is a large number of Doppler bins). Alternatively, we could use a single FFT block to provide the same input to all search channels. Each channel searches a single Doppler bin for a given satellite. Frequency down-conversion in each channel is achieved by rotation in the Doppler domain. Note, however, that the shift must be an integer number of samples in the transform domain, and so the frequency down-conversion achieved in this manner will always be a multiple of the inverse of the observation interval. Thus, the frequency shift will be a multiple of $\frac{1}{T_{\mathrm{CA}}} = 1$ kHz, as illustrated in Figure 2.22.

If the Doppler bin width is less than 1 kHz, such as is the case when coherent accumulation is performed over M ms, then fine Doppler corrections can be made either prior to the FFT [103] or after it [10]. Psiaki's approach in [103] is to generate M copies of the received signal, each one multiplied by an appropriate complex sinusoid to achieve down-conversion by a fraction of 1 kHz. Coarse

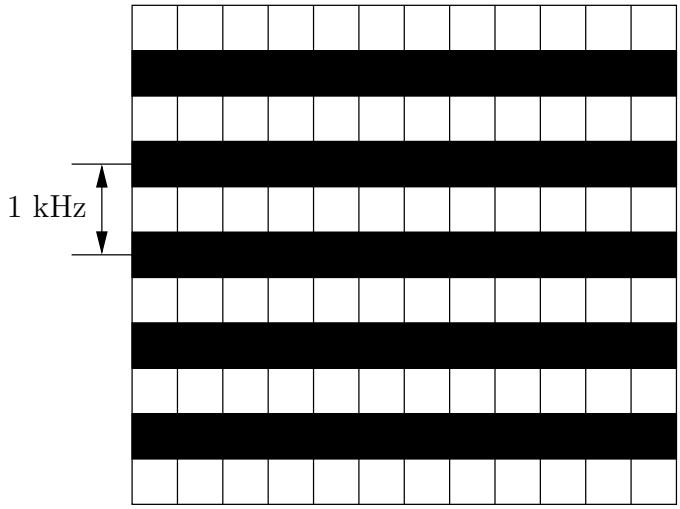


Figure 2.22: Tile Coverage in the Uncertainty Region for the FFT Detector/ Estimator using Doppler Rotation

frequency adjustment is then performed by rotation post FFT. This requires a total of M (N-point) FFT operations for all channels and all Doppler bins. In [10] Akopian applies the shift theorem, not to the received signal, but rather to the stored local code (or local replica, as he calls it). This approach takes advantage of the fact that the carrier frequency down-conversion can also be achieved by shifting the local replica in the opposite direction to the shift to be applied to the received signal. Again, this approach leads to a coarse frequency shift of a multiple of 1 kHz. Fine-frequency compensation is achieved in a similar manner to Psiaki's approach, though Akopian considers a two-dimensional FFT, achieving parallelism in both the code delay and frequency domains. In effect, coherent accumulation and fine-frequency compensation are achieved by a combination of an M-point FFT and multiplication by a complex sinusoid.

In summary, the frequency shift theorem can be applied to achieve down conversion of the carrier frequency. This is achieved by a rotation of the FFT of either the received signal or the local code. This down-conversion is limited to multiples of 1 kHz, so a fine-frequency compensation is required if a resolution better than 1 kHz is desired.

The Time Shift Theorem

The time-domain analogue of the frequency shift theorem can be represented by the equation:

$$\mathcal{F}\{f(t+\tau)\} = F(j\omega)\exp(j\omega\tau). \tag{2.92}$$

The use of this theorem to counter the effects of code Doppler seems to have been first reported in [75], and is also applied in [10, 11].

In Section 2.4.1 we saw that, for the traditional single cell detector, the code Doppler effect is accounted for by modifying the chip rate of the local code to match the current Doppler estimate. In the FFT-based correlator two approaches are possible: 1) code Doppler is compensated for by a modification of the local code [103]; 2) code Doppler is compensated for by modifying the received signal [75]. The latter approach makes use of the time shift theorem. Both of these approaches use the noncoherent combining detector of Section 2.4.1.

Within a coherent accumulation period the effect of code Doppler can be modelled as a degradation in the magnitude of the correlation function. Between coherent accumulation periods, however, the dominant effect is the "slippage" of the true code phase offset ζ_t relative to the estimate $\widehat{\zeta}$. This effect can be accounted for by time-shifting the received signal (or the local code) between coherent accumulations. The time shift is equal to the amount the local code would slip, relative to the received code, if the current Doppler frequency estimate $\widehat{\omega_d}$ was exactly correct. Given $\widehat{\eta} = \widehat{\omega_d}/\omega_0$, then the time shift is given by $\tau = \widehat{\eta} M T_{\mathrm{CA}}$ seconds. By Krasner's technique [75], this time shift is implemented in the frequency domain by multiplying the FFT of the k^{th} coherent accumulator output vector by the complex exponential $\exp(-j2\pi k\tau/T_{\mathrm{CA}})$. We find, however, that this technique introduces significant distortion of the local replica whenever τ is not an integer number of sample periods.

An alternative approach to the treatment of code Doppler effects was given by Psiaki [103] and, although this approach does not rely on the time shift theorem, we describe it here for completeness. In this case, the local code is generated in much the same way as for the serial detector, in that the chip rate is varied with the Doppler estimate. Psiaki uses linear interpolation of both the received signal and the local code to ensure that there is exactly one full code period of each present in the observation interval. This interpolation must be performed for every Doppler frequency estimate, but can be achieved very efficiently. This

approach implies that the resolution of $\widehat{\zeta}$ is a function of $\widehat{\omega_d}$. An advantage of this approach is that it provides code Doppler compensation both within and between coherent accumulation intervals. It also permits storage of the resampled local codes, thereby saving computations during acquisition. The primary disadvantages of Psiaki's approach are the large memory requirements and the difficulty in calculating a 8192-point FFT. Whilst this approach provides a highly accurate code Doppler compensation mechanism, we have already seen that the effect of code Doppler within a coherent observation interval is minimal. Hence this level of accuracy is not usually required, and code Doppler compensation between coherent observation intervals is generally sufficient.

Linearity

The Fourier Transform is a linear operation, thus:

$$\mathcal{F}\left\{f(t)+g(t)\right\} = \mathcal{F}\left\{f(t)\right\} + \mathcal{F}\left\{g(t)\right\}, \tag{2.93}$$

and, given any linear operator $\mathcal{L}\{\cdot\}$, then:

$$\mathcal{F}\left\{\mathcal{L}\left\{f(t)\right\}\right\} = \mathcal{L}\left\{\mathcal{F}\left\{f(t)\right\}\right\}. \tag{2.94}$$

Now, both correlation and coherent accumulation are linear operators, and so any coherent accumulation carried out after the correlation function can equally well be performed prior to the FFT.

The advantage this provides is most readily seen by considering an example. Recall that for low input SNRs it is necessary to increase the coherent integration time to reliably detect the received signal. This was achieved by coherently combining M consecutive correlator outputs. A transform domain implementation of this combining is illustrated in Figure 2.23. Now, by the linearity of the FFT,

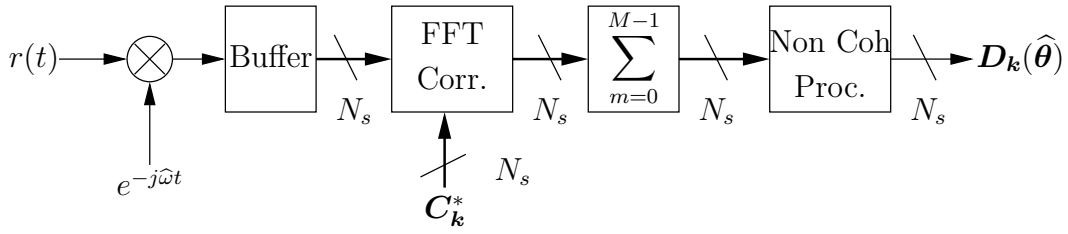


Figure 2.23: FFT Detector with Post-Correlation Coherent Accumulation

this coherent accumulation can be achieved prior to the FFT, block as illustrated in Figure 2.24. Thus, the FFT need only be performed once for every M code

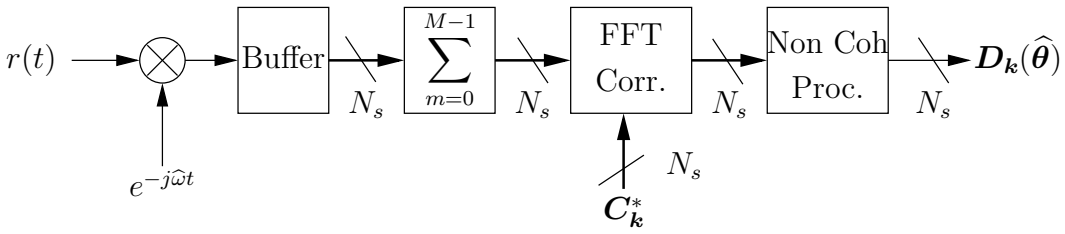


Figure 2.24: FFT Detector with Pre-Correlation Coherent Accumulation

periods, rather than once for every code period. This represents a significant saving if M is large. Note that this approach can be applied to the coherent accumulation of the transform-domain forms of all the correlation-based detectors discussed in Section 2.4. It would appear that this was first observed by Krasner in [75], but it is also implicit in Coenen and van Nee's work on the DCD [29].

It is worth noting, however, that the use of pre-correlation coherent accumulation limits the degree to which code Doppler effects can be mitigated by modification of the local replica. Note that only one copy of the local replica is used for every M received code periods. Hence, local replica code Doppler compensation can at best be achieved between coherent observation intervals (of duration MT_{CA} s) rather than between code periods (of duration T_{CA} s). A simple scheme can be implemented whereby the local code replica is time shifted by one half of the estimated code phase shift over one coherent observation interval. Thus, a finer degree of code Doppler compensation can be achieved if post-correlation coherent accumulation is used. In practice, however, we find that the coarse code Doppler compensation achieved with pre-correlation coherent accumulation is sufficient.

2.5 The Acquisition Process

As discussed in Section 2.3.1, the movement of the detector/estimator through the uncertainty region is controlled by the acquisition process. Various forms of detector/estimator have been considered in the previous section, in this section we characterise it entirely by:

1. Its cell coverage in the uncertainty region, which we term a "tile".

2. The time taken to dwell in one tile, τ_D.

3. The distribution of the decision statistic under H_1 and H_0.

Our analysis of the detector/estimator allows us to calculate each of these quantities for a given implementation. However, the quantity of greatest interest to us is the *time*, T_{ACQ}, taken to acquire the signal. This will be a function, not only of the form of the detector/estimator, but also of the acquisition process. In this section we review the analysis and design of the acquisition process.

Note that, for simplicity, we consider the acquisition of a single satellite signal only. In practice, the receiver must acquire signals from multiple (at least four) satellites. Typically the most difficult acquisition is that of the first signal since, once the first signal is acquired, then the search space for the remaining satellites can be reduced. In practice, therefore, the uncertainty region is not constant but depends both on the *a priori* information available to the receiver and the information obtained from other acquired signals.

2.5.1 Acquisition Modes

The acquisition process is commonly divided into three modes of operation:

1. The search mode.

2. The verification mode.

3. The lock mode.

In the search mode the detector/estimator moves through the uncertainty region looking for the H_1 cell. The acquisition process determines the duration of each dwell, the decision threshold and the order in which tiles are searched. Once a hit has been declared in the search mode the acquisition process enters the verification mode. In this mode, a candidate cell has been chosen and the detector/ estimator will operate as a pure detector. In the verification mode the cell under test remains fixed and the acquisition process controls the dwell time and decision threshold of the detector/estimator. If the candidate cell is rejected by the verification mode the acquisition process returns to the search mode, otherwise the system enters the lock mode. Once the lock mode is entered the acquisition process is complete, the signal is deemed to have been acquired and the tracking

loops are closed. In traditional receiver architectures the detector/estimator circuitry is now used to determine the lock condition of the tracking loop. Again, the detector/estimator operates as a pure detector. The parameter estimate $\widehat{\boldsymbol{\theta}}$ is under the control of the tracking circuit. Once the lock detector indicates loss-of-lock, then control is passed back to the acquisition process which restarts in the search mode. The acquisition modes are summarised in Figure 2.25.

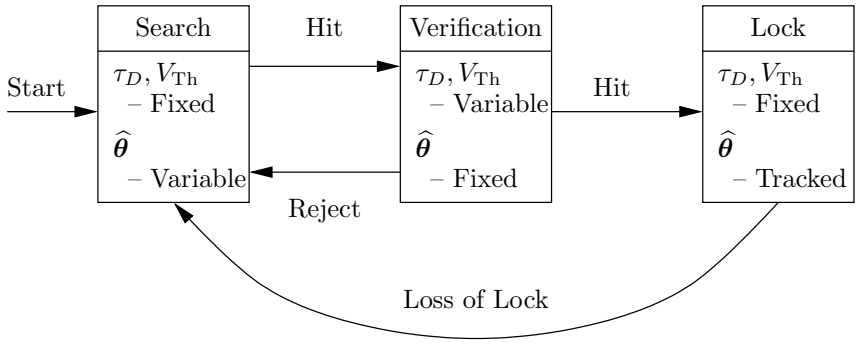


Figure 2.25: An Overview of Acquisition Modes

In both search and verification modes the detector/estimator is in "motion", under the control of the acquisition unit. In the search mode the motion is through the uncertainty region ($\widehat{\boldsymbol{\theta}}$ moves through Θ^*), in the verification mode the motion is through the receiver parameter space (τ_D and V_{Th}). In contrast, in the lock mode the signal parameters are being tracked and $\widehat{\boldsymbol{\theta}}$ is under the control of the tracking loops (and is now an element of the continuous parameter space Θ).

The Search Mode

In the search mode the detector/estimator operates on the Neyman-Pearson criterion [142, p. 33], that is, the thresholds are chosen to maximise the probability of correct detection, for a given probability of false alarm. Movement through the uncertainty region is governed by a search strategy, which determines the order in which tiles are to be investigated.

Various types of search strategy have been considered in the literature, the most common being:

1. Straight serial search [57],

2. Z search [99],

3. Expanding window search [22],

4. Alternate search [68].

The straight serial search strategy simply orders the tiles in a sequential fashion. Once all N_{T} tiles have been considered, the detector/estimator is returned to the first tile and the process repeats. This is most commonly implemented in the case of unknown or uniform *a priori* distributions on the unknown signal parameters, since no effort is made to cover the most likely tiles first.

When some *a priori* information is available regarding the location of the H_1 tile, then either a Z search or an expanding window search strategy may be implemented. Both of these strategies were developed for the single cell detector, in which case it is easiest to move from one trial cell to the next, adjacent cell. Moving from one test cell to another non-adjacent test cell requires "winding" the local code, either forwards or backwards, to reach the new test point. For the FFT-based detector discussed in Section 2.4.4 no such code-winding is required. In this situation the so-called alternate strategies are optimal. In this case the tiles are considered in order of decreasing *a priori* probability. In the remainder of this thesis we assume a uniform *a priori* distribution on the unknown signal parameters and, hence, apply straight serial search strategies only. The results derived are can be readily extended to include other search strategies.

In general, the search mode thresholds are set to yield fast decision making with relatively high probabilities of detection and false alarm.

The Verification Mode

In the verification mode the estimate cell $\widehat{\boldsymbol{\theta}}$ is subject to further testing. Meaningful probabilities can be assigned to the presence or absence of the signal in the cell under test. Bayes' criterion can, therefore, be applied to the detector in this mode [142, p. 24]. In the verification mode longer dwells are made to reduce the overall probability of false alarm into the lock mode.

Another key difference between the verification mode and the search mode is that, in the verification mode, we consider only a single *cell* of the uncertainty region, whereas in the search mode an entire tile is under investigation.

In the verification mode we have a pure detection problem, so we know that the optimum verification strategy is the sequential detector. As discussed in Section 2.3, Wald [145] has shown that the sequential detector takes, on average,

the minimum amount of time for a given P_{fa} and P_d. However, the performance of the sequential detector degrades rapidly when the received SNR is less than the design point SNR.

For this reason, a number of sub-optimal schemes have been suggested in the literature, which we refer to as *verification strategies*, the most common being:

1. Immediate reject verification [39],
2. Up-down counter verification [57] (referred to as the "Tong" detector in [70]),
3. Coincidence detector verification [100] (referred to as the "M-of-N" detector in [70]).

In this mode we consider a number (say N) of detectors, each detector is assumed to have the same form as the detector used in the search mode, but may have different parameters. In general, each detector will be identical, except for the dwell time τ_D and the decision threshold V_{Th}. The i^{th} detector can, therefore, be characterised by the pair $(\tau_{Di}, V_{\mathrm{Th}i})$. The verification strategy determines the order in which the detectors are used.

Consider, for instance, the immediate reject strategy. In this case the detectors are numbered 1 to N, and the tests are run sequentially in numerical order. If all N detectors declare the signal to be present then the cell under test is accepted and the acquisition process moves into the lock mode. On the other hand, if any detector rejects the cell under test then the cell is immediately rejected and the acquisition process returns to the search mode. Thus, to accept the cell under test requires exactly $\sum \tau_{Di}$ seconds, whereas the time to reject a cell is a random variable. The probability of entering the lock mode is given by [39]:

$$P_H = \prod_{i=1}^{N} P_{hi}, \tag{2.95}$$

where P_H is the overall "Hit" probability of the verification mode, $P_{hi} = P_{fa_i}$ in a H_0 cell and $P_{hi} = P_{di}$ in a H_1 cell. A flow chart for this strategy is shown in Figure 2.26 a).

The up-down counter strategy, illustrated in Figure 2.26 b), is similar but differs in the way in which it deals with rejection of the cell under test in a single detector. Consider the case where the cell has been passed by the first

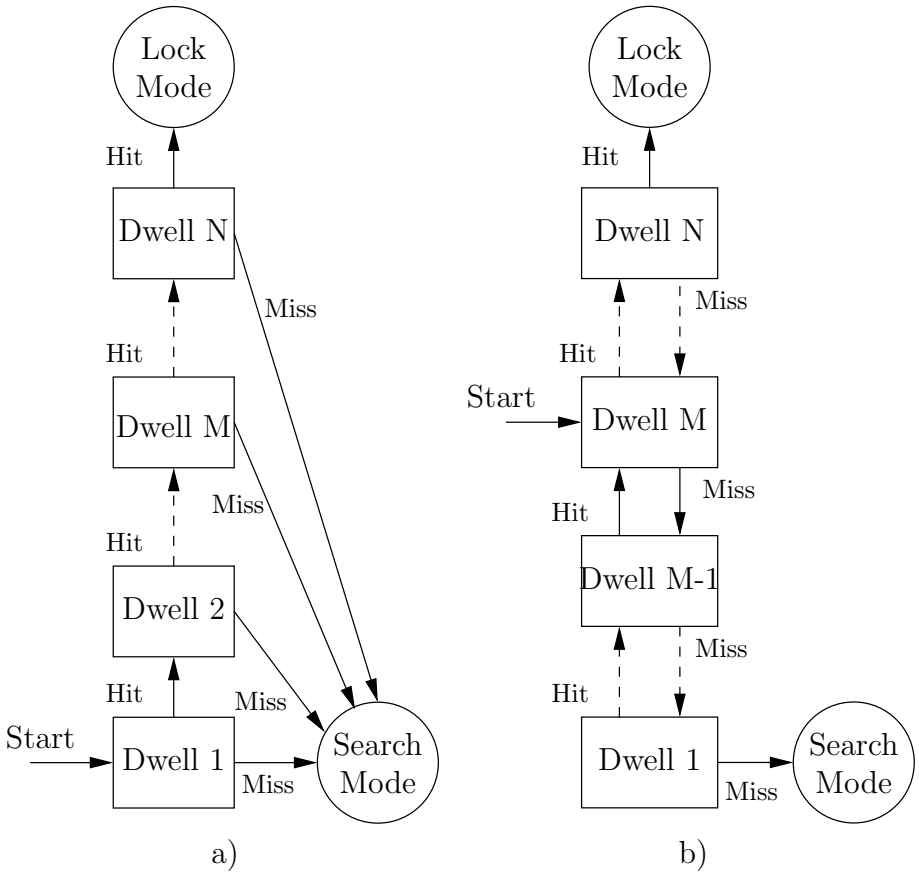


Figure 2.26: Verification Mode Flow Charts. a) Immediate Reject Strategy, b) Up-Down Counter Strategy.

$i-1$ detectors, but is rejected by the i^{th} detector. When the up-down counter strategy is implemented the cell is then passed back to detector $i-1$ for re-consideration, rather than being returned to the search mode. This strategy need not start with detector 1, but may, more generally, be designed to start in, say, the M^{th} detector. The cell is rejected when it fails the test in detector 1 and is accepted when it passes the test in detector N. Note that the total dwell time is, therefore, a random variable, both when the cell is ultimately accepted and when it is rejected. When all N detectors are identical, the probability of entering the lock mode is given by [70]:

$$P_H = \frac{1-\left(\frac{1-P_h}{P_h}\right)^M}{1-\left(\frac{1-P_h}{P_h}\right)^{M+N}}, \tag{2.96}$$

where $P_h = P_{fa}$ in a H_0 cell and $P_h = P_d$ in a H_1 cell. The analysis is more

involved if the detectors are not all identical. Hopkins [57] models the process as a discrete Markov process, and demonstrates a matrix based approach to solving the general problem. We will investigate Markov processes in more detail in Section 2.5.2.

Finally, the coincidence detector strategy involves performing all N tests sequentially. If the threshold is crossed in M or more of these tests then the cell under test is accepted, otherwise it is rejected. In this case the dwell time is deterministic in all cases. Assuming that all dwells are statistically independent and the same detector is used in each dwell, then the probability of entering the lock mode is given by [100]:

$$P_H = \sum_{n=M}^{N} \binom{N}{n} {P_h}^n \left(1 - P_h\right)^{N-n}, \tag{2.97}$$

where, again, $P_h = P_{fa}$ in a H_0 cell and $P_h = P_d$ in a H_1 cell.

A variation on the coincidence detector strategy seems to have been first introduced by Corazza et al. [32]. This is identical to the strategy described above except that, once a total of either M detections or $N - M$ rejections occur, the verification mode stops. This achieves the same probabilities of detection and false alarm as the original form but will, on average, be faster. It then becomes clear that this strategy contains the immediate reject strategy as a special case, with $M = N$. The authors give the following expressions for the probabilities of declaring signal absent after the i^{th} dwell, P_{Ri}, and of declaring the signal present after the i^{th} dwell, P_{Hi}:

$$P_{Ri} = \begin{cases} P_{h1}(1 - P_{hi}) \displaystyle\sum_{k \in \mathcal{B}} \prod_{j=2}^{i-1} (1 - P_{hj})^{n_{k,j}} {P_{hj}}^{1-n_{k,j}}, & N - M + 1 < i \leq N \\ 0 & i \leq N - M + 1 \end{cases} \tag{2.98}$$

$$P_{Hi} = \begin{cases} P_{h1} P_{hi} \displaystyle\sum_{k \in \mathcal{B}'} \prod_{j=2}^{i-1} (1 - P_{hj})^{n_{k,j}} {P_{hj}}^{1-n_{k,j}}, & i \geq M \\ 0 & i < M, \end{cases} \tag{2.99}$$

where $\mathcal{B}$ is the set containing the indices of all binary vectors:

$$\boldsymbol{n_k} = \left[n_{k,2}, n_{k,3}, \ldots, n_{k,i-1}\right],$$

with Hamming weight $N-M-1$[†] and $\mathcal{B}'$ is the set of indices of all binary vectors of the same form having Hamming weight $i-M$.

Much of the early work on the analysis of the acquisition process focused on the single cell detector. In this case, both search and verification modes investigate a single cell from the uncertainty region. Most analyses, therefore, do not differentiate between the search and verification modes, but rather consider either single dwell detectors (search mode only) or multiple dwell detectors (verification mode only). Either of these cases can be modelled as consisting of both search and verification modes, however, if we consider a "null" detector which will declare a hit with probability 1 in zero time. Thus, a single dwell detector can be thought of as having a null verification mode, and a multiple dwell detector can be thought of as having a null search mode.

The question naturally arises as to what combination of search and verification strategies is, in some sense, the best (say, yielding the minimum mean acquisition time for a given probability of correct detection). At the time of writing it appears this question remains unanswered in the literature.

The Lock Mode

Once the lock mode is entered and the tracking loops are closed, the signal will be lost within a finite amount of time with probability equal to one. The purpose of the lock mode is to determine when this loss of lock occurs.

This is a very important task, as once the tracking loops are closed the navigation processor will use the current estimates of the code phase and Doppler offset in its derivation of a navigation solution. Therefore, we would like to detect loss of lock as quickly as possible. On the other hand, we want to maintain lock for as long possible, once the signal has been found. This is the fundamental trade-off of the lock mode detector.

In the lock mode the detector is again configured according to Bayesian criteria and the strategies used to detect loss of lock are similar to those used in the verification mode: immediate reject [90] , up-down counter [57] and coincidence detector [32] logic have all been suggested in the literature.

A detailed analysis of the performance of the detector in the lock mode would require analysing the effect of the tracking loops. In practice, the analysis of the lock mode is achieved in one of two ways. The detection theoretic approach

[†]For example, letting $i=5$ and $N-M-1=2$, then $\mathcal{B}=\{[0,1,1],[1,0,1],[1,1,0]\}$.

ignores the effect of the tracking loops and simply models the acquisition process in the lock mode in the same way as for the verification mode [57]. Alternatively, the tracking loops may be considered to be independent of the lock detector [55]. In this latter approach it is assumed that the code tracking circuit has, at time t, an error $\varepsilon(t)$. It is usually then assumed that when $|\varepsilon(t)|$ exceeds some pre-specified value, the lock detector will declare loss of lock. It would be of theoretical interest to see how these techniques compare, though we do not consider this here.

In most analyses of the acquisition process, however, acquisition is considered to be finished when the lock mode is first entered for a correct (H_1) cell. When the lock mode is entered for a H_0 cell it is normally assumed that the search mode will be re-entered after some penalty time T_P, which is often modelled as a constant number of code chips.

2.5.2 Performance Analysis

The acquisition process, therefore, determines the motion of the detector/estimator through the uncertainty region. We have seen that a number of strategies for searching for and verifying the presence of the signal have been suggested in the literature. To compare these strategies requires some form of analysis of their relative performance. In CDMA signal acquisition the parameters of primary importance are:

1. The time taken to acquire the signal T_{ACQ},
2. The probability of correct detection P_D,
3. The probability of false alarm $P_{FA} = 1 - P_D$.

Since the acquisition time T_{ACQ} is a random variable, the system performance is often given in terms of its mean, denoted $\overline{T}_{ACQ}$, and variance, denoted $\mathrm{Var}\,[T_{ACQ}]$. As mentioned at the end of the previous section, it is often assumed that any false alarm will be detected after some penalty time T_P, so that $P_D = 1$ and $P_{FA} = 0$, in which case the statistics of T_{ACQ} completely determine system performance.

Two distinct approaches to analysing the acquisition system performance have been explored in the literature. The *flow-graph approach* [38, 39, 56, 57, 98–100] relies on the observation that the acquisition process, in all of its modes, can

be identified with a type of random process known as a *Markov chain* [61]. A Markov chain can be completely described by its state diagram, which is a form of flow-graph. By the application of results from flow-graph theory, expressions for the system performance parameters can be derived. The *direct approach* [22, 68, 69, 84, 90, 91, 147], on the other hand, is a combinatorial approach to the derivation of the system performance parameters.

The Flow-Graph Approach

A Markov chain [61, 92] is a type of discrete-time, discrete-state random process. Consider a system consisting of a possibly infinite number (say N) of discrete states. At any given moment in time the system is in one of these states. At discrete time intervals the process moves between states, in the intervening time it stays within the current state. The movement from one state to another is probabilistic. This system is a discrete-time, discrete-state random process. The process is called a Markov chain if it satisfies the following property:

Property 2.1 (Markov) *Let X_n denote the rv giving the state of the process at time instant n, then:*

$$\Pr\{X_{n+1} = x_{n+1} \mid X_n = x_n, X_{n-1} = x_{n-1}, \ldots, \ X_0 = x_0\} = \Pr\{X_{n+1} = x_{n+1} \mid X_n = x_n\}$$

Note that this implies that, knowing the *present* state of the system, the future is conditionally independent of the past (*i.e.* the system contains no memory of previous states).

Hopkins [57] and Holmes and Chen [56] seem to have been the first to identify the acquisition process as a Markov chain. Two analysis procedures are associated with the Markov chain model. The most commonly used approach is based on the representation of the Markov chain as a flow-graph, which we will describe shortly. The alternative is a matrix-based approach [57, 61] which we now describe.

We follow the notation of Iosifescu [61] in our treatment of the state transition matrices of Markov chains. The states in a Markov chain can be divided into two classes:

Recurrent States (Also known as *absorbing* states) Once these states are entered, the process never leaves.

Transient States All other states.

A Markov chain with at least one recurrent state is called an absorbing Markov chain since one of the recurrent states will be entered at some time $t < \infty$ with probability equal to one. Once an absorbing state is entered the Markov chain can be considered to have *terminated*, as no further state transitions are possible.

For any absorbing Markov chain with k absorbing states and N transient states, the state transition probabilities $p_{i,j}$ can be arranged in the canonical matrix form $\boldsymbol{P} = [p_{i,j}]$:

$$\boldsymbol{P} = \begin{pmatrix} \boldsymbol{I} & \boldsymbol{0} \\ \boldsymbol{R} & \boldsymbol{T} \end{pmatrix}, \tag{2.100}$$

where $\boldsymbol{P}$ is the $(N+k) \times (N+k)$ matrix of state transition probabilities called the transition matrix, $\boldsymbol{I}$ is the $k \times k$ identity matrix, $\boldsymbol{R}$ is the $N \times k$ matrix of transition probabilities from transient to absorbing states, called the "recurrent matrix", and $\boldsymbol{T}$ is the $N \times N$ matrix of transition probabilities within the transient states, called the "transient matrix". Here the state vector has been arranged such that the first k elements represent the absorbing (or recurrent) states of the process, the remaining N elements representing the transient states. The element $p_{i,j}$ represents the transition probability from state i to state j. Recall that the state transitions occur only at discrete time intervals. Let $x_{i,n}$ denote the probability that the Markov chain is in state i after the n^{th} state transition (including transitions from a state back into the same state). Denoting by $\boldsymbol{x_n}$ the vector of such probabilities, we have:

$$\boldsymbol{x_{n+1}} = \boldsymbol{P}\boldsymbol{x_n}. \tag{2.101}$$

To simplify the analysis of Markov chains we introduce the *fundamental matrix* $\boldsymbol{N}$, given by [61]:

$$\boldsymbol{N} = (\boldsymbol{I} - \boldsymbol{T})^{-1}, \tag{2.102}$$

where, in this case, $\boldsymbol{I}$ is the $N \times N$ identity matrix. The element $\boldsymbol{N}_{i,j}$ gives the expected value of the number of times the process enters state j given that it started in state i (note that both i and j are transient states). This matrix proves very useful in determining the statistics of the Markov chain. For instance, to determine the probability that the process will terminate in the j^{th} recurrent

state we define the $N \times k$ matrix $\boldsymbol{A}$ by:

$$\boldsymbol{A} = \boldsymbol{N}\boldsymbol{R}. \tag{2.103}$$

Given $\boldsymbol{A} = [a_{i,j}]$ then $a_{i,j}$ is the probability that the process will terminate in the j^{th} recurrent state, given that it started in the i^{th} transient state. To determine the overall probability of terminating in state j, we simply average over i.

We denote by τ_{Di} the dwell time in the i^{th} transient state, and by $\boldsymbol{\tau_D}$ the vector of dwell times. Similarly, we denote by $\overline{T}_{FHi}$ the average amount of time taken to reach *any* absorbing state given that the process starts in the i^{th} transient state, and by $\overline{\boldsymbol{T}}_{\boldsymbol{FH}}$ the vector of such times. Then it can be shown that:

$$\overline{\boldsymbol{T}}_{\boldsymbol{FH}} = \boldsymbol{N}\boldsymbol{\tau_D}. \tag{2.104}$$

Thus, through Equations (2.102) and (2.103), the fundamental matrix can be used to derive all the performance parameters of the Markov chain.

These results were used in [57] to derive an expression for the mean acquisition time $\overline{T}_{ACQ}$:

$$\overline{T}_{ACQ} = \frac{L\overline{\tau}_D}{2\left|\nu\overline{\tau}_D + \delta\right|}\left(\frac{2 - P_D}{P_D}\right), \tag{2.105}$$

where $\overline{\tau}_D$ is the average dwell time per cell, ν is a measure of the code Doppler effect ($\nu = \eta/T_{\text{chip}}$), δ is the difference between adjacent code phase estimates in Θ^* (normally $\approx 1/2$ a chip) and P_D is the probability of correct detection in the H_1 cell, including the verification mode. In fact, in [57] Hopkins uses a combinatorial argument to derive Equation (2.105) above, and uses the matrix method to determine the verification mode parameters $\overline{\tau}_D$ and P_D.

The flow-graph approach to the analysis of the acquisition process as a Markov chain is more commonly employed in the literature than the matrix approach. It seems to have been first suggested by Holmes and Chen [56], for a single dwell, straight serial search system in the absence of Doppler effects. The approach was soon extended to cater for multiple dwell systems by Di Carlo and Weber [39], who considered a form of immediate reject strategy in the verification mode. Polydoros and Weber [99, 100] introduced what they termed the "circular state diagram" to extend the application of the flow-graph approach to arbitrary verification strategies. Finally, Polydoros and Simon [98] extended the approach still further to encompass arbitrary search strategies (as opposed to the simple straight

serial search) by the introduction of what they call the "equivalent circular state diagram". All of the above developments considered only a single cell detector, operating in the absence of Doppler effects† and modelled the false alarm state as a transient state with an associated penalty time. The approach, however, is more generally applicable by simple extension of the results of these papers.

Recall that $p_{i,j}$ denotes the probability that the process moves from state i to state j in one time interval. For the acquisition problem, each time interval corresponds to a dwell in a candidate tile in the search mode, or a dwell in a candidate cell in the verification mode. We can assume, therefore, that each time interval will be a multiple of the code period T_{CA}. Letting $n_{i,j}$ be the number of code periods taken to make the transition from state i to state j, then we denote by $\mathrm{p}_{n_{i,j}}(n)$ the probability mass function (PMF) of this discrete rv.

The flow-graph approach relies on the observation that all the information on the statistics of the Markov chain is contained in the probability generating function (PGF) [92] of $\mathrm{p}_{n_{i,j}}(n)$, for every pair of states (i,j). The PGF of the rv X is defined by (see Appendix C.3.3):

$$\mathrm{P}_X(z) = E_X[z^n] = \sum_{n=0}^{\infty} \mathrm{p}_X(n)\, z^n. \tag{2.106}$$

Two useful properties of the PGF are:

$$\Pr\{i \to j\} = \sum_{n=0}^{\infty} \mathrm{p}_{n_{i,j}}(n) = \mathrm{P}_{n_{i,j}}(z)\big|_{z=1}, \tag{2.107}$$

and

$$E[n^m] = \sum_{i=1}^{m} \left.\frac{\partial^i \mathrm{P}_{n_{i,j}}(z)}{\partial z^i}\right|_{z=1} \qquad 1 \le m \le 2, \tag{2.108}$$

where $\Pr\{i \to j\}$ denotes the probability of making the transition from state i to state j in *any* time period.

We denote by $\mathrm{P}_{\mathrm{acq}}(z)$ the probability generating function of the number of code periods elapsing between the start of the search and entry into the acquisition state. In general, this can be written as the sum of the probabilities of correct and false acquisition respectively: $\mathrm{P}_{\mathrm{acq}}(z) = \mathrm{P}_{\mathrm{acq}_1}(z) + \mathrm{P}_{\mathrm{acq}_0}(z)$. The system

†In fact, all these papers ignore *carrier Doppler*, so the uncertainty space is one dimensional. The effect of code Doppler is taken into account in [56].

parameters are then given by [96]:

$$P_D = \mathrm{P}_{\mathrm{acq}_1}(z)\big|_{z=1} \tag{2.109}$$

$$\overline{T}_{ACQ} = \left.\frac{\partial \mathrm{P}_{\mathrm{acq}}(z)}{\partial z}\right|_{z=1} T_{\mathrm{CA}} \tag{2.110}$$

$$\mathrm{Var}\left[T_{ACQ}\right] = \left[\frac{\partial^2 \mathrm{P}_{\mathrm{acq}}(z)}{\partial z^2} + \frac{\partial \mathrm{P}_{\mathrm{acq}}(z)}{\partial z} - \left(\frac{\partial \mathrm{P}_{\mathrm{acq}}(z)}{\partial z}\right)^2\right]\Bigg|_{z=1} T_{\mathrm{CA}}^2 \tag{2.111}$$

In many ways the flow-graph of a Markov chain is analogous to the block diagram of a linear system. Each state of the Markov chain is assigned a node in the flow-graph, and the path from one state to another has an associated *transfer function*. In systems theory the transfer function from one node in a network to another is given by the Fourier transform of the impulse response of the network between the two nodes. For the Markov chain this transfer function is instead given by the PGF of the transition time between the two nodes.

The circular state diagram due to Polydoros and Weber [99], illustrated in Figure 2.27, is a simple, general representation of the acquisition process flow-graph. It is suitable for arbitrary verification and lock mode strategies, but limited to the straight serial search strategy. In the figure there are $N_{\mathrm{T}} + 2$ states in the acquisition Markov chain. These correspond to the N_{T} tiles of the uncertainty region, plus one state each for the acquisition (ACQ) and false alarm states. The acquisition process proceeds as follows:

- The state associated with the H_1 cell is given the number N_{T}, the remaining cell-states are numbered sequentially in the search order, starting with 1 for the cell immediately following the H_1 cell.
- The search starts in cell i, with probability π_i.
- Once the search enters a H_0 cell, say state $j < N_{\mathrm{T}}$, there are two possibilities:
    1. The cell is rejected and the search moves onto state $j+1$. The transfer function for this path is denoted $H_{r_0}(z)$. This includes the direct path, plus all paths through the verification mode that ultimately result in rejecting the cell under test.
    2. The cell is accepted and the search moves into the false alarm state. The transfer function for this path is denoted $H_{fa}(z)$, and accounts for

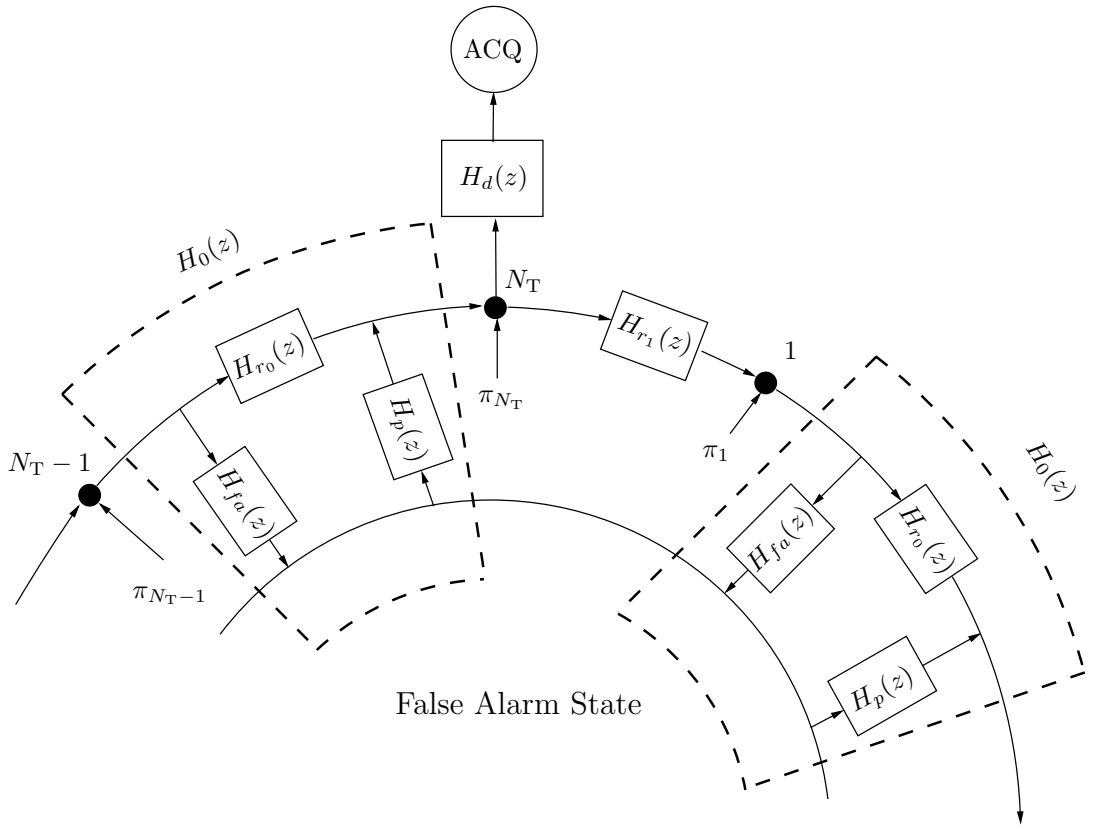


Figure 2.27: Circular State Diagram for the Markov Chain Representation of the Acquisition Process. Note that this State Diagram Represents a Serial Search Process.

all possible paths through the verification mode that result in accepting the cell under test.

- The false alarm state can be modelled either as absorbing or transient. If it is an absorbing state then the transfer function $H_p(z)$ will be zero: there is no return from an absorbing state. If it is a transient state then $H_p(z)$ models the penalty time incurred by false entry into the lock mode.

- Once the search enters the H_1 cell (state N_T), then the signal will either be correctly detected, with transfer function $H_d(z)$, or will be falsely dismissed, with transfer function $H_{r_1}(z)$. Again, both $H_d(z)$ and $H_{r_1}(z)$ include all possible paths through the verification mode.

The transfer function from start to acquisition can be derived directly from the circular state diagram [99, Equation (4)]:

$$\mathrm{P}_{\mathrm{acq}_1}(z) = \frac{H_d(z)}{1 - H_{r_1}(z)H_0^{N_\mathrm{T}-1}(z)} \sum_{i=1}^{N_\mathrm{T}} \pi_i H_0^{N_\mathrm{T}-i}(z), \tag{2.112}$$

where $H_0(z)$ is the complete transfer function from a H_0 state to the next cell state, given by:

$$H_0(z) = H_{r_0}(z) + H_{fa}(z)H_p(z). \tag{2.113}$$

The system performance parameters can then be determined by using Equation (2.112) in Equations (2.109) – (2.111).

The only limitation of the circular state diagram approach is that the search strategy is limited to the straight serial search. In [98] the authors extend this approach by introducing the equivalent circular state diagram. This effectively maps any arbitrary search strategy to a form similar to the circular state diagram above. The resulting expressions for the system performance parameters are more involved than the simple expression of Equation (2.112). Since we shall primarily consider simple serial search strategies in this thesis, we do not reproduce the expressions of [98] here.

While all of the above analysis deals only with the single cell detector, the extension to parallel techniques is straightforward. The only modification to be made to the circular state diagram is to include a path from the H_1 state to the false alarm state, as indicated in [31, Figure 1].

The Direct Approach

The final technique we shall consider is the direct approach. This is a combinatorial approach and does not rely on the Markov property of the acquisition process. It is based on early work by Braun [22] and Weinberg [147], and was modified by Meyr and Polzer [84]. The approach was generalised and given the name "direct approach" by Jovanović [68, 69]. Similar combinatorial arguments were presented by Pan et al. [90, 91].

Letting $f_{T_{ACQ}}(t)$ denote the PDF of the acquisition time, then this approach is most easily understood by considering the treatment of Braun [22], who gave

the following expression:

$$\begin{aligned} f_{T_{ACQ}}(t) &= \sum_{m=1}^{N_{\mathrm{T}}} \Pr\left\{m^{\text{th}} \text{ cell is correct}\right\} \\ &\quad \times \sum_{k=1}^{\infty} \Pr\left\{\text{acq. in } k^{\text{th}} \text{ scan} \mid m\right\} \\ &\quad \times \sum_{l=1}^{\infty} \Pr\left\{l \text{ false alarms } \mid m, k\right\} \\ &\quad \times f_{T_{ACQ}}(t \mid m, k, l), \end{aligned} \tag{2.114}$$

where $f_{\text{acq}}(t \mid m, k, l)$ denotes the conditional PDF of the acquisition time given that the m^{th} cell is the H_1 cell, detection occurs on the k^{th} time the H_1 cell is tested (*i.e.* on the k^{th} "scan") and a total of l false alarms occur during acquisition. This approach can be described as a combinatorial method as Equation (2.114) is simply an enumeration of all the possible ways in which acquisition can occur.

From [22] we have:

$$f_{T_{ACQ}}(t \mid m, k, l) = f_{t_d}(t) * f_{t_{r_0}}(t) *^i *f_{t_{fa}}(t) *^l *f_{t_{r_1}}(t) *^j, \tag{2.115}$$

where i is the total number of times a H_0 cell was tested and rejected (not including false alarms), j is the total number of times the H_1 cell was tested and rejected and the acquisition time is dependent on the following four rvs:

1. t_d: the time taken to correctly detect the signal in the H_1 cell,
2. t_{r_1}: the time taken to reject the signal in the H_1 cell,
3. t_{fa}: the time to declare a hit in a H_0 cell, plus the subsequent false alarm penalty time, and
4. t_{r_0}: the time taken to correctly reject the signal in a H_0 cell,

$a*b$ denotes the convolution of a and b and $f_X(t)*^n$ denotes the n-fold convolution of $f_X(t)$ with itself. Both Braun [22] and Weinberg [147] make use of transform domain techniques to implement the convolution operations. Note that, given m, k and l, the values of i and j are completely determined by the search strategy.

Meyr and Polzer [84] applied a similar method, but derived the following expression for the PMF of the acquisition time as a multiple (n) of the code

period:

$$\mathrm{p}_{T_{ACQ}}(n) = P_d \sum_{i=1}^{\infty} (1-P_d)^{i-1} \sum_{j=1}^{N_\mathrm{T}} \pi_j \, \mathrm{p}_{T_{ACQ}}(n \mid i,j)\,, \tag{2.116}$$

where i denotes the number of times the H_1 tile is tested prior to detection, j is the location of the H_1 tile in the uncertainty space, π_j is the *a priori* probability that the H_1 tile is at location j, and $\mathrm{p}_{T_{ACQ}}(n \mid i,j)$ is the PMF of the acquisition time given i and j:

$$\mathrm{p}_{T_{ACQ}}(n \mid i,j) = f_{t_d}(n) \otimes f_{t_{r_0}}(n) \otimes^{k(i,j)} \otimes f_{t_{r_1}}(t) \otimes^{i-1}, \tag{2.117}$$

where $a \otimes b$ denotes the discrete convolution of a and b. Note that, in this case, the time to reject a H_0 cell, t_{r_0}, is a random variable including all paths through the verification and lock modes. Thus, whereas Braun used four continuous rvs to model the various dwell times, Meyr and Polzer describe the same system using only three (in this case, discrete) rvs.

Jovanović [68] used the work of Meyr and Polzer as a starting point, extending it to include the case where the dwell times are, again, continuous.

The difficulty with the computation of Equations (2.114) and (2.116) is the evaluation of the convolutions in the expression for the conditional PDF of the acquisition time. Transform domain approaches are commonly used in many branches of engineering to overcome the difficulty associated with the computation (or even the analytical treatment) of the convolution operation. For continuous variables, the Fourier or Laplace transforms are often applied to this end whilst, for discrete variables, either the DFT or the Z-transform are more appropriate. In Appendix C.3 we summarise some common transform-based functions used in probability theory.

We consider the characteristic function (CHF) of continuous random variables, which is, in effect, equivalent to the Fourier Transform[†] of the PDF. Thus, the CHF of the convolution of a number of independent rvs is simply the product of the individual CHFs. For a continuous rv X with PDF $f_X(x)$, the CHF of X is defined by (see Appendix C.3.2):

$$\Phi_X(j\omega) = E_X[\exp(j\omega x)] = \int_{-\infty}^{\infty} f_X(x) \exp(j\omega x)\, d\, x. \tag{2.118}$$

[†]The CHF is equivalent to the Fourier Transform except for the sign of the variable ω and a multiplicative constant.

Similarly, for discrete random variables, we consider the PGF, which is essentially equivalent to the Z-transform† of the PMF. We previously discussed the PGF in the context of the flow-graph approach. A summary of some important properties of the PGF can be found in Appendix C.3.3.

The CHF approach was suggested by Braun [22] and Weinberg [147] for application to Equation (2.115), and by Jovanović for application to Equation (2.117), when the dwell times are modelled as continuous. Jovanović also suggested the PGF approach for the case of discrete dwell times. Taking CHFs in Equation (2.115) yields:

$$\Phi_{T_{ACQ}}(j\omega) = \Phi_{t_d}(j\omega)\,\Phi_{t_{r_0}}(j\omega)^i\,\Phi_{t_{fa}}(j\omega)^l\,\Phi_{t_{r_1}}(j\omega)^j\,, \tag{2.119}$$

which is much easier to compute than Equation (2.117). This approach immediately accounts for all possible search, verification and lock strategies. Any *a priori* information is also taken into account through the expression $\Pr\left\{m^{th} \text{ cell is correct}\right\}$ in Equation (2.114) above. The distribution of the acquisition time can be found by numerical methods from the CHF (Braun suggests a discrete Fourier transform approximation, whereas Weinberg suggests an approach based on the Gil-Pelaez inversion theorem [44]).

Jovanović [68], using the technique of Meyr and Polzer, was able to provide an analytic inversion of the CHF for a single dwell (null verification) system with arbitrary search strategy. The primary advantage of Jovanović's approach, however, arises when we consider all dwells to be discrete rvs. In this case, the verification and lock modes are modelled entirely by their PGFs, which can be easily determined using the Markov chain methods discussed above. This general approach, using a mixture of flow-graph and direct techniques, would appear to be the most useful in the determination of system performance.

2.6 Discussion

In this chapter we have given an overview of the DS/CDMA acquisition problem, with emphasis on the GPS application. We have taken an approach based on detection and estimation theory, introducing standard acquisition architectures

†The Z-transform of the discrete function $f(k)$ is simply the DFT of $f(k)$ with the substitution $\exp(j\omega) \to z$.

as approximations to the optimal (maximum likelihood) estimator. We identify two components to acquisition:

- The detector/estimator,
- The acquisition process, which determines the motion of the detector/ estimator through the signal parameter uncertainty space.

We considered a number of forms for the detector/estimator, starting with the optimal form in AWGN and continuing with various sub-optimal approaches introduced to overcome performance degradation due to data modulation and signal power attenuation. Of particular importance are the parallel techniques discussed in Section 2.4.4, which can provide significant performance improvements at the cost of increased hardware requirements. The acquisition of very weak GPS signals (with received C/N_0 in the range -33.8 to -23.8 dB-Hz) would be impossible in reasonable time frames (less than hours) without some form of receiver parallelism.

Finally, we discussed existing techniques used in the analysis of the acquisition process. These techniques are equally applicable for all the detector/estimator designs discussed in Section 2.4.

In the following two chapters we conduct an analysis of all forms of the detector estimator introduced here. We begin in Chapter 3 with an investigation of detector/estimator performance in the absence of noise.

Chapter 3

The Detector/Estimator I: Signal Effects

The detector/estimator was introduced in the previous chapter as the fundamental building block of GPS signal acquisition. In this chapter we present some novel results on the analysis of all four forms of detector/estimator discussed in Section 2.4:

1. The coherent (or ML) detector,
2. The noncoherent combining detector (NCCD),
3. The differentially coherent combining detector (DCCD), and
4. The differentially coherent detector (DCD).

Of these four forms, the first is a discrete form of the maximum likelihood estimator, the following two (NCCD and DCCD) are sub-optimal forms based on the ML form, and the last is a completely different form making use of the shift and add property of Gold codes.

Whilst, the relative merits of each of these forms have been discussed in some detail in Section 2.4, here we will present a formal, comparative performance analysis. We begin with the performance analysis in the absence of noise, postponing consideration of noise effects until Chapter 4.

The performance analysis of a receiver in the absence of noise provides a useful measure of its sensitivity to signal parameters, such as residual code phase and carrier frequency offsets, and modulation effects. From this analysis we can gain

insight into the effect of the various detector parameters on this sensitivity, which will act as a guide in the design and optimisation of a complete acquisition system. It is important to note, however, that this type of analysis is not sufficient for the comparison of different receiver forms, as each form has a unique sensitivity to noise which must also be accounted for, as discussed in Chapter 4.

We have previously seen (Section 2.1) that the signal parameters of primary interest to us, *i.e.* those having the most significant effect on receiver performance, are:

- The residual code phase offset, $\delta\zeta$, which is a function of the true code phase offset and the spacing between estimates.
- The residual Doppler dilation coefficient $\delta\eta$ which, in turn, leads to an observed residual carrier Doppler frequency offset $\delta\omega_d$ and a residual code frequency offset.
- The data signal $d(t)$, which leads to random 180° phase shifts at the (unknown) data bit boundaries.

These parameters are defined in Table 3.1. For each detector form we consider

Symbol	Description	Equation
ζ	Signal code phase offset	$\zeta = \zeta_0 - \eta\frac{t}{T_{\text{chip}}}$
ζ_0	Initial signal code phase offset	—
η	Signal Doppler dilation coefficient	See Equation (2.3)
ω_d	Signal Doppler offset	$\omega_d = \eta\omega_0$
$\widehat{\zeta}$	Local estimate of ζ	$\widehat{\zeta} = \widehat{\zeta_0} - \widehat{\eta}\frac{t}{T_{\text{chip}}}$
$\widehat{\zeta_0}$	Local estimate of ζ_0	—
$\widehat{\eta}$	Local estimate of η	Receiver dependent
$\widehat{\omega_d}$	Local estimate of ω_d	—
$\delta\zeta$	Residual ζ estimation error	$\delta\zeta = \zeta - \widehat{\zeta}$
$\delta\zeta_0$	Residual ζ_0 estimation error	$\delta\zeta_0 = \zeta_0 - \widehat{\zeta_0}$
$\delta\eta$	Residual η estimation error	$\delta\eta = \eta - \widehat{\eta}$
$\delta\omega_d$	Residual ω_d estimation error	$\delta\omega_d = \omega_d - \widehat{\omega_d}$

Table 3.1: List of Symbols for the Estimation Process

the effect of offsets in the parameters to be estimated (the *desired* parameters), as well as the effect of nuisance parameters. For example, for the NCCD, the desired parameters are the code phase offset ζ and the Doppler offset ω_d, whereas

the data signal can be viewed as a nuisance parameter. The detector is essentially defined in terms of its decision function, $D_k(\widehat{\boldsymbol{\theta}})$. All signal effects will be modelled based on how they affect this decision function.

For the most part, the analysis of both the ML and NCCD forms in the absence of noise is well known, though we make some new contributions to the analysis of modulation and code Doppler effects. We present a brief overview of all of this analysis here, however, as it illustrates the method used for the other detector/estimator forms.

In all of the following analysis an infinite bandwidth signal is assumed. Thus, for the sake of simplicity, the effects of front end filtering are ignored.

3.1 The Maximum Likelihood Form

The ML detector structure is illustrated in Figure 2.12 and is reproduced as Figure 3.1 for convenience. If we assume that the parameter estimate $\widehat{\boldsymbol{\theta}} = \left[\widehat{\zeta}, \widehat{\omega_d}\right]$

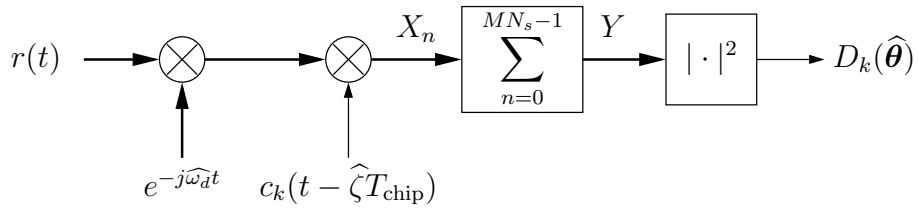


Figure 3.1: The ML Detector

is correct and ignoring, for the moment, the effect of data modulation, then the input to the coherent accumulator will be a (complex) constant:

$$X_n = \sqrt{\frac{P_k}{2}} \exp\left(j\phi_k\right), \tag{3.1}$$

where X_n is the input to the coherent accumulator at time $t = nT_s$, P_k is the received signal power from the satellite of interest (satellite k) and ϕ_k is the initial carrier phase offset. Thus, in the absence of any extraneous signal effects, the output of the coherent accumulator is:

$$Y = \sum_{n=0}^{MN-1} X_n = MN\sqrt{\frac{P_k}{2}} \exp\left(j\phi_k\right). \tag{3.2}$$

The decision statistic $D_k(\widehat{\boldsymbol{\theta}})$ is then given by the square magnitude of Y:

$$D_k(\widehat{\boldsymbol{\theta}}) = 0.5(MN)^2 P_k \,. \tag{3.3}$$

Thus, when all signal effects have been eliminated, the ML detector yields a decision statistic which is a scaled measure of the signal power.

3.1.1 The Effect of a Residual Carrier Frequency Offset

If we now introduce a carrier Doppler offset ω_d and assume all other effects remain unchanged[†], then, at the input to the coherent accumulator, we have:

$$X_n = \sqrt{\frac{P_k}{2}} \exp\left(j\left(\phi_k + \delta\omega_d n T_s\right)\right). \tag{3.4}$$

The output of the coherent accumulator can now be found as follows:

$$\begin{aligned} Y &= \sum_{n=0}^{MN-1} X_n \\ &= \sum_{n=0}^{MN-1} \sqrt{\frac{P_k}{2}} \exp\left(j\left(\phi_k + \delta\omega_d n T_s\right)\right) \\ &= \sqrt{\frac{P_k}{2}} \exp\left(j\phi_k\right) \sum_{n=0}^{MN-1} \left(\exp\left(j\delta\omega_d T_s\right)\right)^n \\ &= \sqrt{\frac{P_k}{2}} \exp\left(j\phi_k\right) \frac{1 - \exp\left(j\delta\omega_d T_s MN\right)}{1 - \exp\left(j\delta\omega_d T_s\right)} \end{aligned}$$

where we have used Equation (A.4) in Appendix A. Rearranging yields:

$$Y = \sqrt{\frac{P_k}{2}} \exp\left(j\left(\phi_k + \frac{\delta\omega_d T_s}{2}\left[MN - 1\right]\right)\right) \frac{\sin\left(\frac{\delta\omega_d T_s MN}{2}\right)}{\sin\left(\frac{\delta\omega_d T_s}{2}\right)}. \tag{3.5}$$

Finally, taking the square magnitude, we obtain:

$$D_k(\widehat{\boldsymbol{\theta}}) = 0.5 P_k \left| \frac{\sin\left(\frac{\delta\omega_d T_s MN}{2}\right)}{\sin\left(\frac{\delta\omega_d T_s}{2}\right)} \right|^2 . \tag{3.6}$$

[†]For the moment we ignore code Doppler effects, though the presence of carrier Doppler implies the presence of code Doppler. Carrier Doppler tends to dominate, however, so this simplification is sufficient for present purposes.

Comparing Equations (3.6) and (3.3) we see that the effect of the carrier Doppler offset is to introduce an effective power attenuation $\alpha_D(\delta\omega_d)$ given by:

$$\alpha_D(\delta\omega_d) = \left| \frac{\sin\left(\frac{\delta\omega_d T_s MN}{2}\right)}{MN \sin\left(\frac{\delta\omega_d T_s}{2}\right)} \right|^2 . \tag{3.7}$$

This is a well known expression, previously introduced in Equation (2.19). The derivation above is due to Ashe [14].

3.1.2 The Effect of Data Modulation

We now introduce an unknown data modulation onto the signal. Initially we assume that there is a single data bit boundary within the observation interval, *i.e.* $M \leq D$. We assume that the bit boundary occurs a fraction δ_T of the way through the observation interval, as illustrated in Figure 3.2. Let $\mu = \lceil \delta_T MN \rceil$

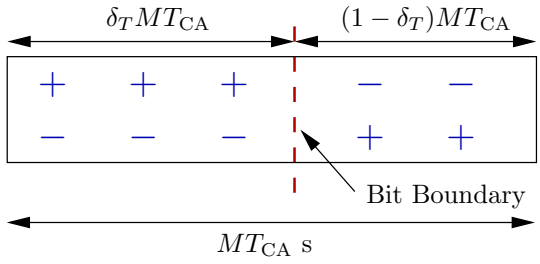


Figure 3.2: Data Transition in a Coherent Integration Period

be the index of the first sample in the second data bit in the observation interval, such that samples $\mu - 1$ and μ are on either side of the bit boundary. Then we can write:

$$Y = \sqrt{\frac{P_k}{2}} \exp(j\phi_k) \left(d_0 \sum_{n=0}^{\mu-1} \exp(j\delta\omega_d n T_s) + d_1 \sum_{n=\mu}^{MN-1} \exp(j\delta\omega_d n T_s) \right), \tag{3.8}$$

where $d_0, d_1 = \pm 1$ are the first and second data bits within the observation interval, respectively. Defining S_r as follows:

$$S_r = \sum_{n=0}^{r-1} \exp(j\delta\omega_d n T_s), \tag{3.9}$$

then we have:

$$Y = \sqrt{0.5P_k}\exp\left(j\phi_k\right)\left(d_1 S_{MN} - (d_1 - d_0)S_\mu\right) \tag{3.10}$$

$$= \sqrt{0.5P_k}S_{MN}\exp\left(j\phi_k\right)\left(d_1 - (d_1 - d_0)\frac{S_\mu}{S_{MN}}\right). \tag{3.11}$$

Taking the square magnitude we obtain:

$$D_k(\widehat{\boldsymbol{\theta}}) = 0.5P_k\left|S_{MN}\right|^2\begin{cases}1 & d_1 = d_0\\ \left|1 - 2\frac{S_\mu}{S_{MN}}\right|^2 & \text{otherwise}\end{cases} \tag{3.12}$$

$$= 0.5(MN)^2 P_k \alpha_D(\delta\omega_d)\alpha_m(\delta\omega_d, \boldsymbol{d}), \tag{3.13}$$

where $\alpha_D(\delta\omega_d)$ is the power attenuation due to carrier Doppler effects (defined in Equation (3.7)) and $\alpha_m(\delta\omega_d, \boldsymbol{d})$ is the power attenuation due to the unknown data signal $\boldsymbol{d}$. From the derivation of Equation (3.5) we have:

$$S_r = \exp\left(j\frac{\delta\omega_d T_s}{2}(r-1)\right)\frac{\sin\left(\frac{\delta\omega_d r T_s}{2}\right)}{\sin\left(\frac{\delta\omega_d T_s}{2}\right)}, \tag{3.14}$$

and so we have:

$$\alpha_m(\delta\omega_d, \boldsymbol{d}) = \begin{cases}1 & d_1 = d_0\\ \left|1 - 2\exp\left(-j\frac{\delta\omega_d T_{\text{coh}}}{2}(1-\delta_T)\right)\frac{\sin\left(\frac{\delta\omega_d T_{\text{coh}}\delta_T}{2}\right)}{\sin\left(\frac{\delta\omega_d T_{\text{coh}}}{2}\right)}\right|^2 & \text{otherwise}\end{cases} \tag{3.15}$$

where $T_{\text{coh}} = MT_{\text{CA}}$ is the duration of the coherent observation interval. This result would appear to be new[†] and is illustrated in Figure 3.3. It is important to note that, as observed by Davisson and Flikkema [37], the power attenuation due to data modulation is not independent of the Doppler offset.

Consider the following two simple special cases. In the absence of any residual

[†]All novel results will be indicated by a surrounding box, as in Equation (3.15).

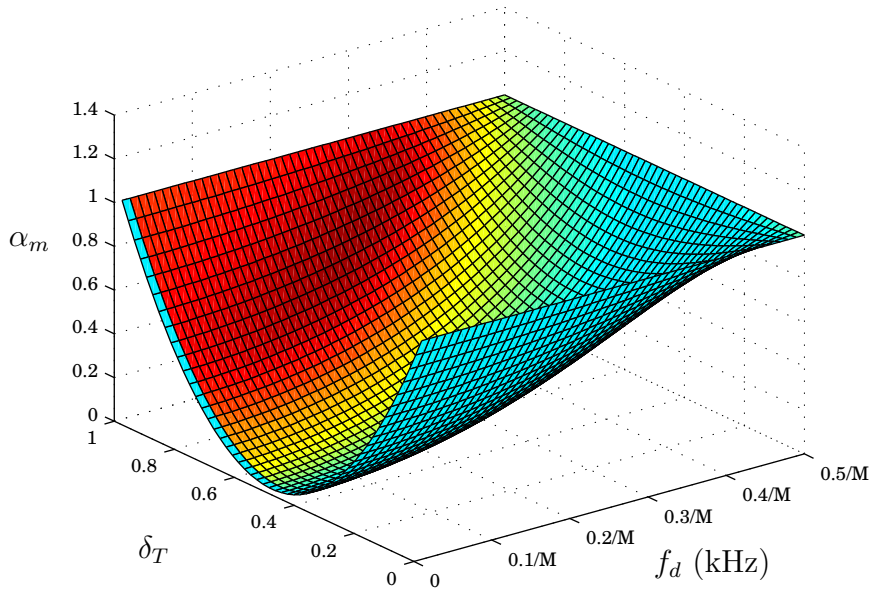


Figure 3.3: Power Attenuation Due to Data Modulation in the ML Detector: f_d is the residual Doppler offset, normalised by the coherent accumulation length M, δ_T is the fraction of the way through the coherent observation at which the bit transition occurs.

carrier Doppler Equation (3.15) reduces to:

$$\alpha_m(0, \boldsymbol{d}) = \begin{cases} 1 & d_1 = d_0 \\ |1 - 2\delta_T|^2 & \text{otherwise.} \end{cases} \tag{3.16}$$

The worst case attenuation occurs when $\delta_T = 1/2$ at which point $\alpha_m = 0$ and the signal is completely eliminated from the decision statistic. The mean attenuation is given by Equation (2.59).

At the other extreme, the Doppler error is at a maximum when the true Doppler offset is right on a boundary between two Doppler bins. In this case, we have $\delta\omega_d = \pi/T_{\text{coh}}$ (see page 28) and:

$$\alpha_m(\pi/T_{\text{coh}}, \boldsymbol{d}) = 1. \tag{3.17}$$

This is a very interesting fact that doesn't seem to have been explicitly pointed out in the literature to date: at the edge of a Doppler bin, data modulation has *absolutely no effect* on the decision statistic. This, again, is clearly visible in

Figure 3.3.

We can use Equation (3.15) above to derive useful expressions for the mean and worst case power attenuation due to data modulation. After some algebraic manipulation of Equation (3.15) we have:

$$\alpha_m\left(\delta\omega_d, \delta_T\right) = 1 + 2t\left[\cot^2\beta - \cot\beta\left(\sin 2\beta\delta_T + \cot\beta\ \cos 2\beta\delta_T\right)\right], \tag{3.18}$$

where we have introduced the random variable t which is equal to one if a transition occurs at the boundary, and equal to zero otherwise, and, for notational convenience, we have introduced:

$$\beta \triangleq \frac{\delta\omega_d T_{\text{coh}}}{2}. \tag{3.19}$$

Note that β is one half of the total phase shift due to carrier Doppler over the coherent observation interval.

The worst case attenuation, denoted $\alpha_{m\text{wc}}$, occurs when $t = 1$ and $\delta_T = 1/2$[†] and is given by:

$$\alpha_{m\text{wc}}(\delta\omega_d) = 1 - 4\frac{\cos\beta\ \sin^2\frac{\beta}{2}}{\sin^2\beta}. \tag{3.20}$$

To determine the mean of α_m we assume a uniform distribution on δ_T[‡]:

$$\begin{aligned}\overline{\alpha}_m(\delta\omega_d \mid t) &\approx \int_0^1 f_{\delta_T}(x)\alpha_m(\delta\omega_d, x)dx \\ &= \int_0^1 1 + 2t\left[\cot^2\beta - \cot\beta\left(\sin 2\beta x + \cot\beta\ \cos 2\beta x\right)\right]dx \\ &= 1 + 2t\left(\cot^2\beta - \frac{\cot\beta}{\beta}\right).\end{aligned} \tag{3.21}$$

There is a bit boundary, on average, every M/D observation intervals and, assuming random data, a bit transition will occur at any given boundary with a probability of 1/2. Therefore, the expected value of t is $M/(2D)$ and the overall

[†]This can be easily seen by minimising Equation (3.18) with respect to δ_T.

[‡]The integral in Equation (3.21) is an approximation, the true average is found by summing over all possible μ. An expression for this true average is derived in Appendix B.1.1, experience has shown that this is a very good approximation when the number of samples is large.

average value of the power attenuation due to modulation effects is given by:

$$\begin{aligned}\overline{\alpha}_m(\delta\omega_d) &= E_t\left[1 + 2t\left(\cot^2\beta - \frac{\cot\beta}{\beta}\right)\right] \qquad M \leq D \\ &\approx 1 - \frac{M}{D}\left(\frac{\cot\beta}{\beta} - \cot^2\beta\right). \end{aligned} \tag{3.22}$$

Note that taking the limit as $\delta\omega_d \to 0$ gives us:

$$\lim_{\delta\omega_d \to 0} \overline{\alpha}_m(\delta\omega_d) = 1 - \frac{M}{3D}, \tag{3.23}$$

which is exactly the expression given in Equation (2.59) for the case $M < D$.

It is instructive to consider the combined effects of data modulation and carrier frequency offset. Consider first of all the combination of carrier Doppler and average data modulation:

$$\alpha_D(\delta\omega_d)\overline{\alpha}_m(\delta\omega_d) = \left|\frac{\sin\beta}{MN\sin\frac{\beta}{MN}}\right|^2 \left[1 - \frac{M}{D}\left(\frac{\cot\beta}{\beta} - \cot^2\beta\right)\right]. \tag{3.24}$$

This is plotted against the normalised Doppler offset in Figure 3.4. Two interesting observations can be made from this figure. Considering the portion of the curve within the Doppler bin (*i.e.* $f_d < \frac{1}{2MT_{\mathrm{CA}}} = 0.5/M$ kHz) it is clear that increasing M increases the receiver's sensitivity to data modulation effects. Secondly, considering the portion outside of the Doppler bin, we see that the presence of data modulation tends to *increase* the average amount of signal power seen in this region. Increasing M, therefore, tends to increase the amount of signal power that is "spread" into adjacent Doppler bins, thereby degrading receiver performance.

As discussed above, data modulation exerts its most extreme influence when $\delta_T = 1/2$, in which case α_m is given by Equation (3.20). This gives us the following expression:

$$\alpha_D(\delta\omega_d)\alpha_{m\mathrm{wc}}(\delta\omega_d) = \left|\frac{\sin\beta}{MN\sin\frac{\beta}{MN}}\right|^2 \left[1 - 4\frac{\cos\beta\ \sin^2\frac{\beta}{2}}{\sin^2\beta}\right]. \tag{3.25}$$

This is illustrated in Figure 3.5. From the diagram, we see that, when the data

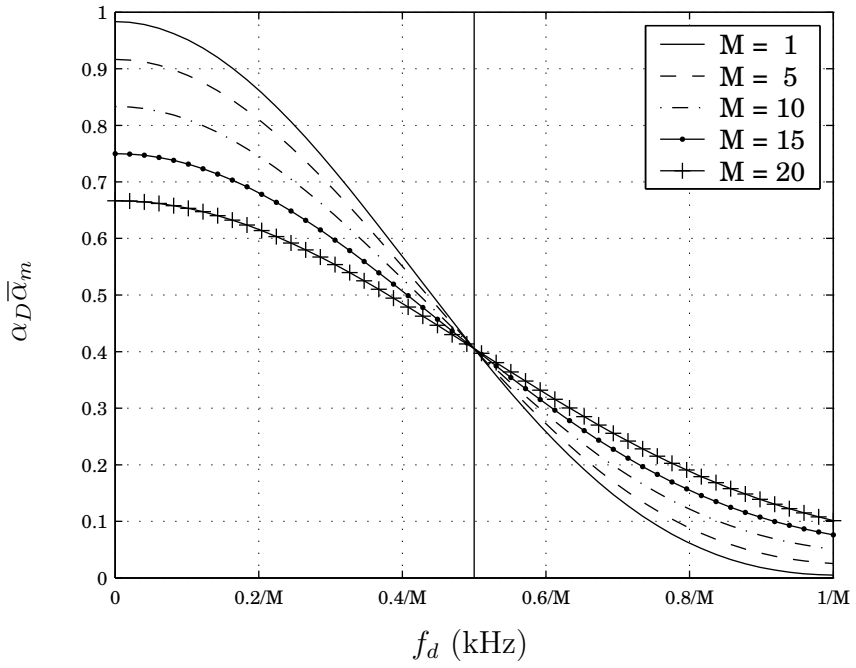


Figure 3.4: Power Attenuation Due to Combined Carrier Doppler and Average Case Data Modulation for the ML Detector: The vertical line indicates the Doppler bin boundary.

modulation is at its most extreme case, the effect is to modulate the energy of the main lobe of the received signal into two side lobes. This introduces a bias in our estimator: the maximum value of the decision statistic no longer corresponds to the true parameters.

So far we have treated only the case $M \leq D$. We can extend the above results to $M > D$ by an approach similar to that of Davisson and Flikkema [37]. The following result is derived in Appendix B.1.2:

$$\overline{\alpha}_m(\delta\omega_d) = \left| \frac{\sin \frac{\beta D}{M}}{\sin \beta} \right|^2 \left(\frac{M}{D} - \frac{M \cot\left(\beta \frac{D}{M}\right)}{\beta D} + \cot^2 \frac{\beta D}{M} \right) \quad M \geq D. \quad (3.26)$$

From this we note that, within a Doppler bin, the mean modulation attenuation is a monotonically decreasing function of M. Likewise, the average amount of signal power spread into the side-lobes is a monotonically increasing function of M. In addition, it is interesting to note that the Doppler bin boundary is no longer a fixed point when $M > D$. The bin width is, therefore, also affected by

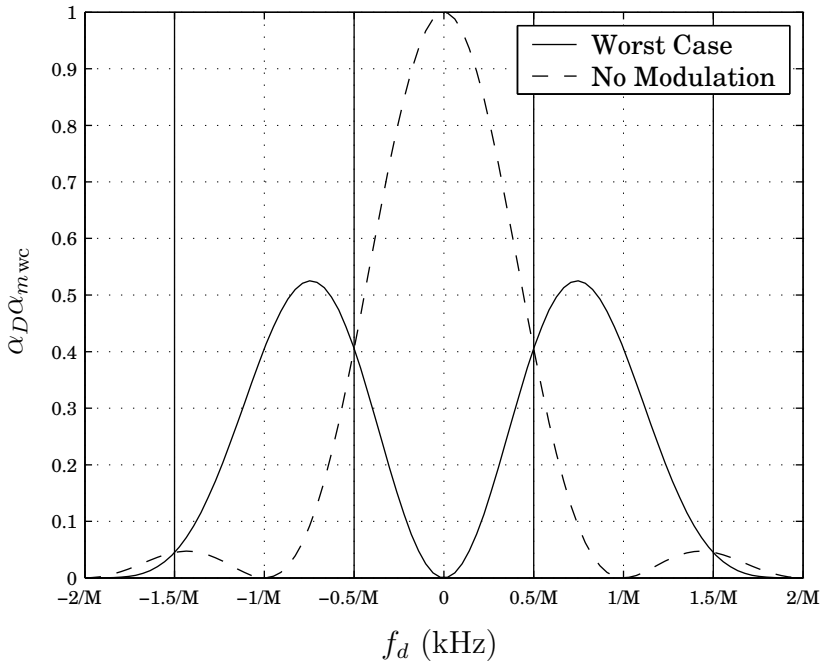


Figure 3.5: Power Attenuation Due to Combined Carrier Doppler and Worst Case Data Modulation for the ML Detector: The vertical lines indicate the Doppler bin boundaries.

modulation effects in this case. For these reasons it is usually desirable to choose $M \leq 10$ to limit the impact of data modulation.

The analysis of the combined effect of carrier Doppler and data modulation presented above is new. Davisson and Flikkema [37] did present results similar to Equations (3.24) and (3.26) above, though there is an error in their expression†. In addition, the approach taken here differs significantly from their approach.

3.1.3 The Effect of Code Doppler

Reverting back to the case $\delta\omega_d = 0$, if we introduce a residual code phase offset $\delta\zeta$ then we have seen in Equation (2.52) that the decision statistic is given by:

$$D_k(\widehat{\boldsymbol{\theta}}) = 0.5(MN)^2 P_k \alpha_s(\delta\zeta), \tag{3.27}$$

where:

$$\alpha_s(\delta\zeta) = (1 - |\delta\zeta|)^2. \tag{3.28}$$

†In Equation (8-5b) the term $(1 + R_s T_b)$ multiplying the cosine terms should be replaced by $(1 - R_s T_b)$ in both cases.

Again, this is a well known result.

Now, let us assume that there is also a residual frequency offset. This frequency offset has previously been modelled simply as a shift in the carrier frequency, leading to a rotation in X at every sample. However, a frequency difference between the received and locally generated signals will also manifest itself as a difference in the chipping rate (or code phase rate) between the local and received codes. We have previously modelled the frequency error through the Doppler dilation coefficient η, defined in Equation (2.3). Thus, the received signal can be modelled, in the absence of data modulation and noise, by:

$$r_k(t) = \sqrt{0.5P_k}c_k\left([1+\eta]t - \zeta_0 T_{\text{chip}}\right)\exp\left(j\left[(1+\eta)\omega_0 t + \phi_k\right]\right), \tag{3.29}$$

where ζ_0 is the initial code phase offset. The Doppler frequency offset is, therefore, given by $\omega_d = \eta\omega_0$, and the code phase offset is in motion:

$$\zeta = \zeta(t) = \zeta_0 - \eta t/T_{\text{chip}}. \tag{3.30}$$

The local code can be modelled as follows (see Table 3.1 on page 96 for a list of the symbols used here):

$$c_k\left(\left[1+\widehat{\eta}\right]t - \widehat{\zeta_0}T_{\text{chip}}\right). \tag{3.31}$$

Therefore, we see that the residual code phase error is a function of time, given by:

$$\delta\zeta(t) = \left(\zeta_0 - \widehat{\zeta_0}\right) - \left(\eta - \widehat{\eta}\right)\frac{t}{T_{\text{chip}}} \tag{3.32}$$

$$= \delta\zeta_0 - \delta\eta\frac{t}{T_{\text{chip}}}. \tag{3.33}$$

Different receiver implementations differ in the estimation of η. We consider three common implementations:

1. The typical hardware implementation [140, Figure 26]: here the local code clock rate is updated by the current carrier frequency estimate. Thus, we have:
$$\widehat{\eta} = \frac{\widehat{\omega_d}}{\omega_0}. \tag{3.34}$$

2. The typical software implementation [137, Section 7.7]: in this case the re-

ceived signal is sampled, buffered and stored in memory. Doppler compensation is achieved simply by multiplying the received signal by $\exp(-j\widehat{\omega_d}t)$, which can be achieved either by direct multiplication, or by rotation in the frequency domain (see Section 2.4.4). In either case, we have:

$$\widehat{\eta} = 0. \tag{3.35}$$

3. The η-estimating implementation [27]: the receiver estimates both the Doppler dilation coefficient and the Doppler frequency offset. As pointed out by Cheng [27], the carrier Doppler effect dominates the code Doppler effect, so a less accurate estimate of the code Doppler rate is tolerable. De-coupling these two estimates can result in a simpler implementation.

While we have identified the first two implementations with hardware and software respectively, it is important to note that one can also have hardware implementations for which Equation (3.35) holds, and software implementations for which Equation (3.34) holds (see [10, 75, 103] for instance).

How can we model the effect of a drift in $\widehat{\zeta}$ relative to ζ? Perhaps the most obvious effect is that the code phase offset at the end of the coherent accumulation period will be different to that at the beginning. In fact, denoting by $\Delta\zeta$ the total change in residual code phase error over one coherent accumulation period, we have:

$$\begin{aligned}\Delta\zeta &\triangleq \delta\zeta(T_{\text{coh}}) - \delta\zeta(0) \\ &= -LM\delta\eta,\end{aligned} \tag{3.36}$$

where we recall that $L = 1023$ is the C/A code length in chips. This poses two problems:

1. The amplitude of Y is affected: either increasing or decreasing, depending on whether $\delta\zeta$ moves toward or away from the origin, respectively.

2. The peak of Y no longer corresponds to the true code phase offset. It can be shown that the value of $\widehat{\zeta_0}$ at which Y is a maximum is given by $\zeta_0 + \Delta\zeta/2$. Thus, the residual code phase error at the start of the observation interval is $\delta\zeta_0 = \zeta_0 - \widehat{\zeta_0} = -\Delta\zeta/2$. At the end of the observation interval, the code phase error is given by $\delta\zeta_0 + \Delta\zeta = \Delta\zeta/2$. The presence of code Doppler, therefore, introduces a bias of $\Delta\zeta/2$ code chips to our estimate $\widehat{\zeta}$.

For the moment we make a simple approximation of the first effect, under the assumption that $\Delta\zeta \ll 1$. In this case the start point and the end point are close to each other and a simple midpoint approximation suffices:

$$\alpha_s\left(\delta\zeta, \delta\eta\right) \approx \left(1 - \left|\delta\zeta - \frac{LM\delta\eta}{2}\right|^2\right). \tag{3.37}$$

To characterise the magnitude of this effect we look at bounds on $|\Delta\zeta|$, *i.e.* we ask: what is the maximum shift in the code phase error in one coherent accumulation period?

Consider initially the typical hardware receiver above, with $\widehat{\eta}$ given by Equation (3.34). Recall that, by our choice of Doppler bins, we have limited the residual Doppler error to $|\delta\omega_d| \leq \pi/T_{\text{coh}}$. Thus, inserting Equation (3.34) into Equation (3.36) gives us:

$$|\Delta\zeta| \leq LM\frac{1}{2MLT_{\text{chip}}f_0} \tag{3.38}$$

$$= \frac{2}{T_{\text{chip}}f_0} \tag{3.39}$$

$$= \frac{1}{3080}\,\text{chips}. \tag{3.40}$$

So, the effect of code Doppler is essentially negligible in comparison to the effect of carrier Doppler.

For the typical software receiver, we have $\widehat{\eta} = 0$ and so $\delta\eta = \delta\omega_d/\omega_0$. In this case the code and carrier Doppler effects are completely de-coupled. Therefore, it is possible for the code Doppler effect to dominate over the carrier Doppler effect. Consider, for example, the extreme case where the received signal has a Doppler offset $\omega_d = 20 \times \pi$ k rad s^{-1}, and the receiver makes the estimate $\widehat{\omega_d} = 20 \times \pi$ k rad s^{-1}, then we have $\delta\omega_d = 0$, but $\delta\eta = 10/1.57542 \times 10^6 = 6.35 \times 10^{-6}$ which leads to a relative code phase drift of:

$$\Delta\zeta = -M6.5 \times 10^{-3}\ \text{chips}. \tag{3.41}$$

A coherent integration period of $M = 77$ will, therefore, result in a code phase shift of 1/2 a chip. Note that both the frequency offset and coherent accumulation period are extreme in this case. Typically, however, carrier Doppler will dominate over code Doppler, even when code Doppler is not accounted for in the receiver.

The simple analysis above does suggest that it is advisable to incorporate code Doppler compensation in receivers subject to both high dynamics (large frequency offsets) and weak signals (large M).

For the η-estimating receiver the designer would like to be able to choose the receiver parameters to meet the design specifications. To do so requires a better understanding of the relationship between the receiver parameters and the maximum allowable residual Doppler dilation coefficient. To gain a better insight into the effect of code Doppler in this situation, we now derive a useful approximate model of code Doppler effects when M is large and carrier Doppler has been accounted for. Consider an arbitrary code chip boundary as illustrated in Figure 3.6. We see that a residual code phase offset of $\delta\zeta$ chips at this boundary

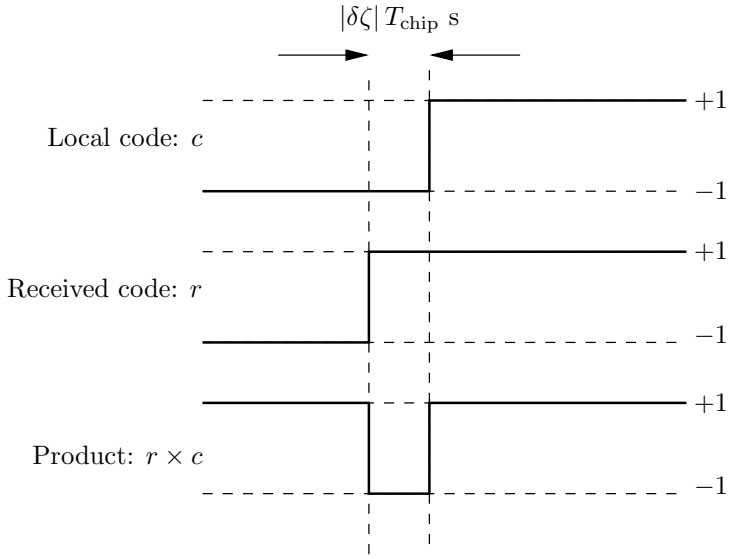


Figure 3.6: Effect of a Residual Code Phase Offset at a Chip Transition.

leads to a negation in the correlation of duration $|\delta\zeta|\,T_{\text{chip}}$ seconds. Thus, given a sample time of T_s, an average of $|\delta\zeta|\,T_{\text{chip}}/T_s$ samples of the accumulator input will be negated. Now, within the C/A codes there are $(L-1)/2$ chip transitions, therefore, over one code period the accumulator output will be:

$$\begin{aligned} Y &= \sqrt{0.5P_k}MN\exp(j\phi_k)\left(1-[L-1]\frac{|\delta\zeta|\,T_{\text{chip}}}{NT_s}\right) \\ &\approx \sqrt{0.5P_k}MN\exp(j\phi_k)\left(1-|\delta\zeta|\right). \end{aligned} \tag{3.42}$$

We now introduce a code frequency offset leading to a total change in $\delta\zeta$ of $\Delta\zeta$ chips. Consider now the partial accumulator sum over one code chip, say the i^{th},

which we denote y_i. Then we have:

$$y_i = \sqrt{0.5P_k}\exp\left(j\phi_k\right)\frac{N}{L}\left(1 - 2\left|\delta\zeta_i\right|t_i\right), \tag{3.43}$$

where $\delta\zeta_i$ is the residual code phase offset at the i^{th} chip boundary and t_i is 1 if a chip transition occurs at the i^{th} chip boundary and 0 if it does not. The average value of t_i is, therefore, 1/2 and so we can approximate the coherent accumulator output by:

$$Y \approx \sqrt{0.5P_k}MN\exp\left(j\phi_k\right)\left(1 - \frac{1}{ML}\sum_{i=0}^{ML-1}\left|\delta\zeta_i\right|\right). \tag{3.44}$$

A first order approximation to the code phase offset at the i^{th} boundary is given by $\delta\zeta_i = \delta\zeta_0 + i\frac{\Delta\zeta}{ML}$, and so we have:

$$Y \approx \sqrt{0.5P_k}MN\exp\left(j\phi_k\right)\left(1 - \frac{1}{ML}\sum_{i=0}^{ML-1}\left|\delta\zeta_0 + i\frac{\Delta\zeta}{ML}\right|\right). \tag{3.45}$$

A general, closed form solution to the above expression is difficult to obtain due to the presence of the absolute value in the summand. We can make a simple, piece-wise linear approximation, however, on making the following observations on the expression:

1. The peak value occurs at the point $\delta\zeta_0 = -\frac{\Delta\zeta}{2}$.
2. It is symmetrical about this peak.
3. Y is approximately zero for $\left|\delta\zeta_0 + \frac{\Delta\zeta}{2}\right| > 1 + \left|\frac{\Delta\zeta}{2}\right|$.

Taking $\delta\zeta_0 = -\frac{\Delta\zeta}{2}$ in Equation (3.45) then, after some manipulation, we have:

$$Y_{\max} \approx \sqrt{0.5P_k}MN\exp\left(j\phi_k\right)\left(1 - \frac{\left|\Delta\zeta\right|}{4}\right). \tag{3.46}$$

Thus, a simple, piece-wise linear approximation to the output of the coherent accumulator in the presence of code Doppler effects is given by:

$$Y \approx \begin{cases} \sqrt{0.5P_k}MN\exp\left(j\phi_k\right)\left(1 - \frac{\left|\Delta\zeta\right|}{4}\right)\left(1 - \frac{\left|\delta\zeta_0 + \frac{\Delta\zeta}{2}\right|}{1 + \frac{\left|\Delta\zeta\right|}{2}}\right) & \left|\delta\zeta_0 + \frac{\Delta\zeta}{2}\right| \le 1 + \left|\frac{\Delta\zeta}{2}\right| \\ 0 & \text{otherwise.} \end{cases} \tag{3.47}$$

Comparing Equations (3.3) and (3.47) we see that we can approximate the combined effects of residual code phase and frequency offsets as a power attenuation factor α_s[†]:

$$\alpha_s\left(\delta\zeta_0, \delta\eta\right) \approx \begin{cases} \left(1 - \frac{|\Delta\zeta|}{4}\right)^2 \left(1 - \frac{\left|\delta\zeta_0 + \frac{\Delta\zeta}{2}\right|}{1 + \frac{|\Delta\zeta|}{2}}\right)^2 & \left|\delta\zeta_0 + \frac{\Delta\zeta}{2}\right| \leq 1 + \left|\frac{\Delta\zeta}{2}\right| \\ 0 & \text{otherwise,} \end{cases} \tag{3.48}$$

where $\Delta\zeta$ is related to $\delta\eta$ through Equation (3.36).

This approximation is shown in Figure 3.7. In the figure there is a frequency offset of 10 kHz, it has been assumed that the carrier frequency has been correctly estimated but no code Doppler compensation has been employed. The accuracy of the approximation can be seen to degrade as M is increased. This approximation

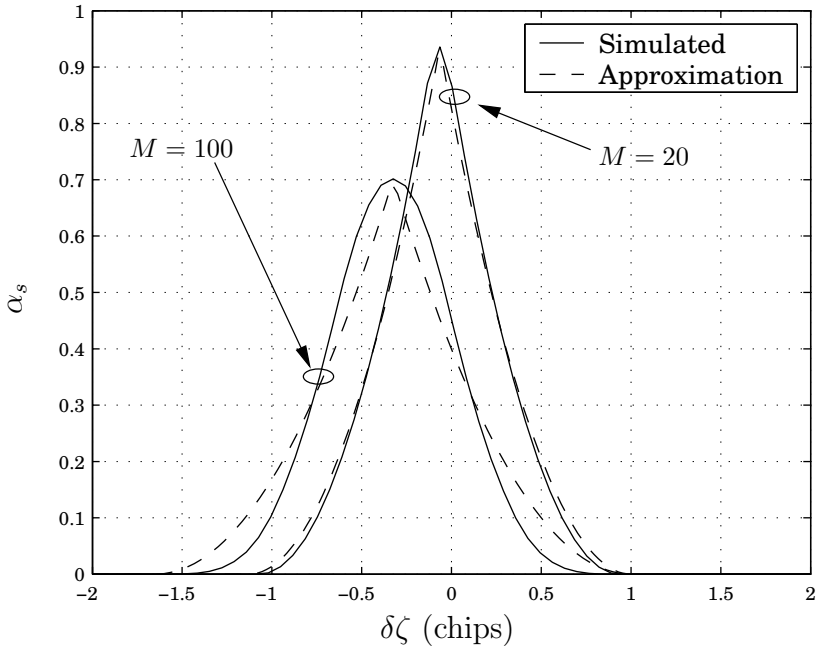


Figure 3.7: Power Attenuation Due to Code Doppler in the ML Detector and an Approximation. Here $\omega_d = 20\pi$ krad s^{-1}.

gives us an appreciation of the three primary effects of code Doppler:

[†]Recall that we assume that the total code phase drift due to Doppler effects is less than one chip.

1. There is an effective power attenuation α_s,
2. A bias of $\frac{\Delta\zeta}{2}$ chips is introduced,
3. The auto-correlation main lobe is spread from a width of one chip to a width of $1 + \left|\frac{\Delta\zeta}{2}\right|$ chips.

Typically $M \leq 10$ is selected to limit the effect of data modulation. In addition, the carrier Doppler estimate is divided into $500/M$ Hzbins. To limit the effects of code Doppler we can also divide the code Doppler estimate (or, rather, the estimate of the Doppler dilation coefficient) into bins. The power loss due to carrier Doppler offset is significantly larger than the power loss due to code Doppler effects for the same frequency offset, and so a much coarser division of the frequency domain can be chosen for the purposes of code Doppler correction in the ML detector. This observation was also made by Cheng et al., though they considered a form of noncoherent detector [27] and did not take into account the power attenuation effect.

The advantage of Equation (3.48) above is that it allows the designer to choose appropriate receiver parameters for a specified level of performance. For instance, if it is decided to limit the power attenuation due to code Doppler to at most 0.5 dB then, from Equation (3.48), we have $|\Delta\zeta| \leq 0.2$. We can then relate this to the maximum allowable frequency offset through Equation (3.36): $f_d \leq \frac{308}{MT_{\mathrm{CA}}} = \frac{308}{M}$ kHz. Clearly the effect of code Doppler is essentially negligible, even in the absence of any correction, except when either M or the frequency uncertainty are very large.

It is important to note that all of the preceding development is based on the assumption of an ideal, triangular correlation peak. In reality, the front-end filter will affect this peak, smoothing its triangular shape. This can be approximately modelled as an appropriate reduction in SNR at the detector input. Note also that, whilst the effect of code Doppler on the *acquisition process* has been considered in the past (see, for example, [19, 57]), the above analysis, treating the effects of code Doppler on the decision statistic alone, is new.

3.2 The Noncoherent Combining Form

The noncoherent combining detector is illustrated in Figure 2.15, reproduced in Figure 3.8 below for convenience. In essence, this detector consists of an ML

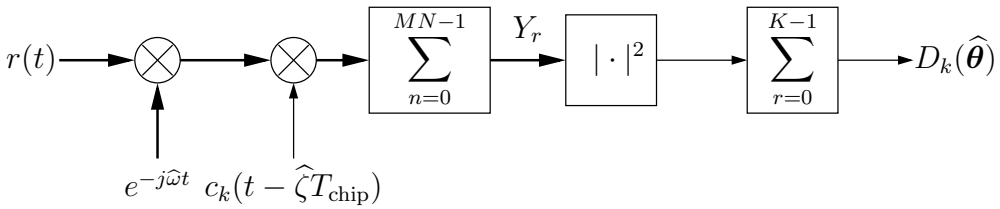


Figure 3.8: Noncoherent Combining Detector

detector followed by a noncoherent accumulator over K successive outputs. The decision statistic is generated as follows:

$$D_k(\widehat{\boldsymbol{\theta}}) = \sum_{r=0}^{K-1} |Y_r|^2 . \tag{3.49}$$

The analysis of this receiver, therefore, follows directly from the analysis of the ML detector.

Consider first of all the case of unknown phase offset in the absence of other signal degradation effects. Inserting the expression for Y from Equation (3.2) into Equation (3.49) gives the following expression for the decision statistic:

$$D_k(\widehat{\boldsymbol{\theta}}) = 0.5K(MN)^2 P_k. \tag{3.50}$$

Once again we see that D_k is a scaled measure of the signal power at the receiver antenna.

3.2.1 The Effect of a Residual Carrier Frequency Offset

Introducing an unknown residual carrier frequency offset $\delta\omega_d$, and again ignoring code Doppler effects for the moment, then the r^{th} output of the coherent accumulator is given by:

$$|Y_r|^2 = 0.5P_k \left| \frac{\sin \frac{\delta\omega_d T_s MN}{2}}{\sin \frac{\delta\omega_d T_s}{2}} \right|^2 . \tag{3.51}$$

Thus, the decision statistic is given by:

$$D_k(\widehat{\boldsymbol{\theta}}) = 0.5K(MN)^2 P_k \alpha_D(\delta\omega_d), \tag{3.52}$$

where $\alpha_D(\delta\omega_d)$ is given in Equation (3.7). Again, this is a well known result. As discussed in Section 2.4.1, this represents one of the major advantages of noncoherent combining. The attenuation due to residual carrier Doppler offset is independent of K. Therefore, to acquire weaker signals, we can increase the noncoherent accumulation period without suffering extra signal degradation due to carrier Doppler.

3.2.2 The Effect of Data Modulation

We now introduce an unknown data signal, which modulates the received signal at a rate of 50 bps. Thus, there is a possibility of a bit transition every $D = 20$ ms. Denoting by B the number of data bit boundaries occurring within the observation interval, then we have:

$$B = \begin{cases} \lfloor \frac{MK}{D} \rfloor & \text{or} \\ \lceil \frac{MK}{D} \rceil, \end{cases} \tag{3.53}$$

depending on where the first boundary occurs within the observation interval. We assume that $M \leq D$, so that there is at most one data bit boundary within a coherent sub-interval. Thus, within the KM ms observation interval, there are B coherent sub intervals containing data bit boundaries and $K - B$ containing no data bit boundaries, as illustrated in Figure 3.9. In our investigation of the ML form above we have investigated the effect of data modulation within a coherent sub-interval. We apply a similar technique here.

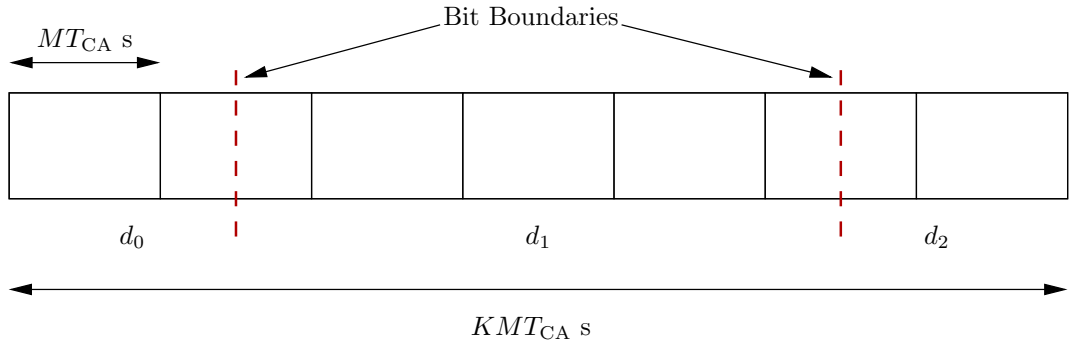


Figure 3.9: Model of Data Effects in the Noncoherent Combining Detector

Let $\boldsymbol{d}$ denote the length $B + 1$ vector of data bits present in the observation interval: $\boldsymbol{d} = [d_0, d_1, \ldots, d_B]$. Similarly, we denote by $\delta_{T,i}$ the fraction of the way

through a coherent sub-interval at which the i^{th} data bit boundary occurs (see Figure 3.2). Letting r_i denote the index of the coherent sub-interval in which the i^{th} boundary occurs, then from Equation (3.13) we have:

$$|Y_{r_i}|^2 = 0.5(MN)^2 P_k \alpha_D(\delta\omega_d)\alpha_{mi}(\delta\omega_d, d_i, d_{i+1}, \delta_{T,i}), \tag{3.54}$$

where α_{mi} denotes the modulation attenuation due to the i^{th} bit boundary and is defined in Equation (3.15). Substituting Equation (3.54) into Equation (3.49) yields:

$$D_k(\widehat{\boldsymbol{\theta}}) = 0.5(MN)^2 P_k \alpha_D(\delta\omega_d)\left[K - B + \sum_{i=0}^{B-1}\alpha_{mi}\right], \tag{3.55}$$

where the dependence of α_{mi} on the signal parameters is implicit. Comparing Equations (3.52) and (3.55) we see that the modulation can be modelled as an attenuation of the received signal power:

$$D_k(\widehat{\boldsymbol{\theta}}) = 0.5K(MN)^2 P_k \alpha_D(\delta\omega_d)\alpha_m(\delta\omega_d, B, \boldsymbol{d}), \tag{3.56}$$

where:

$$\alpha_m(\delta\omega_d, B, \boldsymbol{d}) = 1 - \frac{1}{K}\left(B - \sum_{i=0}^{B-1}\alpha_{mi}\right). \tag{3.57}$$

Note that α_{mi} is a function of: 1) the two data bits within the coherent sub-interval; 2) the point at which the boundary occurs, $\delta_{T,i}$; and 3) the residual Doppler offset $\delta\omega_d$. We can assume that the data bits are statistically independent. The relationships between the $\delta_{T,i}$ require a little more effort. We consider two receiver types:

1. Synchronous receiver: In this case, the local code epoch is synchronised to the start of the coherent observation interval, see Figure 3.10 a). Therefore, when the local code estimate is correct, data bit edges are also synchronised to the local code epoch. This is typically the case in serial hardware receivers.

2. Asynchronous receiver: The local code epochs are not synchronised to the start of the coherent observation interval, see Figure 3.10 b). In this case, a data bit boundary can occur anywhere within a coherent sub-interval. Software and FFT-based receivers are typically asynchronous.

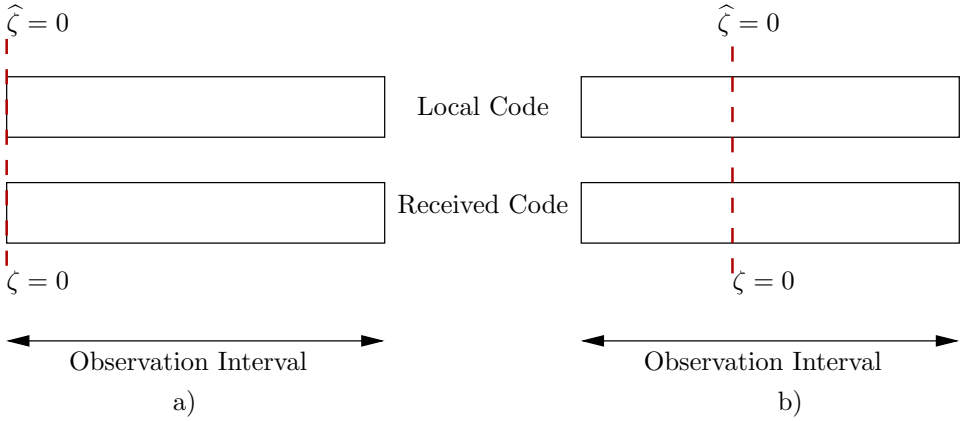


Figure 3.10: a) Synchronous Receiver. b) Asynchronous Receiver.

Synchronous receiver In this case, bit boundaries can only occur at local C/A code epochs. Thus, given that there are M code periods in a coherent observation interval, there are only M discrete points at which a data bit boundary can occur, given by:

$$\delta_{T,i} \in \left\{ \frac{n}{M} \ : \ 0 \leq n \leq M-1 \right\}. \tag{3.58}$$

If we define n_0 such that $\delta_{T,0} = \frac{n_0}{M}$, then we can write:

$$\delta_{T,i} = \frac{(n_0 + iD) \bmod M}{M} \tag{3.59}$$

$$= \left(\delta_{T,0} + \frac{ir}{M} \right) \bmod 1, \tag{3.60}$$

where:

$$r \triangleq D \bmod M. \tag{3.61}$$

It is interesting to note that the bit boundary location returns to $\delta_{T,i}$ whenever $\frac{ir}{M}$ is an integer. Denoting by T the smallest value of i such that $\delta_{T,i} = \delta_{T,0}$, then:

$$T = \frac{M}{\gcd(r, M)}, \tag{3.62}$$

where $\gcd(r, M)$ denotes the greatest common divisor of the integers r and M. Therefore, of the M possible values of $\delta_{T,i}$, a maximum of T will be "visited" during any one KMT_{CA} ms observation interval. This is illustrated in Figure 3.11, where we have $M = 6$ and $T = 3$. Note that we introduce the variable $\overline{\delta}_{T,0}$ to denote the location of that data bit boundary which occurs closest to the start

of a coherent observation interval.

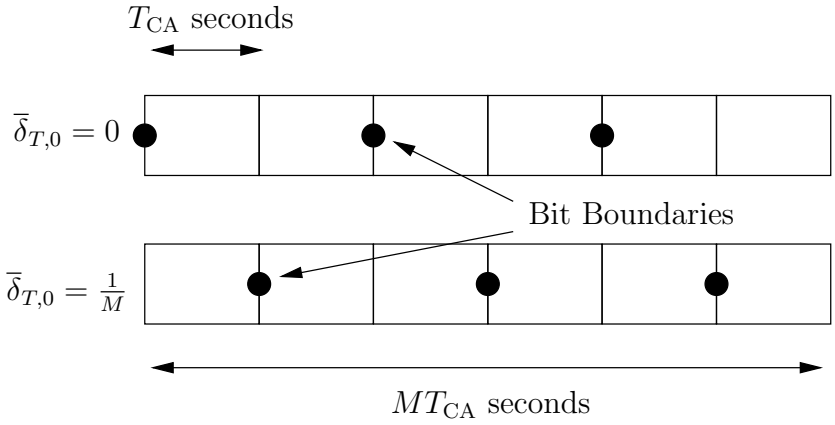


Figure 3.11: All Possible Bit Boundary Locations for the Synchronous Receiver: $M = 6$, $r = 2$ and $T = 3$.

Asynchronous receiver In this case, bit boundaries can occur anywhere within the coherent observation interval. Again, we denote by $\delta_{T,0}$ the fractional offset of the first boundary. The only difference between the synchronous and asynchronous receivers is the set of possible values that can be assumed by $\delta_{T,0}$. In each case we have:

$$\delta_{T,i} = \delta_{T,0} + \frac{ir}{M} \bmod 1, \tag{3.63}$$

where r is defined in Equation (3.61) above and, again, there are T possible values of $\delta_{T,i}$ at which boundaries can occur in any one observation interval, where T is defined in Equation (3.62).

We are particularly interested in weak signal applications, in which case we have $K \gg M$, so that all possible $\delta_{T,i}$ are visited during the observation interval. We can use this to derive simple approximations to the mean and worst case modulation attenuation. We assume that, in a long observation interval, all the $\delta_{T,i}$ occur B/T times. Thus, from Equation (3.57), we have:

$$\alpha_m \approx 1 - \frac{B}{K}\left(1 - \frac{1}{T}\sum_{i=0}^{T-1} \alpha_{mi}\left(\delta\omega_d, \overline{\delta}_{T,i}\right)\right), \tag{3.64}$$

where: $\overline{\delta}_{T,i} = \overline{\delta}_{T,0} + i/T$ and we denote by $\overline{\delta}_{T,0}$ the smallest δ_T occurring in the observation interval and α_{mi} is the modulation attenuation factor for the ML

form, given in Equation (3.18). After some algebraic manipulation we find:

$$\max_t \left(\frac{1}{T} \sum_{i=0}^{T-1} \alpha_{mi} \right) = 1 + 2\cot^2\beta - \frac{2\cot\beta}{T\sin\frac{\beta}{T}} \cos\left(\beta \left[\frac{1}{T} - 2\overline{\delta}_{T,0} \right] \right) \tag{3.65}$$

$$E_t \left[\frac{1}{T} \sum_{i=0}^{T-1} \alpha_{mi} \right] = 1 + \cot^2\beta - \frac{\cot\beta}{T\sin\frac{\beta}{T}} \cos\left(\beta \left[\frac{1}{T} - 2\overline{\delta}_{T,0} \right] \right) . \tag{3.66}$$

where we recall that t denotes the random variable which is equal to one if a data bit transition occurs at a data bit boundary and equal to zero otherwise. These expressions can now be used to determine the mean and worst case modulation attenuation for both the synchronous and asynchronous receivers. The only difference between these receivers is in the range of possible values for $\overline{\delta}_{T,0}$:

$$\overline{\delta}_{T,0} \in \begin{cases} \left\{ \frac{i}{M} \ : \ i \in 0, 1, \ldots, \gcd(r, M) - 1 \right\} & \text{Synchronous} \\ \left[0, \frac{1}{T} \right) & \text{Asynchronous} . \end{cases} \tag{3.67}$$

Referring to the example illustrated in Figure 3.11 we see that, for the synchronous receiver, $\overline{\delta}_{T,0}$ is restricted to the two cases 0 or $1/M$ whereas, for the asynchronous receiver, $\overline{\delta}_{T,0}$ can occur anywhere in the first two code periods.

Consider initially the mean attenuation. Inserting Equation (3.66) into Equation (3.64), and taking expectation over $\overline{\delta}_{T,0}$ yields:

$$\overline{\alpha}_m \approx E_{\overline{\delta}_{T,0}} \left[1 - \frac{M}{D} \left\{ -\cot^2\beta + \frac{\cot\beta}{T\sin\frac{\beta}{T}} \cos\left(\beta \left[\frac{1}{T} - 2\overline{\delta}_{T,0} \right] \right) \right\} \right]. \tag{3.68}$$

Assuming $\overline{\delta}_{T,0}$ is uniformly distributed, we find for the asynchronous receiver:

$$\overline{\alpha}_m \approx 1 - \frac{M}{D} \left\{ \frac{\cot\beta}{\beta} - \cot^2\beta \right\}, \tag{3.69}$$

which is identical to the average attenuation in the ML form (Equation (3.22)).

For the synchronous receiver we have:

$$\overline{\alpha}_m \approx 1 - \frac{M}{D}\left\{\frac{1}{M}\cot\beta\ \cot\left(\frac{\beta}{M}\right) - \cot^2\beta\right\}. \tag{3.70}$$

Both of these expressions are new, though Equation (3.69) is equivalent to [37, Equation (8-5b)] with the correction mentioned in the footnote on page 105. It is interesting to note that:

$$\frac{1}{M}\cot\left(\frac{\beta}{M}\right) \leq \frac{1}{\beta} \quad \text{for } -\frac{\pi}{2} \leq \beta \leq \frac{\pi}{2},$$

so that, on average, the synchronous receiver has better performance in the presence of data modulation. In particular, note that when $M = 1$ data modulation has no effect on the synchronous receiver. The mean power attenuation due to modulation effects for the synchronous and asynchronous receivers are compared in Figure 3.12. The superiority of the synchronous form is clearly visible, though

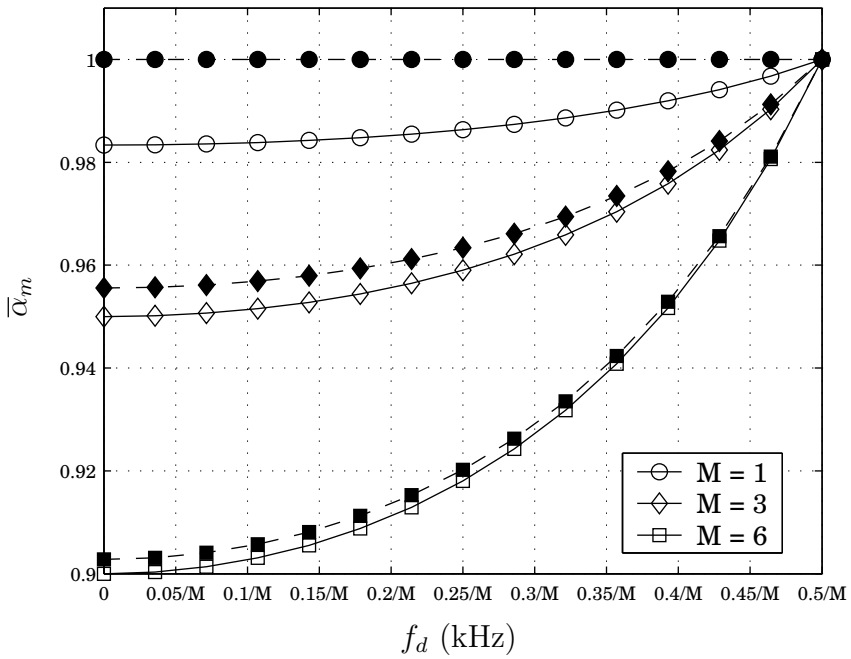


Figure 3.12: Comparison of Mean Power Attenuation Due to Data Modulation for Synchronous and Asynchronous Forms of the NCD Detector: Empty markers represent the asynchronous receiver, filled markers the synchronous.

it is worth noting that the difference between the two forms diminishes rapidly

as M increases.

The worst case attenuation occurs when there is a bit transition at every bit boundary. To minimise α_m with respect to $\overline{\delta}_{T,0}$ requires maximising:

$$\cos\left(\beta\left[\frac{1}{T}-2\overline{\delta}_{T,0}\right]\right).$$

We consider only the effects within one Doppler bin, so $|\delta\omega_d| \leq \pi T_{\text{coh}}/2$, which implies that $-\pi/2 \leq \beta \leq \pi/2$. Hence, the cosine term above is maximised when $\overline{\delta}_{T,0}$ is as close as possible to $1/(2T)$. Therefore, for the asynchronous receiver, we have $\overline{\delta}_{T,0} = 1/(2T)$, which yields:

$$\alpha_{m\text{wc}} \approx 1 - \frac{2M}{D}\left\{-\cot^2\beta + \frac{\cot\beta}{T\sin\frac{\beta}{T}}\right\}. \tag{3.71}$$

For the synchronous receiver we have $\overline{\delta}_{T,0} = 2/M \times \text{nint}\,(\gcd(r,M)/2)$, where $\text{nint}\,(x)$ denotes the nearest integer to x (for example, referring to Figure 3.11, we can see that the worst case attenuation occurs when $\overline{\delta}_{T,0} = 1/M$). This yields an approximate worst case attenuation:

$$\alpha_{m\text{wc}} \approx 1-\frac{2M}{D}\left\{-\cot^2\beta + \frac{\cot\beta}{T\sin\frac{\beta}{T}}\cos\left(\beta\left[\frac{1}{T}-\frac{2}{M}\text{nint}\left(\frac{\gcd(r,M)}{2}\right)\right]\right)\right\}. \tag{3.72}$$

Note that these expressions are approximations to the worst case attenuation, the key approximation being that all T possible bit boundary locations occur an equal number of times. This approximation is asymptotically exact as $K \to \infty$.

A simple lower bound can be found by assuming that the worst case attenuation occurs at each boundary. Thus, substituting Equation (3.20) into Equation (3.57) yields:

$$\alpha_m(\delta\omega_d) \geq 1 - 4\frac{B}{K}\cos(\beta)\frac{\sin^2\frac{\beta}{2}}{\sin^2\beta}. \tag{3.73}$$

Of particular interest is the disparity between Equations (3.71) and (3.73). These expressions are identical when $T = 1$, *i.e.* when $M \,|\, D$. However, when T is large,

the worst case attenuation of Equation (3.71) is significantly better than that predicted by the lower bound of Equation (3.73). The reason for this is that, for $T > 1$, the location of the data bit boundary moves for each bit. Therefore, even if a bit transition occurs exactly half way through one coherent sub-interval, the subsequent bit boundary will, of necessity, not occur at the midpoint. This apparent motion of the data bit boundaries within the coherent accumulation interval produces an averaging effect, limiting the worst case attenuation due to data modulation as K increases.

Thus, while the average attenuation due to data modulation is identical to that for the ML detector, the worst case attenuation can be greatly improved upon, for large values of K, through a suitable choice of M, the coherent accumulation interval. This is illustrated for various values of M in Figure 3.13 (note that, at $f_d = 0.5/M$ kHz, the attenuation is identical for all M since the data modulation has no effect). The most striking difference is between the cases $M = 19$ and $M = 20$, where we see that a significant improvement in worst case data modulation effects can be achieved by a subtle change in parameters. This is an observation that does not appear to have been made in the literature before.

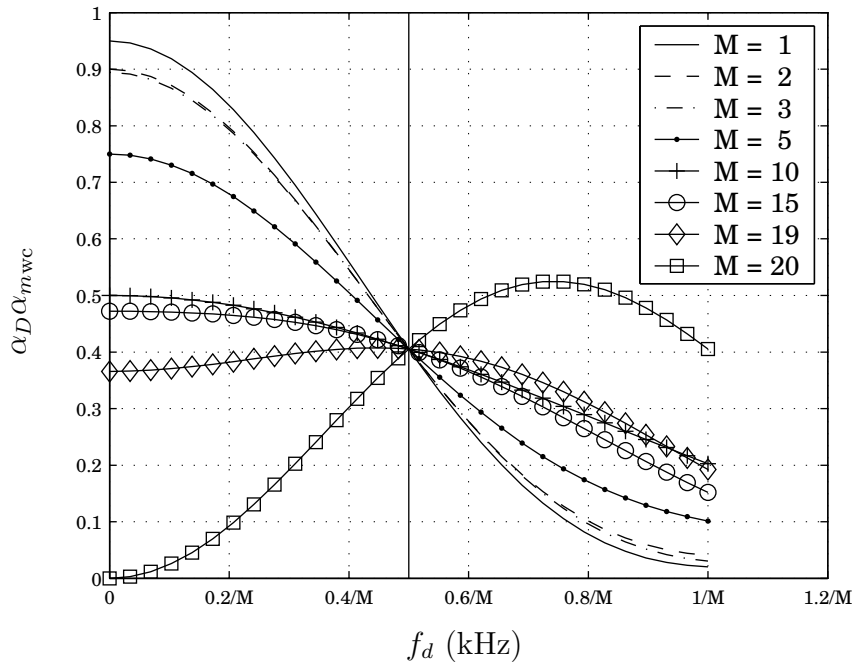


Figure 3.13: Power Attenuation Due to Combined Carrier Doppler and Worst Case Data Modulation for the NCCD Detector as $K \to \infty$.

Another interesting observation is the dependence of α_m on the *true* code

phase offset ζ in the asynchronous receiver. Though we have not made it explicit to date, we can relate ζ to $\overline{\delta}_{T,0}$ through the expression:

$$\overline{\delta}_{T,0} = \frac{\zeta}{LM} + \frac{i}{M}, \tag{3.74}$$

for some integer $i \ : 0 \leq i < \gcd(r, M)$. We can, therefore, write α_m as a function of ζ:

$$\alpha_m(\zeta) \approx 1 - \frac{2B}{K}\left\{-\cot^2\beta + \frac{\cot\beta}{T\sin\frac{\beta}{T}}\cos\left(\beta\left[\frac{1}{T} - \frac{2}{M}\left(\frac{\zeta}{L} + i\right)\right]\right)\right\}. \tag{3.75}$$

We can determine the average modulation attenuation as a function of ζ by again assuming only half of the boundaries result in transitions and taking the expectation over i, which we assume to be uniformly distributed. After some algebraic manipulation we obtain:

$$\overline{\alpha}_m(\zeta) \approx 1 - \frac{M}{D}\left\{-\cot^2\beta + \frac{\cot\beta}{M\sin\frac{\beta}{M}}\cos\left(\frac{\beta}{M}\left[1 - \frac{2\zeta}{L}\right]\right)\right\}. \tag{3.76}$$

This is illustrated in Figure 3.14. Clearly, this variation with ζ does not have a significant affect of receiver performance, introducing only a slight bias in favour of offsets close to the local code epoch. The effect diminishes as M increases. Note that we have assumed $M \leq 20$. It is possible to extend the results derived here to the case $M > 20$ using the technique of Davisson and Flikkema [37], but this is beyond the scope of this work.

3.2.3 The Effect of Code Doppler

Consider now the effect of a residual code Doppler offset. We follow the same procedure as for the ML form: beginning with an initial residual code phase offset $\delta\zeta_0$ and a frequency error $\delta\eta$, we determine the peak power attenuation, from which a piece-wise linear approximation to the power attenuation is derived as a function of $\delta\zeta_0$ and $\delta\eta$.

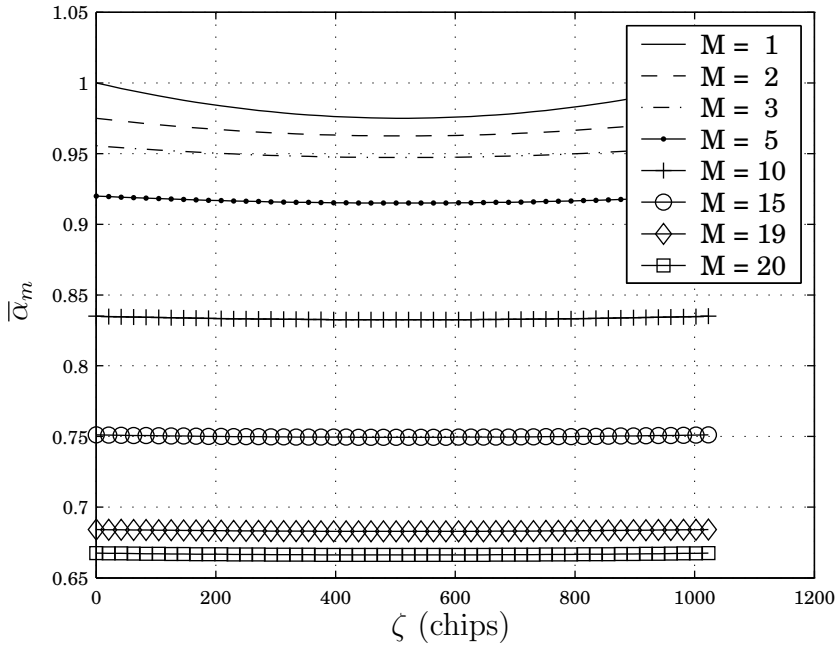


Figure 3.14: Power Attenuation Due to Mean Data Modulation vs Code Phase Offset for the NCCD Detector, $\delta\omega_d = 0$.

From Equation (3.27) we have:

$$|Y_r|^2 = 0.5(MN)^2 P_k \alpha_D(\delta\omega_d)\alpha_s\left(\delta\zeta_r, \delta\eta\right), \tag{3.77}$$

where $\alpha_s\left(\delta\zeta, \delta\eta\right)$ is given by Equation (3.48), and $\delta\zeta_r$ is the residual code phase offset at the start of the r^{th} coherent sub-interval and is given by:

$$\delta\zeta_r = \delta\zeta_0 + r\Delta\zeta. \tag{3.78}$$

In the following analysis we assume that the effect of code Doppler within a coherent sub-interval is negligible. However, the residual code phase offset moves with time, as indicated in Equation (3.78). Note that this assumption is quite accurate for small values of M ($M < 20$), even for reasonably large Doppler offsets, as discussed in Section 3.1.3.

The power attenuation factor within a coherent sub-interval can, therefore, be modelled by $\alpha_s(\delta\zeta)$, as defined in Equation (3.28). Recall that $\sqrt{\alpha_s(\delta\zeta)}$ is triangular about the point $\delta\zeta = 0$, as illustrated in Figure 3.15. Summing over

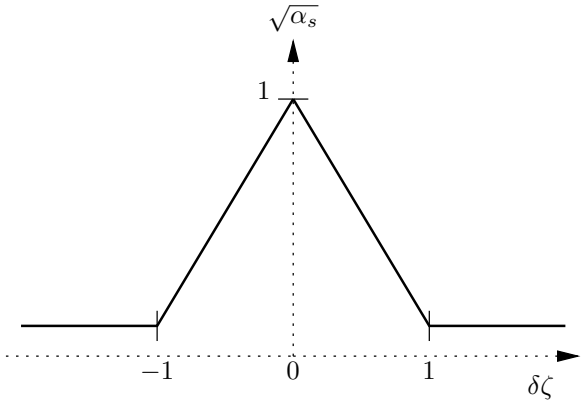


Figure 3.15: Power Attenuation due To Residual Code Phase Offset

r, we have:

$$D_k(\widehat{\boldsymbol{\theta}}) \approx 2(MN)^2 P_k \alpha_D(\delta\omega_d) \sum_{r=0}^{K-1} \left(1 - |\delta\zeta_r|\right)^2 . \tag{3.79}$$

Of particular interest is the peak value of the decision statistic. A little thought shows that this peak occurs when the zero code phase offset point is crossed precisely halfway through the observation interval. This is illustrated in Figure 3.16, if the initial code phase offset is to the left or right of the point illustrated in the diagram then the total sum will be smaller. Thus, the maximum

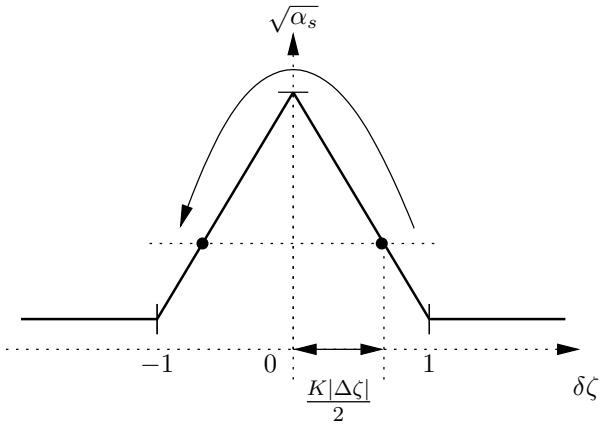


Figure 3.16: The Maximum Decision Statistic Occurs when the Code Phase Offset is Zero at the Midpoint of the Observation Interval

value occurs when $\delta\zeta_0 = -\frac{K\Delta\zeta}{2}$. The sum in Equation (3.79) is then evenly

divided on either side of the point $\delta\zeta = 0$, so we have[†]:

$$\begin{aligned} D_k(\widehat{\boldsymbol{\theta}}) &= 0.5(MN)^2 P_k \alpha_D(\delta\omega_d) 2 \sum_{r=0}^{\frac{K}{2}-1} (1 - r\,|\Delta\zeta|)^2 \\ &= 0.5(MN)^2 P_k \alpha_D(\delta\omega_d) K \left\{ 1 - |\Delta\zeta| \frac{K-2}{2} \left(1 - \frac{|\Delta\zeta|\,(K-1)}{6} \right) \right\}. \end{aligned} \tag{3.80}$$

Using a similar technique to that used for the ML form, the following approximation to the power attenuation due to code phase and frequency offsets can then be derived (note that we again assume that the total code phase drift is less than one chip):

$$\alpha_s\left(\delta\zeta_0, \delta\eta\right) \approx \begin{cases} \left(1 - \dfrac{|\Delta\zeta|\,(K-2)}{2} \left[1 - \dfrac{|\Delta\zeta|\,(K-1)}{6} \right] \right) & \left| \delta\zeta_0 + \dfrac{K\Delta\zeta}{2} \right| \\ \qquad \times \left(1 - \dfrac{\left| \delta\zeta_0 + \frac{K\Delta\zeta}{2} \right|}{1 + \frac{|K\Delta\zeta|}{2}} \right)^2 & \leq 1 + \left| \dfrac{K\Delta\zeta}{2} \right| \\ 0 & \text{otherwise,} \end{cases} \tag{3.81}$$

This approximation is illustrated in Figure 3.17, where it is compared with simulated results. For the simulation we have taken a simple case with $M = 1$ and a carrier Doppler offset of 500 Hz, which is precisely on the border between two Doppler bins. Two cases are shown in the figure, in the first $K = 300$ whilst, in the second, $K = 1000$. These values of K are both realistic for the detection of weak GPS signals. As observed for the ML detector, the three effects of code Doppler offsets can be clearly seen: 1) peak-power attenuation; 2) bias in $\widehat{\zeta}$; 3) broadening of the auto-correlation main-lobe.

3.3 The Differentially Coherent Combining Form

The differentially coherent combining detector was introduced in Section 2.4.2, and is illustrated in Figure 3.18 below. This form of detector is very similar to the

[†]In the following we assume that the total code phase drift due to Doppler effects is less than one code chip, thus $K\Delta\zeta < 1$.

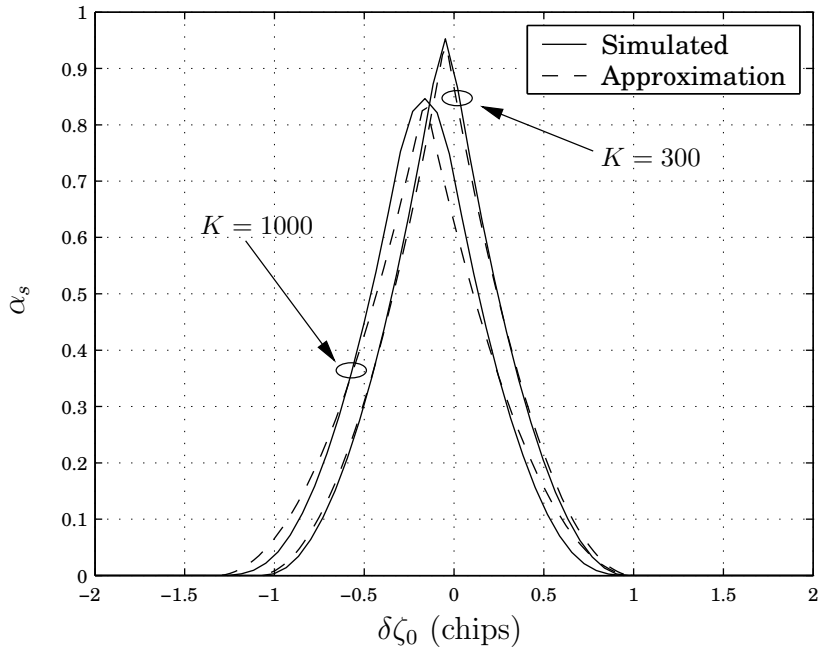


Figure 3.17: Power Attenuation Due to Code Doppler in the NCCD and an Approximation. Here $\omega_d = \pi$ krad s^{-1} and $M = 1$.

noncoherent combining form, with the notable difference in the manner in which the decision statistic is generated. Similar to the NCCD, we assume the receiver

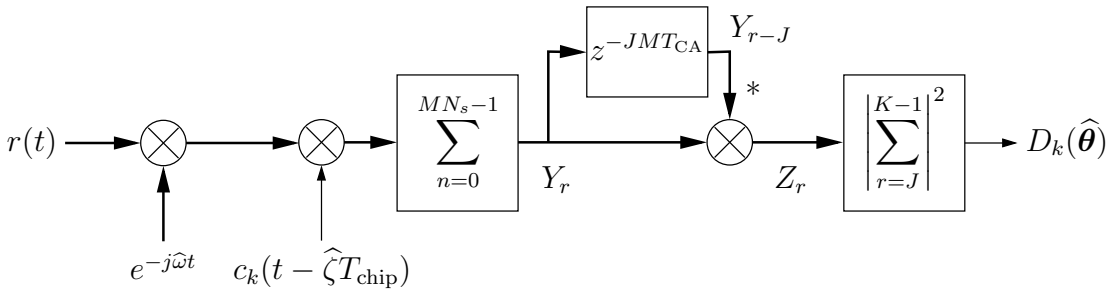


Figure 3.18: Differentially Coherent Combining Detector: z^{-T} denotes a delay of T seconds, * denotes complex conjugation, complex quantities are denoted by heavier lines.

takes K observations of the output of the coherent accumulator. This receiver utilises what we will refer to as the "differentially coherent product"; this is the product of the sample Y_r and the complex conjugate of the observation Y_{r-J}, for which we write:

$$Z_r = Y_r Y_{r-J}^*. \tag{3.82}$$

We refer to the Z_r as the summands, since $R = K - J$ of these are summed, and we denote by W the sum:

$$W = \sum_{r=J}^{K-1} Z_r. \tag{3.83}$$

The square magnitude of the result is computed to give the decision statistic:

$$D_k(\widehat{\boldsymbol{\theta}}) = |W|^2 = \left| \sum_{r=J}^{K-1} Y_r Y_{r-J}^* \right|^2. \tag{3.84}$$

As mentioned in Section 2.4.2, the noncoherent form may be considered to be a special case of the differentially coherent form presented above, with $J = 0$.

An alternative form of differentially coherent combining detector was suggested recently by Ávila-Rodríguez et al. [16] which is restricted to the case $J = 1$ and requires K to be even. The key to this technique is to take the observations of Y in pairs (Y_r, Y_{r-1}), and form the sum:

$$W = \sum_{r=0}^{\frac{K}{2}-1} Y_{2r+1} Y_{2r}^*, \tag{3.85}$$

from which we obtain the decision statistic:

$$D_k(\widehat{\boldsymbol{\theta}}) = |W|^2 = \left| \sum_{r=0}^{\frac{K}{2}-1} Y_{2r+1} Y_{2r}^* \right|^2. \tag{3.86}$$

We refer to this detector as the *pair-wise form* of the DCCD and to the detector of Equation (3.84) as the *standard form*.

It is worth noting at this point that the structure of the DCCD described here differs in two important ways from that typically discussed in the literature (and from that which we have already discussed in Section 2.4.2). Firstly, we have simply extended the original definition from $J = 1$ to arbitrary (positive integer) values of J. The second difference is in the form of $D_k(\widehat{\boldsymbol{\theta}})$: typically the decision statistic has been formed as the real part of W, whilst, in this case, we choose to follow the structure described by Schmid and Neubauer [112] and take the square magnitude of W as the decision statistic. This form of the decision statistic performs significantly better in the presence of residual carrier Doppler offset, as demonstrated below.

3.3.1 The Effect of a Residual Carrier Frequency Offset

We begin our analysis of the performance of the DCCD in the absence of noise with the standard form. We begin, in this instance, with the case where the signal is subject to both an unknown initial phase offset ϕ_k and a constant residual carrier frequency offset $\delta\omega_d$. Adapting Equation (3.5) for the r^{th} output of the coherent accumulator yields[†]:

$$Y_r = \sqrt{0.5P_k}\exp\left(j\left(\phi_k + \frac{\delta\omega_d T_s}{2}\left[(2r+1)MN - 1\right]\right)\right)\frac{\sin\frac{\delta\omega_d T_s MN}{2}}{\sin\frac{\delta\omega_d T_s}{2}}, \quad (3.87)$$

from which we have:

$$|Y_r| = \sqrt{0.5P_k}\left|\frac{\sin\frac{\delta\omega_d T_s MN}{2}}{\sin\frac{\delta\omega_d T_s}{2}}\right| \quad (3.88)$$

$$\angle Y_r = \phi_k + \frac{\delta\omega_d T_s}{2}\left[(2r+1)MN - 1\right], \quad (3.89)$$

where we have ignored, for the moment, the phase component due to the sign of the ratio of sines. Now, from Equation (3.83), we have:

$$\begin{aligned} W &= \sum_{r=J}^{K-1} Y_r Y_{r-J}^* \\ &= \sum_{r=J}^{K-1} |Y_r|\,|Y_{r-J}|\exp\left(j\left(\angle Y_r - \angle Y_{r-J}\right)\right) \\ &= 0.5(K-J)(MN)^2 P_k \alpha_D(\delta\omega_d)\exp\left(j2\beta J\right). \end{aligned} \quad (3.90)$$

Note that the sign of the ratio sines is the same for both Y_r and Y_{r-J}, so we are justified in omitting it from Equation (3.89). It is immediately apparent from Equation (3.90) that a decision statistic based on the real part of W alone will suffer additional losses due to residual Doppler offset when compared to a magnitude (or square magnitude) statistic:

$$\Re\{W\} = 0.5(K-J)P_k\left|\frac{\sin\frac{\delta\omega_d T_s MN}{2}}{\sin\frac{\delta\omega_d T_s}{2}}\right|^2\cos(2\beta J) \quad (3.91)$$

[†]Note that, after $r-1$ coherent accumulations, the phase of the incoming signal will have advanced by $r\delta\omega_d MNT_s$ radians, so Equation (3.87) is obtained from Equation (3.5) with $\phi_k \rightarrow \phi_k + r\delta\omega_d MNT_s$.

$$|W| = 0.5(K-J)P_k \left| \frac{\sin \frac{\delta\omega_d T_s MN}{2}}{\sin \frac{\delta\omega_d T_s}{2}} \right|^2 . \tag{3.92}$$

The loss of the real part relative to the magnitude is given by $\cos(2\beta J)$, and is a function of the Doppler frequency offset. Recall from Section 2.4 that the maximum value of $\delta\omega_d$ is chosen to ensure a certain maximum attenuation at the output of the coherent accumulator. Recall also that a frequency spacing of $1/M$ kHz is a common choice, resulting in a maximum residual Doppler offset of $\delta\omega_{d\max} = \pi/(MNT_s)$. Note, however, that the argument of the cosine function is then $J\pi$. Thus, for some $\delta\omega_d < \delta\omega_{d\max}$, we have $\delta\omega_d T_s MNJ = \pi/2$ and so all the signal power is in the imaginary component. Therefore, if we are to use the real part of W as the decision statistic, we will have to shrink the Doppler bin width considerably. For instance, to ensure a phase shift of no more than $\pi/4$ radians would require a maximum frequency offset of $1/(8MNJT_s)$ or $1/(4J)$ times the bin width set by the coherent accumulator. This is illustrated in Figure 3.19, which shows a normalised Argand diagram of the complex number W. The variation with carrier Doppler is clearly seen as a spiral, beginning at $W = 1+0j$ when $f_d = 0$ Hz and reaching the origin at $f_d = 1$ kHz.

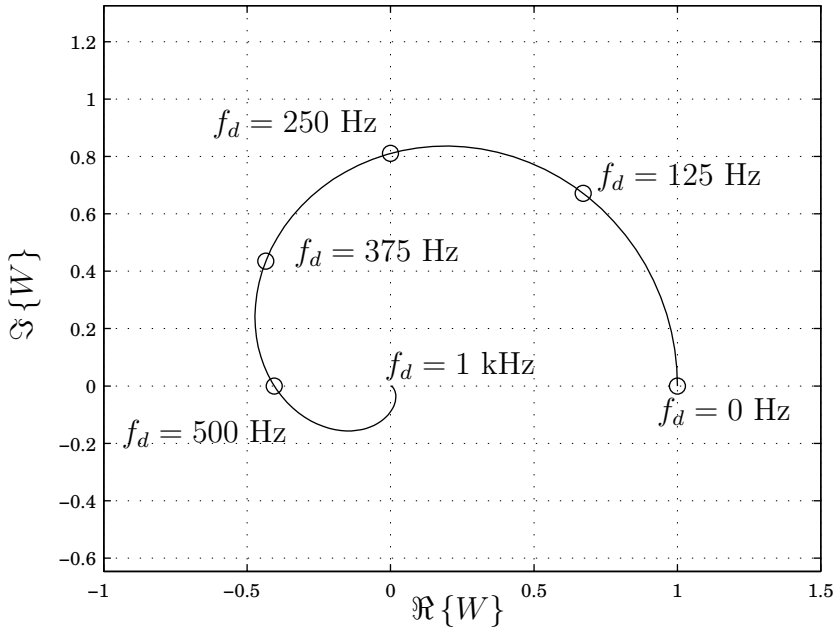


Figure 3.19: The Effect of Carrier Frequency Offset on the DCCD. $M = 1$, $J = 1$ and the carrier Doppler frequency f_d varies from 0 Hz to 1 kHz.

We choose, therefore, to use the square magnitude of W as decision statistic, thereby eliminating this excess frequency-induced loss:

$$D_k(\widehat{\boldsymbol{\theta}}) = \left[0.5(K-J)(MN)^2 P_k \alpha_D(\delta\omega_d)\right]^2. \tag{3.93}$$

We can apply a similar procedure to determine the performance of the pairwise form of the DCCD. Again, we start with the case of unknown, but constant, residual Doppler offset. The coherent accumulator output is again given by Equation (3.87) and so, from Equation (3.85), we have:

$$\begin{aligned} W &= \sum_{r=0}^{\frac{K}{2}-1} Y_{2r+1} Y_{2r}^* \\ &= \sum_{r=0}^{\frac{K}{2}-1} |Y_{2r+1}|\,|Y_{2r}| \exp\left(j\left(\angle Y_{2r+1} - \angle Y_{2r}\right)\right) \qquad (3.94) \\ &= \frac{KP_k}{4}\left|\frac{\sin\frac{\delta\omega_d T_s MN}{2}}{\sin\frac{\delta\omega_d T_s}{2}}\right|^2 \exp\left(j2\beta\right). \qquad (3.95) \end{aligned}$$

Again, as we saw for the standard form, the Doppler offset induces a constant phase shift on W, in addition to the attenuation factor at the coherent accumulator output. Hence, for the reasons outlined previously, we choose a square magnitude decision statistic in preference to one formed from just the real part of W. This gives us:

$$D_k(\widehat{\boldsymbol{\theta}}) = \left[\frac{KP_k}{4}(MN)^2 \alpha_D(\delta\omega_d)\right]^2. \tag{3.96}$$

3.3.2 The Effect of Data Modulation

Introducing a random data sequence to the signal, we proceed in much the same fashion as for the noncoherent form. The observation interval is divided into K coherent sub-intervals, of which B contain data bit boundaries and $K-B$ do not. This situation is illustrated in Figure 3.20. Here we have illustrated a data bit boundary in the coherent interval Y_ν. For the moment we assume that $(J+1)M < D$ so that, given that a bit boundary occurs in Y_ν, there are no other boundaries between $Y_{\nu-J}$ and $Y_{\nu+J}$. The effect of a data transition within Y_ν is twofold:

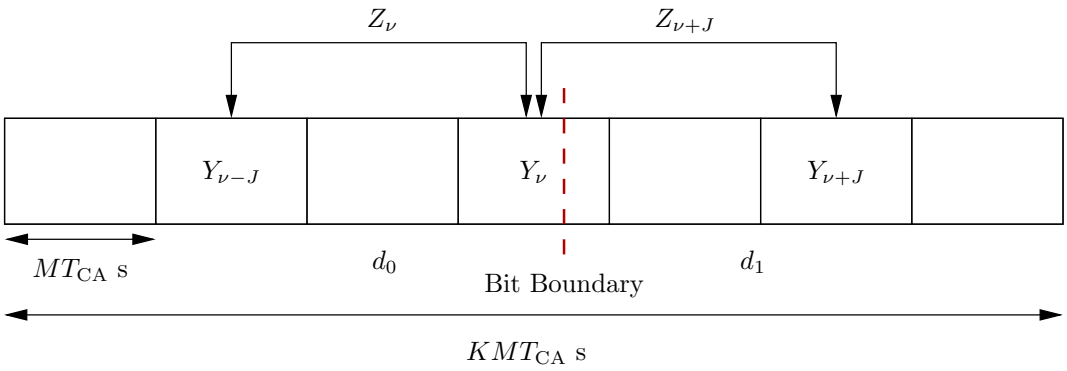


Figure 3.20: Model of Data Effects in the Differentially Coherent Combining Detector

1. The coherent output Y_ν is affected by an attenuation factor α_m defined in Equation (3.15), this affects the two summands Z_ν and $Z_{\nu+J}$.

2. The sign change affects the summands $Z_{\nu+1}, Z_{\nu+2}, \ldots, Z_{\nu+J-1}$.

Considering initially the effect on the coherent accumulator output, we have, from Equation (3.8):

$$Y_\nu = \sqrt{0.5P_k} S_{MN} \exp\left(j\phi_{k,\nu}\right) \left[d_{1,\nu} - \left(d_{1,\nu} - d_{0,\nu}\right) \frac{S_{\mu_\nu}}{S_{MN}} \right], \tag{3.97}$$

where S_r is defined in Equation (3.14), $\phi_{k,\nu}$ is the carrier phase offset at the start of the ν^{th} coherent sub-interval, μ_ν is the index of the first sample on the other side of the bit boundary in Y_ν and $d_{0,\nu}$ and $d_{1,\nu}$ are the data bits at the start and end of the sub-interval, respectively. For the moment, we assume that $J \leq \nu < K - J$. Then we have:

$$Y_r = \begin{cases} d_0 \sqrt{0.5P_k} S_{MN} \exp\left(j\phi_{k,r}\right) & \nu - J \leq r < \nu \\ d_1 \sqrt{0.5P_k} S_{MN} \exp\left(j\phi_{k,r}\right) & \nu < r \leq \nu + J\,. \end{cases} \tag{3.98}$$

Inserting Equations (3.97) and (3.98) into Equation (3.82) we obtain:

$$Z_r = 0.5P_k \left|S_{MN}\right|^2 \exp\left(j2\beta J\right) \times \begin{cases} (-1)^{t_\nu} \left(1 - 2t_\nu \frac{S_{\mu_\nu}}{S_{MN}}\right) & r = \nu \\ (-1)^{t_\nu} & \nu < r < \nu + J \\ \left(1 - 2t_\nu \frac{S_{\mu_\nu}}{S_{MN}}\right)^* & r = \nu + J\,, \end{cases} \tag{3.99}$$

where t_ν is equal to 1 if there is a bit transition in Y_ν and is zero otherwise. Now $|S_{MN}|^2 = \alpha_D(\delta\omega_d)$, so inserting Equation (3.99) into Equation (3.83), we find that, given that a bit transition occurs in Y_ν, then the component of W affected by the transition is given by:

$$\sum_{r=\nu}^{\nu+J} Z_r = 0.5P_k\alpha_D(\delta\omega_d)\exp(j2\beta J)\left\{(-1)^{t_\nu}(J+1) + 2t_\nu\left(1 + 2\Im\left\{\frac{S_{\mu_\nu}}{S_{MN}}\right\}\right)\right\}. \tag{3.100}$$

From Equation (3.14) we find:

$$\Im\left\{\frac{S_{\mu_\nu}}{S_{MN}}\right\} = -\frac{\sin(\beta[1-\delta_{T,i}])\sin\beta\delta_{T,i}}{\sin\beta}, \tag{3.101}$$

where β is defined in Equation (3.19) and δ_T is defined in Figure 3.2. Therefore, given that B boundaries occur in the observation interval, and assuming that none of these boundaries occur in the first J or last J coherent sub-intervals (which we refer to as the "end zones"), then W is given by:

$$W = 0.5P_k\alpha_D(\delta\omega_d)\exp(j2\beta J)\left\{K - J - B(J+1) + \sum_{i=0}^{B-1}\left[(-1)^{t_{\nu_i}}(J+1) + 2t_{\nu_i}\left(1 + 2\Im\left\{\frac{S_{\mu_{\nu_i}}}{S_{MN}}\right\}\right)\right]\right\}, \tag{3.102}$$

where the i^{th} boundary occurs in the coherent interval Y_{ν_i} at the sample point μ_{ν_i} (recall that μ_{ν_i} denotes the first sample of the second data bit within the i^{th} coherent observation interval). By comparison with Equation (3.84) we see that data modulation can be modelled as an attenuation factor A_m, such that, denoting by W_0 the sum of the Z_r in the absence of data modulation:

$$W = A_m W_0, \tag{3.103}$$

where:

$$A_m = 1 - \frac{1}{K-J}\left\{B(J+1) - \sum_{i=0}^{B-1}\left[(-1)^{t_{\nu_i}}(J+1) + 2t_{\nu_i}\left(1 + 2\Im\left\{\frac{S_{\mu_{\nu_i}}}{S_{MN}}\right\}\right)\right]\right\}. \tag{3.104}$$

The average attenuation can be found by taking expectation over the number of transitions B, and the location of the transitions $\delta_{T,i}$. The average value of B is

given by:

$$\overline{B} = \frac{MK}{D}, \tag{3.105}$$

and averaging Equation (3.101) over δ_T we obtain:

$$E_{\delta_T}\left[\Im\left\{\frac{S_\mu}{S_{MN}}\right\}\right] = \frac{1}{2}\left(\cot\beta - \frac{1}{\beta}\right). \tag{3.106}$$

Therefore, the average modulation attenuation, given that no transitions occur within the first J or last J coherent sub-intervals, is given by:

$$\overline{A}_m = 1 - \frac{KM}{D(K-J)}\left[J - \cot\beta + \frac{1}{\beta}\right] \tag{3.107}$$

$$\approx 1 - \frac{M}{D}\left[J - \cot\beta + \frac{1}{\beta}\right], \tag{3.108}$$

where the approximation in the last line is valid for $K \gg J$, which is generally the case in weak signal acquisition. Note that, in the above derivation, we have ignored the effect of data transitions in what we have referred to as the "end zones" of the observation interval. These are the first J and last J coherent sub-intervals. We consider briefly the effect of transitions in these zones.

If $\nu < J$ then the first summand making a contribution to the decision statistic is Z_J and the component of W affected by the bit transition is given by:

$$\sum_{r=J}^{\nu+J} Z_r = 0.5P_k\alpha_D(\delta\omega_d)\exp(j2\beta J)\left\{(-1)^{t_\nu}\nu + \left(1 - 2t_\nu\frac{S_{\mu_\nu}}{S_{MN}}\right)^*\right\}. \tag{3.109}$$

Similarly, if $\nu \geq K - J$, then the component of W affected is given by:

$$\sum_{r=\nu}^{K-1} Z_r = 0.5P_k\alpha_D(\delta\omega_d)\exp(j2\beta J)(-1)^{t_\nu}\left\{K - \nu - 2t_\nu\frac{S_{\mu_\nu}}{S_{MN}}\right\}. \tag{3.110}$$

Now, from Equation (3.14), we have:

$$\frac{S_{\mu_\nu}}{S_{MN}} = \exp(-j\beta(1-\delta_{T,\nu}))\frac{\sin\beta\delta_{T,\nu}}{\sin\beta}. \tag{3.111}$$

After some manipulation we find:

$$\overline{A}_m = 1 - \frac{KM}{D(K-J)}\left[J\frac{K+1}{K} - \frac{K-J}{K}\left(\cot\beta - \frac{1}{\beta}\right)\right], \qquad (3.112)$$

which, for $K \gg J$, is again approximately given by Equation (3.108).

Note $\overline{A}_m$ is the mean attenuation of W due to modulation effects. If the decision statistic is formed as the real part of W, then Equation (3.108) above can be used as a good approximation to the mean attenuation in the decision statistic. However, as we have discussed previously, in the presence of carrier frequency offset it is more desirable to use the square magnitude of W as the decision statistic. The average attenuation due to modulation effects in this case is found from:

$$\overline{\alpha}_m = E\big[A_m^2\big], \qquad (3.113)$$

where A_m is given in Equation (3.104). The evaluation of the expectation operation above is greatly complicated by the interdependence of the rvs ν_i, the location of the data bit boundaries. However, a simple loose lower bound can be easily determined, as follows:

$$\begin{aligned}\overline{\alpha}_m &= E\big[A_m^2\big] \\ &\leq \left(E[A_m]\right)^2 \\ &\approx \left|1 - \frac{M}{D}\left[J - \cot\beta + \frac{1}{\beta}\right]\right|^2 . \end{aligned} \qquad (3.114)$$

We can apply a similar technique to the analysis of the worst case modulation effects. Following the same procedure we used in Section 3.2.2, the worst case attenuation occurs when $t_{\nu_i} = 1$ at all bit boundaries and so, from Equation (3.104), we have:

$$A_{m\mathrm{wc}} \approx 1 - \frac{1}{K-J}\left[B(J+1) - \sum_{i=0}^{B-1}\left(-(J-1) + 2\Im\left\{\frac{S_{\mu_{\nu_i}}}{S_{MN}}\right\}\right)\right], \qquad (3.115)$$

where we have ignored the possibility of bit transitions in the end zones. We again take a limiting form for this expression as $K \to \infty$ by approximating the sum over all B bit boundaries by a, suitably scaled, sum over all T possible bit

boundary locations:

$$A_{m\text{wc}} \approx 1 - \frac{B}{K-J}\left[J - \frac{2}{T}\sum_{i=0}^{T-1}\Im\left\{\frac{S_{\mu_i}}{S_{MN}}\right\}\right], \tag{3.116}$$

where the summand is given in Equation (3.101) and $\delta_{T,i} = \overline{\delta}_{T,0} + i/T$. Performing the summation in Equation (3.116), we have:

$$\frac{1}{T}\sum_{i=0}^{T-1}\Im\left\{\frac{S_{\mu_i}}{S_{MN}}\right\} = \frac{1}{2}\left(\cot\beta - \frac{\cos\beta\left[\frac{1}{T} - 2\overline{\delta}_{T,0}\right]}{T\sin\frac{\beta}{T}}\right). \tag{3.117}$$

The worst case can be seen to occur when $\overline{\delta}_{T,0} = 1/(2T)$, leading to the following approximation for the worst case attenuation due to data modulation in the limit as $K \to \infty$:

$$A_{m\text{wc}} \approx 1 - \frac{M}{D}\left[J - \cot\beta + \frac{1}{T\sin\frac{\beta}{T}}\right]. \tag{3.118}$$

We can also derive a simple lower bound on $A_{m,\text{wc}}$, as we did for the NCCD. The worst possible attenuation occurs when $\delta_{T,i} = 1/2$ at all bit boundaries in the observation interval. In this case, we have:

$$A_{m\text{wc}} \geq 1 - \frac{M}{D}\left[J + 2\frac{\sin^2\frac{\beta}{2}}{\sin\beta}\right]. \tag{3.119}$$

If the decision statistic is generated from the square magnitude of W, then we have:

$$\alpha_{m\text{wc}} \approx \left|1 - \frac{M}{D}\left[J - \cot\beta + \frac{1}{T\sin\frac{\beta}{T}}\right]\right|^2 \tag{3.120}$$

$$\alpha_{m\text{wc}} \geq \left|1 - \frac{M}{D}\left[J + 2\frac{\sin^2\frac{\beta}{2}}{\sin\beta}\right]\right|^2. \tag{3.121}$$

Note that these bounds on performance are quite loose. In general, the determination of modulation effects on the DCCD is significantly more difficult than for the NCCD or ML detectors. This is due to the spreading of the influence of a single bit transition over multiple summands of the differentially coherent accumulator. What is evident, however, is that the DCCD (the standard form in particular) has poorer performance in the presence of data modulation than the

NCCD.

3.3.3 The Effect of Code Doppler

To analyse the effect of code Doppler on the DCCD we follow the same procedure as for the NCCD (see Section 3.2.3). Again, we assume that the effect of code Doppler within a coherent sub-interval is negligible, but that we must account for code phase drift between sub-intervals. Also, we again assume that the correlation function has an ideal, triangular shape.

Consider first of all the effect of a residual code phase offset, $\delta\zeta$, in the absence of code Doppler. The decision statistic is then given by:

$$D_k(\widehat{\boldsymbol{\theta}}) = \left[0.5(K-J)(MN)^2 P_k \alpha_s(\delta\zeta)\right]^2, \tag{3.122}$$

where α_s is as defined in Equation (3.28).

If we now introduce a residual Doppler dilation coefficient offset $\delta\eta$, then there will be a code phase drift between Y_{r-J} and Y_r, as illustrated in Figure 3.21. Note

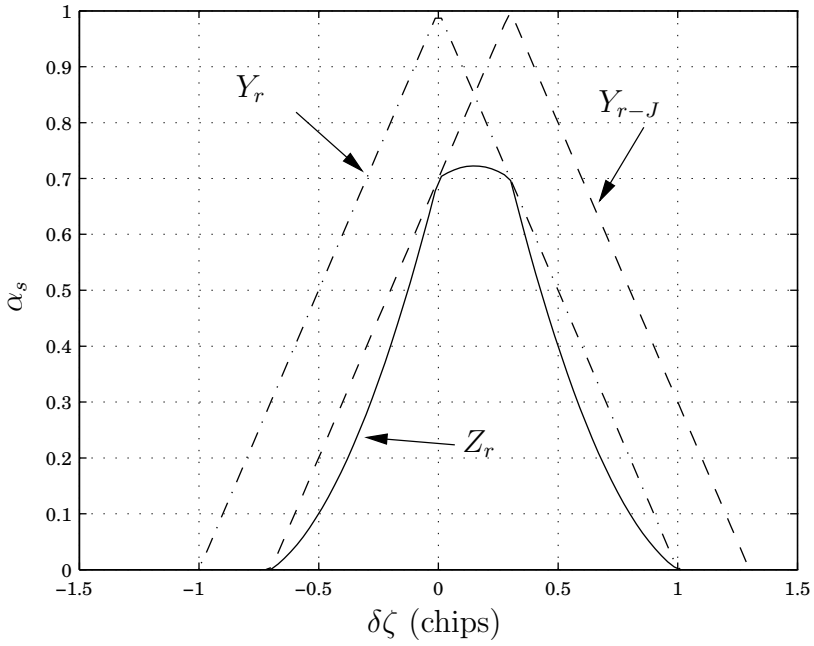


Figure 3.21: Code Doppler Effect on Summand of the DCCD.

that the problem has been greatly exaggerated in the diagram. The actual code phase shift between Y_{r-J} and Y_r is given by $J\Delta\zeta$, where $\Delta\zeta$ is the code phase drift,

in chips, over one coherent observation interval and is defined in Equation (3.36). In general, J will be small, since we have seen from Section 3.3.2 that increasing J increases sensitivity to modulation effects. In addition, $\Delta\zeta$ is usually very small, except in the presence of extremely large Doppler offsets, as we have already discussed in Section 3.1.3. Thus, in reality, the two triangles of Figure 3.21 will be almost co-incident. In this case, we can model the code Doppler effect on the DCCD as being identical to the effect on the NCCD. The power attenuation factor due to the combined effect of an initial residual code phase offset of $\delta\zeta_0$ and a residual Doppler dilation coefficient of $\delta\eta$ is thus approximately given by Equation (3.81).

This approximation is illustrated in Figure 3.22, where a coherent observation interval of 1 ms, a Doppler offset of 500 Hz and a differential delay of $J = 5$ have been used. Again, we include the two cases $K = 300$ and $K = 1000$, as we did

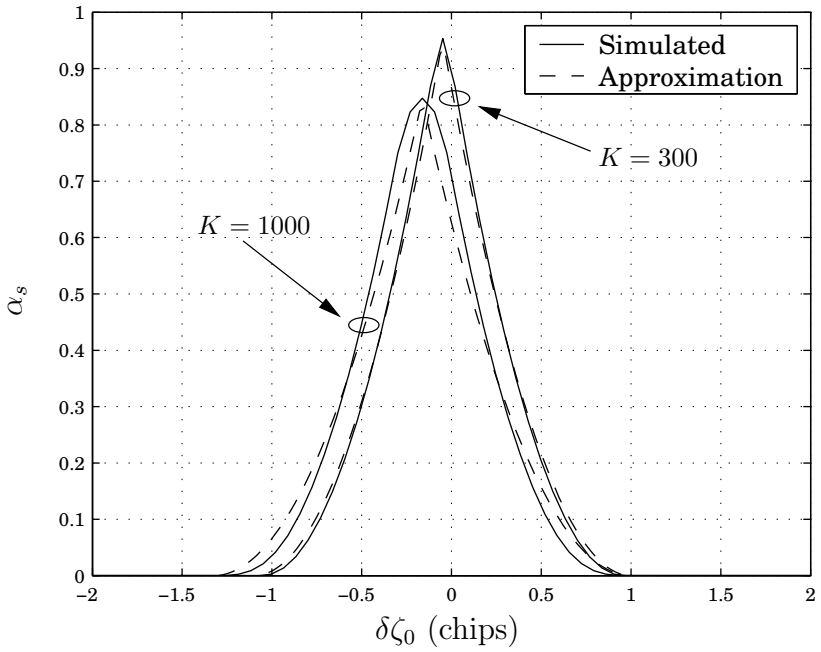


Figure 3.22: Power Attenuation Due to Code Doppler in the DCCD and the Approximation of Equation (3.81). Here $\omega_d = \pi$ krad s^{-1}, $J = 5$ and $M = 1$.

for the NCCD. The accuracy of this approximation can be seen to be about the same as it was for the NCCD: very accurate for low to moderate values of K, with increasing error as K increases.

3.4 The Differentially Coherent Detector

The differentially coherent detector is significantly different to the detector forms we have analysed to date, though it is similar in structure to the differentially coherent combining detector. The DCD structure is illustrated in Figure 3.23. This detector was discussed in Section 2.4.3, here we present a brief overview of

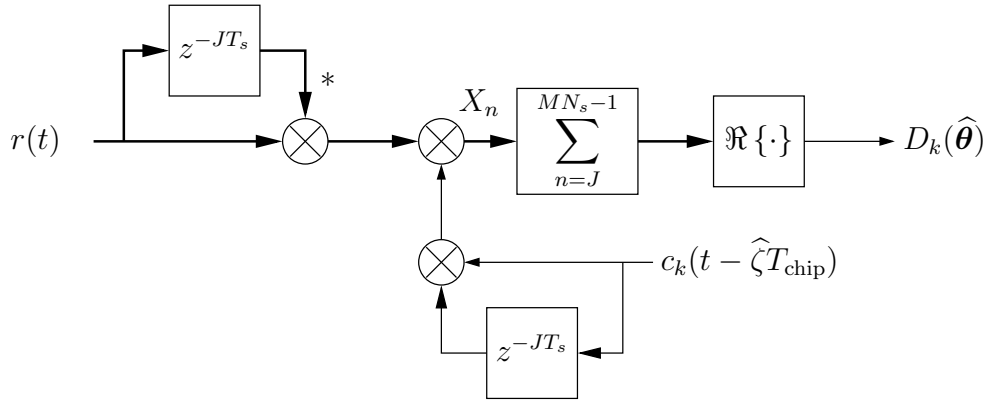


Figure 3.23: Differentially Coherent Detector

its operation in the absence of noise.

We denote by X_n the input to the coherent accumulator at time instant $t = nT_s$:

$$X_n = r_n r_{n-J}^* c_k\left(nT_s - \widehat{\zeta}T_{\text{chip}}\right) c_k\left((n-J)T_s - \widehat{\zeta}T_{\text{chip}}\right), \tag{3.123}$$

where $r_n = r_k(nT_s)$ and $r_k(t)$ is given in Equation (2.10). We denote by Y the output of the coherent accumulator:

$$Y = \sum_{n=J}^{MN_s-1} X_n. \tag{3.124}$$

Note that we again assume that the observation interval consists of an integer number M of C/A code periods (remember that N_s is the number of samples in one code period).

As discussed in Section 2.4.3, this detector relies on the shift-and-add property of Gold codes, *i.e.* the sum of a Gold code and a cyclically shifted version of itself is again a Gold code from the same family. Note, however, that we are not processing actual Gold sequences in this receiver, but rather *re-sampled* Gold sequences. Strictly speaking, for the shift-and-add property to hold, we must shift both the local and received signals by an integer number of code chips. In

the diagram above we represent the shift as an integer number of *samples*, but the signal is not sampled at the code rate. In fact, for the shift-and-add property to hold, we require the sample rate to be an exact multiple of the chip rate so that a shift by an integer number of chips can be achieved as a shift by an integer number of samples. We find in practice, however, that as long as:

$$JT_s \approx J_c T_{\text{chip}} \tag{3.125}$$

where J is an integer, then the new sequence generated by the differential product is not significantly different from a Gold sequence, so that we can assume the auto- and cross-correlation properties of the Gold sequences hold for this new sequence.

3.4.1 The Effect of a Residual Carrier Frequency Offset

Assuming, therefore, that the condition of Equation (3.125) holds, we can proceed with the performance analysis of the DCD in the absence of noise. We begin, as we did for the DCCD, under the assumption that the received signal is subject to an unknown and constant carrier frequency offset ω_d and an initial carrier phase offset of ϕ_k radians. Again, for the moment, we ignore code Doppler and code phase offset effects. The received signal r_n is then given by:

$$r_n = \sqrt{0.5P_k}c_k\left(nT_s - \zeta T_{\text{chip}}\right)\exp\left(j\left(\phi_k + \omega_d n T_s\right)\right), \tag{3.126}$$

and so the input to the coherent accumulator is given by:

$$X_n = 0.5P_k c_{k,n-d}^2 c_{k,n-J-d}^2 \exp\left(j\omega_d T_s J\right), \tag{3.127}$$

where $c_{k,n-d}$ is the re-sampled Gold sequence and $d = \zeta T_{\text{chip}}/T_s$. Now $c_{k,n} \in \{-1, +1\}$ and so we have:

$$X_n = 0.5P_k \exp\left(j\omega_d T_s J\right). \tag{3.128}$$

Inserting Equation (3.128) into Equation (3.124) yields:

$$Y = 0.5(MN_s - J)P_k \exp\left(j\omega_d T_s J\right). \tag{3.129}$$

Clearly, the larger the value of J the greater the imaginary component of Y for a given Doppler offset. It is instructive here to explore the range of values taken on by the phase of Y. For any land user the maximum Doppler frequency offset will be less than 10 kHz [128], thus:

$$|\angle Y| = |2\pi f_d J T_s| \leq 2\pi \frac{10 J_c}{L}, \tag{3.130}$$

where J_c is the number of code chips shifted and recall that $L = 1023$ is the length of the GPS C/A code in chips. Choosing the minimum value $J_c = 1$ we find:

$$\cos \angle Y \geq 0.99811. \tag{3.131}$$

This is the reason that we generate the decision statistic from the real part of Y: the loss incurred is essentially negligible. For high dynamic platforms the maximum frequency offset can be potentially much larger than 10 kHz, in which case it may be advisable to use the magnitude, or square magnitude, of Y as the decision statistic. However, for typical hand-held receiver applications, the DCD decision statistic is essentially independent of the carrier frequency error.

3.4.2 The Effect of Data Modulation

Consider now the effect of data modulation. Again we assume that the code phase estimate, ζ, is correct and ignore code Doppler effects. We start with the simple case of a single data transition within the observation interval. We assume that the transition occurs some time in the range $((\mu - 1)T_s, \mu T_s)$. The observation interval can be divided into three sub-intervals as follows:

$$\begin{aligned} &J \leq n \leq \mu - 1 && d_n = d_{n-J} \\ &\mu \leq n \leq \mu + J - 1 && d_n = -d_{n-J} \\ &\mu + J \leq n \leq MN - 1 && d_n = d_{n-J}. \end{aligned} \tag{3.132}$$

Using Equation (3.132) in Equations (3.123) and (3.124) yields:

$$\begin{aligned} Y &= 0.5 P_k \exp(j\omega_d T_s J) \left(\sum_{n=J}^{MN_s-1} 1 - 2 \sum_{n=\mu}^{\mu+J-1} 1 \right) \\ &= 0.5 P_k (MN_s - J) \exp(j\omega_d T_s J) \left(1 - \frac{2J}{MN_s - J} \right). \end{aligned} \tag{3.133}$$

Comparing this with Equation (3.129) we see that the presence of a single bit transition results in an attenuation of $\left|1 - \frac{2J}{MN_s - J}\right|$ in the decision statistic. It is also interesting to note that this attenuation is independent of the location of the bit transition within the observation interval[†]. Therefore, given a total of B bit transitions within the observation interval, we can model the effect of data modulation as a power attenuation factor:

$$\alpha_m = \left|1 - \frac{2BJ}{MN_s - J}\right|^2 . \tag{3.134}$$

Now, in MN_s code periods there will be at most $B = \lceil M/D \rceil$ data bit transitions, leading to a worst case power attenuation due to data modulation of:

$$\alpha_{mwc} = \left|1 - \left\lceil \frac{M}{D} \right\rceil \frac{2J}{MN_s - J}\right|^2 , \tag{3.135}$$

which, for small values of J, is approximately unity.

Therefore, we find that the decision statistic:

$$D_k(\widehat{\zeta}) = \Re\{W\} , \tag{3.136}$$

is, essentially, independent of data and carrier Doppler effects. This is the major advantage of the DCD.

3.4.3 The Effect of Code Doppler

The final signal effect to consider for the DCD is code Doppler. In this case we must take into account, not only the effect of code phase drift during the observation interval, but also the effect of code Doppler on the differential product. If there is a large code phase shift between the samples X_n and X_{n+J}, what will be the effect on the new code sequence formed from their product?

We denote by f_k the differential product of two re-sampled Gold codes:

$$f_k(nT_s) = c_k\left(nT_s\left[1+\eta\right] - \zeta_0 T_{\text{chip}}\right) c_k\left(\left[n-J\right]T_s\left[1+\eta\right] - \zeta_0 T_{\text{chip}}\right) . \tag{3.137}$$

[†]We ignore the possibility of a bit transition within the first J samples.

Now, by the shift and add property of Gold codes, we have:

$$c_k\left(nT_s-\zeta T_{\text{chip}}\right)c_k\left(nT_s-\left[\tau+\zeta\right]T_{\text{chip}}\right)=c'_k\left(nT_s-\zeta' T_{\text{chip}}\right)\,, \tag{3.138}$$

where τ is an integer, c'_k is another Gold code from the same family as c_k, $\zeta'=\Delta\tau+\zeta$ and $\Delta\tau$ is the delay introduced by the shift and add procedure.

From our previous discussion we want to choose J such that the number of chips shifted, defined in Equation (3.125), is as close to an integer as possible. We need to ensure that code Doppler does not cause excessive drift in J_c.

From Equation (3.137) we have:

$$f_k(nT_s)=c_k\bigg(nT_s-\zeta_n T_{\text{chip}}\bigg)c_k\bigg(nT_s-\left[\zeta_n+J_{c,n}\right]T_{\text{chip}}\bigg)\,, \tag{3.139}$$

where $J_{c,n}=J_{c,0}\left(1+\eta\right)$. Note that $J_{c,n}$ is, in fact, independent of n, depending only on the Doppler dilation coefficient η. So, to maintain the correlation properties of the Gold codes, we require $J_{c,n}$ to be close to an integer value. But $J_{c,0}$ has already been chosen with this property. Therefore, we require $1+\eta\approx 1$. Recall from Section 3.1.3 that, for a maximum Doppler offset of 10 kHz, the maximum value of η is approximately 6.3×10^{-6}. So, except in high dynamic environments, code Doppler will have a negligible effect on the form of the new Gold code generated by the differential product.

We can, therefore, assume that the input to the coherent accumulator in Figure 3.23 is the product of two Gold codes. The effect of code Doppler in this case is identical to that analysed in Section 3.1.3, except that the real part of the accumulator output is chosen as the decision statistic, rather than the magnitude. From Equation (3.48) the sampling attenuation can, therefore, be approximated by (again the total code phase drift is assumed to be less than one chip):

$$\alpha_s\left(\delta\zeta_0,\delta\eta\right)\approx\begin{cases}\left(1-\frac{|\Delta\zeta|}{4}\right)\left(1-\frac{\left|\delta\zeta_0+\frac{\Delta\zeta}{2}\right|}{1+\frac{|\Delta\zeta|}{2}}\right) & \left|\delta\zeta_0+\frac{\Delta\zeta}{2}\right|\leq 1+\left|\frac{\Delta\zeta}{2}\right| \\ 0 & \text{otherwise.}\end{cases} \tag{3.140}$$

This approximation is shown in Figure 3.24, where it is compared with simulated results. In the figure we have $M=100$ and $J_{c,0}=2$. Two cases for the Doppler

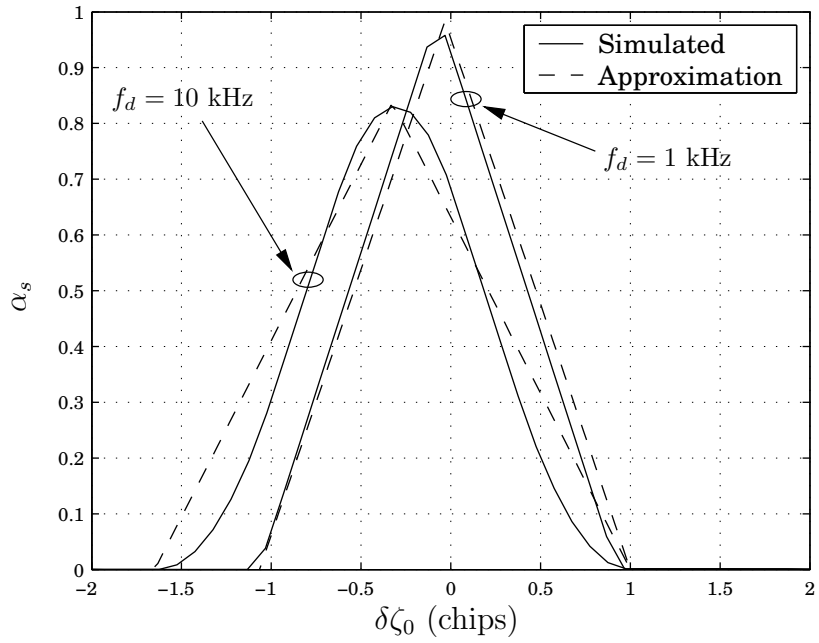


Figure 3.24: Power Attenuation Due to Code Doppler in the DCD and the Approximation of Equation (3.140). Here $J_{c,0} = 2$ and $M = 100$.

offset are shown: $f_d = 1$ kHz and $f_d = 10$ kHz. The linear approximation can be seen to be less accurate for larger Doppler offsets, though it is exact at $f_d = 0$.

3.5 Discussion

Our intention in this chapter has been to provide a quantitative assessment of signal effects on the performance of the detector/estimator. We have focused on three primary effects:

1. Carrier frequency offset,
2. Data modulation, and
3. Code phase and frequency offsets.

We have taken a systematic approach, dealing with each of the four main detector/estimator forms in turn. Each effect has been modelled as a distortion of the decision function $D_k(\widehat{\boldsymbol{\theta}})$, consisting primarily of a power attenuation factor and a bias offset term.

The effect of a carrier frequency offset on both the ML and noncoherent combining forms is well known, though, for completeness, we have provided an overview of the derivation here. In Section 3.3.1 we demonstrate that the sensitivity of the DCCD (in both the standard and pair-wise forms) to carrier Doppler is identical to that of the NCCD. A similar result can be found in [112], though it is not stated explicitly.

The GPS $L1$ C/A signal is continuously modulated by a 50 bps BPSK signal. In many other forms of DS/CDMA a pilot (data-free) signal is transmitted to assist in acquisition. For this reason, much of the literature on DS/CDMA signal acquisition ignores the effect of data modulation, though some notable early exceptions include [26, 37, 119]. Our approach, based on the approach taken in the analysis of carrier Doppler offset, is new, however. In Section 3.1.2 we derive a new expression for the effective power attenuation introduced by data modulation to the ML form (Equation (3.18). This result can be shown to be similar to an expression due to Davisson and Flikkema [37, Equation (8-5b)], though there would appear to be a typographical error in their equation. In Section 3.2.2, this new result is expanded upon in the context of the noncoherent combining detector. We have derived new expressions for the mean and worst-case modulation attenuation for various forms of receiver. In particular, an observation on the motion of the bit boundary location within the coherent sub-interval is new. This motion is shown to limit worst case modulation effects when the number of coherent sub-intervals is large. In other words, given a fixed coherent sub-interval length, the worst case data modulation attenuation is less severe for larger values of K. The average attenuation is unaffected by K. A similar observation was made by Cheng [26], though he did not quantify the effect.

The analysis of the effect of data modulation on DCCD-based acquisition has not previously been considered in the literature. In Section 3.3.2 we provide such an analysis for the case when the decision statistic is formed from the real part of the differentially coherent accumulator. This was subsequently used to provide a loose bound on the average modulation effect on the magnitude-squared decision statistic. The technique used is a modification of the methods developed in Section 3.2.2. A more exact analysis of modulation effects should be possible using a similar technique to that used in Appendix B.1.2.

Finally, we have given an analysis of the effect of code Doppler on each of the four detectors considered in this chapter. Our results provide a simple mechanism

for calculating, not only the estimation error induced by code-phase drift during the observation interval, but also the effective power attenuation introduced by code Doppler. Interestingly, one can observe that code Doppler can actually dominate over carrier Doppler in the combining detectors (NCCD and DCCD) when the number of coherent correlator outputs combined (K) is large relative to the number of code periods coherently correlated (M). This latter condition is not uncommon in the acquisition of very weak signals ($C/N_0 < 24$ dB-Hz).

Our analysis in this chapter provides us with insight into how each of the detectors considered processes the *signal* at its input. In the next chapter we turn our attention to noise performance.

Chapter 4

The Detector/Estimator II: Statistical Analysis

In the previous chapter we considered the effects of various signal parameters on the detector/estimator performance. In the present chapter we consider receiver performance in the presence of noise. We assume the signal is received through an AWGN channel which, upon down-conversion to base-band, can be represented as a complex Gaussian random process. Thus, whereas in Chapter 3 the decision statistic was modelled as a non-random variable, whose value could be determined exactly, in the following it is modelled as an rv and we must, therefore, apply a statistical analysis.

The objectives of this chapter are, therefore, to:

1. Obtain analytical expressions for the PDF of the decision statistic for each of the detector/estimator forms considered in the previous chapter,

2. Develop routines for the numerical evaluation of these PDFs (and the associated CDFs), either exactly or through approximation or bounding,

3. Compare the performance of each detector/estimator form to determine the optimal choice for a given set of design constraints.

We consider initially single cell detector forms, expanding the analysis to include parallel forms in Section 4.5. We begin, however, with an overview of the statistical noise model used throughout this chapter.

4.1 Noise Model

Consider the received signal at the output of the RF front end:

$$r'(t) = s'(t) + n'(t) \tag{4.1}$$

where the superscript denotes real signals in the IF passband, $s'(t)$ is the signal of interest, $f(t)$, modulated by some IF carrier frequency ω_{IF}:

$$s'(t) = f(t)\cos\left(\omega_{\text{IF}}t + \phi_0\right) , \tag{4.2}$$

ϕ_0 is the initial carrier phase offset of the received signal at IF and $n'(t)$ is a zero mean AWGN noise process with power (assuming a 1Ω reference resistor):

$$\sigma_0^2 = N_0 B_{\text{IF}} , \tag{4.3}$$

where N_0 is the single sided noise PSD and B_{IF} is the two-sided IF front-end filter bandwidth (note that we assume an ideal "brick-wall" front-end filter). This is illustrated in Figure 4.1. N_0, measured in W/Hz, can be calculated from:

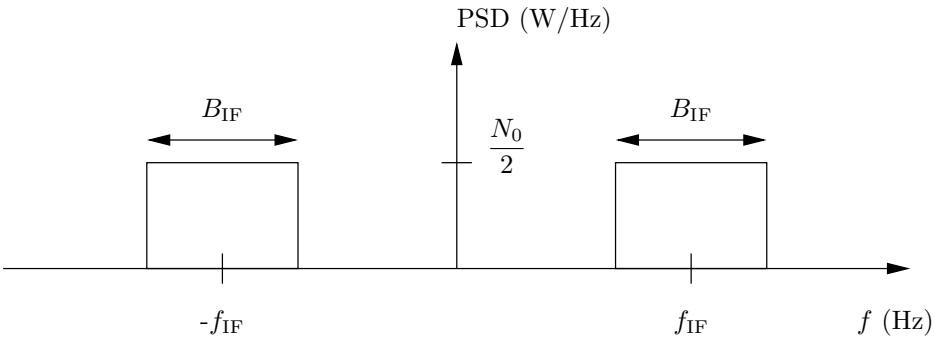


Figure 4.1: Noise Power Spectral Density

$$N_0 = k_B T_{\text{sys}} , \tag{4.4}$$

where k_B is Boltzmann's constant ($\approx 1.381 \times 10^{-23}$ $\text{WK}^{-1}\text{Hz}^{-1}$) and T_{sys} is the effective noise temperature of the receiver (in Kelvin), which can be calculated using Friis' formula [140].

To express the fact that $n(t)$ has a Gaussian (or Normal) distribution with a mean of zero and variance σ_0^2 we write:

$$n(t) \sim \mathrm{N}(\mu = 0, \sigma_0^2)\,. \tag{4.5}$$

Following Proakis [102], we use a complex base-band signal representation, which is valid provided the bandwidth of $f(t)$ is small relative to the carrier frequency. The signal $r'(t)$ is decomposed into its complex representation through multiplication by a complex exponential:

$$\begin{aligned} r(t) &= r'(t)\exp\left(-j\omega_{\mathrm{IF}}t\right) && (4.6)\\ &= 0.5f(t)\exp\left(j\phi_0\right) + n(t)\,, && (4.7) \end{aligned}$$

where $n(t)$ is a complex noise process, defined by:

$$\begin{aligned} n(t) &= n'(t)\exp\left(j\omega_{\mathrm{IF}}t\right) && (4.8)\\ &= n'(t)\cos\omega_{\mathrm{IF}}t - jn'(t)\sin\omega_{\mathrm{IF}}t && (4.9)\\ &= n_I(t) + jn_Q(t) && (4.10) \end{aligned}$$

and we have ignored double frequency terms. Note that $n_I(t)$ and $n_Q(t)$ are zero-mean, independent, AWGN processes with variance:

$$\sigma_I^2 = \sigma_Q^2 = \frac{\sigma_0^2}{2}\,, \tag{4.11}$$

i.e.:

$$n_{I,Q} \sim \mathrm{N}\left(0, \frac{\sigma_0^2}{2}\right)\,. \tag{4.12}$$

The random process $r(t)$ is then said to have a complex Gaussian distribution, with (complex) mean $\mu(t) = 0.5f(t)\exp\left(j\phi_0\right)$ and variance:

$$\begin{aligned} \mathrm{Var}\left[r(t)\right] &\triangleq E_{n(t)}[\left(r(t)-\mu(t)\right)\left(r(t)-\mu(t)\right)^*] && (4.13)\\ &= \sigma_0^2\,. && (4.14) \end{aligned}$$

We represent this as follows:

$$r(t) \sim \widetilde{\mathrm{N}}\left(\mu, \sigma_0^2\right)\,. \tag{4.15}$$

In this thesis we consider only all-digital receivers in which N equally spaced observations of the random process $r(t)$ are made, resulting in the observation vector $\boldsymbol{r}$:

$$\boldsymbol{r} = [r(0), r(T_s), \ldots, r([N-1]T_s)]^{\mathrm{T}} . \tag{4.16}$$

We denote by $\boldsymbol{Y}$ the multi-dimensional complex Gaussian rv of which $\boldsymbol{r}$ is a sample. The distribution of this rv was first defined by Wooding in 1956 for the zero-mean case [151]. Turin [138] gives the following expression for the distribution for arbitrary (complex) mean $\boldsymbol{\mu}$:

$$f_{\boldsymbol{Y}}(\boldsymbol{y}) = \pi^{-N} |\boldsymbol{C}|^{-1} \exp\left(- (\boldsymbol{y}-\boldsymbol{\mu})^{\mathrm{H}} \boldsymbol{C}^{-1} (\boldsymbol{y}-\boldsymbol{\mu}) \right) , \tag{4.17}$$

where $\boldsymbol{C}$ is the covariance matrix of $\boldsymbol{Y}$ defined by:

$$\boldsymbol{C} \triangleq E_{\boldsymbol{Y}}\Big[(\boldsymbol{y}-\boldsymbol{\mu}) (\boldsymbol{y}-\boldsymbol{\mu})^{\mathrm{H}} \Big], \tag{4.18}$$

$|\boldsymbol{C}|$ denotes the determinant of $\boldsymbol{C}$ and $\boldsymbol{x}^{\mathrm{H}}$ denotes the combined operations of transposition and complex conjugation of the vector $\boldsymbol{x}$, known as the *Hermitian transpose*, or simply the Hermitian. To indicate that $\boldsymbol{Y}$ has an N-dimensional complex normal distribution we write:

$$\boldsymbol{Y} \sim \widetilde{\mathrm{N}}_N (\boldsymbol{\mu}, \boldsymbol{C}) . \tag{4.19}$$

Thus, returning to our signal observation vector r, we find:

$$\boldsymbol{\mu} = \boldsymbol{s} \tag{4.20}$$

$$\boldsymbol{C} = \sigma_0^2 \boldsymbol{I} , \tag{4.21}$$

where $\boldsymbol{s}$ is given by:

$$\boldsymbol{s} \triangleq 0.5 \exp(j\phi_0) [f(0), f(T_s), \ldots, f([N-1]T_s)]^{\mathrm{T}} , \tag{4.22}$$

and $\boldsymbol{I}$ is the $N \times N$ identity matrix. The signal at the input to the detector/ estimator is, therefore, completely characterised by Equations (4.17), (4.20) and (4.21).

4.2 The Noncoherent Combining Detector

It is well known that the output of the noncoherent combining detector follows a χ^2 distribution with K degrees of freedom and non-centrality parameter $\lambda = \boldsymbol{\mu}^{\mathrm{H}}\boldsymbol{\mu}$ [140]. Thus, given:

$$D_k = \sum_{i=0}^{K-1} |Y_i|^2 , \tag{4.23}$$

where Y_i is the i^{th} output of the coherent accumulator, then the distribution of D_k is given by [102]:

$$f_{D_k|H_0}(x \mid H_0) = \frac{1}{2\sigma_Y^2} \frac{1}{\Gamma(K)} \left(\frac{x}{2\sigma_Y^2}\right)^{K-1} \exp\left(-\frac{x}{2\sigma_Y^2}\right) \tag{4.24}$$

$$f_{D_k|H_1}(x \mid H_1) = \frac{1}{2\sigma_Y^2} \left(\frac{x}{\lambda}\right)^{\frac{K-1}{2}} \exp\left(-\frac{x+\lambda}{2\sigma_Y^2}\right) I_{K-1}\left(\frac{\sqrt{x\lambda}}{\sigma_Y^2}\right), \tag{4.25}$$

where σ_Y^2 is the noise power in the quadrature components at the output of the coherent accumulator and is defined in Equation (2.31). Similarly, the tail probabilities are given by [102]:

$$P_{fa} = \widetilde{\Gamma}_K\left(\frac{V_{\text{Th}}}{2\sigma_Y^2}\right) \tag{4.26}$$

$$P_d = Q_K\left(\frac{\sqrt{\lambda}}{\sigma_Y}, \frac{\sqrt{V_{\text{Th}}}}{\sigma_Y}\right), \tag{4.27}$$

where $\widetilde{\Gamma}_K(x)$ is the regularised upper incomplete Gamma function, defined in Equation (2.64) and $Q_K(a,b)$ is the generalised Marcum Q-function, defined in Equation (2.43). Note that the dependence of P_d on the signal component is entirely contained in the quantity λ, for which we can write:

$$\lambda = \boldsymbol{\mu}^{\mathrm{H}}\boldsymbol{\mu}, \tag{4.28}$$

which is exactly the form of the decision statistic in the absence of noise. Thus, our treatment of signal effects on the decision statistic from Chapter 3 can be applied directly to Equation (4.27). For instance, to determine the effect of Doppler offset on P_d, we can substitute the expression for $D_k(\widehat{\boldsymbol{\theta}})$ of Equation (3.52) for λ.

The complement of $\widetilde{\Gamma}_K(x)$, defined by:

$$\widetilde{\gamma}_K(x) \triangleq 1 - \widetilde{\Gamma}_K(x), \tag{4.29}$$

and known as the regularised lower incomplete Gamma function, is implemented in most common computer numerical software systems (for example, in Matlab^{TM} it is implemented as `gammainc(x,K)`). Similarly, $\widetilde{\Gamma}_K(x)$ is implemented in Mathematica^{TM} as `GammaRegularized[K,x]`. The Marcum Q-function has greater computational complexity than the incomplete Gamma functions (particularly for large K) and is less commonly implemented. The Matlab^{TM} add-on "Communications Toolbox" [136] does include an implementation, `marcumq(a,b,K)`, based on the series expansions of Cantrell and Ojha [23] and Shnidman [117]. These approaches suffer from lack of accuracy and slow convergence for large values of K. In the following we use a saddle-point integration technique developed by Helstrom [53], which is accurate even for large values of K, and is particularly efficient in the tails of the distribution (*i.e.* away from the mean).

4.2.1 Approximations and Bounds

Due, in particular, to the computational complexity of the Marcum Q-function, much research has been conducted into approximations and bounds on the performance of the NCCD. The simplest approach is to approximate the distribution of the χ^2 rv with a Gaussian distribution whose mean and variance are given by the mean and variance of the χ^2 rv. This approach is common in statistics, and can be applied in a wide variety of circumstances due to the central limit theorem [92]:

Theorem 4.1 (Central Limit Theorem) *The distribution of the sum of n statistically independent random variables with finite mean and variance approaches a Gaussian distribution as $n \to \infty$.*

Thus, as K increases, the Gaussian approximation to the non-central χ^2 distribution becomes more accurate. This Gaussian approximation can be thought of as a curve-fitting approach, with two free parameters: the mean and variance of the distribution. The resulting approximation is quite accurate near the mean of the distribution, but loses accuracy in the tails. Unfortunately, in signal detection problems, we are more interested in operating in the tails of the distribution

rather than near the mean (in practice, a value of P_d in the region of 0.9 is considerably more desirable than one in the region of 0.5).

Various other Gaussian (and non-Gaussian, though we don't consider them here) approximations, which are more accurate in the tails of the distribution, have been developed in the literature [64, 67, 94, 110]. Patnaik [94] showed that the square root of the χ^2 rv approaches normality at a faster rate than the χ^2 rv itself. He used this to derive the following approximation to the Marcum Q-function:

$$Q_K(a,b) \approx \frac{1}{2}\mathrm{erfc}\left(\frac{1}{\sqrt{2}}\left[\sqrt{\frac{b^2(2K+a^2)}{K+a^2}} - \sqrt{\frac{(2K+a^2)^2}{K+a^2} - 1}\right]\right), \tag{4.30}$$

where $\mathrm{erfc}(x) = 1 - \mathrm{erf}(x)$ is the complementary error function and $\mathrm{erf}(x)$ was defined in Equation (2.77). This approximation is more accurate at small values of K than the standard (moment matching) Gaussian approximation. In [67] Johnson derived an interesting Gaussian approximation based on the observation that the CDF of a non-central χ^2 distributed rv is equivalent to the CDF of the difference of two Poisson distributed rvs. This leads to the following approximation:

$$Q_K(a,b) \approx \frac{1}{2}\mathrm{erf}\left(\frac{2K - 1 - b^2 + a^2}{2\sqrt{a^2+b^2}}\right), \tag{4.31}$$

which, according to Johnson, appears to be more accurate than Patnaik's approximation. Finally, Sankaran [110] (and, later, Jensen and Solomon [64]) applied a technique known as a "Wilson–Hilferty transform" [72] to transform the χ^2 rv to a new rv which is more closely Gaussian. Given the non-central χ^2 distributed rv, X, with N degrees of freedom and non-centrality parameter λ, for which we write[†]:

$$X \sim \chi'^2(N,\lambda),$$

this approach is to generate a new rv, Y, as:

$$Y = \left(\frac{X}{N+\lambda}\right)^h,$$

[†]We use the symbol χ'^2 to denote the non-central χ^2 distribution, this notation is in keeping with the statistical literature.

where h is a free parameter, chosen to make Y as close to a Gaussian rv as possible. Sankaran showed that the best choice of h is given by:

$$h = 1 - \frac{2}{3}\frac{(N+\lambda)(N+3\lambda)}{(N+2\lambda)^2}\,. \tag{4.32}$$

Letting $N = 2K$ leads to the following approximation to the Marcum Q-function:

$$Q_K(a,b) \approx \frac{1}{2}\mathrm{erfc}\left(\frac{\left(\frac{b^2}{2K+a^2}\right)^h - \mu_Y}{\sqrt{2\,\mathrm{Var}[Y]}}\right), \tag{4.33}$$

where μ_Y and $\mathrm{Var}[Y]$ are approximations to the mean and variance of Y, respectively, given by:

$$\mu_Y = 1 + h(h-1)\frac{\kappa_2}{2\kappa_1^2} - h(h-1)(2-h)(1-3h)\frac{\kappa_2^2}{8\kappa_1^4} \tag{4.34}$$

$$\mathrm{Var}[Y] = \frac{h^2\kappa_2}{\kappa_1^2}\left(1 - \frac{(1-h)(1-3h)\kappa_2}{4\kappa_1^2}\right)^2 \tag{4.35}$$

$$\kappa_n = 2^{n-1}(n-1)!(2K+n\lambda) \tag{4.36}$$

and κ_n is called the n^{th} *cumulant* of X.

Sankaran's approximation is the most accurate of the above, but is also the most complicated. Thirteen years after Sankaran's paper, Jensen and Solomon [64] derived the same result, though they included only the first two terms of Equation (4.34) and only the first term of Equation (4.35), leading to a less accurate, but simpler, Gaussian approximation.

Bounds

The Chernoff bound is a tight, exponential bound on the tail probability of an rv [102, Section 2.1.5]. The Chernoff bound on the non-central χ^2 distribution seems to have been first derived by Rappaport in 1971 [104], and can be expressed as follows:

$$Q_K(a,b)\begin{cases} \leq (1-2\lambda)^{-K}\exp\left(-\lambda b^2\right)\exp\left(\frac{\lambda K a^2}{1-2\lambda}\right) & b^2 > K(a^2+2) \\ \geq 1-(1-2\lambda)^{-K}\exp\left(-\lambda b^2\right)\exp\left(\frac{\lambda K a^2}{1-2\lambda}\right) & b^2 < K(a^2+2), \end{cases} \tag{4.37}$$

where λ is the Chernoff parameter[†], given by [121, Equation (15)]:

$$\lambda = \frac{1}{2}\left(1 - \frac{K}{b^2} - \frac{K}{b^2}\sqrt{1 + \frac{a^2 b^2}{K}}\right) . \tag{4.38}$$

A tighter "exponential-type" upper bound, derived by Simon and Alouini [121], is given by:

$$\begin{aligned} Q_K(a,b) \leq & \exp\left(-\frac{(b-a)^2}{2}\right) + \frac{1}{\pi}\left[\exp\left(-\frac{(b-a)^2}{2}\right) - \exp\left(-\frac{(b+a)^2}{2}\right)\right] \\ & \times \left(\frac{b}{a}\right)^{K-1}\left(\frac{1-\left(\frac{a}{b}\right)^{K-1}}{1-\frac{a}{b}}\right) \quad b > a. \end{aligned} \tag{4.39}$$

4.3 Differentially Coherent Signal Processing

In Chapter 2 we introduced two commonly used differentially coherent receivers: 1) the differentially coherent combining detector (DCCD); and 2) the differentially coherent detector (DCD). In each case, the decision statistic is formed from the accumulation of what we have termed "differential products" of complex Gaussian rvs. In this section we develop a new analysis of this differentially coherent processing, based on the work of Jeong et al. [65] which is, in turn, based on a result due to Turin [138]. Note, however, that Jeong et al. used Barrett's [18] expression for the PDF of the multi-variate complex Gaussian distribution, which we have shown to be incorrect when $\boldsymbol{\mu} \neq \mathbf{0}$.

We are interested in the statistics of the random variable $Z = Z_I + jZ_Q$ formed as follows (we consider initially the case $J = 1$):

$$Z = \sum_{i=1}^{N-1} Y_i Y_{i-1}^* , \tag{4.40}$$

where $\boldsymbol{Y} = [Y_0, Y_1, \ldots, Y_{N-1}]$ is the N-dimensional complex Gaussian rv discussed in Section 4.1. The technique that we use is based on that of Jeong et al. [65] who made the observation that we can define the *Hermitian* matrices[‡] $\boldsymbol{Q_I}$ and

[†]Although not used further here, it is important to note that the Chernoff parameter λ is *not* the same as the non-centrality parameter λ.

[‡]A matrix $\boldsymbol{A}$ is Hermitian if it satisfies the property $\boldsymbol{A}^{\mathrm{H}} = \boldsymbol{A}$.

$\boldsymbol{Q_Q}$ such that:

$$Z = \boldsymbol{Y}^{\mathrm{H}}\boldsymbol{Q_I}\boldsymbol{Y} + j\boldsymbol{Y}^{\mathrm{H}}\boldsymbol{Q_Q}\boldsymbol{Y} \tag{4.41}$$

$$= Z_I + jZ_Q, \tag{4.42}$$

where:

$$\boldsymbol{Q_I} = \frac{1}{2}\begin{pmatrix} 0 & 1 & 0 & \cdots & 0 \\ 1 & 0 & 1 & \ddots & \vdots \\ 0 & 1 & 0 & \ddots & 0 \\ \vdots & \ddots & \ddots & \ddots & 1 \\ 0 & \cdots & 0 & 1 & 0 \end{pmatrix} \tag{4.43}$$

$$\boldsymbol{Q_Q} = \frac{j}{2}\begin{pmatrix} 0 & -1 & 0 & \cdots & 0 \\ 1 & 0 & -1 & \ddots & \vdots \\ 0 & 1 & 0 & \ddots & 0 \\ \vdots & \ddots & \ddots & \ddots & -1 \\ 0 & \cdots & 0 & 1 & 0 \end{pmatrix}. \tag{4.44}$$

We then consider the joint distribution of the pair of *real* rvs: Z_I and Z_Q. From [138] we have the following expression for the joint characteristic function:

$$\Phi_{Z_I,Z_Q}(j\omega, j\nu) = E_{\boldsymbol{Y}}[\exp(j\omega z_I + j\nu z_Q)] \tag{4.45}$$

$$= E_{\boldsymbol{Y}}\left[\exp\left(j\boldsymbol{y}^{\mathrm{H}}\left[\omega\boldsymbol{Q_I} + \nu\boldsymbol{Q_Q}\right]\boldsymbol{y}\right)\right]. \tag{4.46}$$

Using Turin's technique, it can then be shown that:

$$\Phi_{Z_I,Z_Q}(j\omega, j\nu) = |\boldsymbol{P}|^{-1}\exp\left(-\boldsymbol{\mu}^{\mathrm{H}}\boldsymbol{C}^{-1}\left[\boldsymbol{I} - \boldsymbol{P}^{-1}\right]\boldsymbol{\mu}\right), \tag{4.47}$$

where, for notational convenience, we have introduced the matrix $\boldsymbol{P}$ (note that $\boldsymbol{P}$ is independent of $\boldsymbol{\mu}$):

$$\boldsymbol{P} = \boldsymbol{I} - j\boldsymbol{C}\left[\omega\boldsymbol{Q_I} + \nu\boldsymbol{Q_Q}\right]. \tag{4.48}$$

Thus, we have an expression for the joint characteristic function of the variables Z_I and Z_Q. To determine the joint PDF we can use the Fourier inversion formula:

$$f_{Z_I,Z_Q}(z_I, z_Q) = \left(\frac{1}{2\pi}\right)^2 \int_{-\infty}^{\infty}\int_{-\infty}^{\infty} \Phi_{Z_I,Z_Q}(j\omega, j\nu) \exp\left(-j\omega z_I - j\nu z_Q\right) d\,\omega\, d\,\nu. \tag{4.49}$$

In the following we will be interested in generating a decision statistic D from the observation of the complex rv Z. The three most common forms of D are given by:

$$D = \Re\{Z\} \tag{4.50}$$

$$D = |Z| \tag{4.51}$$

$$D = |Z|^2. \tag{4.52}$$

The first form is the *marginal* PDF of Z_I and can be found by averaging Equation (4.49) over z_Q [92]. To determine the other two forms we define two new rvs, R and Θ, by the relationships:

$$Z_I = R\cos\Theta \tag{4.53}$$

$$Z_Q = R\sin\Theta. \tag{4.54}$$

From [92] we have the relationship:

$$f_{Z_I,Z_Q}(z_I, z_Q) = \frac{f_{R,\Theta}(r,\theta)}{|\boldsymbol{J}|}, \tag{4.55}$$

where $\boldsymbol{J}$ is the *Jacobian* matrix of the change of variables, given by:

$$\boldsymbol{J} \triangleq \begin{pmatrix} \frac{\partial Z_I}{\partial R} & \frac{\partial Z_I}{\partial \Theta} \\ \frac{\partial Z_Q}{\partial R} & \frac{\partial Z_Q}{\partial \Theta} \end{pmatrix}. \tag{4.56}$$

From this we see that $|\boldsymbol{J}| = R$, and so we have:

$$f_{R,\Theta}(r,\theta) = r\, f_{Z_I,Z_Q}(r\cos\theta, r\sin\theta). \tag{4.57}$$

Now, R is the magnitude of the complex rv Z, which is exactly the form of the

decision statistic required in Equation (4.51). To determine the PDF of R alone we average Equation (4.57) over Θ:

$$f_R(r) = \int_{-\pi}^{\pi} f_{R,\Theta}(r,\theta) d\,\theta \tag{4.58}$$

$$= \frac{r}{(2\pi)^2} \int_{-\infty}^{\infty}\int_{-\infty}^{\infty} \Phi_{Z_I,Z_Q}(j\omega, j\nu) \int_{-\pi}^{\pi} e^{-jr(\omega\cos\theta+\nu\sin\theta)} d\,\theta\, d\,\omega\, d\,\nu. \tag{4.59}$$

The technique used by Jeong et al. [65] is essentially to transform the two-dimensional Fourier transform represented above, to a *Hankel* transform. To achieve this the variables ρ and ϕ are introduced by the relationships:

$$\omega = \rho\cos\phi \tag{4.60}$$

$$\nu = \rho\sin\phi, \tag{4.61}$$

from which we get $d\omega d\nu = \rho d\rho d\phi$. Then we have:

$$f_R(r) = \frac{r}{(2\pi)^2} \int_{0}^{\infty}\int_{-\pi}^{\pi} \rho\Phi_{Z_I,Z_Q}(j\rho\cos\phi, j\rho\sin\phi) \int_{-\pi}^{\pi} e^{-jr\rho\cos(\theta-\phi)} d\,\theta\, d\,\phi d\,\rho. \tag{4.62}$$

Now, the integral over θ evaluates to $2\pi J_0(r\rho)$, where $J_\nu(z)$ is the Bessel function of the first kind of order ν, defined by [13]:

$$J_\nu(z) \triangleq \sum_{k=0}^{\infty} \frac{(-1)^k}{\Gamma(k+\nu+1)\,k!} \left(\frac{z}{2}\right)^{2k+\nu}. \tag{4.63}$$

Thus, we have [65, Equation (29)]:

$$f_R(r) = \frac{r}{2\pi} \int_{0}^{\infty}\int_{-\pi}^{\pi} \rho J_0(r\rho)\,\Phi_{Z_I,Z_Q}(j\rho\cos\phi, j\rho\sin\phi)\, d\,\phi\, d\,\rho. \tag{4.64}$$

Note that this expression is quite general, and valid for any characteristic function $\Phi_{Z_I,Z_Q}(j\rho\cos\phi, j\rho\sin\phi)$. We are particularly interested in determining $f_R(r)$ when the characteristic function is given by Equation (4.47). The most common case, and the only one that we consider, is the case of independent and identically distributed samples. This gives us a particularly simple form for the covariance

matrix:

$$\boldsymbol{C} = \sigma_0^2 \boldsymbol{I}. \tag{4.65}$$

To simplify the notation we define:

$$\sigma^2 \triangleq \frac{\sigma_0^2}{2}, \tag{4.66}$$

which can be seen, on comparison with Equation (4.11), to be equal to the noise variance of the in-phase or quadrature component of Y.

As in previous chapters, we consider two forms of differentially coherent processing:

The standard form This is a generalisation of the most common form found in the literature. Typically, the differentially coherent product is taken using successive samples. A more general form can be considered, in which the variable Z is generated as follows:

$$Z = \sum_{i=J}^{N-1} Y_i Y_{i-J}^*,$$

where J is the integer number of samples separating the components of the differentially coherent product. Note that we require $N \geq J$ so that all samples in the observation vector are used in Z. The statistics of Z are difficult to evaluate due to the fact that each sample is used twice (except for the first J and last J).

The pair-wise form This form was recently suggested by Ávila-Rodríguez et al. [16]. Samples are considered in pairs, and no sample is used more than once. This considerably simplifies the analysis. In this case, Z is generated as follows:

$$Z = \sum_{i=0}^{\frac{N}{2}-1} Y_{2i+1} Y_{2i}^*.$$

Note that N must always be even.

Due to its relative simplicity, we consider the pair-wise form first.

4.3.1 The Pair-wise Form

Using the same approach as Jeong et al. [65], we define the matrices $\boldsymbol{Q_I}$ and $\boldsymbol{Q_Q}$. Denoting by ${}_2\boldsymbol{Q_I}$ the matrix $\boldsymbol{Q_I}$ of Equation (4.43) with $N = 2$, then it can be shown that, for the pair-wise case, we have:

$$\boldsymbol{Q_I} = \begin{pmatrix} {}_2\boldsymbol{Q_I} & \mathbf{0}_{2\times 2} & \cdots & \mathbf{0}_{2\times 2} \\ \mathbf{0}_{2\times 2} & {}_2\boldsymbol{Q_I} & \ddots & \vdots \\ \vdots & \ddots & \ddots & \mathbf{0}_{2\times 2} \\ \mathbf{0}_{2\times 2} & \cdots & \mathbf{0}_{2\times 2} & {}_2\boldsymbol{Q_I} \end{pmatrix}, \tag{4.67}$$

where $\mathbf{0}_{i\times j}$ is the $i \times j$ matrix of zeros. Similarly, denoting by ${}_2\boldsymbol{P}$ the matrix $\boldsymbol{P}$ defined in Equation (4.48) with $N = 2$, then we have:

$$\boldsymbol{P} = \begin{pmatrix} {}_2\boldsymbol{P} & \mathbf{0}_{2\times 2} & \cdots & \mathbf{0}_{2\times 2} \\ \mathbf{0}_{2\times 2} & {}_2\boldsymbol{P} & \ddots & \vdots \\ \vdots & \ddots & \ddots & \mathbf{0}_{2\times 2} \\ \mathbf{0}_{2\times 2} & \cdots & \mathbf{0}_{2\times 2} & {}_2\boldsymbol{P} \end{pmatrix}. \tag{4.68}$$

The determinant of the matrix $\boldsymbol{P}$, which we denote $P_N(\rho, \phi)$, is of particular interest, as it entirely defines the characteristic function in the absence of signal. From the diagonal structure of $\boldsymbol{P}$ we have:

$$|\boldsymbol{P}| \stackrel{\Delta}{=} P_N(\rho, \phi) = |{}_2\boldsymbol{P}|^{\frac{N}{2}}.$$

Now, the matrix ${}_2\boldsymbol{P}$ is given by:

$${}_2\boldsymbol{P} = \begin{pmatrix} 1 & -j\rho\sigma^2 e^{-j\phi} \\ -j\rho\sigma^2 e^{j\phi} & 1 \end{pmatrix}, \tag{4.69}$$

so that $|{}_2\boldsymbol{P}| = 1 + (\rho\sigma^2)^2$. From this we can immediately find the determinant of $\boldsymbol{P}$:

$$P_N(\rho, \phi) = \left(1 + \left(\rho\sigma^2\right)^2\right)^{\frac{N}{2}}. \tag{4.70}$$

Noting that this is, in fact, independent of ϕ, we shall henceforth simply write $P_N(\rho)$. The inverse of $\boldsymbol{P}$ is also easily determined:

$$\boldsymbol{P}^{-1} = \begin{pmatrix} {}_2\boldsymbol{P}^{-1} & \mathbf{0}_{2\times 2} & \cdots & \mathbf{0}_{2\times 2} \\ \mathbf{0}_{2\times 2} & {}_2\boldsymbol{P}^{-1} & \ddots & \vdots \\ \vdots & \ddots & \ddots & \mathbf{0}_{2\times 2} \\ \mathbf{0}_{2\times 2} & \cdots & \mathbf{0}_{2\times 2} & {}_2\boldsymbol{P}^{-1} \end{pmatrix}, \tag{4.71}$$

and ${}_2\boldsymbol{P}^{-1}$ is given by:

$${}_2\boldsymbol{P}^{-1} = \frac{1}{1+(\rho\sigma^2)^2} \begin{pmatrix} 1 & j\rho\sigma^2 e^{-j\phi} \\ j\rho\sigma^2 e^{j\phi} & 1 \end{pmatrix}. \tag{4.72}$$

The Noise Alone Case

In this case, the mean value vector is identically zero: $\boldsymbol{\mu} = \mathbf{0}$. The joint characteristic function of Z_I and Z_Q in terms of ρ and ϕ is then given by:

$$\Phi_{Z_I,Z_Q}\left(j\rho\cos\phi, j\rho\sin\phi\right) = \frac{1}{\left[1+(\rho\sigma^2)^2\right]^{\frac{N}{2}}}. \tag{4.73}$$

We begin with the determination of the statistics of Z_I, the real part of the differentially coherent sum. This was the decision statistic chosen by Ávila-Rodríguez et al. in their original introduction of the pair wise form [15, 16]. The CHF of Z_I is given by substituting $\nu = 0$ in Equation (4.45), which is equivalent to setting $\phi = 0$ in Equation (4.73) above:

$$\Phi_{Z_I}\left(j\omega\right) = \frac{1}{\left[1+(\omega\sigma^2)^2\right]^{\frac{N}{2}}}. \tag{4.74}$$

This is identical to the expression given in (for example) [16, Equation (17)]. The PDF is subsequently obtained by applying the Fourier inversion formula to Equation (4.74) to yield [16, Equation (18)]:

$$f_{Z_I}(z_I) = \frac{1}{\sigma^2}\left(\frac{|z_I|}{2\sigma^2}\right)^{\frac{N-1}{2}} \frac{K_{\frac{N-1}{2}}\left(\frac{|z_I|}{\sigma^2}\right)}{\sqrt{\pi}\Gamma\left(\frac{N}{2}\right)}, \tag{4.75}$$

where we recall that $K_N(x)$ denotes the modified Bessel function of the second kind of order N.

Turning our attention now to the distribution of the magnitude, R, of Z, we insert Equation (4.73) into Equation (4.64). There is no dependence on ϕ, so the integral over ϕ evaluates to 2π, resulting in the following expression:

$$f_R(r) = r \int_0^\infty \frac{\rho J_0(r\rho)}{[1+(\rho\sigma^2)^2]^{\frac{N}{2}}} d\rho. \tag{4.76}$$

Now, the above form may be identified as the zeroth order Hankel transform of the denominator term. From tables of Hankel transforms we obtain [87, Entry (4.23)]:

$$f_R(r) = \frac{2}{\sigma^2}\left(\frac{r}{2\sigma^2}\right)^{\frac{N}{2}} \frac{K_{\frac{N}{2}-1}\left(\frac{r}{\sigma^2}\right)}{\Gamma\left(\frac{N}{2}\right)}. \tag{4.77}$$

Integrating Equation (4.76) over r and interchanging the order of integration, a similar methodology can be employed to obtain the following expression for the CDF:

$$F_R(r) = 1 - 2\left(\frac{r}{2\sigma^2}\right)^{\frac{N}{2}} \frac{K_{\frac{N}{2}}\left(\frac{r}{\sigma^2}\right)}{\Gamma\left(\frac{N}{2}\right)}. \tag{4.78}$$

It is interesting to note that this distribution, known as the *K-distribution*, arises frequently in the field of radar and sonar scattering from the ocean surface [63]. The functional forms above are difficult to calculate for large values of N due to the presence of the modified Bessel function. Gordon and Ritcey [47] present a saddle-point integration method which is easy to implement and accurate (particularly in the tails of the distribution) for all values of N.

Thus, we have expressions for the PDF and CDF of the magnitude form of the decision statistic for the pair-wise form in the absence of signal. In practice, it is often preferable to compute the square magnitude form, due to the presence of the square root operation in the magnitude form. The statistics of R^2 are easily

derived from Equations (4.77) and (4.78), to yield:

$$f_{R^2}(x) = \frac{1}{2\sigma^4}\left(\frac{x}{4\sigma^4}\right)^{\frac{N-2}{4}} \frac{K_{\frac{N}{2}-1}\left(\frac{\sqrt{x}}{\sigma^2}\right)}{\Gamma\left(\frac{N}{2}\right)} \tag{4.79}$$

$$F_{R^2}(x) = 1 - 2\left(\frac{x}{4\sigma^4}\right)^{\frac{N}{4}} \frac{K_{\frac{N}{2}}\left(\frac{\sqrt{x}}{\sigma^2}\right)}{\Gamma\left(\frac{N}{2}\right)}. \tag{4.80}$$

It is interesting to note that the following expression for the CHF of the K-distribution was recently derived by Iskander [62]:

$$\Phi_R(j\omega) = \frac{1}{N+1}\left(\frac{2}{1-j\omega\sigma^2}\right)^N {}_2F_1\left(N, \frac{N-1}{2}; \frac{N+3}{2}; -\frac{1+j\omega\sigma^2}{1-j\omega\sigma^2}\right), \tag{4.81}$$

where ${}_2F_1(a,b;c;z)$ is Gauss' hypergeometric function, defined by [13]:

$${}_2F_1(a,b;c;z) \triangleq \sum_{i=0}^{\infty} \frac{(a)_i (b)_i}{(c)_i} \frac{z^i}{i!} \tag{4.82}$$

and $(x)_k$ is the Pochhammer symbol (also known as the rising factorial [49]), given by [13]:

$$(x)_k \triangleq \frac{\Gamma(x+k)}{\Gamma(x)}. \tag{4.83}$$

The moment generating function (MGF) of R (assuming it exists) can be found simply by making the substitution $j\omega \to s$ in Equation (4.81). We see, therefore, that the MGF has a singularity at the point $s = 1/\sigma^2$ and, hence, is convergent in the strip of the s-plane for which $-1/\sigma^2 < \Re\{s\} < 1/\sigma^2$. The existence of this MGF allows us to develop a Chernoff bound on $F_R(r)$, though this does not appear to result in a simple closed form expression, as was possible for the χ^2 distribution.

Jakeman and Pusey give the following expression for the moments of R^2 [63, Equation (23)]:

$$E_{R^2}[x^n] = \left(2\sigma^2\right)^n \frac{n!}{\Gamma\left(\frac{N}{2}\right)} \Gamma\left(\frac{N}{2} + n\right). \tag{4.84}$$

We would, therefore, expect the MGF of R^2 to be given by (see Equation (C.12)):

$$\Psi_{R^2}(s) = \sum_{n=0}^{\infty} E_{R^2}[x^n] \frac{s^n}{n!} \tag{4.85}$$

$$= \sum_{n=0}^{\infty} \left(\frac{N}{2} \right)_n (2\sigma^2 s)^n , \tag{4.86}$$

but this series is *divergent* for all real $s \neq 0$ and, consequently, the MGF of R^2 does not, in fact, exist. It is not possible, therefore, to derive a Chernoff bound on $F_{R^2}(x)$. However, the non-existence of $\Psi_{R^2}(s)$ does provide us with some insight into the behaviour of this distribution. Recall that the MGF is defined by:

$$\Psi_{R^2}(s) = E_{R^2}[\exp(xs)] = \int_0^{\infty} \exp(xs) f_{R^2}(x) dx. \tag{4.87}$$

The non-existence of the MGF implies that the integral above is divergent for real $s > 0$[†], which in turn implies that the rate at which the PDF decays towards zero as $x \to \infty$ is sub-exponential. Thus, the distribution of R^2 may be described as "heavy-tailed".

The Signal plus Noise Case

We now remove the assumption that $\boldsymbol{\mu} = \mathbf{0}$. Note, from Equation (4.47), that the characteristic function is no longer completely defined by the determinant of the matrix $\boldsymbol{P}$. To account for the effect of non-zero $\boldsymbol{\mu}$ it is necessary to consider the exponent in Equation (4.47). Using Equations (4.71) and (4.72) in Equation (4.47), and multiplying through, we obtain:

$$\boldsymbol{\mu}^{\mathrm{H}} \boldsymbol{C}^{-1} \left(\boldsymbol{I} - \boldsymbol{P}^{-1} \right) \boldsymbol{\mu} = \frac{\rho}{1 + (\rho\sigma^2)^2} \left[\frac{\lambda}{2} \rho\sigma^2 - j \left(\Re\{\kappa\} \cos\phi + \Im\{\kappa\} \sin\phi \right) \right] , \tag{4.88}$$

where we have introduced:

$$\lambda \triangleq \sum_{i=0}^{N-1} |\mu_i|^2 = \boldsymbol{\mu}^{\mathrm{H}} \boldsymbol{\mu} \tag{4.89}$$

[†]Its existence at $s = 0$ is assured by the convergence of the integral of the PDF.

$$\kappa \triangleq \sum_{i=0}^{\frac{N}{2}-1} \mu_{2i+1}\mu_{2i}^{*} = \boldsymbol{\mu}^{\mathrm{H}}\boldsymbol{Q_I}\boldsymbol{\mu} + j\boldsymbol{\mu}^{\mathrm{H}}\boldsymbol{Q_Q}\boldsymbol{\mu}\,. \tag{4.90}$$

Note that κ is identically the decision statistic in the absence of noise. The joint characteristic function of Z_I and Z_Q is, therefore, given by:

$$\Phi_{Z_I,Z_Q}\left(j\rho\cos\phi, j\rho\sin\phi\right) = \frac{\exp\left(-\frac{\rho}{1+(\rho\sigma^2)^2}\left[\frac{\lambda}{2}\rho\sigma^2 - j\left(\Re\left\{\kappa\right\}\cos\phi + \Im\left\{\kappa\right\}\sin\phi\right)\right]\right)}{\left[1+\left(\rho\sigma^2\right)^2\right]^{\frac{N}{2}}}\,. \tag{4.91}$$

Note in this case that the CHF is dependent on both ρ and ϕ, so the integral over ϕ remains.

Starting again with the distribution of Z_I, we find, upon setting $\phi = 0$ in Equation (4.91):

$$\Phi_{Z_I}\left(j\omega\right) = \frac{\exp\left(-\frac{\omega}{1+\omega^2\sigma^4}\left[\frac{\lambda}{2}\omega\sigma^2 - j\Re\left\{\kappa\right\}\right]\right)}{\left[1+\omega^2\sigma^4\right]^{\frac{N}{2}}}\,. \tag{4.92}$$

It can be shown that this expression corresponds to the CHF of the difference of two *non-central* χ^2 variates (see Appendix B.2.1):

$$Z_I = X_1 - X_2, \tag{4.93}$$

where:

$$X_1 \sim \chi'^2\left(N, \frac{1}{2}\boldsymbol{\mu}^{\mathrm{H}}\left(\boldsymbol{I}+\boldsymbol{Q_I}\right)\boldsymbol{\mu}, \frac{\sigma^2}{2}\right) \tag{4.94}$$

$$X_2 \sim \chi'^2\left(N, \frac{1}{2}\boldsymbol{\mu}^{\mathrm{H}}\left(\boldsymbol{I}-\boldsymbol{Q_I}\right)\boldsymbol{\mu}, \frac{\sigma^2}{2}\right)\,. \tag{4.95}$$

This result is similar to the one obtained by Ávila-Rodríguez et al., with the exception that they modelled X_2 as a *central* χ^2 variate. This would appear to account for the discrepancy between predicted and simulated results reported in [15]†.

As reported in [15], there does not appear to be any simple closed-form expression for the difference of two χ^2 rvs and so one must resort to numerical techniques to determine the PDF and CDF of Z_I under H_1. A number of such

†The error in [15] arises in Equation (8): the authors assume that the means of the rvs X_I and Y_I are identical, which is only the case in the absence of Doppler and data modulation.

techniques have been reported in the literature [35, 36, 44, 54, 114], the approach that we have taken is that of saddle-point integration to calculate the Laplace inversion of the MGF [54]. It is a well-known fact that the CDF of *any* Hermitian quadratic form in complex Gaussian variates can be written as a weighted sum of CDFs of χ^2 variates [73, 74], so this result should come as no surprise.

To determine the statistics of R we apply a technique similar to that used in the noise alone case. Substituting Equation (4.91) into Equation (4.64) yields:

$$f_R(r) = \frac{r}{2\pi} \int_0^\infty \frac{\rho J_0(r\rho)\, e^{-\frac{\lambda\sigma^2\rho^2}{2[1+(\rho\sigma^2)^2]}}}{\left[1+(\rho\sigma^2)^2\right]^{\frac{N}{2}}} \int_{-\pi}^{\pi} e^{j\frac{\rho}{1+(\rho\sigma^2)^2}(\Re\{\kappa\}\cos\phi+\Im\{\kappa\}\sin\phi)} d\phi\, d\rho\,. \quad (4.96)$$

The integral over ϕ in this case evaluates to a Bessel function of the first kind of order zero (see Appendix B.2.2), yielding:

$$f_R(r) = r \int_0^\infty \frac{\rho J_0(r\rho)\, e^{-\frac{1}{2}\frac{\lambda\sigma^2\rho^2}{1+(\rho\sigma^2)^2}}}{\left[1+(\rho\sigma^2)^2\right]^{\frac{N}{2}}} J_0\left(\frac{\rho|\kappa|}{1+(\rho\sigma^2)^2}\right) d\rho\,. \quad (4.97)$$

Making the substitution $u = \rho\sigma^2$ and letting $\gamma = \lambda/\sigma^2$ and $\tau = |\kappa|/\sigma^2$ gives:

$$f_R(r) = \frac{r}{\sigma^4} \int_0^\infty \frac{u J_0\left(\frac{r}{\sigma^2}u\right)}{\left[1+u^2\right]^{\frac{N}{2}}} \exp\left(-\frac{\gamma}{2}\frac{u^2}{1+u^2}\right) J_0\left(\frac{u\tau}{1+u^2}\right) du\,. \quad (4.98)$$

It is interesting to note that λ is a measure of the total signal energy in the observation vector and $|\kappa|$ is the value of R in the absence of noise. Note that the distribution of R depends on the signal component *only* through λ and $|\kappa|$. We have already investigated the effect of Doppler and data modulation on these quantities in Chapter 3, and so can apply that analysis directly to the determination of the influence of these effects on receiver performance in the presence of noise.

4.3.2 The Standard Form

In the standard form differentially coherent combining detector the variable Z is generated as follows:

$$Z = \sum_{i=J}^{N-1} Y_i Y_{i-J}^*. \tag{4.99}$$

In general, J can be any positive integer. We consider initially the (simplest) case $J = 1$. The matrix $\boldsymbol{P}$, defined in Equation (4.48), is then given by:

$$\boldsymbol{P} = \boldsymbol{I} - j\sigma^2 \begin{pmatrix} 0 & \omega - j\nu & 0 & \cdots & 0 \\ \omega + j\nu & 0 & \omega - j\nu & \ddots & \vdots \\ 0 & \omega + j\nu & 0 & \ddots & 0 \\ \vdots & \ddots & \ddots & \ddots & \omega - j\nu \\ 0 & \cdots & 0 & \omega + j\nu & 0 \end{pmatrix} \tag{4.100}$$

$$= \begin{pmatrix} 1 & -j\rho\sigma^2 e^{-j\phi} & 0 & \cdots & 0 \\ -j\rho\sigma^2 e^{+j\phi} & 1 & -j\rho\sigma^2 e^{-j\phi} & \ddots & \vdots \\ 0 & -j\rho\sigma^2 e^{+j\phi} & 1 & \ddots & 0 \\ \vdots & \ddots & \ddots & \ddots & -j\rho\sigma^2 e^{-j\phi} \\ 0 & \cdots & 0 & -j\rho\sigma^2 e^{+j\phi} & 1 \end{pmatrix}. \tag{4.101}$$

Denoting by $P_N(\rho, \phi)$ the determinant of $\boldsymbol{P}$ given that there are N samples in the observation vector, then it can be shown that (see Appendix B.2.3):

$$P_N(\rho, \phi) = \begin{cases} 1 & N = 1 \\ 1 + (\rho\sigma^2)^2 & N = 2 \\ P_{N-1}(\rho, \phi) + (\rho\sigma^2)^2 P_{N-2}(\rho, \phi) & N > 2. \end{cases} \tag{4.102}$$

In fact, if we define $P_0(\rho, \phi) = 1$ then the recursion holds for all $N \geq 2$. The interesting thing to note here is that all the $P_N(\rho, \phi)$ are, in fact, *independent* of ϕ, so we will replace $P_0(\rho, \phi)$ by $P_N(\rho)$. Indeed, it can be shown that (see

Appendix B.2.4):

$$P_N(\rho) = \sum_{i=0}^{\lfloor \frac{N}{2} \rfloor} \binom{N-i}{i} \left(\rho\sigma^2\right)^{2i}. \tag{4.103}$$

These polynomials are related to the *Fibonacci* polynomials (see [124, Sequence A011973] and [148]) and, by comparison, it can be shown that the roots of $P_N(\rho)$, denoted $\lambda_{k,+}$ and $\lambda_{k,-}$, are given by:

$$\lambda_{k,\pm} = \frac{\pm j}{2\sigma^2 \cos\frac{k\pi}{N+1}} \qquad k = 1, 2, \ldots, \left\lfloor \frac{N}{2} \right\rfloor. \tag{4.104}$$

Note that the roots occur as complex conjugate pairs.

When $J > 1$ we denote by $P_{J,N}(\rho)$ the determinant of the matrix $\boldsymbol{P}$. A simple technique involving Gaussian elimination can then be applied to derive the following useful result (see Appendix B.2.5):

$$P_{J,N}(\rho) = P_{1,a}^{J-b}(\rho) P_{1,a+1}^{b}(\rho), \tag{4.105}$$

where a and b are the unique integers for which $N = aJ + b$ such that $b < J$.

The Noise Alone Case

Again, we consider the case $\boldsymbol{\mu} = \mathbf{0}$ first. In addition, we consider the simple case $J = 1$. The CHF is then given by:

$$\Phi_{Z_I, Z_Q}\left(j\rho\cos\phi, j\rho\sin\phi\right) = \frac{1}{P_N(\rho)}. \tag{4.106}$$

Recall that the roots of the polynomial $P_N(\rho)$ are given by Equation (4.104), and that they occur in complex conjugate pairs $\lambda_{k,\pm}$. We can, therefore, write:

$$\begin{aligned} P_N(\rho) &= K_N \prod_{k=1}^{\lfloor \frac{N}{2} \rfloor} \left(\rho - \lambda_{k,+}\right)\left(\rho - \lambda_{k,-}\right) \\ &= K_N \prod_{k=1}^{\lfloor \frac{N}{2} \rfloor} \left(\rho^2 + \gamma_k\right) \end{aligned} \tag{4.107}$$

where K_N is the coefficient of the leading term of $P_N(\rho)$ which is given by (see Equation (4.103)):

$$K_N = \binom{N - \left\lfloor \frac{N}{2} \right\rfloor}{\left\lfloor \frac{N}{2} \right\rfloor} = \sigma^{4\left\lfloor \frac{N}{2} \right\rfloor} \times \begin{cases} \frac{N+1}{2} & \text{N odd} \\ 1 & \text{N even,} \end{cases} \tag{4.108}$$

and the γ_k are given by the product of the complex conjugate pairs of roots of $P_N(\rho)$. Hence, from Equation (4.104), the γ_k's are given by:

$$\gamma_k = \frac{1}{4\sigma^4 \cos^2 \frac{k\pi}{N+1}} \qquad 1 \leq k \leq \left\lfloor \frac{N}{2} \right\rfloor . \tag{4.109}$$

We can, therefore, apply a partial fraction expansion [97, p. 63] to Equation (4.106) yielding:

$$\Phi_{Z_I,Z_Q}\left(j\rho\cos\phi, j\rho\sin\phi\right) = \sum_{k=1}^{\left\lfloor \frac{N}{2} \right\rfloor} \frac{A_{N,k}}{\rho^2 + \gamma_k} , \tag{4.110}$$

where:

$$A_{N,k} = \lim_{\rho^2 \to -\gamma_k} \frac{\rho^2 + \gamma_k}{P_N(\rho)} . \tag{4.111}$$

Applying L'Hôpital's rule [132] to Equation (4.111), we obtain:

$$A_{N,k} = \frac{1}{\sum_{i=0}^{\left\lfloor \frac{N}{2} \right\rfloor} \binom{N-i}{i} i\sigma^{4i} \left(-\gamma_k\right)^{i-1}} . \tag{4.112}$$

Considering now the distribution of Z_I, recall that this can be represented as a quadratic form in complex Gaussian variates, and so the CDF can be expressed as a weighted sum of χ^2 variates. This is easily seen by applying the partial fraction expansion of Equation (4.110) and setting $\rho = \omega$ and $\phi = 0$:

$$\Phi_{Z_I}\left(j\omega\right) = \sum_{k=1}^{\left\lfloor \frac{N}{2} \right\rfloor} \frac{A_{N,k}}{\omega^2 + \gamma_k} . \tag{4.113}$$

Applying the Fourier inversion formula yields:

$$f_{Z_I}(z_I) = \sum_{k=1}^{\lfloor \frac{N}{2} \rfloor} \frac{A_{N,k}}{2\sqrt{\gamma_k}} \exp\left(-\sqrt{\gamma_k}\,|z_I|\right) . \tag{4.114}$$

The CDF of Z_I is easily found by integrating Equation (4.114):

$$F_{Z_I}(z_I) = \begin{cases} \displaystyle\sum_{k=1}^{\lfloor \frac{N}{2} \rfloor} \frac{A_{N,k}}{2\gamma_k} \exp\left(-\sqrt{\gamma_k} z_I\right) & z_I < 0 \\ \\ \displaystyle 1 - \sum_{k=1}^{\lfloor \frac{N}{2} \rfloor} \frac{A_{N,k}}{2\gamma_k} \exp\left(\sqrt{\gamma_k} z_I\right) & z_I \geq 0. \end{cases} \tag{4.115}$$

The distribution of the magnitude, R, is given by:

$$f_R(r) = r \int_0^\infty \frac{\rho J_0\left(r\rho\right)}{P_N(\rho)} d\,\rho. \tag{4.116}$$

Applying the partial fraction expansion of Equation (4.110) to the integrand in Equation (4.116) yields:

$$\begin{aligned} f_R(r) &= r \int_0^\infty \sum_{k=1}^{\lfloor \frac{N}{2} \rfloor} A_{N,k} \frac{\rho J_0\left(r\rho\right)}{(\rho^2 + \gamma_k)} d\,\rho \\ &= \sum_{k=1}^{\lfloor \frac{N}{2} \rfloor} A_{N,k}\, r K_0\left(r\sqrt{\gamma_k}\right), \end{aligned} \tag{4.117}$$

where again we have used the Hankel transform [87, Entry (4.23)].

Employing the same methodology, the following expression for the CDF of R

can be obtained (see Appendix B.2.6):

$$F_R(r) = 1 - \sum_{k=1}^{\left\lfloor \frac{N}{2} \right\rfloor} \frac{A_{N,k}}{\sqrt{\gamma_k}} \, r K_1 \left(r\sqrt{\gamma_k} \right) . \tag{4.118}$$

Whilst the expressions of Equations (4.114), (4.115), (4.117) and (4.118) are exact, they are not generally useful forms for computation. As N increases, the $A_{N,k}$ terms become large and oscillatory, resulting in a loss of accuracy even at moderate values of N (in Matlab$^{\text{TM}}$ this loss of accuracy becomes apparent for N as low as 26, particularly for small values of r). Numerical results can be obtained using Mathematica$^{\text{TM}}$ to arbitrary required precision†, but computation times increase dramatically with N.

A similar partial fraction expansion can be applied for the case $J \neq 1$, though this results in more complicated forms.

The Signal plus Noise Case

We have not been able to determine any simple closed form expression for $\boldsymbol{P}^{-1}$ for the standard form. Thus, we have no analogue to Equation (4.88). The PDF of Z_I is, again, a quadratic form in complex Gaussian variates and so can be expressed as a weighted sum of χ^2 variates [16]. The PDF of R, however, is given by the double integral:

$$f_R(r) = \frac{r \exp\left(-\boldsymbol{\mu}^{\text{H}} \boldsymbol{C}^{-1} \boldsymbol{\mu}\right)}{2\pi} \int_0^{\infty} \int_{-\pi}^{\pi} \frac{\rho J_0\left(r\rho\right)}{P_N(\rho)} \exp\left(\boldsymbol{\mu}^{\text{H}} \boldsymbol{C}^{-1} \boldsymbol{P}^{-1} \boldsymbol{\mu}\right) d\,\phi \, d\,\rho \,, \tag{4.119}$$

which does not appear to lead to a simple form for numerical evaluation. In particular, for large N the inversion of $\boldsymbol{P}$ poses a significant challenge. We, therefore, wish to determine an approximation to the distribution of the decision statistic which is suitable for numerical evaluation.

It is also interesting to note that, in this case, we cannot state with certainty that our analysis of signal effects in Chapter 3 can be applied directly to the

†We found that this required setting the internal Mathematica$^{\text{TM}}$ variable `$MaxExtraPrecision` to a suitably large value (for $N = 200$, `$MaxExtraPrecision` must be of the order of 300).

performance analysis in the presence of noise. Consider the term $\boldsymbol{P}^{-1}$ in the exponent of the integrand of Equation (4.119). From Equation (4.48) we can write this as:

$$\boldsymbol{P}^{-1} = \left(\boldsymbol{I} - j\boldsymbol{C}\left[\omega \boldsymbol{Q}_{\boldsymbol{I}} + \nu \boldsymbol{Q}_{\boldsymbol{Q}}\right] \right)^{-1} = \sum_{i=0}^{\infty} (j2\sigma^2)^i \left[\omega \boldsymbol{Q}_{\boldsymbol{I}} + \nu \boldsymbol{Q}_{\boldsymbol{Q}}\right]^i , \qquad (4.120)$$

which includes all positive powers of $\boldsymbol{Q}_{\boldsymbol{I}}$ and $\boldsymbol{Q}_{\boldsymbol{Q}}$. Our analysis of Section 3.3, however, considered only the decision statistic in the absence of noise, which can be expressed as:

$$D_k(\widehat{\boldsymbol{\theta}}) = \boldsymbol{\mu}^{\mathrm{H}} \left(\boldsymbol{Q}_{\boldsymbol{I}} + j\boldsymbol{Q}_{\boldsymbol{Q}}\right) \boldsymbol{\mu}\boldsymbol{\mu}^{\mathrm{H}} \left(\boldsymbol{Q}_{\boldsymbol{I}} - j\boldsymbol{Q}_{\boldsymbol{Q}}\right) \boldsymbol{\mu} , \qquad (4.121)$$

which, clearly, does not include all positive powers of $\boldsymbol{Q}_{\boldsymbol{I}}$ and $\boldsymbol{Q}_{\boldsymbol{Q}}$. It is also interesting to recall that every matrix is a solution to its own characteristic equation (a result known as the Cayley-Hamilton Theorem [76]). We have seen that the characteristic polynomial of the matrix $\boldsymbol{P}$ is of degree N for $J = 1$. Thus, $\boldsymbol{P}^N$ can be expressed as a sum of lower powers of $\boldsymbol{P}$. This is the major difference between the pair-wise and standard forms of differentially coherent combining. For the pair-wise form, the characteristic polynomial can be expressed as a degree two polynomial raised to the power $N/2$. Thus, higher powers of $\boldsymbol{P}$ for the pair-wise form can be expressed in terms of the matrix $\boldsymbol{P}$ itself. Ultimately, the effect of this result is to limit the influence of a given coherent output to just one summand of the differentially coherent accumulator in the pair-wise form, whereas, in the standard form, the influence of each coherent accumulator output spreads through all subsequent summands of the differentially coherent accumulator.

4.3.3 Gaussian Approximations

In the preceding sections we have used the joint characteristic function of the real and imaginary parts of the differentially coherent sum to derive expressions for the distribution of the decision statistic. Unfortunately, this approach does not always lead to usable results. In fact, the expression for the distribution of the decision statistic for the pair-wise form under the noise alone condition (Equation (4.77)) and the expression for the standard form under noise alone when $N \leq 27$ (Equation (4.117)) are the only useful closed-form expressions obtained in this manner.

In this section we invoke the central limit theorem to derive a bivariate Gaussian approximation to the distribution of the differentially coherent sum. This approach has been previously used by Chung [28] in the context of the DCD, where the real part of the sum was taken as the decision statistic, and by Schmid and Neubauer [112] in the context of the DCCD, where the decision statistic is formed as the square magnitude of the sum.

Recall that the (complex) differentially coherent sum can be written as:

$$Z = Z_I + jZ_Q = \boldsymbol{Y}^{\mathrm{H}}\boldsymbol{Q_I}\boldsymbol{Y} + j\boldsymbol{Y}^{\mathrm{H}}\boldsymbol{Q_Q}\boldsymbol{Y},$$

where $\boldsymbol{Q_I}$ and $\boldsymbol{Q_Q}$ are Hermitian matrices (which implies that the variables Z_I and Z_Q are real) and $\boldsymbol{Y}$ is an N-dimensional complex Gaussian rv. This representation is valid for both the DCD and the DCCD in both the pair-wise and standard forms. If we make the further assumption that the components of $\boldsymbol{Y}$ are mutually independent, then we can invoke the central limit theorem for both Z_I and Z_Q independently. However, we cannot yet make any assertion as to whether or not Z_I and Z_Q can be modelled as *independent* Gaussian variables. For this we require the following theorem [106]:

Theorem 4.2 (Craig's Theorem) *For real vector* $\boldsymbol{y} \sim \mathrm{N}(\boldsymbol{\mu}, \boldsymbol{C})$*, then* $x_1 = \boldsymbol{y}^{\mathrm{T}}\boldsymbol{A}\boldsymbol{y}$ *and* $x_2 = \boldsymbol{y}^{\mathrm{T}}\boldsymbol{B}\boldsymbol{y}$ *are independently distributed if and only if* $\boldsymbol{ACB} = \boldsymbol{0}$.

While this theorem is defined for real rvs, the extension to a complex Gaussian distribution is straightforward.

Thus, if $\boldsymbol{Q_I}\boldsymbol{Q_Q} = \boldsymbol{0}$ then we can model Z_I and Z_Q as independent Gaussian rvs, by invoking the central limit theorem. If this condition is not met, then the central limit theorem can still be applied to each term separately, but the resulting rvs are statistically dependent. Thus, by the central limit theorem, as $N \to \infty$, the joint distribution of Z_I and Z_Q approaches a *bivariate* Gaussian distribution[†] [102]. We denote by $\widetilde{Z}_I$ and $\widetilde{Z}_Q$ the Gaussian rvs with distribution:

$$f_{\widetilde{Z}_I,\widetilde{Z}_Q}(\widetilde{z}_I, \widetilde{z}_Q) = \frac{1}{2\pi\sigma_I\sigma_Q\sqrt{1-\rho^2}} \exp\left(-\frac{1}{2(1-\rho^2)}\right.$$

[†]In fact, whilst we have shown that Z_I and Z_Q are *marginally* Gaussian, we have not shown that they are *jointly* Gaussian. We do, however, make the assumption that this is the case, and this appears to be borne out in practice.

$$\times \left[\frac{\left(\widetilde{z}_I - \mu_I\right)^2}{\sigma_1^2} - \frac{2\rho\left(\widetilde{z}_I - \mu_I\right)\left(\widetilde{z}_Q - \mu_Q\right)}{\sigma_I \sigma_Q} + \frac{\left(\widetilde{z}_Q - \mu_Q\right)^2}{\sigma_Q^2} \right] \Bigg) , \tag{4.122}$$

where:

$$\mu_I = E[Z_I] \qquad \mu_Q = E[Z_Q] \tag{4.123}$$

$$\sigma_I^2 = \mathrm{Var}\left[Z_I\right] \qquad \sigma_Q^2 = \mathrm{Var}\left[Z_Q\right] \tag{4.124}$$

$$\rho = \frac{\sigma_{IQ}}{\sigma_I \sigma_Q} \qquad \sigma_{IQ} = E[Z_I Z_Q] - \mu_I \mu_Q. \tag{4.125}$$

This bivariate Gaussian distribution can be used as an approximation to the joint distribution of the real and imaginary components of the differentially coherent sum. We require expressions for the mean, variance and covariance of Z_I and Z_Q to complete this Gaussian approximation.

The Moments of Z_I and Z_Q

We use a characteristic function approach to determine the moments of Z_I and Z_Q. From the properties of CHFs we have:

$$E\left[Z_I^m Z_Q^n\right] = j^{-(m+n)} \left. \frac{\partial^{m+n} \Phi_{Z_I, Z_Q}\left(j\omega, j\nu\right)}{\partial \omega^m \partial \nu^n} \right|_{\omega=0, \nu=0} . \tag{4.126}$$

The generic form of the CHF, valid for all the forms of differentially coherent processing considered in this thesis, is given in Equation (4.47). Applying the generalised product rule for multiple derivatives [48] we obtain:

$$\begin{aligned} E\left[Z_I^m Z_Q^n\right] =& j^{-(m+n)} e^{-\boldsymbol{\mu}^{\mathrm{H}} \boldsymbol{C}^{-1} \boldsymbol{\mu}} \\ & \times \sum_{i=0}^{m} \sum_{k=0}^{n} \binom{m}{i} \binom{n}{k} \frac{\partial^{m+n-(i+k)} \left|\boldsymbol{P}\right|^{-1}}{\partial \omega^{m-i} \partial \nu^{n-k}} \frac{\partial^{i+k} e^{\boldsymbol{\mu}^{\mathrm{H}} \boldsymbol{C}^{-1} \boldsymbol{P}^{-1} \boldsymbol{\mu}}}{\partial \omega^i \partial \nu^k} \Bigg|_{\substack{\omega=0 \\ \nu=0}} . \end{aligned} \tag{4.127}$$

The evaluation of the above expression is straightforward, but tedious. The results are summarised below[†]:

$$E[Z_I] = \boldsymbol{\mu}^{\mathrm{H}} \boldsymbol{Q_I} \boldsymbol{\mu} \qquad E[Z_Q] = \boldsymbol{\mu}^{\mathrm{H}} \boldsymbol{Q_Q} \boldsymbol{\mu} \tag{4.128}$$

[†]In Equations (4.128) to (4.130) we have made use of the fact that the odd order derivatives of $|\boldsymbol{P}|$ are zero at $\omega = 0$, $\nu = 0$.

$$\mathrm{Var}\left[Z_I\right] = \left.\frac{\partial^2 \left|\boldsymbol{P}\right|}{\partial \omega^2}\right|_{\substack{\omega=0\\ \nu=0}} + 2\boldsymbol{\mu}^{\mathrm{H}}\boldsymbol{C}\boldsymbol{Q}_{\boldsymbol{I}}^2\boldsymbol{\mu} \qquad \mathrm{Var}\left[Z_Q\right] = \left.\frac{\partial^2 \left|\boldsymbol{P}\right|}{\partial \nu^2}\right|_{\substack{\omega=0\\ \nu=0}} + 2\boldsymbol{\mu}^{\mathrm{H}}\boldsymbol{C}\boldsymbol{Q}_{\boldsymbol{Q}}^2\boldsymbol{\mu} \tag{4.129}$$

$$\sigma_{IQ} = \boldsymbol{\mu}^{\mathrm{H}}\left(\boldsymbol{Q}_{\boldsymbol{I}}\boldsymbol{C}\boldsymbol{Q}_{\boldsymbol{Q}} + \boldsymbol{Q}_{\boldsymbol{Q}}\boldsymbol{C}\boldsymbol{Q}_{\boldsymbol{I}}\right)\boldsymbol{\mu} \qquad \rho = \frac{\sigma_{IQ}}{\sigma_I\sigma_Q}. \tag{4.130}$$

As would be expected, the means of Z_I and Z_Q correspond to the real and imaginary components of the differentially coherent sum in the absence of noise. Note also that the covariance component is zero in the absence of signal (*i.e.*, when $\boldsymbol{\mu} = \mathbf{0}$). We can also see that Craig's theorem is evident in Equation (4.130), since $\sigma_{IQ} = 0$ if $\boldsymbol{Q}_{\boldsymbol{I}}\boldsymbol{C}\boldsymbol{Q}_{\boldsymbol{Q}} = \mathbf{0}$.

Equations (4.128) to (4.130) are valid for all forms of differentially coherent processing considered in this thesis. The only differences between one form and another are: 1) the structure of the matrices $\boldsymbol{Q}_{\boldsymbol{I}}$ and $\boldsymbol{Q}_{\boldsymbol{Q}}$; and 2) the determinant of $\boldsymbol{P}$. The values of some derivatives of $|\boldsymbol{P}|$ at $\omega = 0$, $\nu = 0$ are tabulated in Table 4.1.

	Pair Wise Form	Standard Form $\left(J \leq \frac{N}{2}\right)$
$\left.\frac{\partial \left\|\boldsymbol{P}\right\|}{\partial \omega}\right\|_{\substack{\omega=0\\ \nu=0}} = \left.\frac{\partial \left\|\boldsymbol{P}\right\|}{\partial \nu}\right\|_{\substack{\omega=0\\ \nu=0}} =$	0	0
$\left.\frac{\partial^2 \left\|\boldsymbol{P}\right\|}{\partial \omega^2}\right\|_{\substack{\omega=0\\ \nu=0}} = \left.\frac{\partial^2 \left\|\boldsymbol{P}\right\|}{\partial \nu^2}\right\|_{\substack{\omega=0\\ \nu=0}} =$	$N\sigma^4$	$2\sigma^4(N-J)$
$\left.\frac{\partial^2 \left\|\boldsymbol{P}\right\|}{\partial \omega \partial \nu}\right\|_{\substack{\omega=0\\ \nu=0}} =$	0	0
$\left.\frac{\partial^3 \left\|\boldsymbol{P}\right\|}{\partial \omega^3}\right\|_{\substack{\omega=0\\ \nu=0}} = \left.\frac{\partial^3 \left\|\boldsymbol{P}\right\|}{\partial \nu^3}\right\|_{\substack{\omega=0\\ \nu=0}} =$	0	0
$\left.\frac{\partial^4 \left\|\boldsymbol{P}\right\|}{\partial \omega^4}\right\|_{\substack{\omega=0\\ \nu=0}} = \left.\frac{\partial^4 \left\|\boldsymbol{P}\right\|}{\partial \nu^4}\right\|_{\substack{\omega=0\\ \nu=0}} =$	$4!\binom{\frac{N}{2}}{2}\sigma^8$	$4!\left[\binom{N-J-1}{2} + J - 1\right]\sigma^8$
$\left.\frac{\partial^4 \left\|\boldsymbol{P}\right\|}{\partial \omega^2 \partial \nu^2}\right\|_{\substack{\omega=0\\ \nu=0}} =$	$8\binom{\frac{N}{2}}{2}\sigma^8$	$8\left[\binom{N-J-1}{2} + J - 1\right]\sigma^8$

Table 4.1: Derivatives of the Determinant of the Matrix $\boldsymbol{P}$ at $\omega = 0$, $\nu = 0$.

Approximations for the Pair Wise Form

The pair wise form leads to a particularly simple approximation. The matrix $\boldsymbol{Q_I}$ is given by Equation (4.67), and $\boldsymbol{Q_Q}$ is similar. Both matrices share the property:

$$\boldsymbol{Q}_{\boldsymbol{I}}^2 = \boldsymbol{Q}_{\boldsymbol{Q}}^2 = \frac{1}{4}\boldsymbol{I}\,. \tag{4.131}$$

In addition, $\boldsymbol{Q_I Q_Q} \neq \boldsymbol{0}$ and thus, by Craig's theorem, Z_I and Z_Q are not statistically independent. However, by Equation (4.129), the variances of Z_I and Z_Q are identical and independent of the signal component, $\boldsymbol{\mu}$.

In addition, we have:

$$\boldsymbol{Q_I Q_Q} + \boldsymbol{Q_Q Q_I} = \boldsymbol{0}\,, \tag{4.132}$$

so, by Equation (4.130), Z_I and Z_Q are *uncorrelated* (assuming $\boldsymbol{C} = \sigma^2\boldsymbol{I}$). We, therefore, model Z_I and Z_Q as independent[†] Gaussian rvs, with means given by Equation (4.128) and variances:

$$\mathrm{Var}\left[Z_I\right] = \mathrm{Var}\left[Z_Q\right] = N\sigma^4 + \boldsymbol{\mu}^{\mathrm{H}}\boldsymbol{\mu}\sigma^2 \stackrel{\Delta}{=} \sigma_{\mathrm{pw}}^2, \tag{4.133}$$

where σ^2 is the variance of Y_I and Y_Q and the subscript pw denotes pair-wise. Note that the term $\boldsymbol{\mu}^{\mathrm{H}}\boldsymbol{\mu}$ is simply the total signal energy in the observation vector and is equivalent to the noncentrality parameter of the χ^2 distribution. Recall that the three most common forms of decision statistic generated from Z are: 1) $D = \Re\{Z\} = Z_I$; 2) $D = |Z| = \sqrt{Z_I^2 + Z_Q^2}$; and 3) $D = |Z|^2 = Z_I^2 + Z_Q^2$. From the above analysis, we see that we can approximate the distribution of Z_I with a Gaussian distribution, $|Z|$ can be approximated by a Rice distribution [102] and $|Z|^2$ can be approximated by a χ^2 distribution with two degrees of freedom [102].

[†]Jointly Gaussian rv's which are uncorrelated are also independent. Since Z_I and Z_Q are uncorrelated, we model them as independent Gaussian variates, even though they are, in fact, statistically dependent.

This leads us to the following approximations:

$$f_{Z_I}(z_I) \approx \frac{1}{\sqrt{2\pi\sigma_{\text{pw}}^2}} \exp\left(\frac{1}{2\sigma_{\text{pw}}^2}\left(z_I - \mu_I\right)^2\right) \tag{4.134}$$

$$F_{Z_I}(z_I) \approx \frac{1}{2}\text{erf}\left(\frac{z_I - \mu_I}{\sqrt{2\sigma_{\text{pw}}^2}}\right) \tag{4.135}$$

$$f_{Z_Q}(z_Q) \approx \frac{1}{\sqrt{2\pi\sigma_{\text{pw}}^2}} \exp\left(\frac{1}{2\sigma_{\text{pw}}^2}\left(z_Q - \mu_Q\right)^2\right) \tag{4.136}$$

$$F_{Z_Q}(z_Q) \approx \frac{1}{2}\text{erf}\left(\frac{z_Q - \mu_Q}{\sqrt{2\sigma_{\text{pw}}^2}}\right) \tag{4.137}$$

$$f_R(r) \approx \frac{r}{\sigma_{\text{pw}}^2} \exp\left(-\frac{r^2 + \mu_I^2 + \mu_Q^2}{2\sigma_{\text{pw}}^2}\right) I_0\left(\frac{r\sqrt{\mu_I^2 + \mu_Q^2}}{\sigma_{\text{pw}}^2}\right) \tag{4.138}$$

$$F_R(r) \approx 1 - Q_1\left(\frac{\sqrt{\mu_I^2 + \mu_Q^2}}{\sigma_{\text{pw}}}, \frac{r}{\sigma_{\text{pw}}}\right) , \tag{4.139}$$

where $R = |Z| = \sqrt{Z_I^2 + Z_Q^2}$.

The accuracy of this approximation is demonstrated in Figures 4.2 and 4.3. We consider a DCCD system with $C/N_0 = 30$ dB-Hz, $M = 1$, $K = 150$. Four cases are shown:

1. Noise alone,
2. Signal plus noise with no Doppler offset,
3. Signal plus noise with 250 Hz constant Doppler offset,
4. Signal plus noise with 450 Hz constant Doppler offset.

Figure 4.2 shows a scatter plot for 100 samples from the joint distribution of Z_I and Z_Q. For each case we include a contour of constant probability density based on the Gaussian approximation (which, for the pair-wise form, is a circle). The circles are drawn such that probability that the random point (Z_I, Z_Q) is inside the circle is $p = 0.9$. From the figure we can clearly see the effects of Doppler offset, as we have previously modelled in Section 3.3.1. Firstly, the Doppler offset introduces a rotation of the centre of mass about the origin; a Doppler

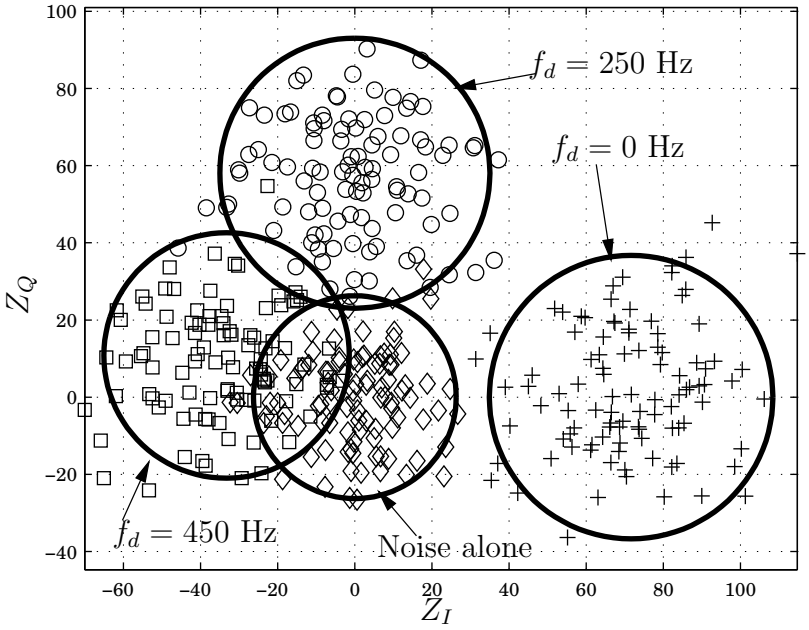


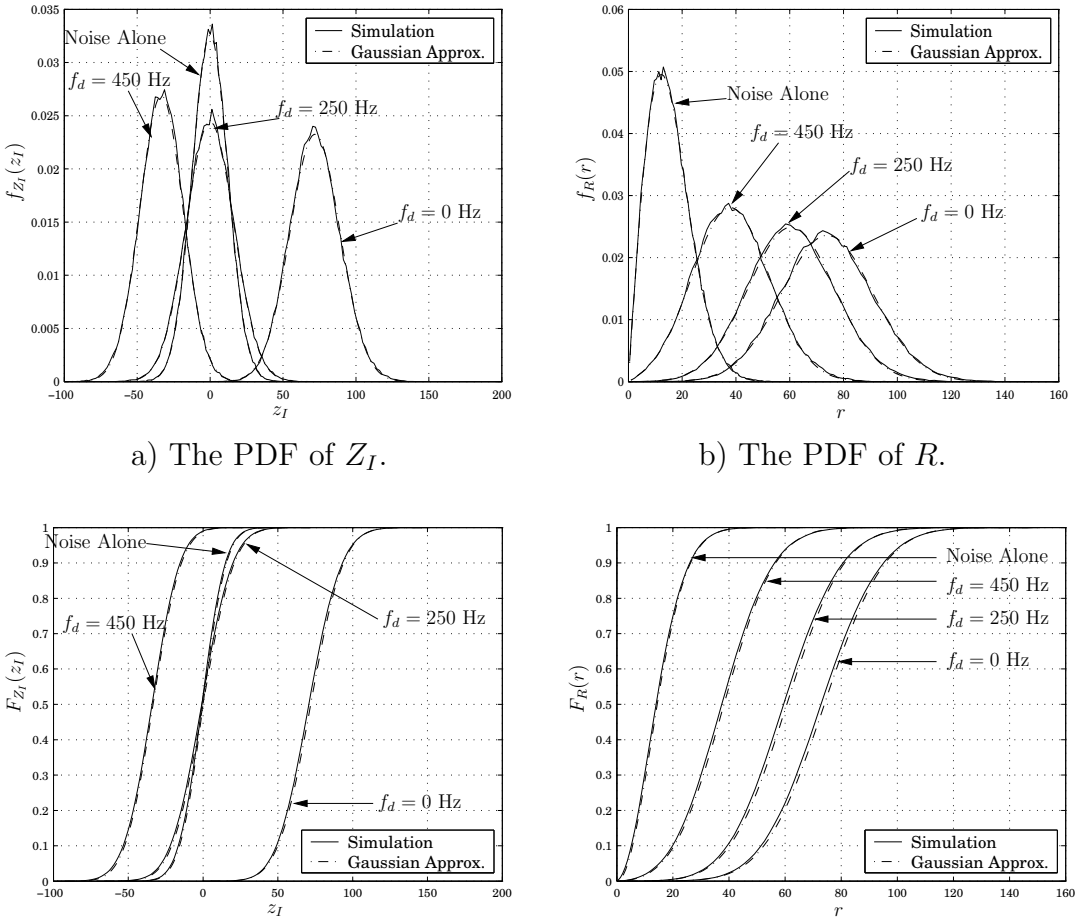
Figure 4.2: Scatter Plot for the Pair Wise Form of the DCCD. Four cases are shown: 1) Noise alone; 2) Signal plus noise, with zero Doppler offset; 3) Signal plus noise $f_d = 250$ Hz; and 4) Signal plus noise $f_d = 450$ Hz. In each case a circle has been drawn such that the probability that the random point (Z_I, Z_Q) is inside that circle is 0.9. One hundred random points are plotted in each case.

offset of 250 Hz moves all of the signal power into the quadrature component Z_Q. Secondly, the effective signal power is reduced. This is manifested as a movement towards the origin, and is most clearly seen by a comparison of the zero Doppler and 450 Hz Doppler cases.

In Figure 4.3 the PDF and CDF of both the real component, Z_I, and the magnitude, R, are shown. The accuracy of the Gaussian approximation in this case is clear from the plots. In addition, we can clearly see that R is a superior choice of decision statistic, relative to Z_I alone, when the signal is subject to Doppler offset. For instance, in Figure 4.3 c) it can be seen that the CDFs of the noise alone case and the signal plus noise case with $f_d = 250$ Hz are virtually indistinguishable.

Approximations for the Standard Form

The Gaussian approximation for the standard form is complicated by the fact that the covariance terms do not vanish, as they did for the pair wise form. Thus, we



a) The PDF of Z_I. b) The PDF of R.

c) The CDF of Z_I d) The CDF of R.

Figure 4.3: PDFs and CDFs of Z_I and $R = \sqrt{Z_I^2 + Z_Q^2}$ for the Pair Wise Form of the DCCD. In each case $100,000$ trial points were generated and the result compared with the Gaussian approximation.

cannot make a simple χ^2 approximation to the distribution of R^2. In fact, to the best of the author's knowledge, no closed-form analytical expression is known for the distribution of the sum of the squares of two correlated Gaussian variables. In the following we use an algorithm due to Sheil and O'Muircheartaigh [114] to calculate the density and distribution of the sum of the squares of two correlated Gaussian rvs.

Recall, from Equation (4.130), that the covariance term is proportional to

$\boldsymbol{Q_I Q_Q} + \boldsymbol{Q_Q Q_I}$. For the standard form with $J = 1$ we have:

$$\boldsymbol{Q_I Q_Q} + \boldsymbol{Q_Q Q_I} = \frac{j}{2} \begin{pmatrix} 0 & 0 & -1 & 0 & \cdots & 0 \\ 0 & 0 & 0 & -1 & \ddots & \vdots \\ 1 & 0 & 0 & 0 & \ddots & 0 \\ 0 & 1 & 0 & 0 & \ddots & -1 \\ \vdots & \ddots & \ddots & \ddots & \ddots & 0 \\ 0 & \cdots & 0 & 1 & 0 & 0 \end{pmatrix}. \tag{4.140}$$

More generally, if we denote by $\boldsymbol{Q_{I,J}}$ and $\boldsymbol{Q_{Q,J}}$ the $\boldsymbol{Q_I}$ and $\boldsymbol{Q_Q}$ matrices for the standard form with a delay of J samples, then (see Appendix B.2.7):

$$\boldsymbol{Q_{I,J}} \boldsymbol{Q_{Q,J}} + \boldsymbol{Q_{Q,J}} \boldsymbol{Q_{I,J}} = \boldsymbol{Q_{Q,2J}}. \tag{4.141}$$

Thus, Z_I and Z_Q are uncorrelated only when $\boldsymbol{\mu}^{\mathrm{H}} \boldsymbol{Q_{Q,2J}} \boldsymbol{\mu} = \mathbf{0}$. This can easily be seen to correspond to the case $Z_Q = 0$ (*i.e.* either in the case of no signal, or in the presence of signal with zero Doppler shift and no data modulation) for the DCCD with a delay of $2J$ samples.

It is also interesting to note, from Equation (4.129), that the variances of Z_I and Z_Q are generally different. We, therefore, approximate the joint distribution of Z_I and Z_Q as a bivariate normal distribution with mean and covariance matrix given by:

$$\boldsymbol{\mu}_Z = \begin{pmatrix} \boldsymbol{\mu}^{\mathrm{H}} \boldsymbol{Q_I} \boldsymbol{\mu} \\ \boldsymbol{\mu}^{\mathrm{H}} \boldsymbol{Q_Q} \boldsymbol{\mu} \end{pmatrix} \tag{4.142}$$

$$\boldsymbol{C}_Z = \begin{pmatrix} 2\sigma^4(N-J) + 4\sigma^2 \boldsymbol{\mu}^{\mathrm{H}} \boldsymbol{Q_I^2} \boldsymbol{\mu} & 2\sigma^2 \boldsymbol{\mu}^{\mathrm{H}} \boldsymbol{Q_{Q,2J}} \boldsymbol{\mu} \\ 2\sigma^2 \boldsymbol{\mu}^{\mathrm{H}} \boldsymbol{Q_{Q,2J}} \boldsymbol{\mu} & 2\sigma^4(N-J) + 4\sigma^2 \boldsymbol{\mu}^{\mathrm{H}} \boldsymbol{Q_Q^2} \boldsymbol{\mu} \end{pmatrix}, \tag{4.143}$$

respectively. Subsequent to the discussion of Section 4.3.2, it is interesting to note that this Gaussian approximation essentially limits our consideration of the effect of $\boldsymbol{P}^{-1}$ in the exponent of Equation (4.119) to the first three terms of the

power series expansion of Equation (4.120).

When the signal is subject to a constant residual Doppler frequency offset $\delta\omega_d$, such that:

$$\mu_i = A \exp\left(j\delta\omega_d T_{\text{coh}} J i\right), \tag{4.144}$$

then we can use the following identities:

$$\boldsymbol{\mu}^{\text{H}} \boldsymbol{Q_I} \boldsymbol{\mu} = (N-J)A^2 \cos(\delta\omega_d T_{\text{coh}} J) \tag{4.145}$$

$$\boldsymbol{\mu}^{\text{H}} \boldsymbol{Q_Q} \boldsymbol{\mu} = (N-J)A^2 \sin(\delta\omega_d T_{\text{coh}} J) \tag{4.146}$$

$$\boldsymbol{\mu}^{\text{H}} \boldsymbol{Q_I}^2 \boldsymbol{\mu} = A^2 \left\{ \frac{J}{2} + [N-2J] \cos^2\left(\delta\omega_d T_{\text{coh}} J\right) \right\} \tag{4.147}$$

$$\boldsymbol{\mu}^{\text{H}} \boldsymbol{Q_Q}^2 \boldsymbol{\mu} = A^2 \left\{ \frac{J}{2} + [N-2J] \sin^2\left(\delta\omega_d T_{\text{coh}} J\right) \right\} \tag{4.148}$$

$$\boldsymbol{\mu}^{\text{H}} \boldsymbol{Q}_{\boldsymbol{Q},2J} \boldsymbol{\mu} = (N-2J)A^2 \sin(2\delta\omega_d T_{\text{coh}} J), \tag{4.149}$$

to simplify Equations (4.142) and (4.143). Note also that when there is no signal present (*i.e.* $\boldsymbol{\mu} = \mathbf{0}$) the model reduces to a central χ^2 distribution with two degrees of freedom, generated from Gaussian rvs with variance $2\sigma^4(N-J)$.

This model is compared with simulated results in Figures 4.4 and 4.5. We use the same receiver setup as for the pair-wise form, *i.e.* a DCCD with: $J = 1$, $M = 1$, $K = 150$, $C/N_0 = 30$ dB-Hz; and the same test scenarios: 1) noise alone, 2) signal plus noise with no Doppler offset, 3) signal plus noise with 250 Hz constant Doppler offset and 4) signal plus noise with 450 Hz constant Doppler offset.

Figure 4.4 illustrates a scatter plot for each of the four test cases. Again, we include a contour of constant probability density in the (Z_I, Z_Q) plane, such that the probability (under the Gaussian model) that a random point is inside this contour is $p = 0.9$. In this case, the constant probability contours are ellipses (due to the fact that the variances are unequal) and not necessarily parallel to the $x-$ or $y-$axes (due to the correlation between Z_I and Z_Q). In [112] the authors also derived a Gaussian model of Z. However, they assumed that Z_I and Z_Q are independent with equal variances. Figure 4.4 clearly illustrates that this is not the case.

The accuracy of the new model is illustrated in Figure 4.5. Similar to Figure 4.3, we illustrate simulated and modelled plots of the PDFs and CDFs of Z_I and $R = \sqrt{Z_I^2 + Z_Q^2}$. In addition, in Figure 4.5 b) and d) we also include the

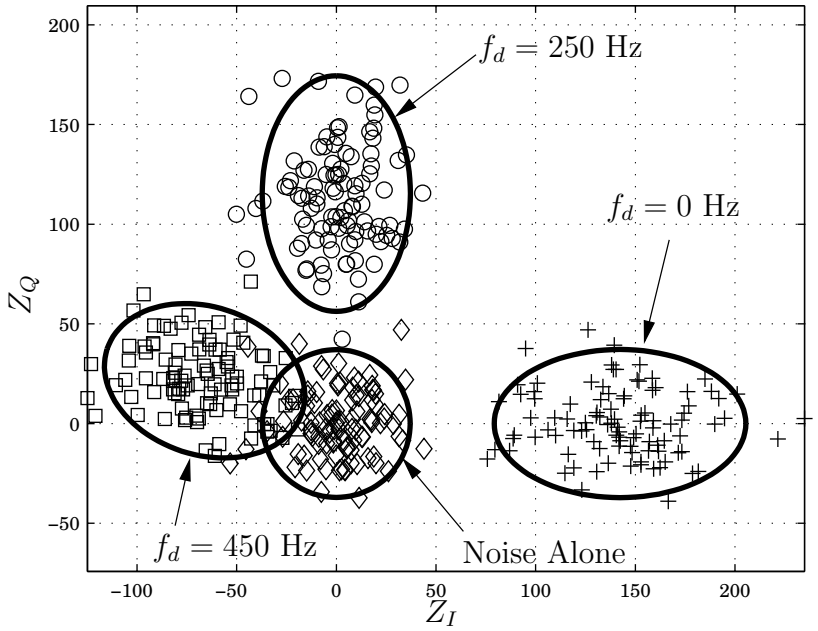


Figure 4.4: Scatter Plot for the Standard Form of the DCCD. Four cases are shown: 1) Noise alone; 2) Signal plus noise, with zero Doppler offset; 3) Signal plus noise $f_d = 250$ Hz; and 4) Signal plus noise $f_d = 450$ Hz. In each case an ellipse has been drawn such that the probability that the random point (Z_I, Z_Q) is inside that ellipse is 0.9. One hundred random points are plotted in each case.

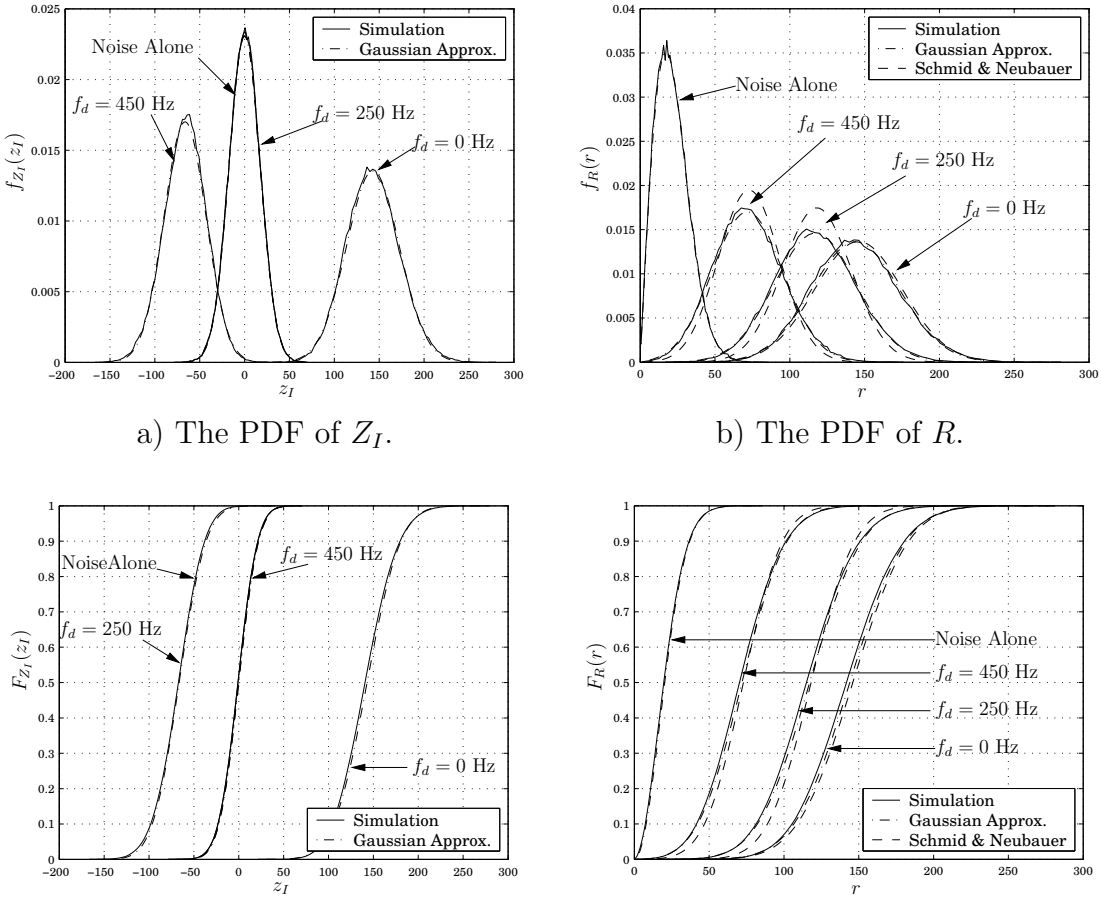
Schmid and Neubauer [112] approximation. The accuracy of our model, and its superiority to the previous model, is clear from the plots.

4.4 Performance Comparisons

Having obtained expressions for P_d and P_{fa} for all the detector forms above, we now endeavour to determine which detector is most suited to any given application.

Recall that, for a received signal with a given set of parameters $\boldsymbol{\theta}$, the performance of a detector is completely defined by three quantities:

1. The probability of correct detection P_d.
2. The probability of false alarm P_{fa}.
3. The dwell time τ_D.



a) The PDF of Z_I.

b) The PDF of R.

c) The CDF of Z_I

d) The CDF of R.

Figure 4.5: PDFs and CDFs of Z_I and $R = \sqrt{Z_I^2 + Z_Q^2}$ for the Standard Form of the DCCD. In each case $100,000$ trial points were generated and the result compared with the Gaussian approximation.

In addition, we have already seen (in Section 2.3) that, given perfect estimation of the signal parameters, the ML detector is optimal, in the sense that it yields the maximum P_d for a given P_{fa} and τ_D. However, in practice we cannot achieve perfect signal parameter estimation, and so must resort to sub-optimal techniques. The question of interest in this section is: what is the best choice of detector, for a given set of design constraints, given an imperfect estimate of the signal parameters?

We consider two criteria for determining the best detector:

1. Minimisation of the dwell time for a given operating point (P_{fa}, P_d).

2. Maximisation of P_d for a given dwell time and P_{fa}.

The second criterion above is essentially the Neyman-Pearson criterion. The first, however, is of greater interest in the acquisition problem. Recall from Section 2.3 that Wald and Wolfowitz [145] showed that the sequential detector is optimal according to this criterion. The sequential detector is very sensitive to variation in SNR, however, and so is not considered in this thesis.

In the following sections, we apply two common techniques of receiver performance analysis:

1. Deflection coefficients (also known as detection indices).
2. Receiver operating characteristic (ROC) curves.

4.4.1 Deflection Coefficients

For a given signal parameter vector, $\boldsymbol{\theta}$, the performance of a receiver is described by a point in the three dimensional space (τ_D, P_{fa}, P_d). When determining receiver performance it is often useful to have a single metric, d, which encapsulates as much information about this point as possible. This can be thought of as a form of compression, or a projection from three dimensional space onto a single dimension.

A commonly used metric is the *deflection coefficient*, or *detection index*, defined by [54]:

$$d^2 \triangleq \frac{\left(E[D_k(\boldsymbol{\theta}) \mid H_1] - E[D_k(\boldsymbol{\theta}) \mid H_0]\right)^2}{\mathrm{Var}\left[D_k(\boldsymbol{\theta}) \mid H_0\right]}\,, \tag{4.150}$$

where $D_k(\boldsymbol{\theta})$ is the detector decision statistic for satellite k with signal parameters $\boldsymbol{\theta}$. The utility of this metric arises from the assumption that the statistics of the receiver are approximately Gaussian under both H_0 and H_1. In this case, d encapsulates *all* the information regarding receiver performance. In other words, if:

$$D_k(\boldsymbol{\theta}) \sim \mathrm{N}(\mu, \sigma^2)\,,$$

for some μ and σ, then a receiver with larger d will always outperform a receiver with smaller d in terms of (P_{fa}, P_d). Note that this makes no assumption about τ_D.

It has been clearly demonstrated in Section 4.3 that the distribution of $D_k(\boldsymbol{\theta})$ for differentially coherent receivers is not Gaussian.

The deflection coefficient for the NCCD is well known [142] to be given by:

$$d_{NCCD} = \frac{\boldsymbol{\mu}^{\mathrm{H}}\boldsymbol{\mu}}{2\sqrt{K}\sigma_Y^2} = \frac{\lambda}{2\sqrt{K}\sigma_Y^2} \tag{4.151}$$

Applying the results of the previous two sections to Equation (4.150) yields new expressions for the deflection coefficients of the differentially coherent detector/ estimator forms:

$$d_{DCCD} = \frac{\left(\boldsymbol{\mu}^{\mathrm{H}}\boldsymbol{Q_I}\boldsymbol{\mu}\right)^2 + \left(\boldsymbol{\mu}^{\mathrm{H}}\boldsymbol{Q_Q}\boldsymbol{\mu}\right)^2 + 4\sigma_Y^2\boldsymbol{\mu}^{\mathrm{H}}\left(\boldsymbol{Q_I}^2 + \boldsymbol{Q_Q}^2\right)\boldsymbol{\mu}}{\sigma_Y^4\sqrt{48\alpha - 64\beta}} \tag{4.152}$$

$$d_{DCD} = \frac{\boldsymbol{\mu}^{\mathrm{H}}\boldsymbol{Q_I}\boldsymbol{\mu}}{\sigma^2\sqrt{2(NM-J)}}\,, \tag{4.153}$$

where:

$$\alpha = \begin{cases} (K-J)^2 & \text{standard form} \\ \left(\frac{K}{2}\right)^2 & \text{pair-wise form} \end{cases} \quad \beta = \begin{cases} \binom{K-J-1}{2} + J - 1 & \text{standard form} \\ \binom{\frac{K}{2}}{2} & \text{pair-wise form.} \end{cases} \tag{4.154}$$

Recall that σ^2 is the noise variance in either the in-phase or quadrature component at the output of the RF front-end, whilst σ_Y^2 is the noise variance in either the in-phase or quadrature component at the output of the coherent accumulator. Equations (4.152) and (4.153) are new.

As noted above, the Gaussian assumption made in the derivation of the deflection coefficient above is not valid for the DCCD. Another useful metric, based on Equation (4.150) can be obtained in a heuristic fashion. All of the statistics we deal with consist of *unimodal* distributions, by which we mean distributions consisting of a single peak. The deflection coefficient of Equation (4.150) can be viewed as a (normalised) measure of the distance between the peak of the decision statistic under H_0 and its peak under H_1. In Equation (4.150) the metric is normalised by the variance of the statistic under H_0, which is a measure of the spread of the distribution about the mean. In Gaussian detection the variance under H_1 is the same as the variance under H_0. In non-Gaussian systems the

following alternative deflection coefficient has been suggested in the literature:

$$d^2 = \frac{\left(E[D_k(\boldsymbol{\theta}) \mid H_1] - E[D_k(\boldsymbol{\theta}) \mid H_0]\right)^2}{\frac{1}{2}\left(\mathrm{Var}\left[D_k(\boldsymbol{\theta}) \mid H_1\right] + \mathrm{Var}\left[D_k(\boldsymbol{\theta}) \mid H_0\right]\right)} \,. \tag{4.155}$$

Note that this differs from Equation (4.150) only in the denominator term. In effect, the normalisation factor $\mathrm{Var}\left[D_k(\boldsymbol{\theta}) \mid H_0\right]$ has been replaced by the average of the variances under H_0 and H_1.

We were unable to obtain a simple closed-form expression for $\mathrm{Var}\left[R^2\right]$ for the standard form of the DCCD. For the pair-wise form, however, the following relatively simple expression can be obtained using the CHF approach of Section 4.3.3:

$$\mathrm{Var}\left[R^2\right] = 4\sigma^8\left[3K^2 - 16\binom{\frac{K}{2}}{2}\right] + 8\sigma^2\left(|\kappa|^2 + \sigma^2\lambda\right)\left[(K+4)\sigma^2 + \frac{\lambda}{2}\right] \tag{4.156}$$

4.4.2 Receiver Operating Characteristic Curves

The receiver operating characteristic (ROC) curve is a plot of P_d vs P_{fa} for a given set of receiver and signal parameters [142]. Some useful properties of receiver operating characteristic (ROC) curves include:

1. The ROC curve of the ML detector is always concave down, *i.e.* the slope dP_d/dP_{fa} is always positive and the rate of change of slope, *i.e.* $d^2P_d/{dP_{fa}}^2$, is less than or equal to zero.

2. Every ROC curve contains the points $(0, 0)$ and $(1, 1)$.

3. The curve is always above the line $P_d = P_{fa}$ (called the "chance line"). If the ROC dipped below this line then random guessing would yield better performance.

4. The ML detector is optimal and, consequently, the ROC of any detector must be on or below the ROC of the ML detector.

Note that points 3 and 4 above give (loose) bounds on detector performance.

A sample ROC curve is given in Figure 4.6, which depicts the curves for the ML detector (upper bound), NCCD detector and DCCD in both pair-wise and standard forms, for a received signal with $C/N_0 = 29.8$ dB-Hz and system parameters $M = 1$, $J = 1$ and $K = 74$. There are no residual frequency or code

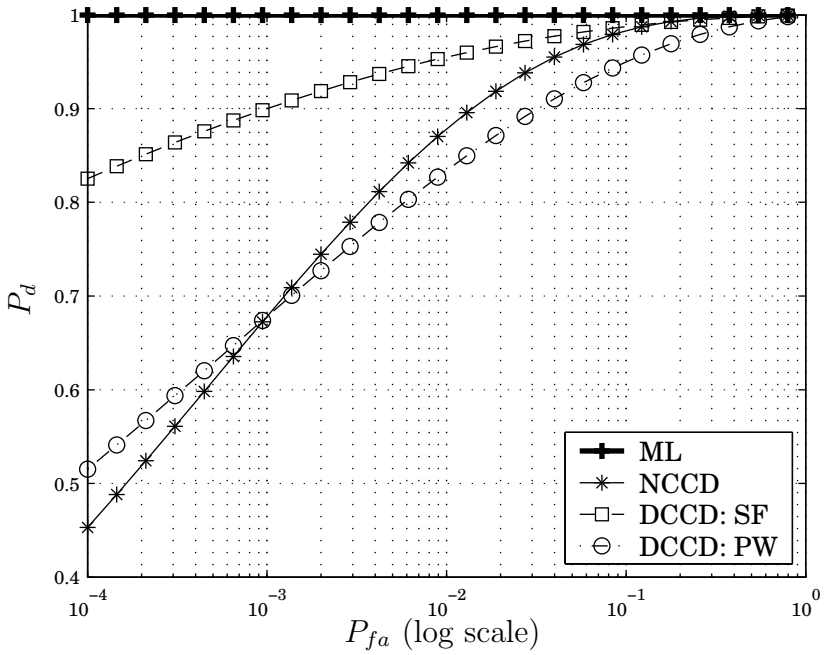


Figure 4.6: ROC Curve Comparison for NCCD and the Two Forms of DCCD. $C/N_0 = 29.8$ dB-Hz, $M = 1$, $J = 1$, $K = 74$. Note that P_{fa} is shown on a logarithmic scale, whereas P_d is shown on a linear scale.

phase offsets and the signal is assumed free of data modulation. Note that the ideal receiver has a curve that is as close as possible to the upper left corner.

The particular set of curves shown in Figure 4.6 is interesting for a number of reasons. Firstly, for C/N_0, M and J given as above, then, according to our Gaussian model, the choice of $K = 74$ is the smallest value of K for which the standard form of the DCCD achieves the performance point ($P_{fa} = 10^{-3}, P_d = 0.9$). Secondly, we can clearly see that the curves for the NCCD and the pair-wise form of the DCCD meet in the region of $P_{fa} = 10^{-3}$. Thirdly, we see that the performances of all detector types are significantly poorer than the optimal, ML form[†].

Whilst from the figure it would appear that both forms of the DCCD significantly outperform the NCCD when $P_{fa} < 10^{-4}$, it is important to be aware that this figure is generated using the Gaussian models of the preceding sections. As previously discussed, these approximations are *least* accurate in the tails of the distribution. We have also already remarked, in Section 4.3.1, that the distribution of the decision statistic of the DCCD is heavy–tailed, and for this reason

[†]Note that, while the ML receiver appears to yield a P_d of unity this is not, in fact, the case.

also one should not expect a high degree of accuracy at very low P_{fa}. Thus, we cannot be certain, from the models that we have developed, that the performance gain of the DCCD at low P_{fa} (in particular in the standard form) is as significant as it would appear.

This is illustrated in the (extreme) example of Figure 4.7. Again, we consider a system operating in the absence of data modulation and parameter estimation error. The receiver parameters in this case are $C/N_0 = 29.8$ dB-Hz, $M = 5$, $J = 1$ and $K = 6$. From Figure 4.7 a), it would appear that both forms of the

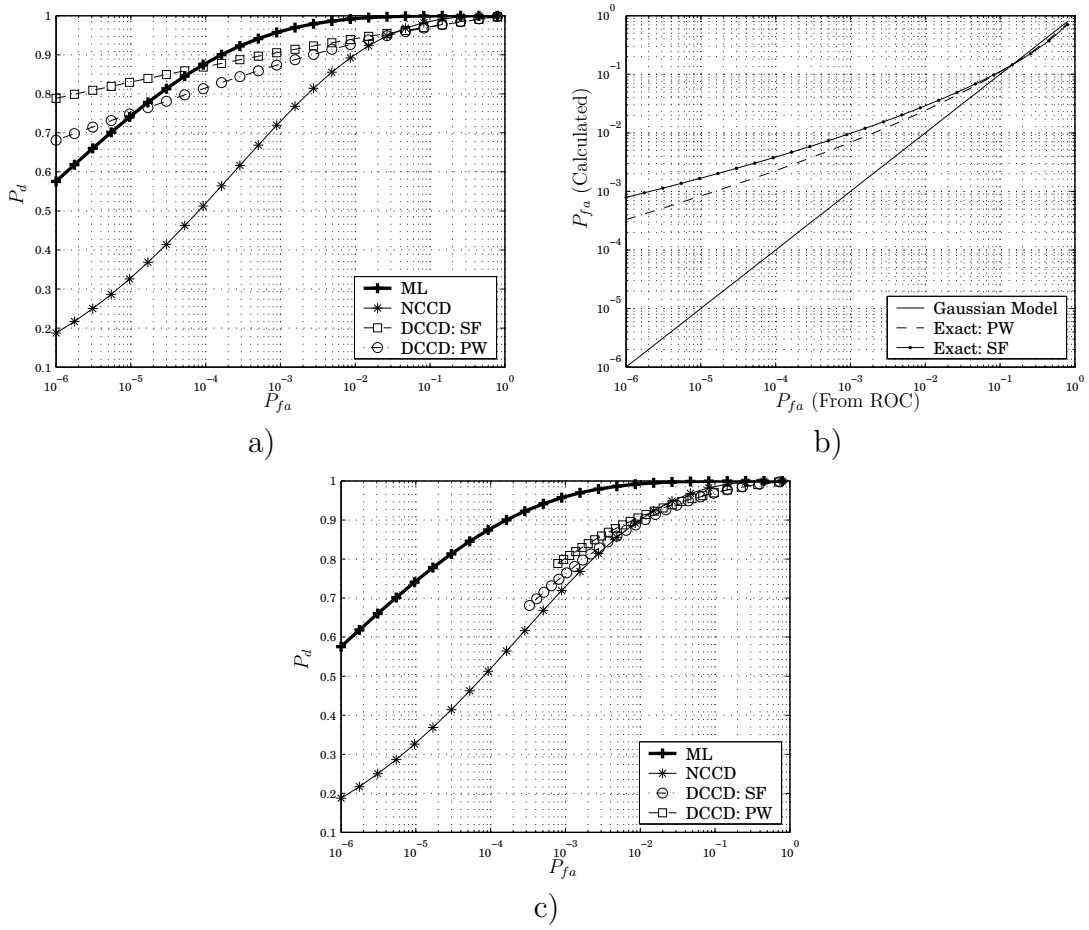


Figure 4.7: ROC Curve Demonstrating Limitations of the Gaussian Model. $C/N_0 = 29.8$ dB-Hz, $M = 5$, $J = 1$ and $K = 6$. a) Shows the ROC curve calculated using the Gaussian model. b) Plots the value of P_{fa} determined using Equations (4.78) and (4.118) (y-axis) vs the value of P_{fa} calculated using the Gaussian model (x-axis). c) Shows the same ROC curve calculated using the exact equations for P_{fa}.

DCCD actually *outperform* the ML detector at $P_{fa} < 10^{-5}$. This is impossible

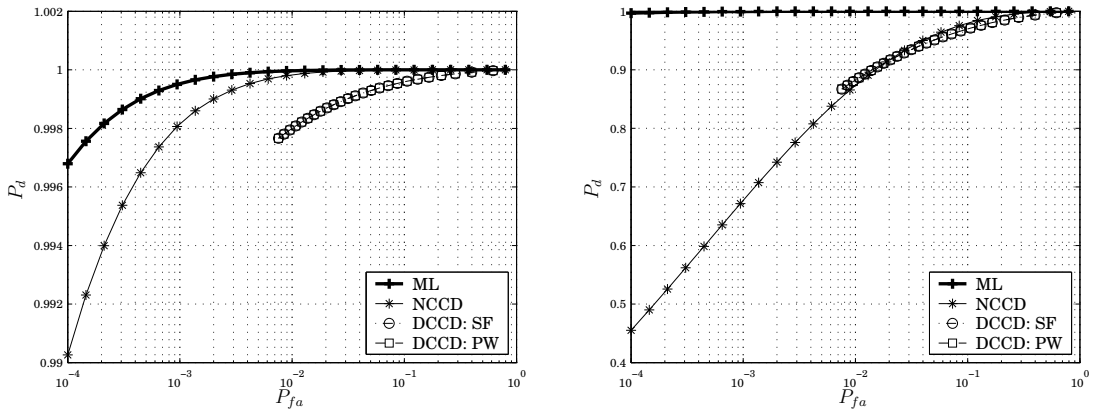
by the definition of the ML detector. The reason for this error can be seen in Figure 4.7 b), where we have used two methods to determine P_{fa}. In the first case we have used the set of values for the threshold voltage V_{Th} used in generating Figure 4.7 a) in the Gaussian model of Equation (4.139) (solid line). In the second case we have used the same values of V_{Th} in the exact expression for the CDF of the decision statistic of Equation (4.78) (dashed line). Note that when the Gaussian model indicates that $P_{fa} = 10^{-5}$, the exact model indicates that it is, in fact, closer to 10^{-3}, a factor of two orders of magnitude. Finally, in Figure 4.7 c), the same ROC curve is illustrated, with the same values of V_{Th} but using the exact expressions for the calculation of P_{fa}[†]. It is clear from this figure that the DCCD does not, in fact, violate the optimality of the ML detector. We have referred to this an extreme case because, in addition to the sources of error discussed above, K is small and our Gaussian model is based on the application of the central limit theorem, which is more accurate as $K \to \infty$.

Two important points should be noted from the above analysis: 1) one should be skeptical of results obtained using the Gaussian model, particularly in the tails of the distribution; 2) the exact expression for the distribution of the decision statistic under H_0 in the pair-wise form (Equation (4.78)) provides us with a very useful tool for detecting false results of this kind.

In the following we use the exact expressions for P_{fa} when $K < 27$, otherwise the Gaussian approximations are used. The effect of Doppler offset on the ROC curve is illustrated in Figure 4.8, which shows the ROC curves for a receiver with $C/N_0 = 43.8$ dB-Hz, $M = 1$, $J = 1$ and $K = 2$. In Figure 4.8 a) there is no Doppler offset and in Figure 4.8 b) there is a Doppler offset of 500 Hz. Note that, for $K = 2$, the standard and pair-wise forms of the DCCD are identical. Due to the small value of K, the exact method is used in the calculation of P_{fa}. Note that the NCCD significantly outperforms the DCCD forms in the absence of Doppler shift. At $f_d = 500$ Hz the performance of the DCCD is very similar to that of the NCCD.

As we have previously seen in Chapter 3, the presence of a Doppler shift leads to a degradation in system performance. However, from Figure 4.8 we see that the NCCD seems to suffer greater degradation than the DCCD, under the conditions described above. Note that, from our consideration of the signal effects alone in Chapter 3, it would have been expected that the DCCD would experience greater

[†]The Gaussian model is used to calculate P_d.

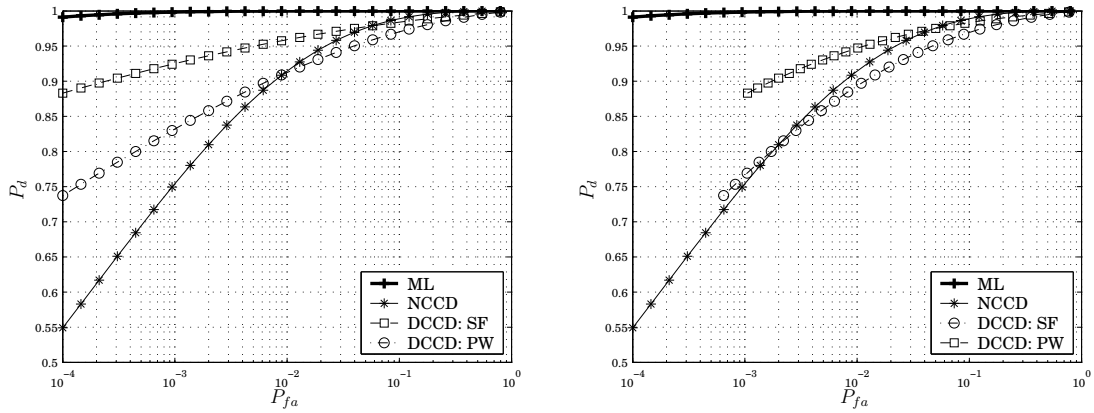


a) b)

Figure 4.8: Doppler Effect on ROC Curve. $C/N_0 = 43.8$ dB-Hz, $M = 1$, $J = 1$ and $K = 2$. a) $f_d = 0$ Hz, b) $f_d = 500$ Hz.

losses due to carrier Doppler than the NCCD. In taking noise effects into account, however, we see that the opposite is true. Nonetheless, the NCCD is a superior choice of receiver given the signal parameters discussed above.

A comparison of the Gaussian model and the exact approach is given in Figure 4.9, in which a system with $C/N_0 = 33.8$ dB-Hz, $M = 1$, $J = 1$, $K = 18$ and $f_d = 0$ is illustrated. In Figure 4.8 a) both P_{fa} and P_d are calculated using the Gaussian approximation whereas, in Figure 4.8 b), P_{fa} is calculated using the exact equations. While the inaccuracy of the Gaussian model is clear from the



a) b)

Figure 4.9: Gaussian Model vs Exact Calculation for ROC Curves. $C/N_0 = 33.8$ dB-Hz, $M = 1$, $J = 1$ and $K = 18$. a) Gaussian model, b) Exact calculation of P_{fa}.

curves, we see that the trend is similar in both figures. In this case, the NCCD seems to be superior for large values of P_{fa}, whereas the standard form of DCCD is superior at very low P_{fa}.

In Figure 4.10 the ROC curves (left hand column) and the corresponding plots showing the accuracy of the Gaussian approximation (right hand column) are shown for various received power levels. In each case, the receiver parameters have been chosen to yield the operating point ($P_{fa} = 10^{-3}, P_d = 0.9$). A number of observations can be noted from these plots. Firstly, whereas we have previously seen that the NCCD outperforms the DCCD when the signal level is relatively high ($C/N_0 \geq 35$), it is clear from Figure 4.10 that the standard form of the DCCD is significantly better at lower received power levels (in each case the NCCD has $P_d < 0.7$). Secondly, from the right hand column plots, we see that our Gaussian approximation is increasingly accurate as K increases, as expected. Thirdly, for each 5 dB decrease in signal power, an approximately eight-fold increase in dwell time is required to achieve the operating point ($P_{fa} = 10^{-3}, P_d = 0.9$). Finally, the pair-wise form of the DCCD is always a poorer choice than either the NCCD or the standard form of the DCCD for all the cases considered in Figure 4.10. Therefore, the pair-wise form will not be considered further here.

It is important to note that all these ROC curves have been generated using the Gaussian approximation and code Doppler, data modulation and Doppler rate effects have been ignored.

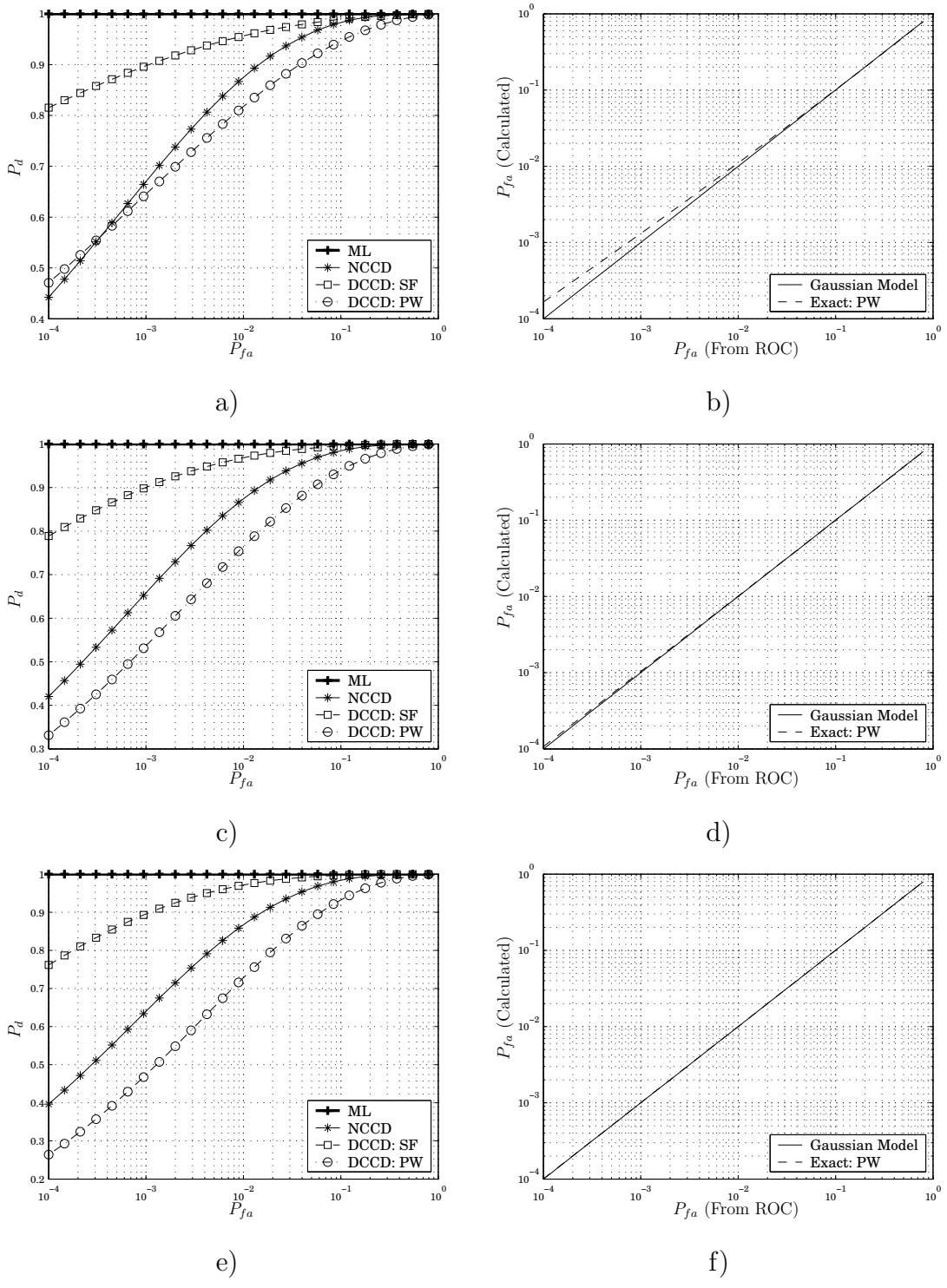


Figure 4.10: Effect of Received Power Level on ROC Curves. $M = 1$, $J = 1$. Left hand plots: ROC curves. Right hand plots: Gaussian model vs exact calculation of P_{fa}. a) and b) $C/N_0 = 28.8$ dB-Hz, $K = 110$. c) and d) $C/N_0 = 23.8$ dB-Hz, $K = 925$. e) and f) $C/N_0 = 18.8$ dB-Hz, $K = 8500$.

4.5 Parallel Forms

Thus far in this chapter, we have considered only the analysis of the single cell detector. We now turn our attention to the analysis of parallel forms of the detector/estimator.

Recall that the parallel form of the detector/estimator calculates the decision statistic $D_k(\widehat{\boldsymbol{\theta}})^{\dagger}$ for multiple parameter estimates simultaneously. We denote by C_{T} the number of such statistics calculated and denote by $D_{k,i}$ the i^{th} output, where the dependence on the parameter estimate $\widehat{\boldsymbol{\theta}}_i$ is implicit. We assume that the set $\{D_{k,i} \ : \ i = 0, 1, \ldots C_{\mathrm{T}} - 1\}$ covers an area of C_{T} *cells* of the uncertainty region. We call this coverage a *tile* and denote by Θ_l the area of the uncertainty space covered by the l^{th} tile. We assume that the total uncertainty space Θ is divided into N_{T} *disjoint* tiles, containing C_{T} cells each (see Figure 2.18). The advantage of this model is that we can assume that the C_{T} decision statistics within any given tile are statistically independent. Thus, our analysis of the SCD can be applied to each component of the parallel form.

Denoting by $\boldsymbol{\theta_t}$ the true vector of signal parameters, then the hypothesis that $\boldsymbol{\theta_t} \notin \Theta_l$ is denoted H_0, and the alternate hypothesis, $\boldsymbol{\theta_t} \in \Theta_l$, is denoted H_1. A tile containing $\boldsymbol{\theta_t}$ is referred to as a H_1 tile, in general we assume that there is only on H_1 tile in the uncertainty region, though in Section 5.2 we shall consider the effect of two H_1 tiles on the acquisition process. All other tiles are referred to as H_0 tiles.

Denoting by $f_{D_{k,i}}(x)$ the PDF of $D_{k,i}$ and by $F_{D_{k,i}}(x)$ its CDF, then the probability that all the decision statistics within a tile fall below the decision threshold is given by (see Section 2.4.4):

$$\Pr\left\{\max_i D_{k,i} < V_{\mathrm{Th}}\right\} = \prod_{i=0}^{C_{\mathrm{T}}-1} F_{D_{k,i}}(V_{\mathrm{Th}})\,. \tag{4.157}$$

Thus, under H_0, we have:

$$P_{r_0} = \prod_{i=0}^{C_{\mathrm{T}}-1} F_{D_{k,i}}(V_{\mathrm{Th}}) \tag{4.158}$$

$$P_{fa_0} = 1 - P_{r_0},, \tag{4.159}$$

[†]Remember that the subscript k indicates that the detector is testing for the presence of a signal from satellite k.

where P_{r_0} and P_{fa_0} denote the probability of rejection and false alarm under H_0, respectively. Under H_1 it is assumed that at least one of the $D_{k,i}$ contains both signal and noise. Let $\mathcal{I}$ denote the set of indices such that $\forall i \in \mathcal{I}$, $D_{k,i}$ contains signal and noise and $\forall i \notin \mathcal{I}$, $D_{k,i}$ contains noise alone. From Equation (2.81) we then have:

$$P_{r_1} = \prod_{i=0}^{C_\mathrm{T}-1} F_{D_{k,i}}(V_\mathrm{Th}) \tag{4.160}$$

$$P_d = \sum_{n\in\mathcal{I}} \int_{V_\mathrm{Th}}^{\infty} f_{D_{k,n}}(x) \prod_{\substack{i=0 \\ i\neq n}}^{C_\mathrm{T}-1} F_{D_{k,i}}(x) d\,x \tag{4.161}$$

$$P_{fa_1} = 1 - P_{r_1} - P_d\,, \tag{4.162}$$

where P_d denotes the probability of detection and P_{r_1} and P_{fa_1} denote the probabilities of rejection and false alarm under H_1, respectively. Note that in the parallel form there is a possibility of a false alarm occurring within a H_1 tile, which was impossible in the SCD. In the following we assume that there is only one H_1 cell within a H_1 tile, or $\mathcal{I} = \{n\}$, where n is the index of the H_1 cell within the H_1 tile. Thus, we can re-write Equation (4.161) as:

$$P_d = \int_{V_\mathrm{Th}}^{\infty} f_{D_{k,n}}(x) \prod_{\substack{i=0 \\ i\neq n}}^{C_\mathrm{T}-1} F_{D_{k,i}}(x) d\,x\,. \tag{4.163}$$

Note that Equation (4.163) resembles the expression for the complement of the CDF of an rv representing the maximum (or peak) of C_T χ^2 rvs, given that the n^{th} χ^2 rv is the largest. This rv is denoted $P_{k,n}$ and its distribution is given by:

$$f_{P_{k,n}}(x) = f_{D_{k,n}}(x) \prod_{\substack{i=0 \\ i\neq n}}^{C_\mathrm{T}-1} F_{D_{k,i}}(x)\,. \tag{4.164}$$

Note that $f_{P_{k,n}}(x)$ is not a true PDF[†], since:

$$\int_{-\infty}^{\infty} f_{P_{k,n}}(x) d\,x \neq 1. \tag{4.165}$$

However, we can treat it as the parallel analogue of $f_{D_{k,n}}(x)$, the PDFof the decision statistic under H_1 for the SCD.

A number of important observations can be made using this model. Firstly:

$$\int_{V_{\mathrm{Th}}}^{\infty} f_{D_{k,n}}(x) \prod_{\substack{i=0 \\ i\neq n}}^{C_{\mathrm{T}}-1} F_{D_{k,i}}(x) d\,x \leq \int_{V_{\mathrm{Th}}}^{\infty} f_{D_{k,n}}(x) d\,x\,, \tag{4.166}$$

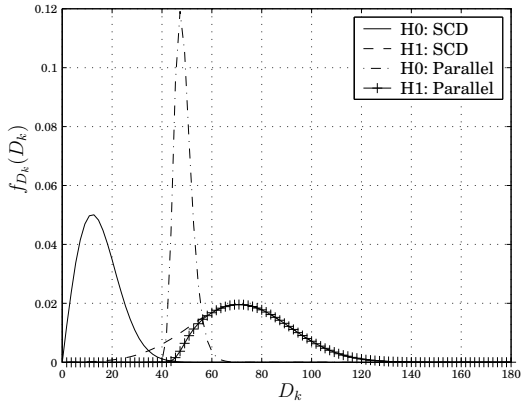
i.e. the probability of correct detection in a H_1 tile in the parallel detector is *less* than the probability of correct detection in a H_1 cell in the SCD, for the same V_{Th}. Similarly, the probability of false alarm in a H_0 tile in the parallel form is *greater* than or equal to the P_{fa} in a H_0 cell in the SCD, again for the same V_{Th}. Thirdly, at $V_{\mathrm{Th}} = 0$, $P_{fa_0} = 1$ but $P_d < 1$.

These three observations imply that the ROC curve of a parallel detector will always be inferior to that of the equivalent single cell form. The benefit of the parallel form, of course, is that the SCD takes C_{T} times as long to cover the same area of the uncertainty space. To achieve the same performance level in terms of (P_{fa_0}, P_d) the parallel form requires a longer dwell time. Provided this dwell time increase factor is less than C_{T} then the parallel detector can achieve better performance than the single cell detector.

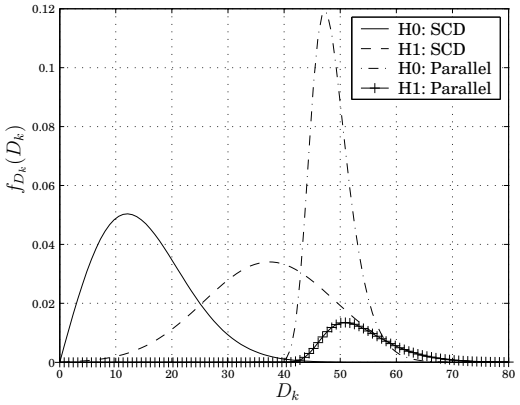
This is demonstrated in Figure 4.11, which illustrates the same system and signal parameters as those of Figure 4.6, and also includes the effect of parallelism with $C_{\mathrm{T}} = 2048$. In each case, we see that the parallel form leads to a significant shift to the right in the distribution under H_0. This, in turn, leads to an erosion of the main lobe of the distribution under H_1. Thus, the effect of parallelism for a given V_{Th} is two-fold: 1) P_{fa_0} is increased; 2) P_d is decreased.

Recall that, for the single cell detector, as the threshold tends to zero both P_{fa_0} and P_d tend to one. In the parallel form, however, there is a non-zero probability of false alarm in the H_1 tile when the threshold is zero and, hence, $P_d < 1$. Thus

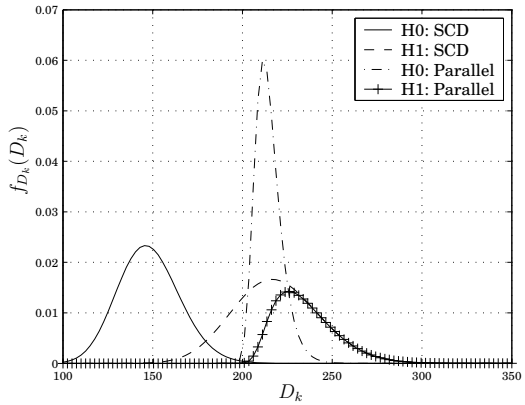
[†]In fact $f_{P_{k,n}}(x)$ can be viewed as the conditional PDF of $D_{k,n}$ *given* that $D_{k,n}$ is the largest decision statistic in the tile, multiplied by the probability that $D_{k,n}$ is, in fact, the largest statistic in the tile. Thus $P_{k,n}$ denotes a normalisation of the value of the peak decision statistic, given that $D_{k,n}$ is the peak.



a) DCCD Standard Form



b) DCCD Pair Wise Form



c) NCCD.

Figure 4.11: Effect of Parallelism on the Distribution of the Decision Statistic. $C/N_0 = 29.8$ dB-Hz, $M = 1$, $J = 1$, $K = 74$ and $C_{\mathrm{T}} = 2048$.

there is a maximum possible probability of detection, denoted $P_{d\max}$, that can be achieved by the parallel detector. Similarly, there is a corresponding maximum value of P_{fa_1}, denoted $P_{fa_{1\max}}$, which occurs when $V_{\mathrm{Th}} = 0$ and is related to $P_{d\max}$ by the simple relationship:

$$P_{fa_{1\max}} = 1 - P_{d\max}. \tag{4.167}$$

Following Milstein et al. [85], a union bound for $P_{fa_{1\max}}$ can be obtained as follows:

$$P_{fa_{1\max}} \leq \sum_{\substack{j=1 \\ j\neq n}}^{C_{\mathrm{T}}} \Pr\left\{D_k(\boldsymbol{\theta_j}) > D_k(\boldsymbol{\theta_n}) \;\middle|\; \boldsymbol{\theta_t} = \boldsymbol{\theta_n}\right\}. \tag{4.168}$$

Letting $P_{j,n}$ denote the probability that the j^{th} component of the decision statistic

vector exceeds the n^{th}, Milstein et al. [85] derived the following expression for the ML detector:

$$P_{j,n}\Big|_{\text{ML}} = \frac{1}{2}\left[1 - Q_1\left(\sqrt{b}, \sqrt{a}\right) + Q_1\left(\sqrt{a}, \sqrt{b}\right)\right], \tag{4.169}$$

where a and b are the SNR in the H_0 and H_1 cells, respectively. This is the probability that one χ^2 distributed rv with two degrees of freedom exceeds another. For the NCCD the equivalent expression involves the probability that one χ^2 distributed rv with $2K$ degrees of freedom exceeds another. This quantity has received much attention in the past in the context of the determination of error probabilities in binary multichannel communications (see [101, 120, 122] and [102, Appendix B], for example). In Appendix B.2.8 we derive the following simple analytic expression for the probability that the decision statistic in a H_0 cell exceeds that in the H_1 cell for the NCCD:

$$P_{j,n}\Big|_{\text{NCCD}} = \frac{1}{2^{2K-1}} \sum_{k=0}^{2K-1} \binom{2K-1}{k} Q_{K-k}\left(\sqrt{a}, \sqrt{b}\right). \tag{4.170}$$

Note that this expression involves the Marcum Q-function of *negative* order, which has been defined in Appendix B.2.8. Equation (4.170) can easily be re-arranged to include only Marcum Q-functions with positive order, to yield:

$$P_{j,n}\Big|_{\text{NCCD}} = \frac{1}{2^{2K-1}} \sum_{k=1}^{K} \binom{2K-1}{K-k} \left\{Q_k\left(\sqrt{a}, \sqrt{b}\right) + \left[1 - Q_k\left(\sqrt{b}, \sqrt{a}\right)\right]\right\}. \tag{4.171}$$

Note that Equation (4.171) reduces to Equation (4.169) when $K = 1$.

For large values of K, Equations (4.170) and (4.171) become difficult to compute, due to the large values of the binomial coefficients and the Marcum Q-functions of large order. In such cases, we use a saddle point integration technique

to evaluate the complex contour integral (see [102, 135]):

$$P_{j,n}\Big|_{\text{NCCD}} = \frac{1}{2^{2K-1}} \frac{1}{2\pi j} \oint_{\Gamma_0} \frac{(1+z)^{2K-1} f\left(\sqrt{a}, \sqrt{b}; z\right)}{(1-z)z^K} dz, \tag{4.172}$$

where Γ_0 denotes a closed contour in the complex z-plane enclosing the origin in an anti-clockwise direction, and:

$$f(a, b; z) \triangleq \exp\left(-\frac{1}{2}\left[a^2\left(1 - \frac{1}{z}\right) + b^2(1-z)\right]\right). \tag{4.173}$$

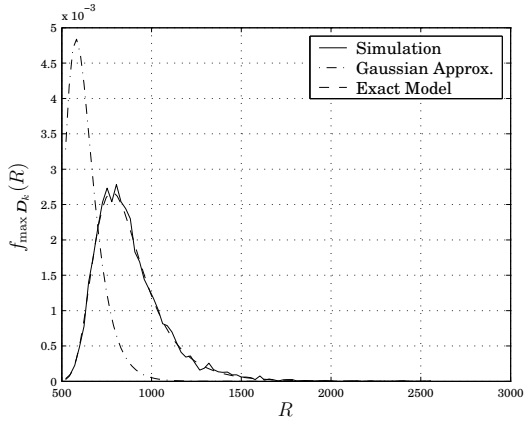
Note that this is a loose bound when K is large.

4.5.1 Analysis Issues

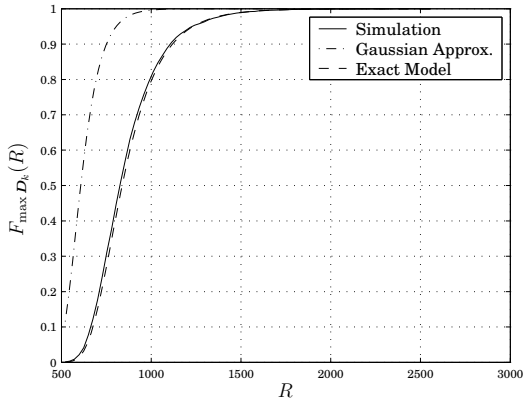
In Section 4.3 new analytical forms for the distribution of the decision statistic of differentially coherent forms of detector/estimator were introduced. For long observation intervals it was also seen that these new expressions are difficult to evaluate numerically, so a Gaussian approximation was made. This approximation was shown to be quite accurate for moderate to large observation intervals. However, as with all Gaussian approximations, this approximation is most accurate near the mean of the distribution and less accurate in the tails.

This poses a significant problem when analysing parallel forms. The decision statistic of the parallel form detector/estimator is given by the largest of C_{T} single cell forms, where C_{T} is typically of the order of 10^3. Additionally, the majority of those C_{T} cells are typically H_0 cells, *i.e.* they contain noise alone. The statistics of the parallel form detector/estimator are, therefore, dominated by the *tail* of the distribution of the single cell form under H_0, which is precisely where the Gaussian model is least accurate.

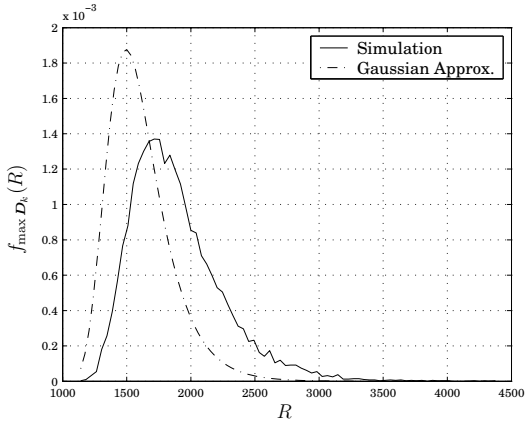
This difficulty is illustrated in 4.12, where the PDF and CDF of the decision statistic of the parallel form of DCCD under H_0 are illustrated. In each case the Gaussian approximation, a simulated result and, where possible, the exact form are represented. Note that, for $K = 20$ the Gaussian approximation, which is quite accurate for the single cell detector, is grossly inaccurate for the parallel form. Similarly, for $K = 50$ the Gaussian approximation is still not sufficiently accurate for use in system analysis or design. However, for $K = 500$ we see a very close alignment between the Gaussian approximation and the simulated results.



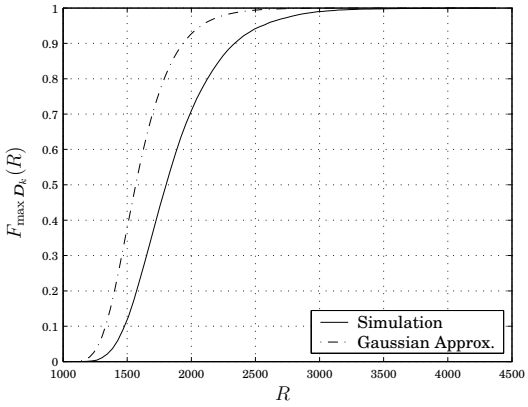
a) PDF: $K = 20$



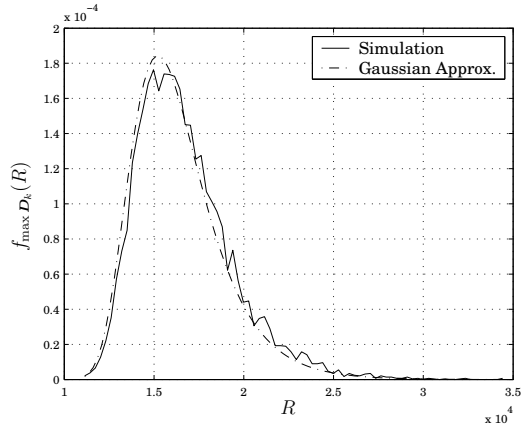
b) CDF: $K = 20$



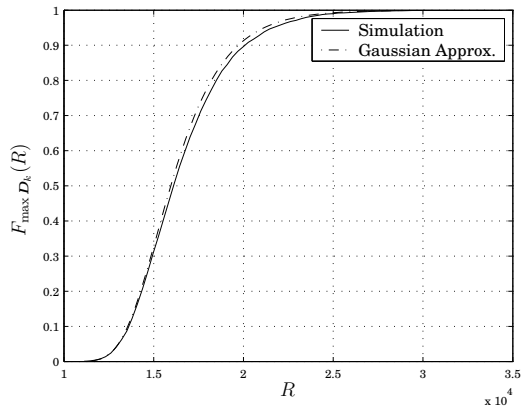
c) PDF: $K = 50$



d) CDF: $K = 50$



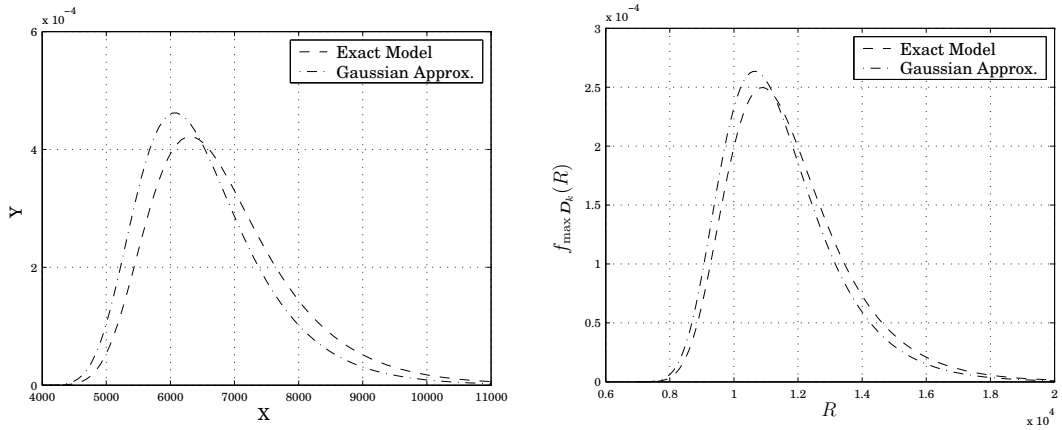
e) PDF: $K = 500$



f) CDF: $K = 500$

Figure 4.12: Error in Gaussian Approximation to the Maximum of $\boldsymbol{D}_k$ under H_0 for the standard form DCCD. $M = 1$, $J = 1$ and $C_{\mathrm{T}} = 2048$. Note that when $K \leq 27$ we can use the exact model, otherwise we must use the Gaussian model.

Ideally, to overcome this problem, a numerically stable and efficient method for computing Equation (4.117) would be devised. This is beyond the scope of this thesis, but would certainly be of interest. Alternatively, the near arbitrary precision capabilities of Mathematica$^{\text{TM}}$ can be leveraged to evaluate this expression. As previously mentioned, we have found that this requires increasing the internal variable `$MaxExtraPrecision`, and the resulting function evaluation, while accurate, takes a long time to compute (on the order of hours for K of the order of 10^2). Comparisons of the Gaussian approximation and the exact form as calculated in Mathematica$^{\text{TM}}$ are illustrated in Figure 4.13 for the cases $K = 200$ and $K = 350$.



a) $K = 200$ b) $K = 350$

Figure 4.13: Comparison of Gaussian Approximation and Exact Results from Mathematica$^{\text{TM}}$ of the PDF of the Maximum of $\boldsymbol{D}_k$ under H_0.

A third manner in which this computational difficulty can be overcome is simply to run Monte Carlo simulations to determine the system performance. Whilst this is not an attractive alternative, it may, in some cases, be less time consuming than using the exact form in Mathematica$^{\text{TM}}$.

4.6 Discussion

In Section 4.1 we demonstrated that a commonly used model for the PDF of the multi-dimensional complex Gaussian distribution is, in fact, not exact, but that it may be accurate at low SNR.

In Section 4.2, we briefly reviewed the well-known statistics of the NCCD, highlighting a useful technique for the calculation of the probability of detection.

We also summarised some useful approximations and bounds.

In Section 4.3, we derived some new results on the statistics of differentially coherent techniques. We adopted a characteristic function approach based on that of Jeong et al. [65] to derive a new, closed form, analytical expression for the distribution of the magnitude decision statistic of the pair-wise form of the DCCD. It was also demonstrated that this expression is identical to the K-distribution, which arises frequently in the (apparently unrelated) context of radar sea-echo. This result was subsequently extended to model the standard form, but the resulting expression is not suitable for numerical evaluation. A new, bivariate Gaussian approximation, valid for all forms of differentially coherent detector/estimator, was also derived, and was shown to be more accurate than existing models of the square magnitude statistic.

In Section 4.4, a brief performance comparison of the various forms of detector/estimator was conducted. This comparison centred around two performance metrics: 1) the deflection coefficient, 2) the receiver operating characteristic (ROC). New expressions for the deflection coefficients of each of the detector/ estimator forms were derived, and a new form of deflection coefficient introduced. The ROC curves, on the other hand, demonstrate that the single deflection coefficient provides insufficient information for a fair comparison of different detector types. From our Gaussian models it would appear that the NCCD outperforms the other detector types both in high SNR environments and when a large value of P_{fa} (*e.g.* $P_{fa} > 0.1$) can be tolerated. As SNR decreases, however, the standard form of the DCCD becomes a better choice.

The pair-wise form of differentially coherent combining detector would appear to have limited utility in practical situations. However, it is a very useful theoretical tool, as it is much easier to analyse than the standard form. In fact our analysis of the standard form arises directly from that of the pair-wise form, without which many of the results derived in this chapter might not have been so readily obtained.

Chapter 5

The Acquisition Process

Thus far, we have investigated the performance of the detector/estimator within a single search tile. In this chapter we begin our investigation of the acquisition process. Recall that this is the process which controls the detector/estimator, determining the search order for all tiles in the uncertainty region. Thus, whereas the detector/estimator determines the probabilities of correct detection, false alarm, etc. and dwell time within a tile, the acquisition process determines the search strategy, which has a significant effect on the overall acquisition time, T_{ACQ}.

In Section 2.5 we introduced the three *modes* of the acquisition process:

1. The search mode.
2. The verification mode.
3. The lock mode.

It has been common practice in the literature to consider a system wherein all three modes are specified and to provide a complete analysis in terms of the mean acquisition time $\overline{T}_{ACQ}$. Our analysis differs from the traditional approach only in that we consider each of the acquisition modes independently. Our logic in choosing such an approach is two-fold:

1. In essence, each mode can be viewed as an independent random process, thus each mode may be optimised independently.
2. In situations where weak signals are prevalent it is common to employ a positioning technique known as "snap-shot" positioning. In this case, a

position estimate is derived directly from the satellite signal parameter estimates obtained from the acquisition process, no tracking mode is employed and hence, no lock mode is required.

Our analysis in this chapter focuses on the search mode, as this is the most time-consuming part of the acquisition process. The results of this chapter were published in part in [88].

5.1 The One H_1 Tile Approximation

As discussed in Section 2.5, we model the search mode as a type of process known as a Markov chain.

5.1.1 The Markov Chain Model

In the search mode we assume the detector/estimator parameters are fixed. The state of the process is given by the search tile under investigation; the tiles being numbered in some appropriate manner. Two additional states are included to denote the possible end states of the search process; namely the detection state (D) and the false alarm state (FA). Thus, given N_{T} tiles in the uncertainty region, there are $N_{\mathrm{T}} + 2$ states in the Markov chain model of the search mode.

Following the convention of the circular state diagram method of Polydoros and Weber [99], the states are numbered according to how far away they are from the true H_1 state. The H_1 state itself is labelled state $N_{\mathrm{T}} - 1$.

Since here we consider the search mode only, the false alarm state will be treated as absorbing. Consequently, the statistics of the search mode will be the statistics of the first entry into the verification and lock modes, and will sometimes be called the "first hit statistics" of the receiver.

The circular state diagram is given in Figure 5.1 and is valid for any tile structure that divides the uncertainty space into N_{T} *disjoint* tiles. Under this model we make the assumption that only one tile in the uncertainty region is the correct, *i.e.* H_1, tile. Thus correct detection can only occur in one tile. We refer to this model as the "one H_1 tile approximation". In Section 5.2 we will investigate an improved model which allows for two H_1 tiles in the uncertainty region. The one H_1 tile approximation results in simpler, but less accurate, expressions for

the receiver performance parameters. Each approximation, therefore, has its advantages.

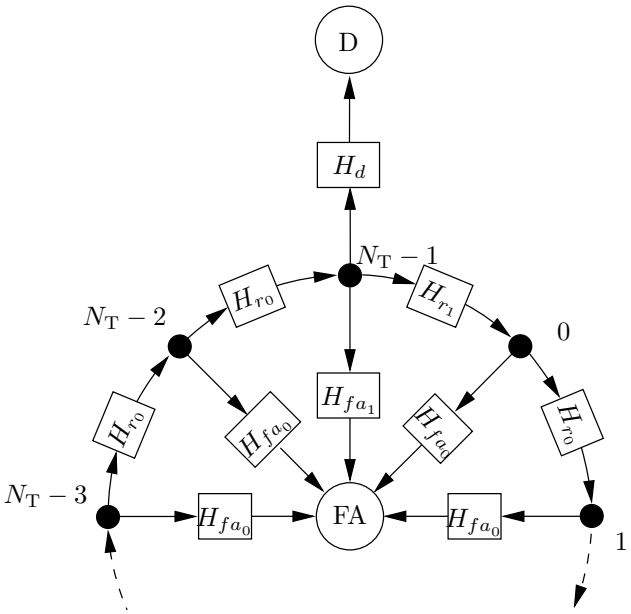


Figure 5.1: Circular State Diagram for the Search Mode Under the One H_1 Tile Approximation

Each path through the state space has a corresponding path transfer function, denoted by H. This transfer function incorporates information about the probability that the path is followed and the time taken to traverse the path. Each of the H_0 states has two paths associated with it: 1) H_{r_0}: in which the tile is rejected and the process moves on to the next state; 2) H_{fa_0}: in which the tile is incorrectly identified as a H_1 tile and the process moves into the false alarm state. The H_1 state has three paths associated with it since, in addition to the rejection and false alarm paths, there is also a correct detection path, H_d.

The detection and false alarm probabilities (P_D and P_{FA}, respectively), as well as the mean time to first hit $\overline{T}_{FH}$, for this system have been derived by the author using flow graph techniques [88]. In the following the same quantities are derived using matrix methods, which are then used to derive an expression for the variance of the time to first hit, $\mathrm{Var}\,[T_{FH}]^{\dagger}$.

We follow the notation of Iosifescu [61] in our treatment of the state transition matrices of Markov chains. For any absorbing Markov chain with k absorbing

†The matrix approach facilitates the calculation of the second order statistics. This is also possible using the flow-graph approach, but requires considerably more work.

states and N_T transient states, the state transition probabilities $p_{i,j}$ can be arranged in the canonical matrix form:

$$\boldsymbol{P} = \begin{pmatrix} \boldsymbol{I} & \boldsymbol{0} \\ \boldsymbol{R} & \boldsymbol{T} \end{pmatrix} \tag{5.1}$$

where $\boldsymbol{P}$ is the $(N_\mathrm{T}+k)\times(N_\mathrm{T}+k)$ matrix of state transition probabilities, $\boldsymbol{I}$ is the $k\times k$ identity matrix, $\boldsymbol{R}$ is the $N_\mathrm{T}\times k$ matrix of transition probabilities from transient to absorbing states, called the "recurrent matrix", and $\boldsymbol{T}$ is the $N_\mathrm{T}\times N_\mathrm{T}$ matrix of transition probabilities within the transient states, called the "transient matrix". Here, the state vector has been arranged such that the first k elements represent the absorbing (or recurrent) states of the process, the remaining N_T elements represent the transient states. The element $p_{i,j}$ represents the transition probability from state i to state j.

Thus, given the circular state diagram of Figure 5.1, the state transition matrix is given by:

$$\boldsymbol{P} = \left(\begin{array}{cc|ccccc} 1 & 0 & 0 & 0 & \dots & \dots & 0 \\ 0 & 1 & 0 & 0 & \dots & \dots & 0 \\ \hline 0 & P_{fa_0} & 0 & P_{r_0} & 0 & \dots & 0 \\ 0 & P_{fa_0} & 0 & 0 & P_{r_0} & \dots & 0 \\ \vdots & \vdots & \vdots & \vdots & \ddots & \ddots & \vdots \\ 0 & P_{fa_0} & 0 & 0 & \dots & 0 & P_{r_0} \\ P_d & P_{fa_1} & P_{r_1} & 0 & 0 & \dots & 0 \end{array}\right) \tag{5.2}$$

Since the transient matrix $\boldsymbol{T}$ will be of great importance in the following analysis, we present it explicitly here:

$$\boldsymbol{T} = \begin{pmatrix} 0 & P_{r_0} & 0 & \dots & 0 \\ 0 & 0 & P_{r_0} & \dots & 0 \\ \vdots & \vdots & \ddots & \ddots & \vdots \\ 0 & 0 & \dots & 0 & P_{r_0} \\ P_{r_1} & 0 & 0 & \dots & 0 \end{pmatrix} \tag{5.3}$$

5.1.2 The Fundamental Matrix

Let ν denote the (random) number of state transitions occurring from commencement to absorption in one instantiation of the Markov chain. Assuming all state transitions take an equal amount of time, given by τ_D, then the quantities of interest to us are the first and second order moments of ν. The analysis of these statistics is facilitated through the use of the fundamental matrix, $\boldsymbol{N}$, given by [61]:

$$\boldsymbol{N} = (\boldsymbol{I} - \boldsymbol{T})^{-1} = \sum_{i=0}^{\infty} \boldsymbol{T}^i \,. \tag{5.4}$$

Let $m_{n,i}$ denote the n^{th} order moment of ν given the process starts in the i^{th} transient state, *i.e.* $m_{n,i} = E_\nu[\nu^n \mid i]$, where $E_\nu[\cdot]$ denotes mathematical expectation over the random variable ν. It can then be shown [61] that the vector $\boldsymbol{m}_1 = [m_{1,0}, m_{1,1}, \ldots, m_{1,N_\text{T}-1}]^\text{T}$ is given by:

$$\boldsymbol{m}_1 = \boldsymbol{N}\boldsymbol{e} \tag{5.5}$$

where $\boldsymbol{e}$ is the length N_T vector of 1's, $\boldsymbol{e} = [1, 1, \ldots, 1]^\text{T}$. The mean number of dwells from start to finish, independent of the starting state, is then given by taking the expectation over the distribution of the starting state:

$$\begin{aligned} m_1 &\triangleq E_i[\boldsymbol{m}_{1,i} \mid i] && (5.6)\\ &= \sum_{i=0}^{N_\text{T}-1} \pi_i m_{1,i} && (5.7)\\ &= \boldsymbol{\pi}^\text{T}\boldsymbol{N}\boldsymbol{e} && (5.8) \end{aligned}$$

where π_i is the *a priori* probability that search starts in state i and

$$\boldsymbol{\pi} = [\pi_0, \pi_1, \ldots, \pi_{N_\text{T}-1}]^\text{T} \,.$$

Similarly, given $\boldsymbol{m}_2 = [m_{2,0}, m_{2,1}, \ldots, m_{2,N_\text{T}-1}]^\text{T}$, it can be shown that [61]:

$$\boldsymbol{m}_2 = (2\boldsymbol{N} - \boldsymbol{I})\,\boldsymbol{N}\boldsymbol{e}. \tag{5.9}$$

Again, taking expectation over the distribution of the starting state, we have:

$$m_2 \triangleq E_i[\boldsymbol{m}_{2,i} \mid i] \tag{5.10}$$

$$= \boldsymbol{\pi}^{\mathrm{T}}\boldsymbol{m}_2 \tag{5.11}$$

where m_2 is the mean square number of dwells from start to finish.

Finally, letting $a_{i,j}$ denote the probability that the Markov chain will terminate in the j^{th} recurrent state, given that it started in the i^{th} transient state, then the $N_{\mathrm{T}} \times k$ matrix $\boldsymbol{A} = [a_{i,j}] \ : \ 0 \leq i \leq N_{\mathrm{T}} - 1 \ , 0 \leq j \leq k-1$ is given by:

$$\boldsymbol{A} = \boldsymbol{N}\boldsymbol{R}. \tag{5.12}$$

The determination of the fundamental matrix $\boldsymbol{N}$ is, therefore, very important. The sparsity of the transient matrix $\boldsymbol{T}$ means that $\boldsymbol{N}$ can be quite easily computed using the infinite summation formula of Equation (5.4).

Denoting the (i,j) element of $\boldsymbol{T}^n$ by $(\boldsymbol{T}^n)_{i,j}$, then we have that $(\boldsymbol{T}^n)_{i,j}$ is non-zero only if $j \equiv (i+n) \bmod N_{\mathrm{T}}$. In fact, for $n < N_{\mathrm{T}}$ we have:

$$(\boldsymbol{T}^n)_{i,j} = \begin{cases} P_{r_0}^n & j \equiv (i+n) \bmod N_{\mathrm{T}} \quad i \leq j \\ P_{r_1}P_{r_0}^{n-1} & j \equiv (i+n) \bmod N_{\mathrm{T}} \quad i > j \\ 0 & \text{otherwise} \end{cases} \tag{5.13}$$

or, explicitly:

$$\boldsymbol{T}^n = \begin{pmatrix} \mathbf{0}_{(N_{\mathrm{T}}-n)\times n} & P_{r_0}^n \boldsymbol{I}_{N_{\mathrm{T}}-n} \\ \\ P_{r_1}P_{r_0}^{n-1}\boldsymbol{I}_n & \mathbf{0}_{n\times(N_{\mathrm{T}}-n)} \end{pmatrix} \tag{5.14}$$

$$= \left(\begin{array}{cccc|cccc} 0 & 0 & \dots & 0 & P_{r_0}^n & 0 & \dots & 0 \\ 0 & 0 & \dots & 0 & 0 & P_{r_0}^n & \dots & 0 \\ \vdots & \vdots & \vdots & \vdots & \vdots & \ddots & \ddots & \vdots \\ 0 & 0 & \dots & 0 & 0 & 0 & \dots & P_{r_0}^n \\ \hline P_{r_1}P_{r_0}^{n-1} & 0 & \dots & 0 & 0 & 0 & \dots & 0 \\ 0 & P_{r_1}P_{r_0}^{n-1} & \ddots & 0 & 0 & 0 & \dots & 0 \\ \vdots & \ddots & \ddots & \ddots & \vdots & \vdots & \dots & \dots \\ 0 & 0 & \dots & P_{r_1}P_{r_0}^{n-1} & 0 & 0 & \dots & 0 \end{array}\right) \tag{5.15}$$

where $\mathbf{0}_{n\times m}$ is the $n \times m$ matrix of zeros, and $\boldsymbol{I}_n$ is the $n \times n$ identity matrix. Thus, when $n = N_{\mathrm{T}}$, we have $\boldsymbol{T}^{N_{\mathrm{T}}} = P_{r_1} P_{r_0}^{N_{\mathrm{T}}-1} \boldsymbol{I}$. The term $P_{r_1} P_{r_0}^{N_{\mathrm{T}}-1}$ is the probability of completing one full loop through the uncertainty region without making a D_1 decision, and we term it the loop probability P_L. In general, for any integer n, we have $n = lN_{\mathrm{T}} + m$ where $l \in \mathbb{Z}^+$ and $0 \leq m < N_{\mathrm{T}}$. Therefore, $\boldsymbol{T}^n$ can be decomposed as follows:

$$\boldsymbol{T}^n = \boldsymbol{T}^{lN_{\mathrm{T}}+m} = P_L^l \boldsymbol{T}^m \tag{5.16}$$

Thus, we can write:

$$\begin{aligned} \boldsymbol{N} &= \sum_{n=0}^{\infty} \boldsymbol{T}^n \\ &= \sum_{l=0}^{\infty} \sum_{m=0}^{N_{\mathrm{T}}-1} \boldsymbol{T}^{lN_{\mathrm{T}}+m} \\ &= \sum_{l=0}^{\infty} \left(P_{r_1} P_{r_0}^{N_{\mathrm{T}}-1} \right)^l \sum_{m=0}^{N_{\mathrm{T}}-1} \boldsymbol{T}^m \\ &= \frac{1}{1-P_L} \sum_{m=0}^{N_{\mathrm{T}}-1} \boldsymbol{T}^m \end{aligned} \tag{5.17}$$

where the last step has been achieved using Equation (A.3) from Appendix A[†]. Now from Equation (5.13) we see that the matrices given by $\boldsymbol{T}^m \ : \ 0 \leq m < N_{\mathrm{T}}$ have no common non-zero elements. Thus, the fundamental matrix is given by:

$$(\boldsymbol{N})_{i,j} = \frac{1}{1-P_L} \begin{cases} P_{r_0}^{j-i} & i \leq j \\ P_{r_1} P_{r_0}^{N_{\mathrm{T}}-1-(i-j)} & i > j \end{cases} \tag{5.18}$$

[†]Note that this requires $P_L < 1$, which will always be the case in practical situations.

which implies:

$$\boldsymbol{N} = \frac{1}{1-P_L}\begin{pmatrix} 1 & P_{r_0} & P_{r_0}^2 & \dots & P_{r_0}^{N_\mathrm{T}-1} \\ P_{r_1}P_{r_0}^{N_\mathrm{T}-2} & 1 & P_{r_0} & \dots & P_{r_0}^{N_\mathrm{T}-2} \\ P_{r_1}P_{r_0}^{N_\mathrm{T}-3} & P_{r_1}P_{r_0}^{N_\mathrm{T}-2} & 1 & \dots & P_{r_0}^{N_\mathrm{T}-3} \\ \vdots & \vdots & \ddots & \ddots & \vdots \\ P_{r_1} & P_{r_1}P_{r_0} & \dots & P_{r_1}P_{r_0}^{N_\mathrm{T}-2} & 1 \end{pmatrix}. \quad (5.19)$$

A graphical representation of $\boldsymbol{N}$ is given in Figure 5.2. The matrix is shown divided into two triangular submatrices: the upper triangular matrix including the main diagonal, and a lower triangular matrix. All the elements within a submatrix share similar properties.

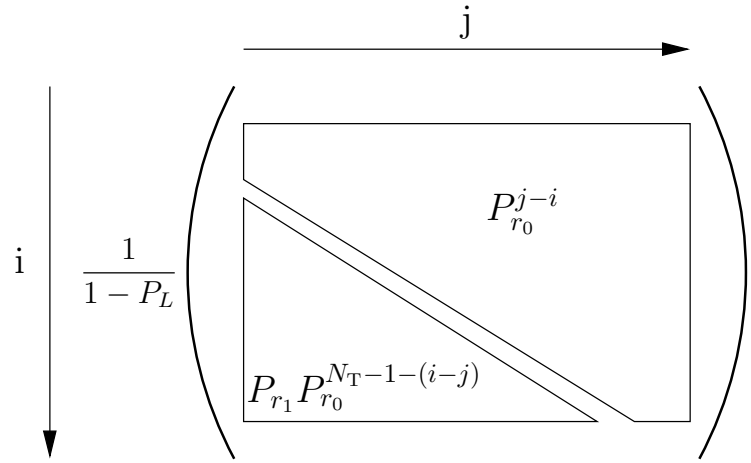


Figure 5.2: Graphical Representation of $\boldsymbol{N}$ under the One H_1 Approximation

5.1.3 Probabilities of Detection and False Alarm

Given the definitions above, the calculation of the probabilities of detection (P_D) and false alarm (P_{FA}) proceeds as follows. Using Equation (5.19) in Equa-

tion (5.12) we get:

$$\boldsymbol{A} = \frac{1}{1-P_L}\begin{pmatrix} 1 & P_{r_0} & \dots & P_{r_0}^{N_\mathrm{T}-1} \\ P_{r_1}P_{r_0}^{N_\mathrm{T}-2} & 1 & \dots & P_{r_0}^{N_\mathrm{T}-2} \\ \vdots & \vdots & \ddots & \vdots \\ P_{r_1} & P_{r_1}P_{r_0} & \dots & 1 \end{pmatrix}\begin{pmatrix} 0 & P_{fa_0} \\ 0 & P_{fa_0} \\ \vdots & \vdots \\ P_d & P_{fa_1} \end{pmatrix}. \tag{5.20}$$

Now, the probability of detection given starting state i, denoted $P_{D,i}$, is given by the first column of the i^{th} row of $\boldsymbol{A}$, $a_{i,0}$ (since recurrent state 0 is the detection state). Denoting by $\boldsymbol{A}_{-,0}$ the first column of $\boldsymbol{A}$, then we have:

$$\begin{aligned} \boldsymbol{A}_{-,0} &= \frac{1}{1-P_L}\begin{pmatrix} 1 & P_{r_0} & \dots & P_{r_0}^{N_\mathrm{T}-1} \\ P_{r_1}P_{r_0}^{N_\mathrm{T}-2} & 1 & \dots & P_{r_0}^{N_\mathrm{T}-2} \\ \vdots & \vdots & \ddots & \vdots \\ P_{r_1} & P_{r_1}P_{r_0} & \dots & 1 \end{pmatrix}\begin{pmatrix} 0 \\ 0 \\ \vdots \\ P_d \end{pmatrix} \\ \therefore P_{D,i} &= \frac{P_{r_0}^{N_\mathrm{T}-1-i}P_d}{1-P_L} \end{aligned} \tag{5.21}$$

Hence, the overall probability of detection is given by:

$$\begin{aligned} P_D &= E_i[P_{D,i} \mid i] \\ &= \sum_{i=0}^{N_\mathrm{T}-1} \pi_i P_{D,i}\,. \end{aligned}$$

Assuming a uniform distribution, $\pi_i = 1/N_\mathrm{T}$ and we have:

$$\begin{aligned} P_D &= \frac{1}{N_\mathrm{T}}\frac{P_d}{1-P_L}\sum_{i=0}^{N_\mathrm{T}-1} P_{r_0}^{N_\mathrm{T}-1-i} \\ &= \frac{1}{N_\mathrm{T}}\frac{P_d}{1-P_L}\frac{1-P_{r_0}^{N_\mathrm{T}}}{1-P_{r_0}} \end{aligned} \tag{5.22}$$

where we have used Equation (A.4).

Finally, given that there are only two possible end states, we must have:

$$P_{FA} = 1 - P_D \,. \tag{5.23}$$

5.1.4 First Order Statistics

To determine the first order statistics of the time to first hit we use Equation (5.19) in Equation (5.5) to yield:

$$\begin{aligned} m_{1,i} &= \frac{1}{1-P_L}\left(P_{r_1}\sum_{j=0}^{i-1} P_{r_0}^{N_\mathrm{T}-1-(i-j)} + \sum_{j=i}^{N_\mathrm{T}-1} P_{r_0}^{j-i}\right) \\ &= \frac{1}{1-P_L}\left(P_{r_1}P_{r_0}^{N_\mathrm{T}-1-i}\frac{1-P_{r_0}^{i}}{1-P_{r_0}} + \frac{1-P_{r_0}^{N_\mathrm{T}-i}}{1-P_{r_0}}\right) \\ &= \frac{1}{(1-P_L)(1-P_{r_0})}\left(1-P_L+P_{r_0}^{N_\mathrm{T}-1-i}\left(P_{r_1}-P_{r_0}\right)\right) \\ &= \frac{1}{1-P_{r_0}} + \frac{P_{r_1}-P_{r_0}}{(1-P_L)(1-P_{r_0})}P_{r_0}^{N_\mathrm{T}-1-i}. \end{aligned} \tag{5.24}$$

Again, we assume a uniform *a priori* distribution on the starting cell, *i.e.* $\pi_i = 1/N_\mathrm{T}$. Using Equation (5.8) yields:

$$\begin{aligned} m_1 &= \frac{1}{1-P_{r_0}} + \frac{P_{r_1}-P_{r_0}}{(1-P_L)(1-P_{r_0})}\frac{1}{N_\mathrm{T}}\sum_{i=0}^{N_\mathrm{T}-1} P_{r_0}^{N_\mathrm{T}-1-i} \\ &= \frac{1}{P_{fa_0}} + \frac{1}{N_\mathrm{T}}\frac{P_{r_1}-P_{r_0}}{1-P_L}\frac{1-P_{r_0}^{N_\mathrm{T}}}{P_{fa_0}^2}\,. \end{aligned} \tag{5.25}$$

Equation (5.25) above gives us an expression for the mean number of dwells occurring between the start of the search process and the first entry into the verification mode. Given that each dwell takes a fixed amount of time, τ_D, the mean time to first hit is simply calculated from:

$$\overline{T}_{FH} = m_1\tau_D \,. \tag{5.26}$$

5.1.5 Second Order Statistics

Rewriting Equation (5.9) gives:

$$\begin{aligned} \boldsymbol{m}_2 &= 2\boldsymbol{N}^2\boldsymbol{e} - \boldsymbol{N}\boldsymbol{e} && (5.27) \\ &= 2\boldsymbol{M}\boldsymbol{e} - \boldsymbol{m}_1 && (5.28) \end{aligned}$$

where $\boldsymbol{M} \triangleq \boldsymbol{N}^2$. Once again, the structure of the fundamental matrix allows us to calculate $\boldsymbol{M}$ with relative ease. The construction of $\boldsymbol{M}$ is demonstrated graphically in Figure 5.3 where the matrix $\boldsymbol{N}$ is shown, each element of $\boldsymbol{M}$ is formed as the dot product of a row times a column of $\boldsymbol{N}$. The diagram shows two cases: a) $i \leq j$ and b) $i > j$. The structure of $\boldsymbol{N}$, as illustrated in Figure 5.2, is clearly visible.

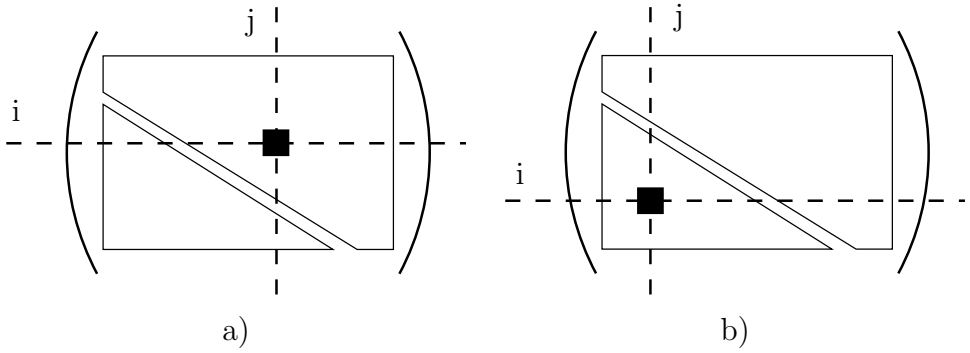


Figure 5.3: Construction of $\boldsymbol{M}$, the dashed lines indicate the row-column product being taken and the filled square indicates the element of $\boldsymbol{M}$ being calculated. Two cases are shown: a) $i \leq j$, b) $i > j$.

In the following we use the variable k as an *iterator* along rows and down columns of $\boldsymbol{N}$. For example, for the calculation of $M_{i,j}$ when $i \leq j$, we use Figure 5.3 a) :

$$\begin{aligned} M_{i,j} &= \frac{1}{(1-P_L)^2}\left(\sum_{k=0}^{i-1} P_{r_1} P_{r_0}^{N_\mathrm{T}-1-(i-k)} P_{r_0}^{j-k} + \sum_{k=i}^{j} P_{r_0}^{k-i} P_{r_0}^{j-k} + \right. \\ &\quad \left. \sum_{k=j+1}^{N_\mathrm{T}-1} P_{r_0}^{k-i} P_{r_1} P_{r_0}^{N_\mathrm{T}-1-(k-j)}\right) \\ &= \frac{1}{(1-P_L)^2}\left[iP_{r_1}P_{r_0}^{N_\mathrm{T}-1-(i-j)} + (j-i+1)P_{r_0}^{j-i} + \right. \\ &\quad \left. (N_\mathrm{T}-1-j)P_{r_1}P_{r_0}^{N_\mathrm{T}-1-(i-j)}\right] \end{aligned}$$

$$M_{i,j} = \frac{P_{r_0}^{j-i}}{(1-P_L)^2}\left[(j-i+1)(1-P_L)+N_{\mathrm{T}}P_L\right] \quad i \le j. \tag{5.29}$$

Similarly, using Figure 5.3 b) for $i > j$, we obtain:

$$M_{i,j} = \frac{P_{r_1}P_{r_0}^{N_{\mathrm{T}}-1-(i-j)}}{(1-P_L)^2}\left[N_{\mathrm{T}}-(i-j-1)(1-P_L)\right] \quad i > j. \tag{5.30}$$

The structure of $\boldsymbol{M}$ is, therefore, similar to that of $\boldsymbol{N}$, consisting of two triangular submatrices with similar properties. This structure is highlighted in Figure 5.4.

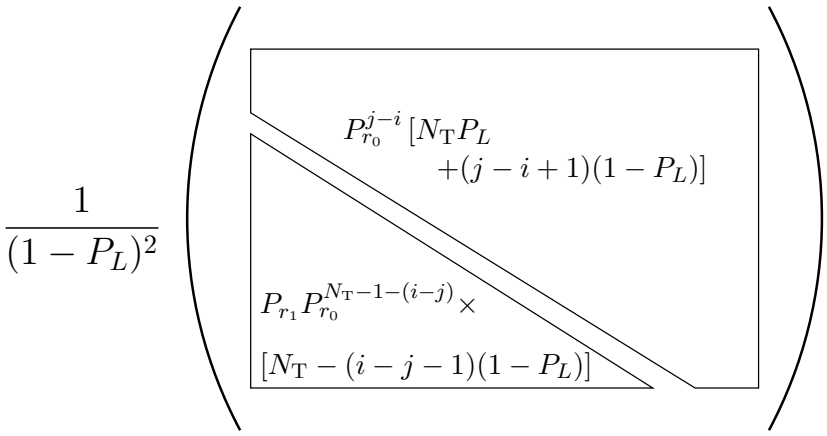


Figure 5.4: Structure of the matrix $\boldsymbol{M}$ under the One H_1 Approximation

Inserting Equation (5.11) into Equation (5.28) gives:

$$m_2 = 2\boldsymbol{\pi}^{\mathrm{T}}\boldsymbol{M}\boldsymbol{e} - m_1.$$

Once again, assuming a uniform distribution, we have $\boldsymbol{\pi} = \frac{1}{N_{\mathrm{T}}}\boldsymbol{e}$ and simplifying yields:

$$\boldsymbol{e}^{\mathrm{T}}\boldsymbol{M}\boldsymbol{e} = \frac{N_{\mathrm{T}}}{(1-P_{r_0})^2} + 2\frac{P_{r_1}-P_{r_0}}{1-P_L}\frac{1-P_{r_0}^{N_{\mathrm{T}}}}{(1-P_{r_0})^3} + N_{\mathrm{T}}\frac{(P_{r_1}-P_{r_0})^2P_{r_0}^{N_{\mathrm{T}}-1}}{(1-P_L)^2(1-P_{r_0})^2}\,. \tag{5.31}$$

Inserting Equation (5.31) and Equation (5.25) into Equation (5.11) and simpli-

fying gives:

$$m_2 = \frac{1+P_{r_0}}{P_{fa_0}^2} + \frac{2(P_{r_1}-P_{r_0})^2 P_{r_0}^{N_\mathrm{T}-1}}{(1-P_L)^2 P_{fa_0}^2} + \frac{(3+P_{r_0})(P_{r_1}-P_{r_0})(1-P_{r_0}^{N_\mathrm{T}})}{N_\mathrm{T}(1-P_L)P_{fa_0}^3}\,. \tag{5.32}$$

The quantity of interest here is the variance of the time to first hit, $\mathrm{Var}\left[T_{FH}\right]$, which is obtained from:

$$\begin{aligned} \mathrm{Var}\left[T_{FH}\right] &\triangleq E\Big[\big(T_{FH}-\overline{T}_{FH}\big)^2\Big] \\ &= E\big[T_{FH}^2\big] - \overline{T}_{FH}{}^2 \\ &= \big(m_2 - m_1^2\big)\,\tau_D{}^2. \end{aligned} \tag{5.33}$$

5.1.6 Numerical Results

To verify these expressions for the performance parameters of the search mode, we compare them with results obtained by Monte Carlo simulation [109]. For the purposes of simulation we use simplified models of both the signal and the receiver. The receiver under test has the following properties:

- Correlation is implemented as a 2048-point FFT.
- Circular correlation is implemented.
- A noise PSD of -203.8 dBW/Hz is assumed (note that this is a pessimistic assumption, see [140, Equation (12)]).
- Serial search is performed over the frequency uncertainty region.
- A straight serial search strategy is implemented.
- Floating point operations are used throughout (quantisation effects are ignored).
- Local oscillator effects are ignored.
- The detector/estimator uses noncoherent combining: correlation is performed over M ms coherently, with K of these M ms coherent blocks subsequently being non-coherently combined. The dwell time is MKT_CA s.

We choose to implement noncoherent combining, rather than differentially coherent techniques, due to the superiority of our models of signal effects on the noncoherent combining detector.

The simplified signal model has the following properties:

- Only one satellite signal is present in the channel.
- The SVN, initial code phase, initial carrier phase and Doppler offset are all uniformly distributed over the uncertainty regions.
- The Doppler offset is constant (higher order Doppler effects are ignored), a η-estimating receiver is assumed.
- The data signal is random.
- The signal power is fixed (fading effects are ignored).

Now, the expressions for P_D, $\overline{T}_{FH}$ and $\mathrm{Var}\,[T_{FH}]$ obtained above (Equations (5.22), (5.26) and (5.33) respectively) are all functions of the received signal, and take no account of the signal effects discussed in Chapter 3. The determination of the search mode performance must be achieved by averaging over these signal effects. Taking the probability of detection as an example, we have:

$$\overline{P_D} \;=\; E_{\boldsymbol{d},\delta\zeta,\delta\omega_d}[P_D]$$

where: $\boldsymbol{d}$ is the data sequence modulating the received signal, $\delta\zeta$ is the residual code phase offset when correct detection occurs and $\delta\omega_d$ is the residual Doppler offset when correct detection occurs. Thus, the calculation of P_D requires a triple integral over the expression of Equation (5.22). Similarly the determination of $\overline{T}_{FH}$ and $\mathrm{Var}\,[T_{FH}]$ also require the evaluation of triple integrals.

Recall that the signal effects can be modelled as an attenuation of the signal power seen by the receiver:

$$P_{\text{eff}} = \alpha_D(\delta\omega_d)\alpha_s(\delta\zeta,\delta\omega_d)\alpha_m(\boldsymbol{d},\delta\omega_d)P$$

where: $\alpha_D(\delta\omega_d)$ is the power attenuation due to the Doppler offset, $\alpha_s(\delta\zeta)$ is the power attenuation due to the code phase offset (which is a function of the sampling frequency) and $\alpha_m(\boldsymbol{d})$ is the power attenuation due to the modulation of

the received signal. To simplify the calculation of the search mode performance parameters we model both the sampling and modulation attenuation by their average values and, hence, we have:

$$P_{\text{eff}} = \alpha_D(\delta\omega_d)\overline{\alpha}_s\overline{\alpha}_m P$$

Thus, assuming a uniform *a priori* distribution on $\delta\omega_d$, we calculate the performance parameters as follows:

$$P_D = \frac{1}{\Delta\omega}\int_{-\frac{\Delta\omega}{2}}^{\frac{\Delta\omega}{2}} P_D\Big(P_{\text{eff}}\Big)d(\delta\omega_d) \tag{5.34}$$

$$\overline{T}_{FH} = \frac{MKT_{\text{CA}}}{\Delta\omega}\int_{-\frac{\Delta\omega}{2}}^{\frac{\Delta\omega}{2}} m_1\Big(P_{\text{eff}}\Big)d(\delta\omega_d) \tag{5.35}$$

$$\text{Var}\left[T_{FH}\right] = \frac{(MKT_{\text{CA}})^2}{\Delta\omega}\int_{-\frac{\Delta\omega}{2}}^{\frac{\Delta\omega}{2}}\left[m_2\Big(P_{\text{eff}}\Big) - m_1\Big(P_{\text{eff}}\Big)^2\right]d(\delta\omega_d) \tag{5.36}$$

where: $P_D(P)$ is the probability of detection as a function of the received signal power (Equation (5.22)), $m_1(P)$ is the mean number of dwells as a function of the received signal power (Equation (5.25)), and $m_2(P)$ is the mean square number of dwells as a function of the received signal power (Equation (5.32)).

The results for two sample signal scenarios are shown in Figure 5.5; scenario a) $C/N_0 = 40.8$ dB-Hz, the coherent integration time $M = 1$ ms and there are $N_{\text{T}} = 5$ Doppler bins in the uncertainty region; scenario b) $C/N_0 = 33.8$ dB-Hz, $M = 3$ ms and, again, there are $N_{\text{T}} = 5$ Doppler bins. For each case, the receiver was configured for a constant false alarm rate $P_{fa_0} = 0.01$ and the system was simulated for various values of K (the number of coherent samples non-coherently combined). It is interesting to note form the graphs that an "optimum" choice of K exists in terms of minimum $\overline{T}_{FH}$. Figure 5.5 clearly indicates good agreement between theory and simulation, particularly for P_D. For $\overline{T}_{FH}$ and $\text{Var}\left[T_{FH}\right]$ the theory and simulation results have similar shapes, but the theoretical results are slightly greater than those obtained by simulation. The discrepancy tends to increase as K decreases.

This latter effect is to be expected due to the simplifying approximations made in our calculations. In particular, as K increases our dwell time increases and there are, therefore, a greater number of data-bit transitions within the dwell. We should, therefore, expect that as K increases the modulation attenuation will

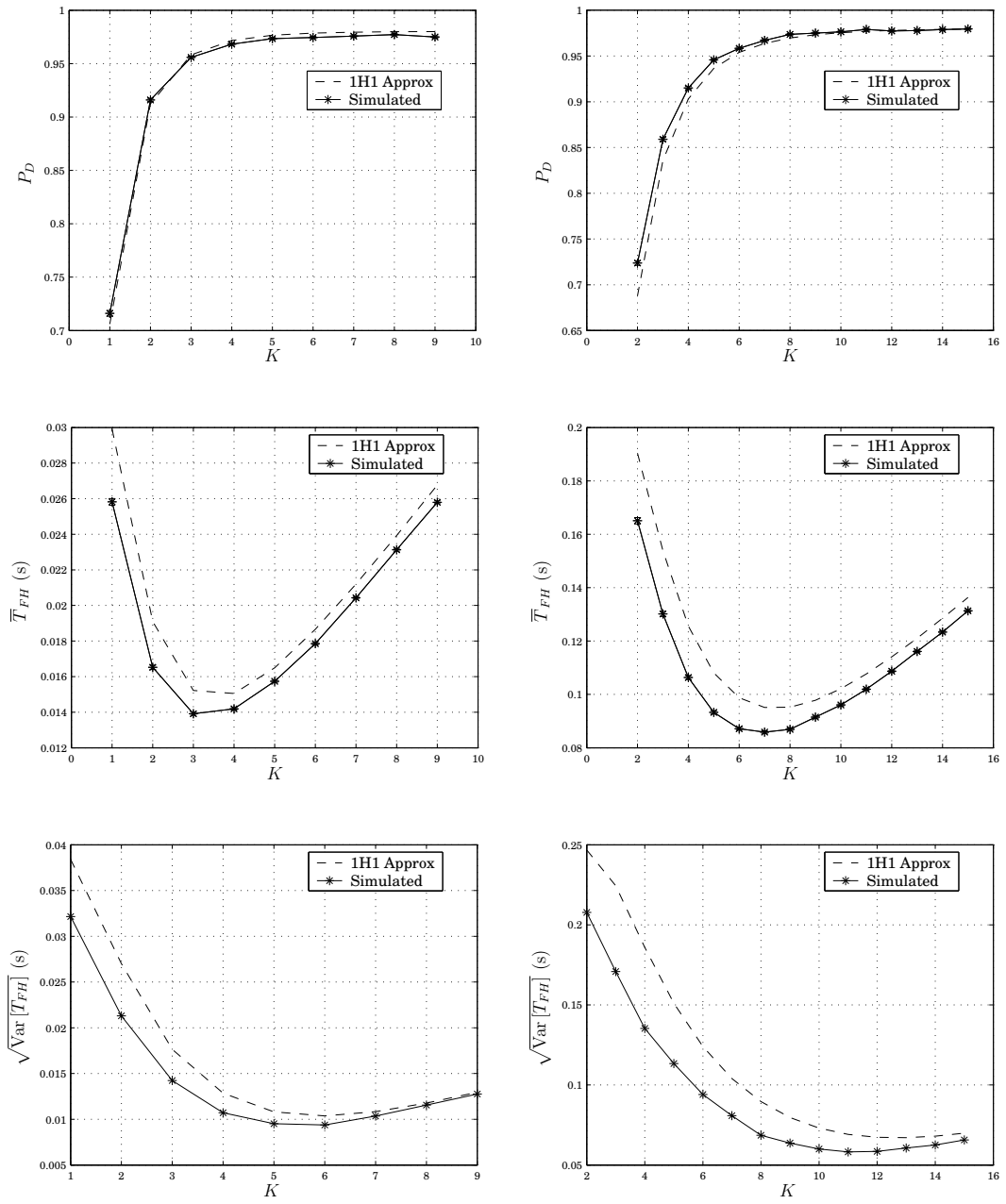


Figure 5.5: P_D, Mean and Standard Deviation of T_{FH} vs K, for $P_{fa_0} = 0.01$: a) $C/N_0 = 40.8$ dB-Hz, $M = 1$ ms, $N_{\mathrm{T}} = 5$; b) $C/N_0 = 33.8$ dB-Hz, $M = 3$ ms, $N_{\mathrm{T}} = 5$. Note that calculation time is not considered in the calculation of T_{FH}.

approach its average value. Conversely, for small values of K we would expect this approximation to degrade, which is indeed the case.

The remaining discrepancy between theory and simulation will be accounted for by taking into consideration the effect of multiple H_1 tiles.

5.2 The Effect of Two H_1 Tiles

From the numerical results of the previous section we see that there is a slight discrepancy between our model and the simulation results, this is particularly noticeable for the statistics of T_{FH} as the power level decreases. We show now that this can, at least partly[†], be accounted for by the presence of signal power in tiles adjacent to the H_1 tile.

The one H_1 tile approximation developed in the previous section models the signal as an impulse function in the search space. In reality, however, the signal will have a finite bandwidth in the frequency domain, and a finite main-lobe width in the code-phase domain. Thus, there may be significant signal power in two or more adjacent tiles in the search space. Correct detection may, therefore, occur in more than one tile.

In the remainder of this thesis we focus primarily on the FFT type detector/ estimator in which each search tile covers one full Doppler bin in the search space. The effect of multiple H_1 cells within the search tile must be accounted for in the detector/estimator model. We now investigate the effect of multiple H_1 *tiles*; that is, we investigate the effects of the frequency spread of the received signal. This effect is modelled by an adjustment to the Markov chain model of the search mode, leading to new expressions for the probabilities of detection and false alarm, and the mean and variance of the time to first hit.

5.2.1 The Markov Chain Model

Under the two H_1 tile approximation the Markov chain model of the search state is modified to incorporate a second path to the correct detection state. The two H_1 tiles are denoted H_{11} and H_{10}, where the majority of the signal power resides in the H_{11} tile (except when the true signal parameters lie on the boundary between two tiles, in which case the H_{11} and H_{10} tiles contain an equal portion of the

[†]At least part of this discrepancy arises due to our approximation in averaging over signal effects.

signal power). Assuming a straight serial search strategy there are two possible state diagrams, as illustrated in Figure 5.6. In case a) the H_{10} tile is encountered first during the search process, in case b) the H_{11} tile is encountered first.

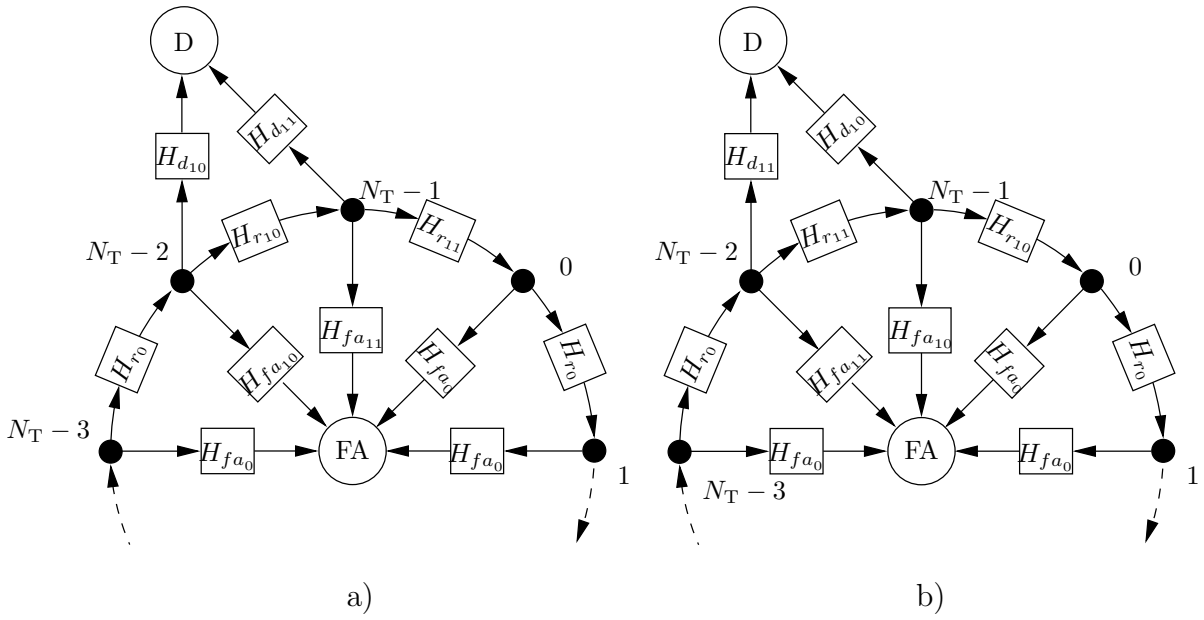


Figure 5.6: Circular State Diagram for the Search Mode Under the Two H_1 Tile Approximation: a) the H_{10} tile is encountered before the H_{11} tile; b) the H_{11} tile is encountered first.

As can be seen from the figure, paths associated with the H_{11} tile are denoted by the 11 subscript, while those associated with the H_{10} tile are denoted by the 10 subscript. Note that there are now two paths to *correct* detection of the signal.

We define the following probabilities to assist in our analysis:

$$\overline{P}_{d_1} = 0.5(P_{d_{11}} + P_{d_{10}}) \tag{5.37}$$

$$\overline{P}_{r_1} = 0.5(P_{r_{11}} + P_{r_{10}}) \tag{5.38}$$

$$\overline{P}_{fa_1} = 0.5(P_{fa_{11}} + P_{fa_{10}}) \tag{5.39}$$

$$P_L = P_{r_{11}} P_{r_{10}} P_{r_0}^{N_T - 2} \tag{5.40}$$

$$P_m = P_{r_{11}} P_{r_{10}}. \tag{5.41}$$

We follow the same procedure as for the one H_1 tile case in the last section, beginning with the fundamental matrix $\boldsymbol{N}$, and continuing through to the second order statistics of the time to first hit. Each of the two cases in Figure 5.6 must

be accounted for. The following expressions for P_D, m_1 and m_2 are derived in Appendix B.3.1:

$$P_D = \frac{1}{N_{\mathrm{T}}(1-P_L)} \left\{ \left(\overline{P}_{d_1} + \overline{P}_{rd_1}\right) \frac{1-P_{r_0}^{N_{\mathrm{T}}-1}}{1-P_{r_0}} + \overline{P}_{d_1} + \overline{P}_{rd_1} P_{r_0}^{N_{\mathrm{T}}-2} \right\} \quad (5.42)$$

$$\begin{aligned} m_1 =& \frac{N_{\mathrm{T}}-1}{N_{\mathrm{T}} P_{fa_0}} + \frac{1}{N_{\mathrm{T}}(1-P_L)} + \frac{(P_m - P_{r_0})(1-P_{r_0}^{N_{\mathrm{T}}-1})}{N_{\mathrm{T}}(1-P_L)P_{fa_0}^2} \\ &+ \frac{(P_{r_{11}} + P_{r_{10}})(1-P_{r_0}^{N_{\mathrm{T}}-1})}{N_{\mathrm{T}}(1-P_L)P_{fa_0}} \end{aligned} \quad (5.43)$$

$$\begin{aligned} m_2 =& \frac{(N_{\mathrm{T}}-1)(1+P_{r_0})}{N_{\mathrm{T}} P_{fa_0}^2} + \frac{2P_L}{(1-P_L)^2} + \frac{1}{N_{\mathrm{T}}(1-P_L)} + \frac{2P_m(1-P_{r_0}^{N_{\mathrm{T}}-1})^2}{N_{\mathrm{T}}(1-P_L)^2 P_{fa_0}^2} \\ &+ \frac{2(N_{\mathrm{T}}-1)(P_m - P_{r_0})^2 P_{r_0}^{N_{\mathrm{T}}-2}}{N_{\mathrm{T}}(1-P_L)^2 P_{fa_0}^2} + \frac{(3+P_{r_0})(P_m - P_{r_0})(1-P_{r_0}^{N_{\mathrm{T}}-1})}{N_{\mathrm{T}}(1-P_L)P_{fa_0}^3} \\ &+ \frac{P_{r_{11}} + P_{r_{10}}}{(1-P_L)P_{fa_0}} \left\{ \frac{2(P_m - P_{r_0})P_{r_0}^{N_{\mathrm{T}}-2}}{1-P_L} + \frac{(3-P_{r_0})}{N_{\mathrm{T}} P_{fa_0}} - \frac{P_{r_0}^{N_{\mathrm{T}}-1}}{N_{\mathrm{T}}} \right\}. \end{aligned} \quad (5.44)$$

5.2.2 Numerical Results

We consider again the two scenarios presented in Section 5.1.6. The same simulation results are presented in Figure 5.7, together with the results of the two H_1 tile approximation. Clearly, the two H_1 tile approximation provides more accurate measures of $\overline{T}_{FH}$ and $\mathrm{Var}\left[T_{FH}\right]$, but at considerable extra computational cost. Once again, we see that the discrepancy between theory and simulation increases as K decreases, as is to be expected for the reasons given in Section 5.1.6.

5.3 Optimisation

In this section we apply the models derived in the preceding section to the optimisation problem. We consider a sample system wherein the signal from a single satellite is sought. It is assumed that the carrier Doppler frequency is known to within ± 2.5 kHz. A design point $P_D = 0.9$ is also assumed. The problem, therefore, is to determine the optimum choice of detector/estimator parameters to achieve the design criterion with minimum $\overline{T}_{FH}$. We assume an FFT-based detector/estimator is to be used, with $N_s = 2048$ samples per code period.

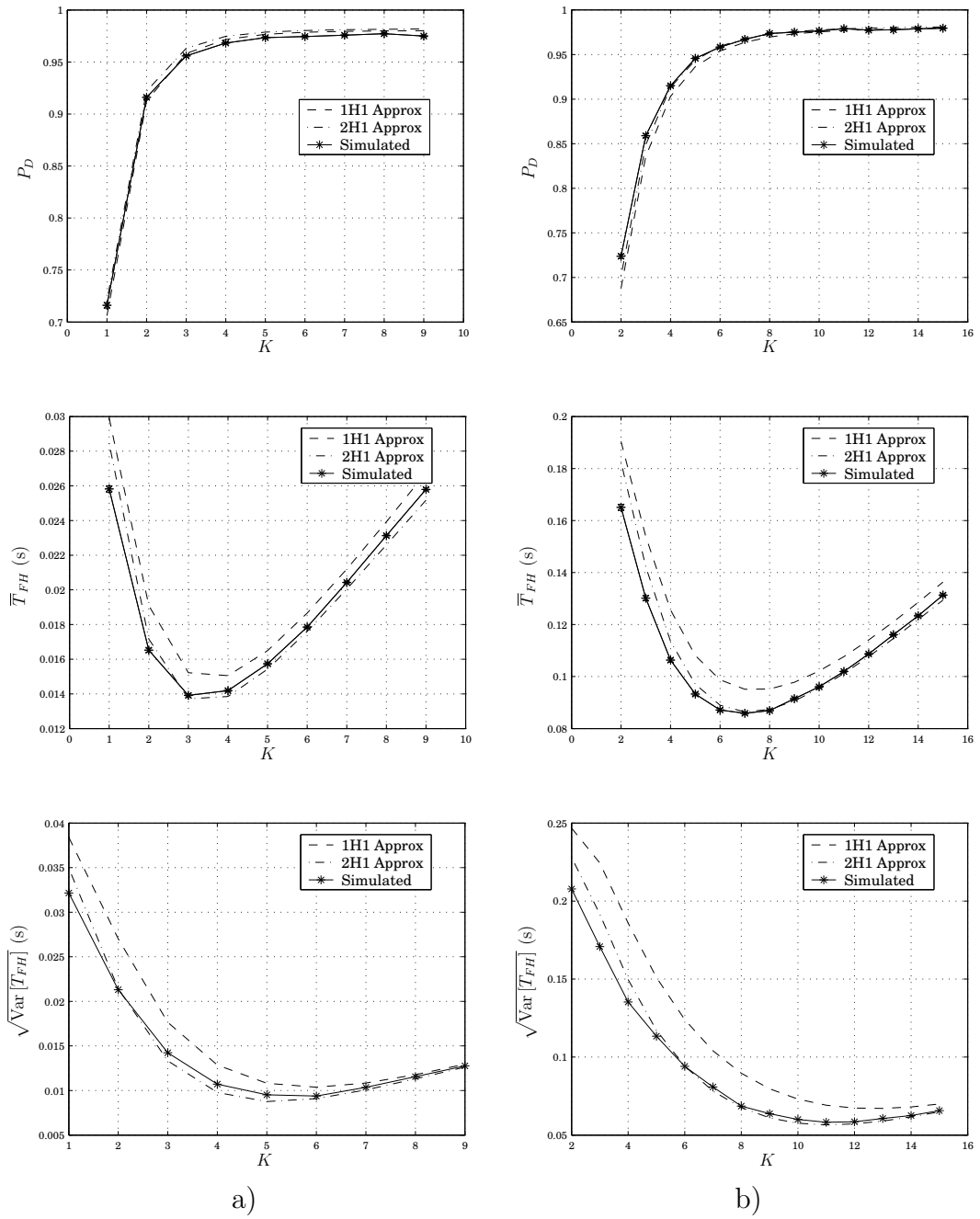


Figure 5.7: P_D, Mean and Standard Deviation of T_{FH} vs K, for $P_{fa_0} = 0.01$: a) $C/N_0 = 40.8$ dB-Hz, $M = 1$ ms, $N_{\mathrm{T}} = 5$; b) $C/N_0 = 33.8$ dB-Hz, $M = 3$ ms, $N_{\mathrm{T}} = 5$

Note that we consider only the optimisation of the search mode for a single satellite. In practice, a multiple satellite optimisation criterion would be considered, for example, the minimum mean time to acquire four satellites, or the maximum probability of acquiring four satellites within a specified time period. Whereas the particular optimum choice of parameters would vary from case to case, the technique is essentially identical to the one we adopt below.

Ideally, an analytical optimum would be obtained by minimising $\overline{T}_{FH}$ with respect to the detector/estimator parameters, subject to the constraint $P_D \geq 0.9$. In practice, however, such constrained optimisation is not easy to achieve in analytical form. For this reason a numerical optimisation procedure is applied to the problem.

To simplify the procedure we assume a uniform distribution on the Doppler frequency, and so apply a straight serial search strategy. In addition, we maintain a fixed Doppler bin width of $\Delta f = \frac{1}{MT_{\mathrm{CA}}}$ Hz. From our analysis of the DCCD it is clear that $J = 1$ is the best choice for the differential delay. So for each detector/estimator there are three parameters to be chosen:

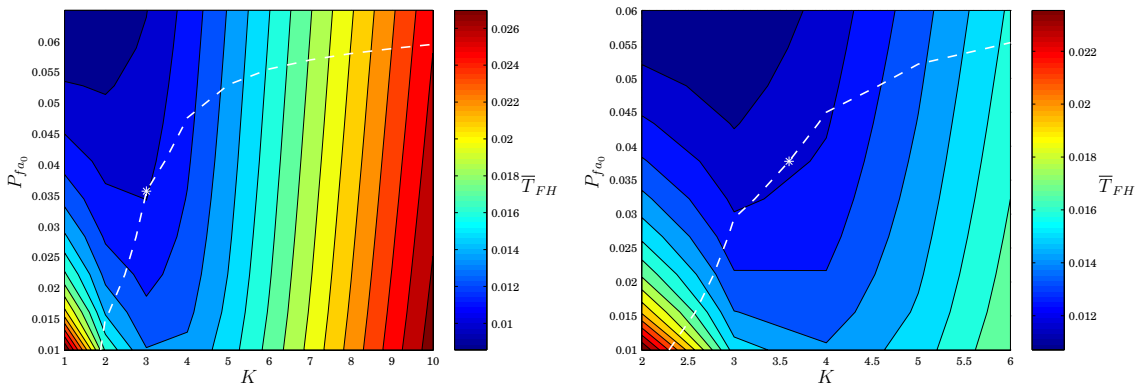
1. M, the duration of the coherent observation interval, in code periods,
2. K, the number of coherent sub-intervals combined,
3. V_{Th}, the decision threshold.

Note that, given M and K the threshold V_{Th} determines the probability of false alarm in a H_0 tile, P_{fa_0}. In the remainder of this section we consider the three parameters M, K and P_{fa_0}.

Five cases for the received signal to noise ratio are considered. Beginning with $C/N_0 = 43.8$ dBW/Hz, which corresponds to the nominal received signal strength at the surface of the earth of $P = -160$ dBW [6], the signal power is then reduced in steps of 5 dB to a minimum $C/N_0 = 23.8$ dBW/Hz, corresponding to a received signal power of -180 dBW, which is typical indoors [51]. The optimum receiver parameters are derived for each of these cases, for both the NCCD and DCCD detector/estimator forms.

Figures 5.8 to 5.12 show contour plots of $\overline{T}_{FH}$ vs K and P_{fa_0} for both the NCCD and DCCD. In each case the value of M is fixed and, hence, so is the Doppler bin width. In each figure the contour of constant $P_D = 0.9$ is indicated by a dashed line. P_D is a monotonic function of both P_{fa_0} and K, thus all points

"below" this contour (*i.e.* towards the lower right hand side of the graph) have $P_D > 0.9$ while all points "above" the contour correspond to $P_D < 0.9$. The point of minimum $\overline{T}_{FH}$ is indicated by an asterisk. Note that this point is determined by numerical interpolation on the contour and may not be realisable (for example in Figure 5.8 b) the optimum point appears at $K = 3.5$, which is not physically possible).



a) NCCD b) DCCD, standard form

Figure 5.8: Contour Plot of $\overline{T}_{FH}$ vs K and P_{fa}. $C/N_0 = 43.8$ dB-Hz, $M = 1$. The dashed line is the contour of constant $P_D = 0.9$.

The results of the numerical optimisation of the receiver parameters are recorded in Table 5.1. In each case we include the minimum attainable mean time to first hit, denoted $\overline{T}_{FH\min}$. In addition, the maximum possible code phase drift due to residual code Doppler effects, denoted $\Delta\zeta_{\max}$, is also recorded. This is calculated using the formula:

$$\Delta\zeta_{\max} = \frac{KML\Delta\omega}{2\omega_0}, \tag{5.45}$$

where $L = 1023$ is the C/A code length in chips, $\Delta\omega$ is the Doppler bin width and ω_0 is the carrier frequency in radians per second. For each design point SNR the minimum $\overline{T}_{FH}$ is indicated in bold face font. It is interesting to note that whereas this minimum is achieved using NCCD for the case $C/N_0 = 43.8$ dB-Hz, for all other cases the minimum is achieved using the DCCD.

It is important to note that, as before, the performance of the DCCD has been calculated using the exact expression for P_{fa_0} when $K \leq 27$, but the Gaussian approximation has been used when $K > 27$. Recall that, for the parallel form, we have previously shown (in Section 4.5) that this Gaussian approximation is highly inaccurate for $K < 500$, due to the dependence of the parallel detector/estimator

C/N_0 (dB-Hz)	M	NCCD K	NCCD P_{fa_0}	NCCD $\overline{T}_{FH\min}$ (s)	NCCD $\Delta\zeta_{\max}$ (chips)	DCCD ($J=1$) K	DCCD ($J=1$) P_{fa_0}	DCCD ($J=1$) $\overline{T}_{FH\min}$ (s)	DCCD ($J=1$) $\Delta\zeta_{\max}$ (chips)
43.8	1	3	0.0317	**0.0113**	0.0010	4	0.0442	0.0123	0.0013
38.8	1	16	0.0365	0.05793	0.0052	13	0.0366	**0.0454**	0.0042
33.8	1	105	0.0345	0.3946	0.0341	50	0.0282	**0.2098**	0.0162
28.8	1	900	0.0359	3.317	0.2922	550	0.0284	**2.087**	0.1786
28.8	2	261	0.0158	3.820	0.0847	150	0.0118	2.383	0.0487
23.8	2	2378	0.0167	33.83	0.7721	1895	0.0078	**25.92**	0.6153
23.8	3	1300	0.0087	38.95	0.4221	900	0.0064	28.26	0.2922

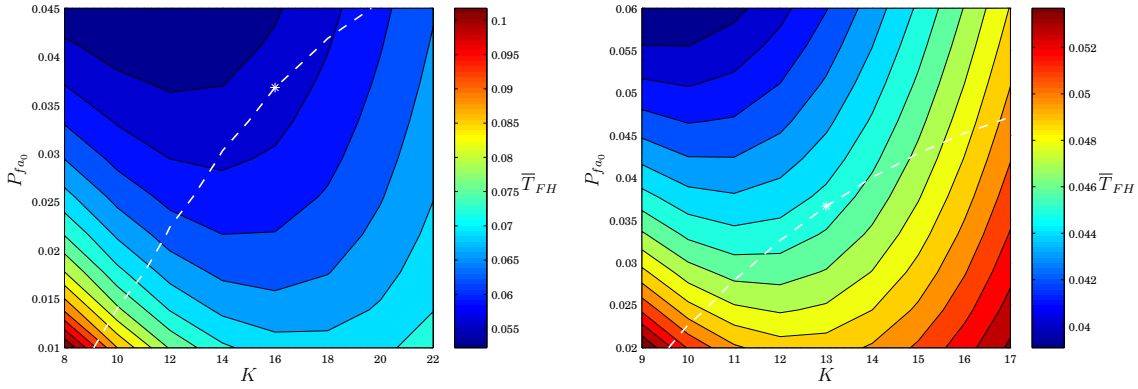
Table 5.1: Parameters for Minimum $\overline{T}_{FH}$ for NCCD and DCCD.

on the tails of the distribution of the single cell decision statistics. Thus, the results presented for the case $C/N_0 = 33.8$ dB-Hz for the DCCD in Table 5.1 are likely to be highly inaccurate.

To verify these theoretical results they are compared with results obtained by Monte Carlo simulation. The simulation model is identical to that described in Section 5.1.6, except for the manner in which code Doppler effects are accounted for. In our previous simulations code Doppler was perfectly eliminated within a bin. In the following, we apply an alternative technique, whereby code Doppler compensation is achieved by resampling the local code. This effectively implements a shift of the local replica after every coherent subinterval, and is similar to Psiaki's technique [103]. The results are illustrated in Figures 5.13 to 5.17. Note that the simulation results agree well with the predicted receiver performance, particularly for the NCCD, with the exception of the performance of the DCCD when $27 < K < 500$. This is as expected. Consider, for instance, Figure 5.15. The predicted and simulated receiver performances for the DCCD detector/estimator are considerably different. Similarly, in Figure 5.16, the disparity between the predicted and simulated DCCD performances can be seen to decrease as K increases.

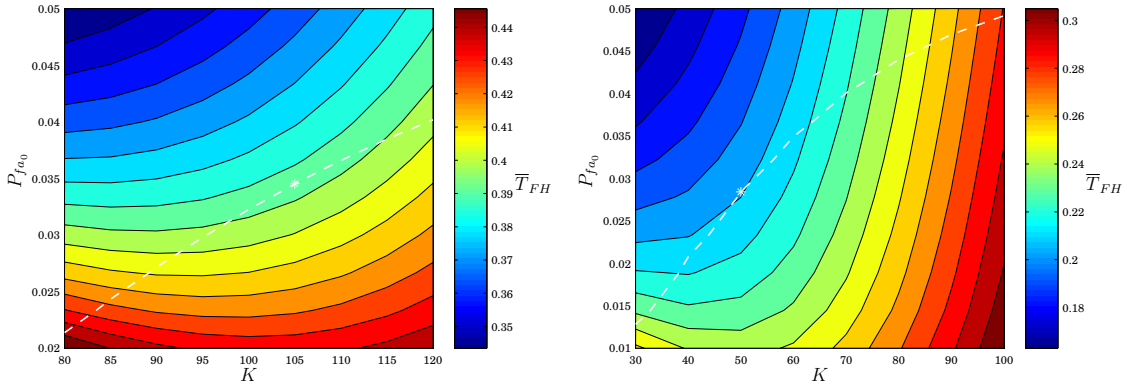
5.4 Discussion

In this chapter a new analysis of the search mode of the acquisition process was conducted. New expressions for the probability of detection and the mean and



a) NCCD b) DCCD, standard form

Figure 5.9: Contour Plot of $\overline{T}_{FH}$ vs K and P_{fa}. $C/N_0 = 38.8$ dB-Hz, $M = 1$. The dashed line is the contour of constant $P_D = 0.9$.

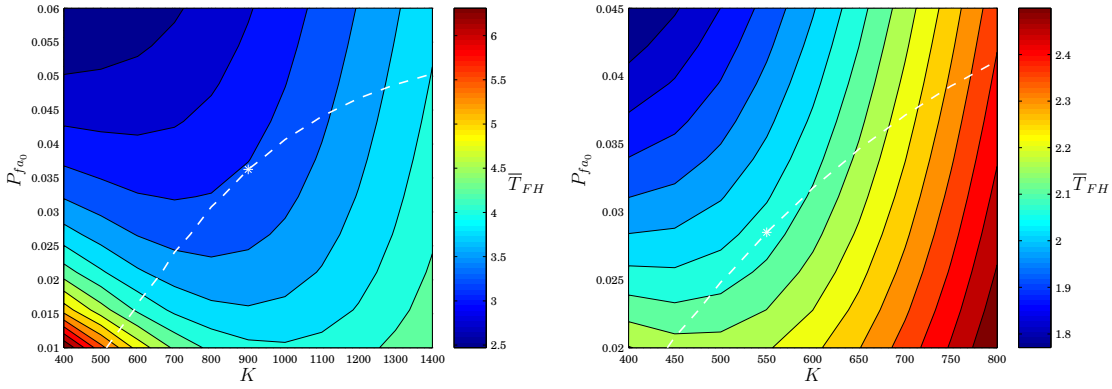


a) NCCD b) DCCD, standard form

Figure 5.10: Contour Plot of $\overline{T}_{FH}$ vs K and P_{fa}. $C/N_0 = 33.8$ dB-Hz, $M = 1$. The dashed line is the contour of constant $P_D = 0.9$.

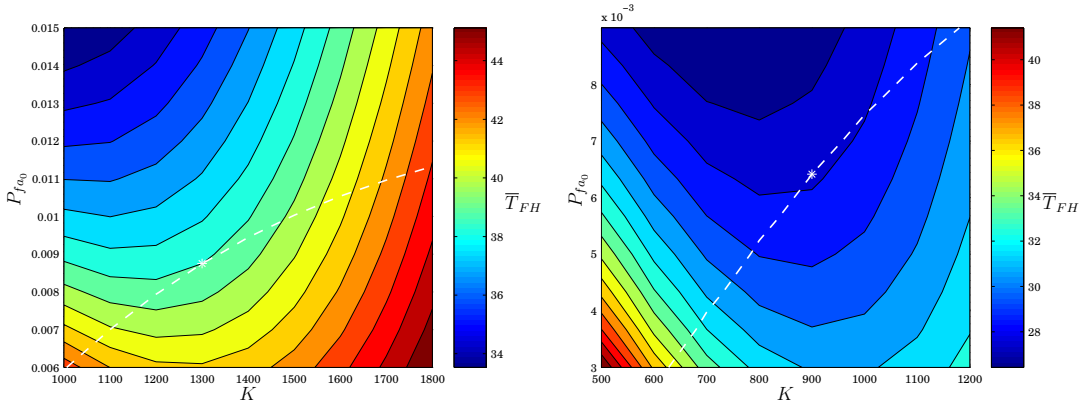
variance of the time to first hit were introduced. The effect of multiple H_1 tiles in the uncertainty region was investigated in Section 5.2. It was demonstrated that more accurate measures of acquisition performance can be obtained by including this effect.

In Section 5.3 the results of this chapter were applied to the optimisation problem. A simple test case was considered and the receiver parameters were numerically optimised to achieve the minimum time to first hit for a design point probability of detection of $P_D = 0.9$. It was shown that the best choice of detector/estimator is dependent on the received SNR. For large SNR, the traditional NCCD outperforms the DCCD. For signal powers lower than -165 dBW (or a carrier to noise ratio $C/N_0 \leq 38.8$ dBW/Hz), however, the use of the DCCD can



a) NCCD b) DCCD, standard form

Figure 5.11: Contour Plot of $\overline{T}_{FH}$ vs K and P_{fa}. $C/N_0 = 28.8$ dB-Hz, $M = 1$. The dashed line is the contour of constant $P_D = 0.9$.

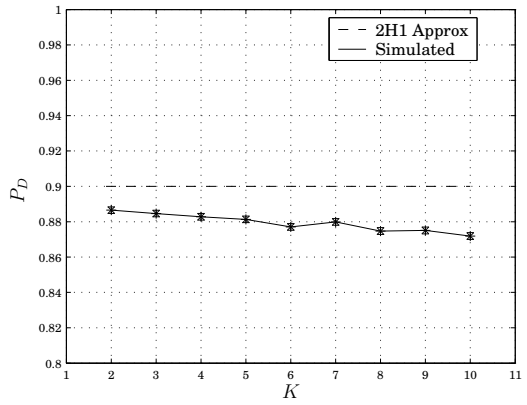


a) NCCD b) DCCD, standard form

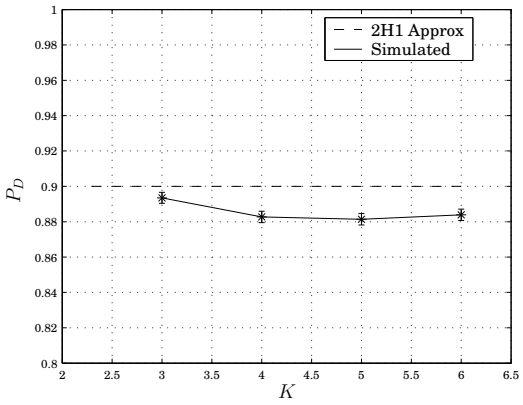
Figure 5.12: Contour Plot of $\overline{T}_{FH}$ vs K and P_{fa}. $C/N_0 = 23.8$ dB-Hz, $M = 3$. The dashed line is the contour of constant $P_D = 0.9$.

lead to a reduction in $\overline{T}_{FH}$ of up to 33%. The resulting optimised receiver parameters are recorded in Table 5.1. All the results presented in this chapter were verified by Monte Carlo simulation using a simplified signal model as discussed in Section 5.1.6.

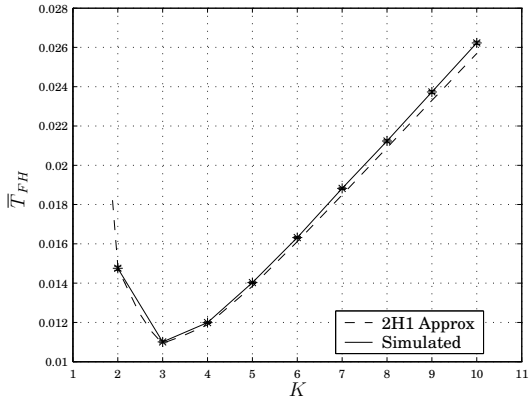
In the following chapter we briefly outline how the results of this chapter can be extended to the case of the acquisition of signals with unknown power levels from multiple satellites.



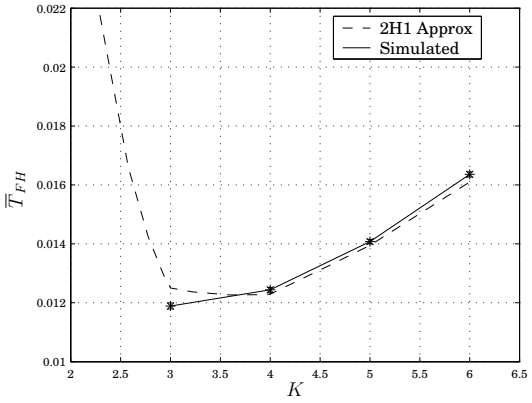
a) NCCD



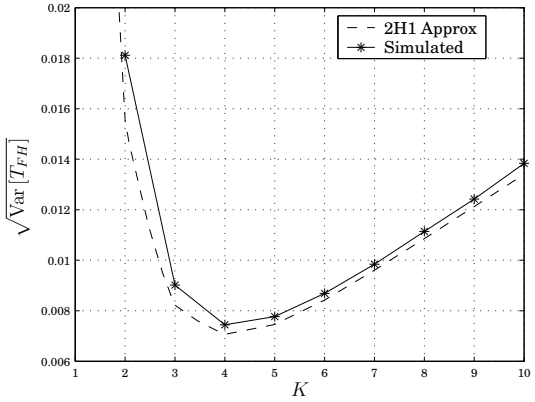
b) DCCD, standard form.



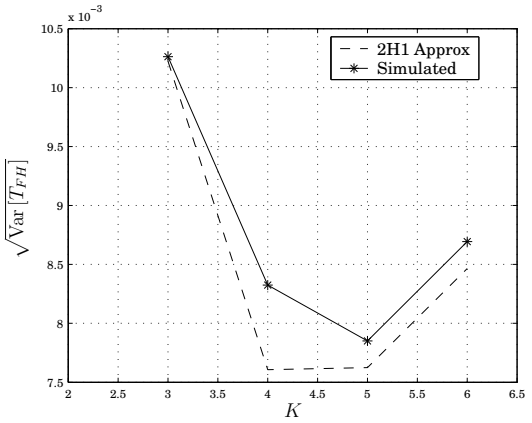
a) NCCD



b) DCCD, standard form.

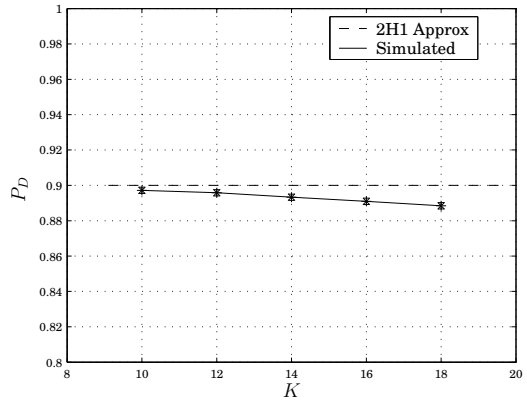


a) NCCD

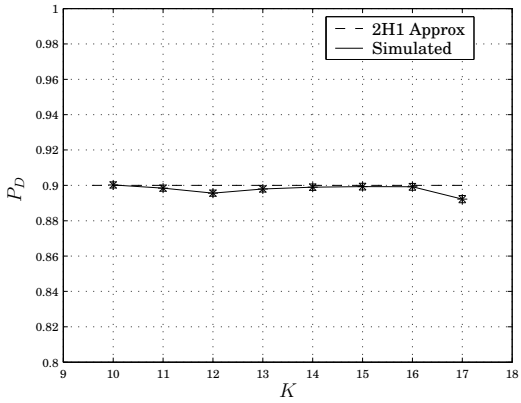


b) DCCD, standard form.

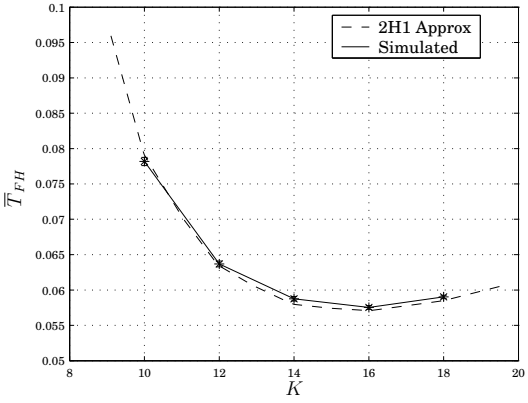
Figure 5.13: Comparison of P_D, $\overline{T}_{FH}$ and $\sqrt{\mathrm{Var}\,[T_{FH}]}$ along the Contour $P_D = 0.9$. $C/N_0 = 43.8$ dB-Hz, $M = 1$, $N_{\mathrm{T}} = 5$.



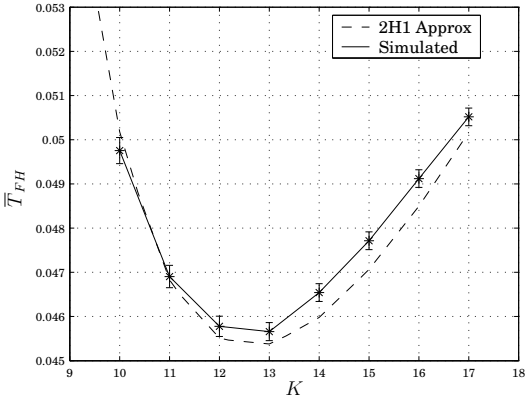
a) NCCD



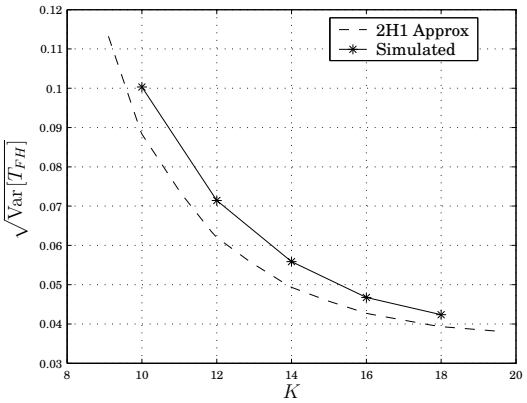
b) DCCD, standard form.



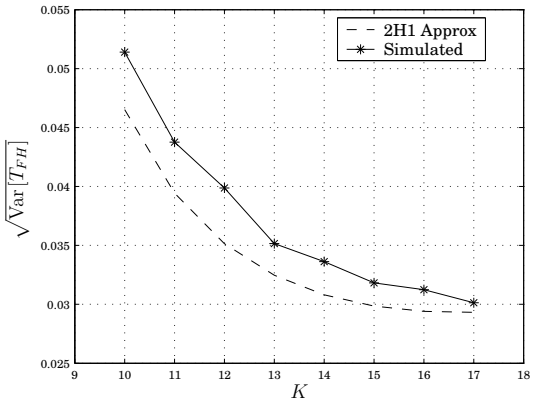
a) NCCD



b) DCCD, standard form.

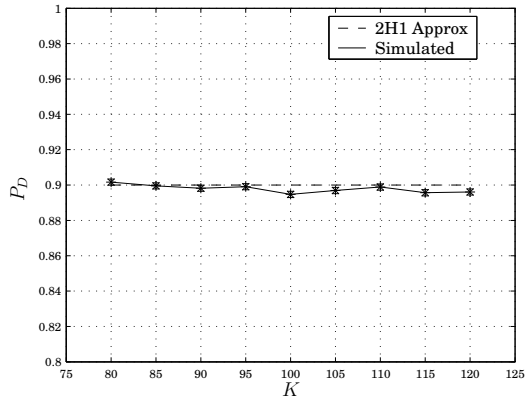


a) NCCD

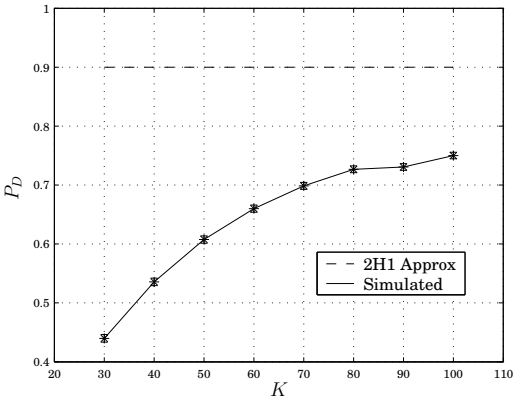


b) DCCD, standard form.

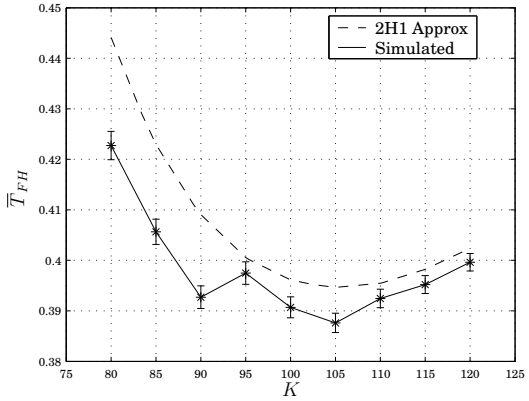
Figure 5.14: Comparison of P_D, $\overline{T}_{FH}$ and $\sqrt{\mathrm{Var}\left[T_{FH}\right]}$ along the Contour $P_D = 0.9$. $C/N_0 = 38.8$ dB-Hz, $M = 1$, $N_{\mathrm{T}} = 5$.



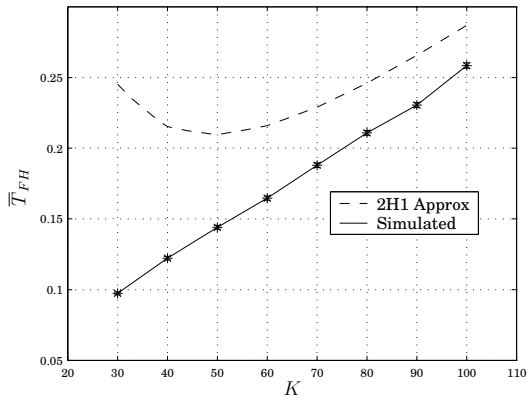
a) NCCD



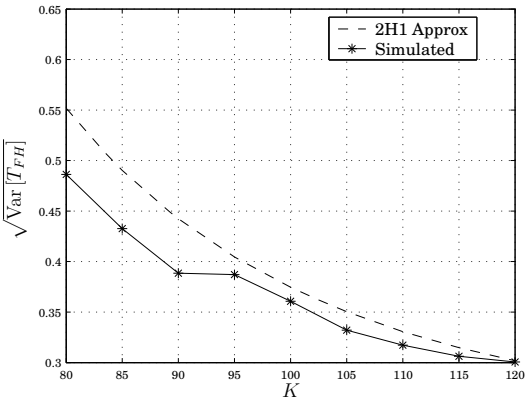
b) DCCD, standard form.



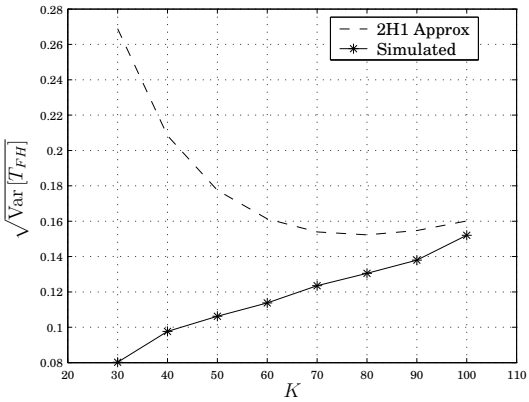
a) NCCD



b) DCCD, standard form.

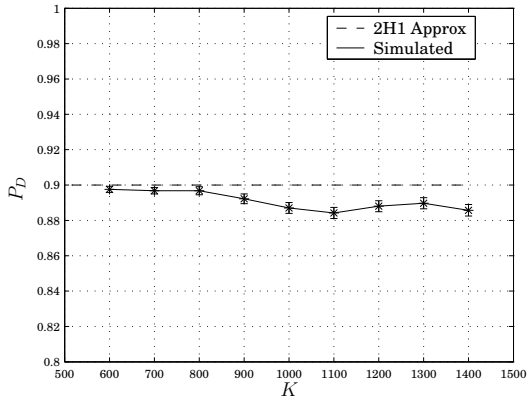


a) NCCD

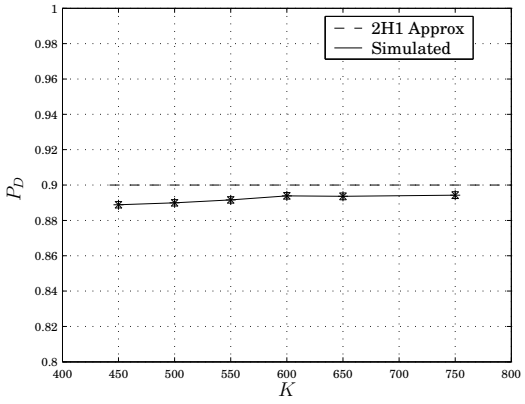


b) DCCD, standard form.

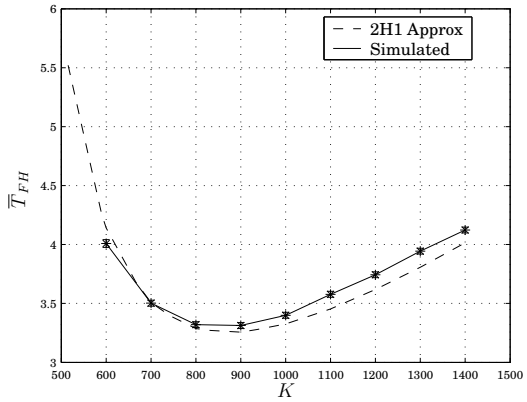
Figure 5.15: Comparison of P_D, $\overline{T}_{FH}$ and $\sqrt{\mathrm{Var}\left[T_{FH}\right]}$ along the Contour $P_D = 0.9$. $C/N_0 = 33.8$ dB-Hz, $M = 1$, $N_{\mathrm{T}} = 5$.



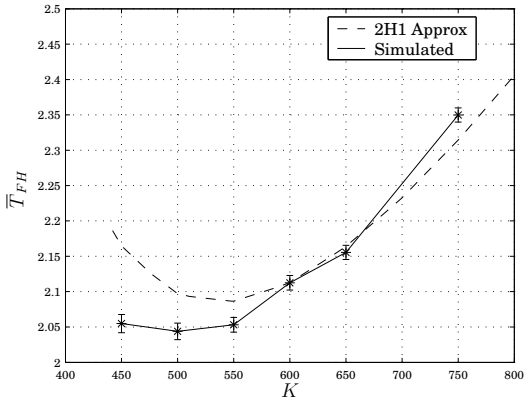
a) NCCD



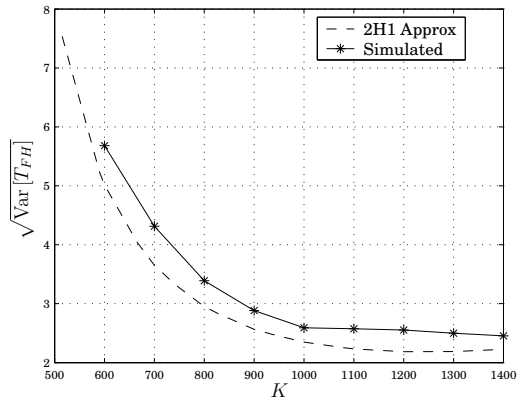
b) DCCD, standard form.



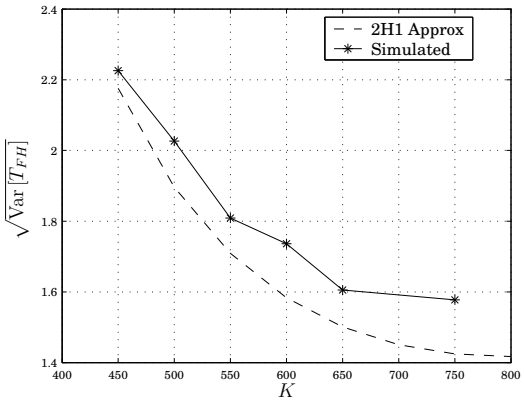
a) NCCD



b) DCCD, standard form.

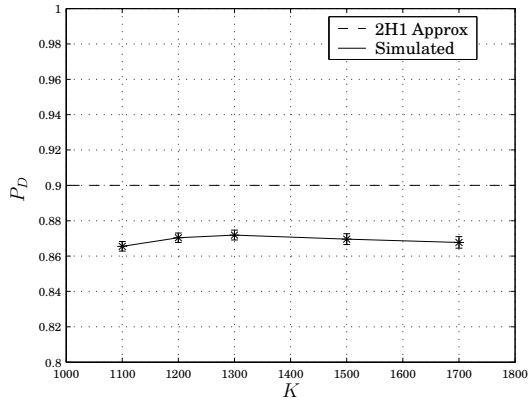


a) NCCD

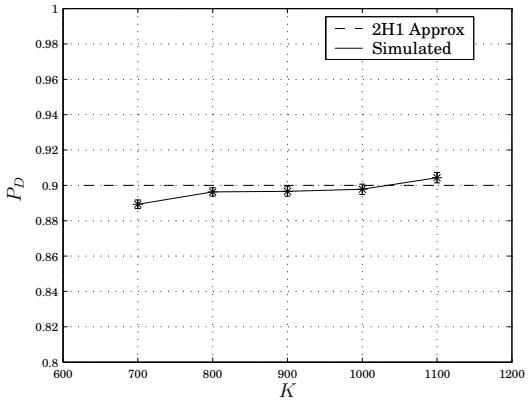


b) DCCD, standard form.

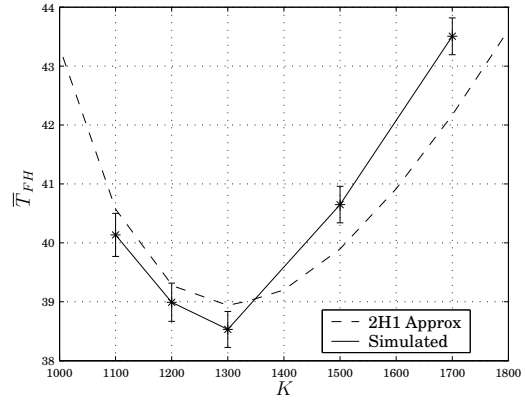
Figure 5.16: Comparison of P_D, $\overline{T}_{FH}$ and $\sqrt{\mathrm{Var}\left[T_{FH}\right]}$ along the Contour $P_D = 0.9$. $C/N_0 = 28.8$ dB-Hz, $M = 1$, $N_{\mathrm{T}} = 5$.



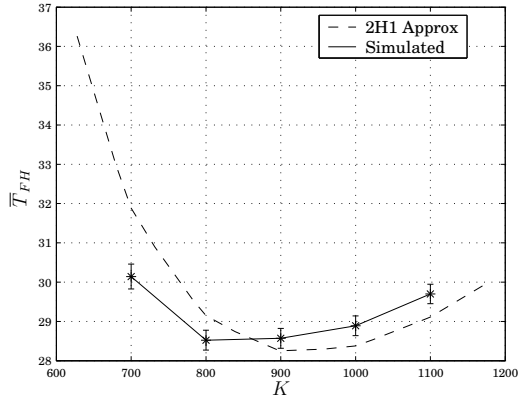
a) NCCD



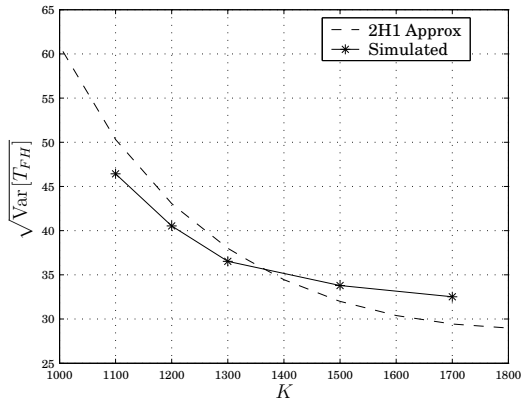
b) DCCD, standard form.



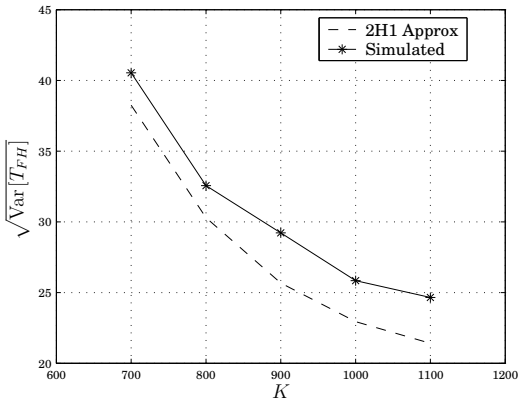
a) NCCD



b) DCCD, standard form.



a) NCCD



b) DCCD, standard form.

Figure 5.17: Comparison of P_D, $\overline{T}_{FH}$ and $\sqrt{\mathrm{Var}\left[T_{FH}\right]}$ along the Contour $P_D = 0.9$. $C/N_0 = 23.8$ dB-Hz, $M = 3$, $N_{\mathrm{T}} = 15$.

Chapter 6

Acquisition in the Presence of Multiple Satellites and Unknown Power Levels

The major results of this thesis have been presented in the previous three chapters. In this chapter we present an overview of how these new results may be applied in the implementation of a practical weak signal acquisition system. In particular, two key factors affecting acquisition performance for weak GPS signals are considered:

1. Unknown power levels. Thus far we have assumed that the power of the received signal is known and that a suitable threshold can be chosen.

2. Multiple satellites. In addition, it has been assumed that MAI can be modelled as part of the AWGN process affecting the signal. At low power levels, however, MAI can have a significant effect on receiver performance.

In this chapter we address these two issues. We treat the received signal power as an unknown (random) signal parameter. We treat this parameter as one of the so-called desired parameters and, therefore, attempt to estimate it. Following the principle used in estimation of the other desired parameters (*i.e.* the code-phase and Doppler offsets), we introduce the signal power for satellite k, P_k, as a third dimension in the uncertainty region Θ, which is discretised in the acquisition process.

As discussed in Section 2.1, the GPS spreading codes are members of the family of sequences known as Gold codes. They are chosen for their cross-correlation

properties: for any two members of the GPS spreading codes, the maximum cross-correlation value is approximately 24 dB down relative to the auto-correlation main lobe. In open-air environments, where all satellites are received with similar power levels, this provides sufficient protection against multi-access interference such that the sum of the signal contributions from all satellites in the sky is below the noise floor. Note, however, that if the satellite signals are received with widely varying power levels, then this 24 dB of MAI protection is no longer sufficient, and MAI can dominate over thermal noise effects. In the following we introduce a detection theoretic approach to the MAI problem.

6.1 Acquisition in the Presence of MAI

Recall that the SCD generates a single decision statistic for a single parameter estimate $\widehat{\boldsymbol{\theta}}$. The detector operates on the principle that there are two hypotheses regarding the underlying observation vector:

1. H_0: the observation vector contains noise alone.

2. H_1: the observation vector contains both signal and noise.

The presence of a strong interferer is not accounted for in either of these hypotheses, which necessitates the introduction of two further hypotheses:

3. H_2: the observation vector contains thermal noise and one or more strong interferers.

4. H_3: the observation vector contains signal, thermal noise and one or more strong interferes.

If the power level of the interferer is unknown, then hypotheses H_1, H_2 and H_3 are indistinguishable for the SCD.

For the parallel detector/estimator, the situation is similar but, significantly, not identical. We consider, in particular, the case of the FFT-based detector/ estimator, in which case the decision statistic for one full Doppler bin is calculated. This corresponds to a sampling of the complete correlation function of the received signal with the spreading sequence of interest. Under H_0, therefore, the decision statistics all consist of thermal noise alone. Under H_1, most of the statistics consist of thermal noise only, whilst a small subset consist of both signal

and noise, corresponding to the auto-correlation main lobe. Under H_2, approximately half of the decision statistics consist of noise only, with the remainder corresponding to signal power from the strong interferer(s) in the form of cross correlation side-lobes. Under H_3, the decision statistics are similar to those under H_1, with the exception that the side-lobes will be of considerably greater magnitude, possibly even exceeding the main lobe. Each of these hypotheses are illustrated in Figure 6.1, which shows a simple test case consisting of the signal being sought at $C/N_0 = 44$ dB-Hz and a strong interferer at $C/N_0 = 59$ dB-Hz†. The detector/estimator is chosen to yield minimum $\overline{T}_{FH}$ subject to $P_D \geq 0.9$ in accordance with Table 5.1. Note that the presence of the strong interferer is clearly indicated by the elevated values of the decision statistic across the entire range of ζ. Note also that, in the sample case considered in Figure 6.1, the presence of the signal is still detectable in the presence of MAI. However, the detector is very likely to yield a false alarm under H_2. Note that, unlike the H_0 case, the side-lobe peak under H_2 looks just like the main lobe under H_1 and so can be tracked. Thus, even a 15 dB difference in received power levels can lead to a significant performance degradation due to MAI.

Denoting by $\boldsymbol{D_k}$ the vector of decision statistics output by the parallel detector/estimator, we wish to determine whether or not there is a strong interfering signal present in $\boldsymbol{D_k}$. Expressing the problem as a detection problem allows us to use the techniques of detection theory. From Section 2.3 we have seen that the optimal detector takes on the form of a likelihood ratio test. We denote by H_{nmai} the hypothesis that there is no MAI in $\boldsymbol{D_k}$ and by H_{mai} the hypothesis that MAI is present in $\boldsymbol{D_k}$. The likelihood ratio is then given by:

$$\boldsymbol{\Lambda}\left(\boldsymbol{D_k}\right) = \frac{f_{\boldsymbol{D_k}|H_{\text{mai}}}(\boldsymbol{D_k} \mid H_{\text{mai}})}{f_{\boldsymbol{D_k}|H_{\text{nmai}}}(\boldsymbol{D_k} \mid H_{\text{nmai}})}\,. \tag{6.1}$$

The multi-dimensional PDFs in the numerator and the denominator of Equation (6.1) are difficult to determine, however, so we prefer to generate a sufficient statistic which is easier to calculate. In the absence of an analytic expression for the likelihood ratio we resort to an *ad hoc* approach.

Considering Figure 6.1, one obvious difference in $\boldsymbol{D_k}$ caused by MAI is the significant increase in power in many components of $\boldsymbol{D_k}$. We would, therefore,

†To keep simulation times manageable we consider only the presence of strong signals and stronger interferers. The results are equally applicable when the signal sought is weak and the interferer is received with normal (line of sight) power levels.

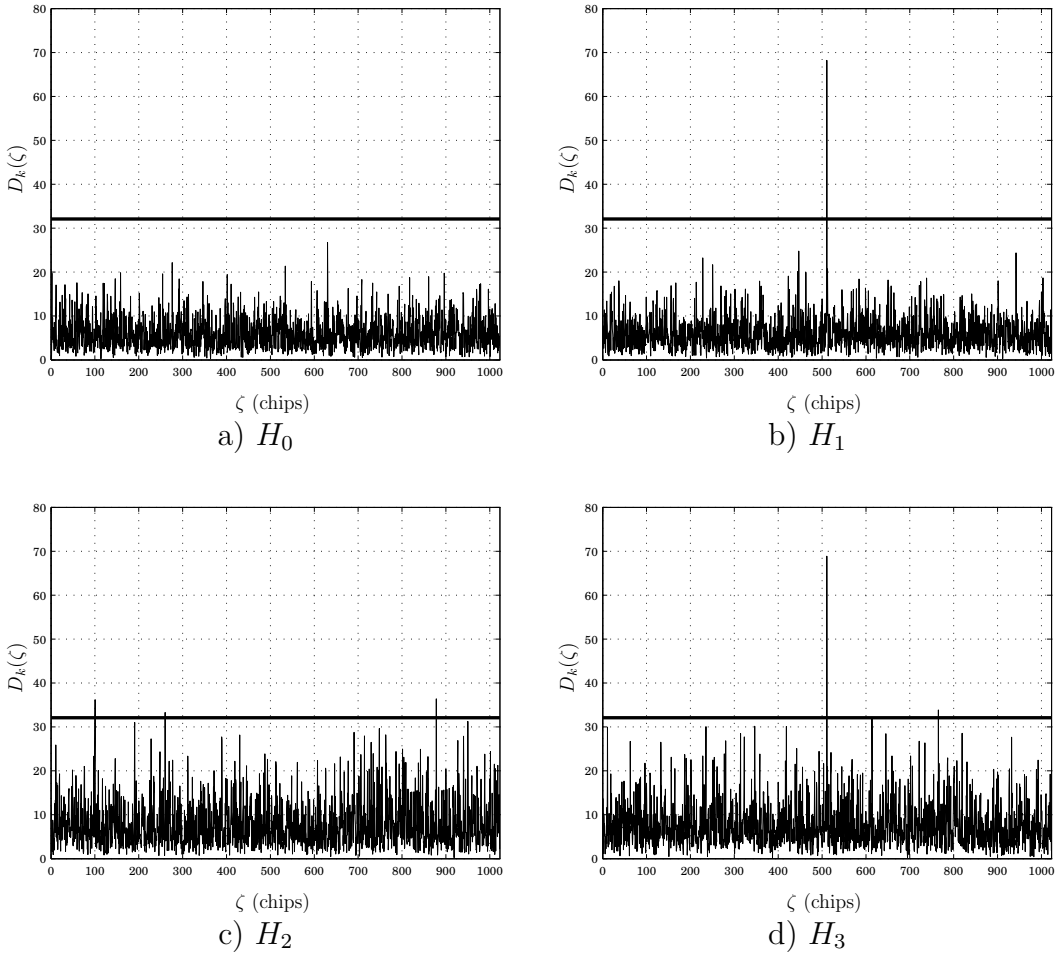


Figure 6.1: Sample Plots of the Decision Vector $\boldsymbol{D_k}$ in the Presence and Absence of MAI. a) H_0: noise only, b) H_1: signal plus noise, c) H_2: noise plus interference, d) H_3: signal plus noise plus interference. In all cases, the NCCD detector is used with $M = 1$, $K = 3$ and $C_{\mathrm{T}} = 2048$. The signal being sought (sv 1) has $C/N_0 = 44$ dB-Hz and $\zeta = 511$ chips, the interfering signal (sv 30) has $C/N_0 = 59$ dB-Hz and $\zeta = 255$ chips. Both signals have zero Doppler and no data modulation. The decision threshold V_{Th} is indicated by a horizontal bar and has been chosen to yield $P_{fa_0} = 0.0317$, in accordance with the first row of Table 5.1.

expect the average value of $\boldsymbol{D_k}$ to be significantly greater in the presence of MAI than in its absence. We, therefore, suggest the statistic ν, defined by:

$$\nu \stackrel{\Delta}{=} \sum_{i=0}^{C_{\mathrm{T}}-1} D_{k,i}\,, \tag{6.2}$$

as a suitable metric for the detection of MAI. We refer to this statistic as the *power level detector* for MAI.

6.1.1 Statistics of the Power Level Detector

To determine the performance of our proposed MAI detector it is necessary to obtain expressions for the detector statistics. Ideally, we would like to obtain exact expressions for the PDF and CDF of ν under all hypotheses, though this will not always be possible. Alternatively, if expressions for the mean and variance can be obtained, then we can invoke the central limit theorem to derive a Gaussian approximation.

The distribution of ν depends on the form of detector/estimator used in the generation of the vector $\boldsymbol{D_k}$. We now consider each detector/estimator form in turn.

The ML Form

We now demonstrate that, when the ML detector/estimator is used in the generation of $\boldsymbol{D_k}$, then ν can be expressed as an Hermitian quadratic form in complex Gaussian variables [138].

Consider the parallel (FFT-based) form of the ML detector/estimator illustrated in Figure 6.2. The output of the coherent accumulator has been labelled

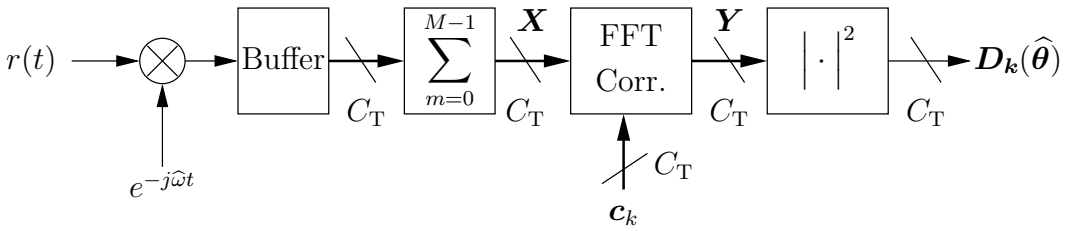


Figure 6.2: Parallel Form of the ML Detector/Estimator.

$\boldsymbol{X}$, which is a C_{T}-dimensional complex Gaussian random variable with mean $\boldsymbol{\mu}_X$ and covariance matrix $\boldsymbol{C}_X$. The output of the correlator has been labelled $\boldsymbol{Y}$ and this, too, is a multi-dimensional complex rv. Denoting by $\boldsymbol{c}_k$ the re-sampled spreading code of the satellite of interest (satellite k), then we can relate $\boldsymbol{Y}$ to $\boldsymbol{X}$ through the matrix equation:

$$\boldsymbol{Y} = \boldsymbol{S}_k \boldsymbol{X}, \tag{6.3}$$

where $\boldsymbol{S}_k$ is the matrix:

$$\boldsymbol{S}_k = \begin{pmatrix} c_{k,0} & c_{k,1} & \cdots & c_{k,C_\mathrm{T}-1} \\ c_{k,C_\mathrm{T}-1} & c_{k,0} & \cdots & c_{k,C_\mathrm{T}-2} \\ \vdots & \vdots & \ddots & \vdots \\ c_{k,1} & c_{k,2} & \cdots & c_{k,0} \end{pmatrix}. \tag{6.4}$$

$\boldsymbol{S}_k$ is an example of a *circulant* matrix [50]. A circulant matrix is a square matrix in which each row is formed by a cyclic shift of the preceding row. Thus, the matrix is completely defined once any one row or column is known. In the case of $\boldsymbol{S}_k$, the first row is simply the re-sampled spreading code of satellite k.

Since the rv $\boldsymbol{Y}$ is a linear transformation $\boldsymbol{X}$, it also is a C_T-dimensional complex Gaussian rv, with mean $\boldsymbol{\mu}_Y$ and covariance $\boldsymbol{C}_Y$, given by:

$$\boldsymbol{\mu}_Y = \boldsymbol{S}_k \boldsymbol{\mu}_X \tag{6.5}$$

$$\boldsymbol{C}_Y = \boldsymbol{S}_k \boldsymbol{C}_X \boldsymbol{S}_k^\mathrm{H}. \tag{6.6}$$

The decision statistic of the ML detector/estimator is formed as follows:

$$D_{k,i} = |Y_i|^2 = Y_i^* Y_i,$$

and, consequently, the power level detector decision statistic, ν, can be written as:

$$\nu = \sum_{i=0}^{C_\mathrm{T}-1} D_{k,i} = \boldsymbol{Y}^\mathrm{H} \boldsymbol{Y}. \tag{6.7}$$

Thus, ν is an Hermitian quadratic form in complex Gaussian variables.

The advantage of expressing ν in such a form is that it enables us to make use of many existing results for quadratic forms. In particular, whilst there is no known closed form expression for the distribution of a general quadratic form, it has been previously shown that any such form can be written as a weighted sum of χ^2 rvs [73, 74]. In addition, numerical routines for the evaluation of the PDF and CDF are readily available in the literature (see [114] and [36], for example). However, in the present application, numerical routines are difficult to implement due to the large value of C_T (of the order of 1000). In this case, we make use of the central limit theorem to obtain a Gaussian approximation to ν and, hence,

we require expressions for its mean and variance. Once again, we make use of Turin's result on the characteristic function of Hermitian quadratic forms [138] to derive expressions for the first two central moments of ν.

From [138], we have the following expression for the CHF of ν:

$$\Phi_{\nu}(j\omega) = |\boldsymbol{P}|^{-1} \exp\left(-\boldsymbol{\mu}_{\boldsymbol{Y}}^{\mathrm{H}} \boldsymbol{C}_{Y}^{-1} \left[\boldsymbol{I} - \boldsymbol{P}^{-1}\right] \boldsymbol{\mu}_{\boldsymbol{Y}}\right), \tag{6.8}$$

where, by analogy with Equation (4.48), we have introduced the matrix $\boldsymbol{P}$, defined by:

$$\boldsymbol{P} \triangleq \boldsymbol{I} - j\omega \boldsymbol{C}_{Y}. \tag{6.9}$$

Recall that the moments of ν can be obtained from its characteristic function, $\Phi_{\nu}(j\omega)$, through the formula:

$$E_{\nu}\left[\nu^{i}\right] = \frac{1}{j^{i}} \left. \frac{d^{i}\Phi_{\nu}(j\omega)}{d\omega^{i}} \right|_{\omega=0}. \tag{6.10}$$

Using Equation (6.10), in conjunction with a useful result on the eigenvalues of circulant matrices [50, Section 3.1], we derive the following expressions for the mean and variance of ν in Appendix B.4.1:

$$E[\nu] = 2\sigma_{Y}^{2} C_{\mathrm{T}} + \boldsymbol{\mu}_{Y}^{\mathrm{H}} \boldsymbol{\mu}_{Y} \tag{6.11}$$

$$\mathrm{Var}[\nu] = \frac{4\sigma_{Y}^{4}}{C_{\mathrm{T}}} \sum_{i=0}^{C_{\mathrm{T}}-1} |\boldsymbol{\theta}_{i}|^{2} + 2\boldsymbol{\mu}_{Y}^{\mathrm{H}} \boldsymbol{C}_{Y} \boldsymbol{\mu}_{Y}, \tag{6.12}$$

where $\boldsymbol{\theta}_{i}$ is the i^{th} component of the auto-correlation function of the re-sampled spreading sequence.

The Noncoherent Combining Form

In this case, we assume that the noncoherent combining detector/estimator is used to generate the decision vector $\boldsymbol{D}_{k}$ from which the power level detector decision statistic, ν, is subsequently formed. The decision statistic is simply the sum of K statistically independent ML form decision statistics and, hence, the mean and variance are, respectively, given by:

$$E[\nu] = 2K\sigma_{Y}^{2} C_{\mathrm{T}} + K\boldsymbol{\mu}_{Y}^{\mathrm{H}} \boldsymbol{\mu}_{Y} \tag{6.13}$$

$$\mathrm{Var}\left[\nu\right] = \frac{4K\sigma_Y^4}{C_\mathrm{T}} \sum_{i=0}^{C_\mathrm{T}-1} \left|\boldsymbol{\theta}_i\right|^2 + 2K\boldsymbol{\mu}_Y^\mathrm{H}\boldsymbol{C}_Y\boldsymbol{\mu}_Y. \tag{6.14}$$

To demonstrate the accuracy of this Gaussian approximation we consider again the situation presented in Figure 6.1. In this case we run $10,000$ trials for each hypothesis and generate a simulated PDF of ν, $f_\nu(\nu)$, for each. The results are compared with our Gaussian model for each case H_0, H_1 and H_2. The H_3 case requires more work, and is not essential, in that we would expect ν to be greater under H_3 than H_2. Hence, the H_2 case forms a lower bound on ν in the presence of MAI. The results are shown in Figure 6.3. We can clearly see that the power level

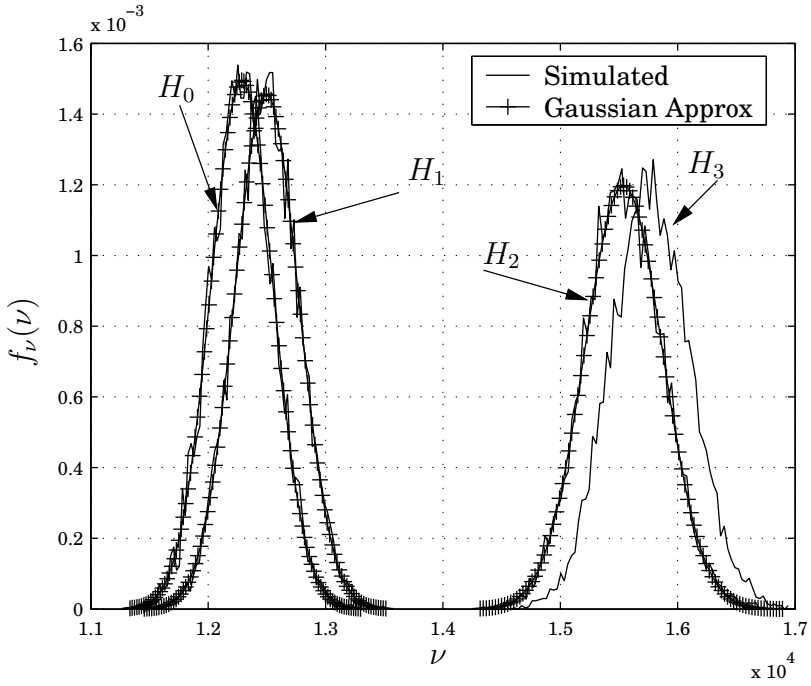


Figure 6.3: Distribution of ν for the Power Level Detector. The signal parameters are identical to those described in Figure 6.1.

detector has no trouble distinguishing MAI from non-MAI situations in this case. What is particularly interesting here is that, as the difference in received power levels decreases, the power level detector is less likely to detect MAI. However, at the same time, MAI has a less significant impact in this situation.

Differentially Coherent Forms

Unfortunately we have been unable to derive simple expressions for the mean and variance of the power level detector decision statistic for the differentially coherent combining detector. The differentially coherent product introduces an extra degree of complexity, such that ν is not expressible as a quadratic form.

Consider the parallel DCCD of Figure 6.4, where $\boldsymbol{X}_r$ is the r^{th} output of the pre-correlation coherent accumulator as in Figure 6.2. We define the $K \times C_{\text{T}}$

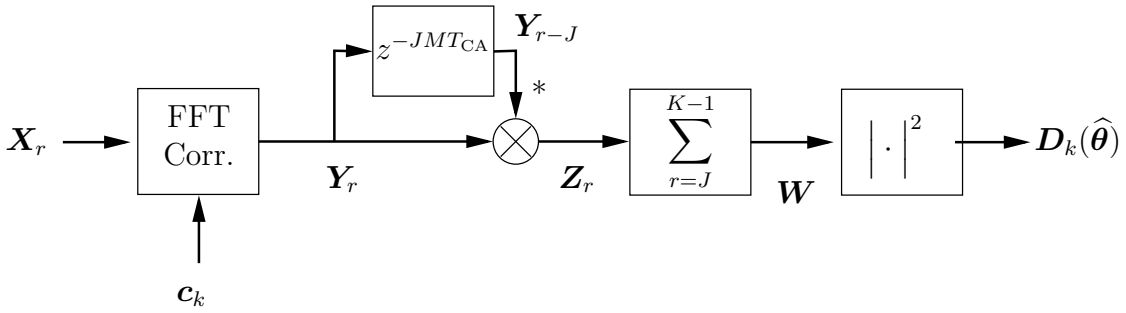


Figure 6.4: Parallel Form of the DCCD Detector/Estimator.

dimensional complex Gaussian *matrix* $\boldsymbol{\Gamma}$ by:

$$\boldsymbol{\Gamma} = \begin{bmatrix} \boldsymbol{Y}_0^{\text{T}} \\ \boldsymbol{Y}_1^{\text{T}} \\ \vdots \\ \boldsymbol{Y}_{K-1}^{\text{T}} \end{bmatrix} \tag{6.15}$$

where $\boldsymbol{Y}_i$ denotes the i^{th} coherent accumulator output. The output of the differentially coherent accumulator, denoted $\boldsymbol{W}$, is then given by:

$$\boldsymbol{W} = \text{diag}(\boldsymbol{\Gamma}^{\text{H}} \boldsymbol{Q} \boldsymbol{\Gamma}), \tag{6.16}$$

where $\text{diag}(\boldsymbol{M})$ denotes the vector consisting of the diagonal elements of the matrix $\boldsymbol{M}$, $\boldsymbol{Q} = \boldsymbol{Q_I} + j\boldsymbol{Q_Q}$, and $\boldsymbol{Q_I}$ and $\boldsymbol{Q_Q}$ are the Hermitian matrices defined in Equations (4.43) and (4.44). The power level detector decision statistic is then given by:

$$\nu = \boldsymbol{W}^{\text{H}} \boldsymbol{W}. \tag{6.17}$$

Thus, ν is an Hermitian quadratic form in $\boldsymbol{W}$, but $\boldsymbol{W}$ is *not* distributed as a

complex Gaussian random vector. In fact, $\boldsymbol{W}$ is a vector of (statistically dependent) quadratic forms in complex Gaussian rvs. Thus, we might describe ν as a *quartic form*. There does not appear to be any treatment of such forms in the literature, and we have been unable to obtain even the first order moments.

For this reason, we suggest the use of the noncoherent power level detector in conjunction with the DCCD. This requires some extra processing (the square magnitude of all elements of $\boldsymbol{Y}_r$ must be taken and added to an accumulator for each $r \ : \ 0 \leq r \leq K-1$), but has the advantage that the analysis of the preceding sections can be directly applied.

In Figure 6.5, simulated PDFs for ν are shown for all four hypotheses. As with the NCCD form of the power level detector, we again see that this detector has no trouble distinguishing H_{nmai} from H_{mai}. It would, therefore, be valuable to have a model of ν for this detector. This would permit a simpler detector structure when detecting MAI when using the DCCD.

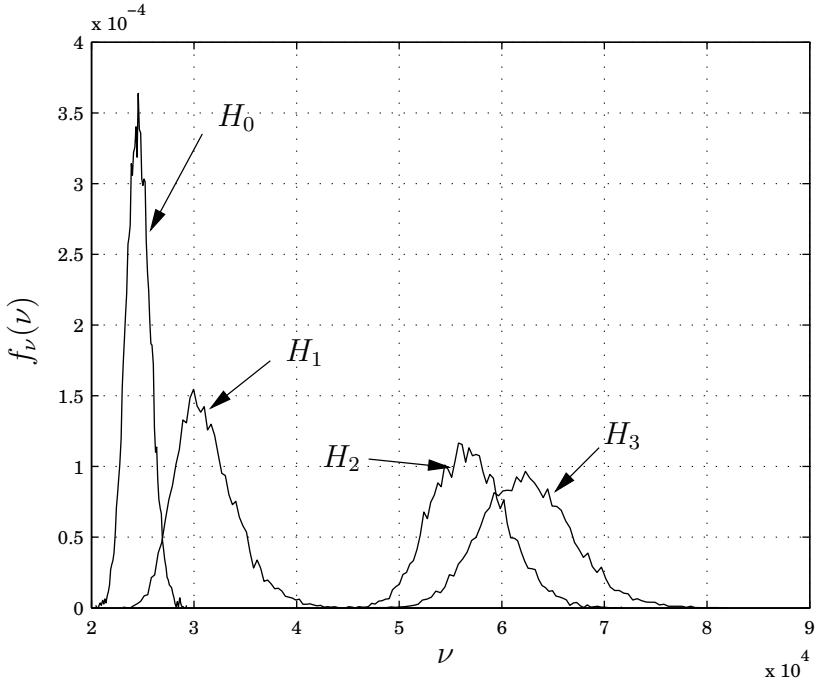


Figure 6.5: Distribution of ν for the Power Level Detector: DCCD. The signal parameters are identical to those described in Figure 6.1.

6.2 Acquisition in the Presence of Unknown Power Levels

Our treatment of the acquisition process in Chapter 5 operated under the assumption that the signal power level is known. This allows the designer to choose appropriate parameters for the detector/estimator, such as the observation interval and the decision threshold. In the absence of any *a priori* information regarding the signal power level, it becomes increasingly difficult to design for a specified performance level.

One technique, which we adopt here, is to treat the signal power from satellite k, P_k, as an extra signal parameter. We treat this as one of the desired parameters from the signal and, hence, we must modify our system to provide an estimate of P_k. We follow the same approach as was used for the estimation of the other desired parameters, ω_d and ζ. The presence of this third desired signal parameter adds a third dimension to the search space, which we discretise. For a given estimate of the signal power $\widehat{P}_k$, the uncertainty region in ω_d and ζ has the form of a plane in parameter space, which we refer to as a "power strip". The design problem, therefore, is to choose an optimal discretisation of the uncertainty space.

The Markov chain model of the acquisition process in this three dimensional uncertainty space is illustrated in Figure 6.6. In each power strip the detector/ estimator and acquisition process are designed as if the power level were known. Thus, using the results we have obtained in Chapter 4, a noncoherent combining form would be implemented in the highest power strip, moving to a differentially coherent combining form in lower power strips. The strips are searched in order of decreasing power level, to counter the effect of MAI. This increases the probability that stronger signals are acquired first. Additional MAI protection is achieved through the implementation of the power level detector discussed in Section 6.1.1.

Using the techniques derived in this thesis we can choose, for each estimated received signal power level, to implement either a NCCD or a DCCD. The expressions of Chapters 4 and 5 permit the determination of the optimum signal parameters for each detector/estimator type in each power strip. The performance of such a system can be analysed by an extension of the Markov chain discussed in Chapter 5.

One of the major advantages accruing from such a system is the similarity in receiver structures between the NCCD and DCCD forms. In each case the corre-

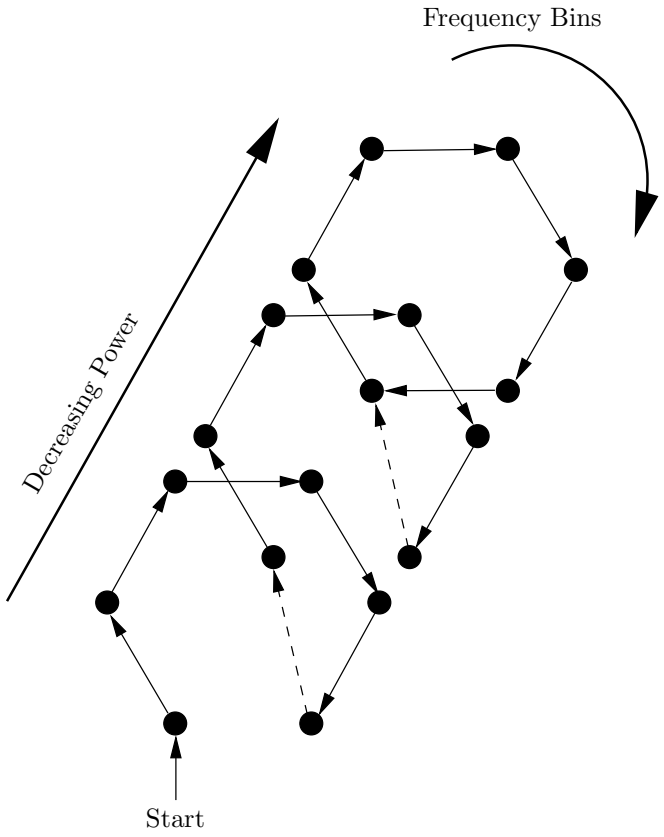


Figure 6.6: Three Dimensional Markov Chain Model for Acquisition in the Presence of Unknown Power Levels. An FFT-based detector/estimator is assumed, each filled circle in the diagram represents a single Doppler bin, including all possible code phase offsets.

lator/coherent accumulator forms the basis of the receiver structure. In addition, each form entails multiplication by complex conjugate and further accumulation. Thus, the use of a flexible NCCD/DCCD receiver requires very little extra hardware, but, as we have seen can yield significant savings in mean acquisition times.

Whilst the technique outlined in this section is quite straightforward, following naturally from our detection/estimation theoretic exposition of the acquisition problem, it is not one that we have seen presented previously in the literature.

6.3 Discussion

In this chapter we have given a brief overview of how the new results obtained in this thesis may be applied in a practical situation to the acquisition of a GPS signal of unknown power level in the presence of multiple interfering satellites.

The problem of multi-access interference (MAI) becomes significant at low received power levels. We have presented a novel, simple device for the detection of MAI, which we call the power level detector. We have derived an accurate Gaussian approximation which can be used to analyse its performance.

Finally, we concluded with a brief overview of a strategy for acquiring signals of unknown power level. By introducing the power level as an unknown signal parameter which is to be estimated we can apply the techniques of estimation theory outlined in Section 2.2.

Chapter 7

Conclusions and Future Work

This chapter presents a summary of the conclusions reached in each of the preceding chapters and makes some recommendations for future work on the topic of weak signal acquisition.

7.1 Conclusions

Recall, from Chapter 1, that the motivation for this work has been the fast, reliable, parallel acquisition of weak GPS signals. Traditionally, noncoherent combining has been utilised in this context. In this work we have developed an analysis technique for a class of alternative acquisition techniques called differentially coherent processing. This analysis was subsequently applied to a simplified received signal model, for which it was demonstrated that differentially coherent techniques can yield a significant performance improvement (of the order of 33% in terms of mean time to first hit) when signals are weak ($C/N_0 \leq 38.8$ dB-Hz).

The analysis of the acquisition problem presented in this thesis is based on a detection- and estimation-theoretic treatment. To this end, the dual concepts of the detector/estimator and the acquisition process were introduced, each being analysed in turn. Four forms of detector/estimator were considered:

1. The optimal, or maximum likelihood (ML), form.
2. The noncoherent combining detector (NCCD) form.
3. The differentially coherent combining detector (DCCD) form.
4. The differentially coherent detector (DCD) form.

Chapters 3 and 4 provided a comprehensive analysis of all forms of detector/ estimator considered in this thesis. The analysis was divided into two components. Chapter 3 presented an analysis of the effects of unknown signal parameters on the detector/estimator. The unknown signal paramters considered were:

1. Data modulation.
2. Carrier Doppler offset.
3. Code phase offset.
4. Code frequency offset (code Doppler).

Our analysis procedure was to consider the decision variable, denoted D_k, as a function of the received signal parameters, denoted by the vector $\boldsymbol{\theta}$, in the absence of noise. The presence of undesired, or incorrectly estimated, signal parameters results in a distortion of $D_k(\boldsymbol{\theta})$. This distortion is manifested in two ways:

1. The value of $\boldsymbol{\theta}$ for which D_k is a peak moves away from the true signal parameter vector $\boldsymbol{\theta}_t$. This introduces an *estimation* error.
2. The magnitude of the peak value of D_k is reduced, which results in a reduced probability of *detection*.

Our approach was to derive the results directly for the all-digital receiver, rather than to use existing results for the analogue receiver. This technique proves useful in determining some new expressions for the effect of data modulation and Doppler effects, in particular. Our analysis of the NCCD yields new results for the combined effects of data modulation and carrier Doppler. In effect, it is shown that the presence of data modulation causes a spreading of signal power into adjacent frequency bins. The expressions derived are simple and more accurate than previously published results.

Chapter 4 provided a comprehensive treatment of the statistics of the detector/estimator, both in single-cell and parallel forms. New results for the distribution of the decision statistic for the DCCD were derived, including a demonstration that the magnitude statistic under the pair-wise form follows a K-distribution and that the magnitude statistic under the standard form can be represented as a weighted sum of K-distributed rvs. In addition, new Gaussian approximations, based on an application of the central limit theorem, were

derived for all differentially coherent forms. These approximations were shown to be more accurate than existing Gaussian approximations for the magnitude statistics. It was also observed that the designer cannot rely on the accuracy of Gaussian approximations when considering a parallel acquisition strategy, unless the observation interval is very long (of the order of 500 ms).

These results were subsequently used in a comparative performance analysis of all the detector/estimator forms. It was shown that the NCCD demonstrates superior performance at high SNR, or when a large probability of false alarm can be tolerated. At lower SNRs, or when a very low P_{fa} is required, then the standard form of the DCCD is the optimal choice of detector. In addition, a new expression for the union bound on the maximum attainable probability of detection for the parallel form of the NCCD was derived. This expression is based on our observation on the Marcum Q-function [89].

Armed with the preceding results on the detector/estimator, the focus of thesis turned to the acquisition process in Chapters 5 and 6. Beginning in Chapter 5, under the assumption that there is only one satellite in view and that the received signal power is a known quantity, new expressions for the mean and variance of the time to first hit were derived. These results are based on the application of matrix methods to the Markov chain model of the acquisition process. These expressions were subsequently used in the numerical optimisation of the receiver parameters. Both the differentially coherent and noncoherent detector/estimators were optimised independently, for a variety of received SNRs. It was demonstrated that the differentially coherent techniques outperform noncoherent techniques when the SNR is as little as 5 dB below nominal. The results of this chapter were published, in part, in [88].

Finally, in Chapter 6, the acquisition process model was extended to include the effects of multiple satellites and unknown received power levels. A new technique for the detection of MAI, referred to as the power level detector, was introduced. A simple Gaussian model for this detector was derived for the NCCD, though the same technique failed to produce a simple model for the differentially coherent forms. A new technique for signal acquisition when the received power level is unknown was also introduced. The method consists of introducing the signal power as a third parameter to be estimated (in addition to the code phase offset and the Doppler frequency shift) and applying the same parameter estimation techniques as are applied to the other signal parameters. Thus, the three

dimensional signal uncertainty space is discretised and the detector/estimator is optimised for each strip to yield minimum $\overline{T}_{FH}$ for a given probability of correct detection.

All the results derived in this thesis have been verified by Monte Carlo simulation. It is worth noting that these simulations operated under a simplified signal model. The effects of quantisation, front end filtering and Doppler rate were all ignored. To provide more realistic figures these effects should be taken into account. In particular, Doppler rate can have a significant effect on system performance when dwell times are long [113].

7.2 Future Work

As discussed above, all of the results in this thesis are derived based on a simplified signal model. The use of this simplified model renders a difficult problem somewhat more tractable. To continue with this work it is necessary first of all to expand the model to include, for instance, Doppler drift and quantisation effects.

Various results derived in this thesis could be developed further, for instance:

- More accurate models of the effect of data modulation on the DCCD could be derived.
- A numerically stable technique for the calculation of the distribution of the magnitude decision statistic of the standard form of the DCCD would be of particular interest. This would permit a more accurate analysis of DCCD performance in its parallel form for the range of values $26 < K < 500$.
- It may be possible to obtain a closed form expression for the distribution of the magnitude decision statistic of the pair-wise form of the DCCD by the application of the integral equation on *p.* 428 of [146] to Equation (4.97) in this thesis. We have made some progress using this approach, but were unable to obtain a closed form expression. This should, in turn, lead to an equivalent expression for the standard form.
- Perhaps an alternative approach could be applied to obtain a Gaussian (or other) approximation for the power level detector for the DCCD.

Our treatment of A-GPS was quite rudimentary, it was assumed that the receiver did not need to perform data demodulation and the Doppler frequency

shift was assumed to be known to within an accuracy of 5 kHz. In reality, depending on the mobile network type, much more accurate information may be provided by the A-GPS supplier. A detailed comparison of the various A-GPS scenarios would be of considerable interest (see [71, 77], for example).

At a more general level, GNSS is currently undergoing major development. In addition to the modernisation of the existing GPS, Europe is currently developing its own system, called Galileo, and Russia has recently decided to re-activate its GLONASS system. With these new and upgraded systems come many research opportunities. New signals, with new modulation schemes, transmitted at new frequencies provide new challenges to be overcome and new opportunities for improved performance. Some obvious future work arising from this thesis is the application of the techniques developed herein to these new GNSS signals. Many of these new signals are specifically designed to provide enhanced tracking performance and, hence, greater accuracy. However, as previously discussed, the major emerging market for GPS and, more generally, GNSS receivers is in mobile-embedded chipsets, where speed of acquisition and reliable operation under weak signal conditions are of greater importance than positioning accuracy. Determining the relative advantages and disadvantages the new signal structures bring to the acquisition problem is a very interesting open problem in the field, and one which may be approached using the techniques developed in this thesis.

Appendix A

Summation Identities

In the following: $0 \leq p < 1$; $N, L \in \mathbb{Z}^+$; and $L > N$.

$$\sum_{i=0}^{L-1} i = \frac{L(L-1)}{2} \tag{A.1}$$

$$\sum_{i=0}^{L-1} i^2 = \frac{L(L-1)(2L-1)}{6} \tag{A.2}$$

$$\sum_{i=0}^{\infty} p^i = \frac{1}{1-p} \tag{A.3}$$

$$\sum_{i=0}^{L-1} p^i = \frac{1-p^L}{1-p} \tag{A.4}$$

$$\sum_{i=N}^{L-1} p^i = \frac{p^N - p^L}{1-p} \tag{A.5}$$

$$\sum_{i=0}^{\infty} ip^i = \frac{p}{(1-p)^2} \tag{A.6}$$

$$\sum_{i=0}^{L-1} ip^i = \frac{p(1-p^L)}{(1-p)^2} - \frac{Lp^L}{1-p} \tag{A.7}$$

$$\sum_{i=N}^{L-1} ip^i = \frac{p(p^N - p^L)}{(1-p)^2} - \frac{Lp^L - Np^N}{1-p} \tag{A.8}$$

Appendix B

Mathematical Derivations

B.1 Derivations from Chapter 3

B.1.1 Average Modulation Attenuation when $M \leq D$

In Equation (3.21) we derived an approximation to the mean value of the modulation attenuation in the ML detector given that a transition occurs under the assumption that the bit transition can occur at *any* point during the observation interval.

In reality, our signal is discrete, so the bit transition can only occur at discrete points. Thus, we replace the continous variable δ_T with the discrete variable $\mu = \lfloor \delta_T(MN_s) \rfloor$, yielding:

$$\overline{\alpha}_m(\delta\omega_d \mid t) = \frac{1}{MN_s} \sum_{\mu=0}^{MN_s-1} \alpha_m(\delta\omega_d, \mu) \tag{B.1}$$

$$= \frac{1}{MN_s} \sum_{\mu=0}^{MN_s-1} 1 + 2t \left[\cot^2\beta - \cot\beta \ \left\{ \sin 2\beta \frac{\mu}{MN_s} + \cot\beta \ \cos 2\beta \frac{\mu}{MN_s} \right\} \right]. \tag{B.2}$$

Now, the summation over μ involves sine and cosine terms. Making note of the identities:

$$\sin x = \Im\left\{\exp\left(jx\right)\} \qquad \cos x = \Re\left\{\exp\left(jx\right)\right\} \tag{B.3}$$

$$\sum_i \Im\left\{x_i\right\} = \Im\left\{\sum_i x_i\right\} \qquad \sum_i \Re\left\{x_i\right\} = \Re\left\{\sum_i x_i\right\}, \tag{B.4}$$

we can use Equation (A.4) to write:

$$\sum_{\mu=0}^{MN_s-1} \exp\left(j\frac{\beta}{MN_s}\mu\right) = \exp\left(j\beta\left[1-\frac{1}{MN_s}\right]\right)\frac{\sin\beta}{\sin\frac{\beta}{MN_s}}\,. \tag{B.5}$$

Thus, we have:

$$\sum_{\mu=0}^{MN_s-1}\left\{\sin\left(2\beta\frac{\mu}{MN_s}\right) + \cot\beta\,\cos\left(2\beta\frac{\mu}{MN_s}\right)\right\} \tag{B.6}$$

$$= \frac{\sin\beta}{\sin\frac{\beta}{MN_s}}\left\{\sin\left(\beta\left[1-\frac{1}{MN_s}\right]\right) + \cot(\beta)\cos\left(\beta\left[1-\frac{1}{MN_s}\right]\right)\right\} \tag{B.7}$$

$$= \cot\frac{\beta}{MN_s}\,, \tag{B.8}$$

where we have used some standard trigonometric identities in the last step. Finally, inserting Equation (B.8) into Equation (B.2) we obtain:

$$\overline{\alpha}_m(\delta\omega_d \mid t) = 1 + 2t\left(\cot^2\beta - \frac{1}{MN_s}\cot\beta\cot\frac{\beta}{MN_s}\right)\,. \tag{B.9}$$

Recall that β is one half of the phase shift due to Doppler offset occurring in one coherent observation interval. Thus, $\beta/(MN_s)$ is one half of the phase shift occurring in one sampling interval, and so $\beta/(MN_s) \ll 1$. Thus:

$$\cot\left(\frac{\beta}{MN_s}\right) \approx \frac{MN_s}{\beta}\,, \tag{B.10}$$

and so Equation (B.9) is approximately equal to Equation (3.21).

B.1.2 Average Modulation Attenuation when $M > D$

In Section 3.1.2 we derived an expression for the average power attenuation due to modulation effects ($\overline{\alpha}_m$) in the ML detector when the coherent observation interval is less than or equal to the data bit period, *i.e.* $M \leq D$. The technique used proves useful in determining similar expressions for the NCCD and DCCD forms, but is not directly applicable to the determination of $\overline{\alpha}_m$ for the ML form when $M > D$. Here we apply the technique of Davisson and Flikkema [37] to derive the expression of Equation (3.26).

We start with the following:

$$X_n = \sqrt{0.5P_k}d_n \exp\left(j\omega_d T_s n\right) \tag{B.11}$$

$$Y = \sum_{n=0}^{MN_s-1} X_n \tag{B.12}$$

$$D_k = |Y|^2 = YY^* \tag{B.13}$$

$$= 0.5P_k \sum_{n=0}^{MN_s-1} \sum_{m=0}^{MN_s-1} d_n d_m \exp\left(j\omega_d T_s (n-m)\right) , \tag{B.14}$$

where X_n, Y, and D_k are defined in Figure 3.1 and d_n is the value data bit at time nT_s. We can view D_k as being the sum over all the elements of the matrix $\boldsymbol{A}$ defined such that:

$$\boldsymbol{A}_{n,m} = d_n d_m \exp\left(j\omega_d T_s (n-m)\right) , \tag{B.15}$$

and we have:

$$D_k = 0.5P_k \boldsymbol{e}^{\mathrm{T}} \boldsymbol{A} \boldsymbol{e} , \tag{B.16}$$

where $\boldsymbol{e}$ is the length MN_s vector of ones. Note that the matrix $\boldsymbol{A}$ is Hermitian, *i.e.* $\boldsymbol{A}^{\mathrm{H}} = \boldsymbol{A}$, or $\boldsymbol{A}_{n,m} = \boldsymbol{A}^*_{m,n}$. Thus

$$\boldsymbol{A}_{n,m} + \boldsymbol{A}_{m,n} = 2d_n d_m \Re\left\{\exp\left(j\omega_d T_s (n-m)\right)\right\} . \tag{B.17}$$

We can, therefore, write D_k as the sum over all the sub-diagonal elements of $\boldsymbol{A}$:

$$D_k = 0.5P_k \left[\sum_{m=0}^{MN_s-1} d_m d_m + 2 \sum_{p=1}^{MN_s-1} \Re\left\{\exp\left(j\omega_d T_s p\right)\right\} \sum_{m=0}^{MN_s-1-p} d_m d_{m+p} \right] , \tag{B.18}$$

where p denotes the index of the sub-diagonal and m is the row index. Now, the product $d_m d_{m+p}$ is an rv which can only take on values $\{-1, +1\}$, so we can

define a probability mass function as follows[†]:

$$\mathrm{p}_{d_m d_{m+p}}(x) = \begin{cases} 1 & x = 1 \quad p = 0 \\ 0 & x = -1 \quad p = 0 \\ 1 - \frac{p}{2DN_s} & x = 1 \quad 0 < p < DN_s \\ \frac{P}{2DN_s} & x = -1 \quad 0 < p < DN_s \\ \frac{1}{2} & x = 1 \quad p \geq DN_s \\ \frac{1}{2} & x = -1 \quad p \geq DN_s \,. \end{cases} \tag{B.19}$$

Taking expectation yields:

$$E_{d_m d_{m+p}}[x] = \begin{cases} 1 & p = 0 \\ 1 - \frac{p}{DN_s} & 0 < p < DN_s \\ 0 & p \geq DN_s \,. \end{cases} \tag{B.20}$$

Thus, taking expectation in Equation (B.18) yields:

$$E_{\boldsymbol{d}}[D_k] = 0.5P_k \left[MN_s + 2 \sum_{p=1}^{\min(D,M)N_s - 1} \Re\left\{\exp\left(j\omega_d T_s p\right)\right\} \sum_{m=0}^{MN_s - 1 - p} \left(1 - \frac{p}{DN_s}\right) \right] \tag{B.21}$$

$$= 0.5P_k \left[MN_s + 2 \sum_{p=1}^{\min(D,M)N_s - 1} \Re\left\{\exp\left(j\omega_d T_s p\right)\right\} \left(MN_s - p\right) \left(1 - \frac{p}{DN_s}\right) \right] \tag{B.22}$$

$$= 0.5P_k \left[MN_s + \frac{2}{DN_s} \sum_{p=1}^{\min(D,M)N_s - 1} \Re\left\{\exp\left(j\omega_d T_s p\right)\right\} \left(MN_s - p\right) \left(DN_s - p\right) \right] . \tag{B.23}$$

Now, although the summation in Equation (B.23) can be evaluated using the identities in Appendix A, the procedure is quite laborious. We can, instead, use our knowledge of the result when $M \leq D$, in conjunction with the symmetry of the summands when M and D are interchanged, to arrive at the result with less effort.

[†]Note that this expression is essentially identical to [37, Equation (8-4)].

So, assuming $M \leq D$, then Equation (B.22) becomes:

$$E_{\boldsymbol{d}}[D_k \mid M \leq D] = 0.5P_k \left[MN_s + 2 \sum_{p=1}^{MN_s-1} \Re\left\{\exp\left(j\omega_d T_s p\right)\right\} \left(MN_s - p\right) - 2 \sum_{p=1}^{MN_s-1} \Re\left\{\exp\left(j\omega_d T_s p\right)\right\} \frac{p}{DN_s} \left(MN_s - p\right) \right] . \tag{B.24}$$

Now, in the limit as $D \to \infty$, data modulation will have no effect and, from Equation (3.6), we have:

$$\lim_{D\to\infty} E_{\boldsymbol{d}}[D_k \mid M \leq D] = 2P_k \left| \frac{\sin \frac{\omega_d T_s MN_s}{2}}{\sin \frac{\omega_d T_s}{2}} \right|^2 . \tag{B.25}$$

Comparing Equation (B.25) and Equation (B.24) we obtain the result:

$$2 \sum_{p=1}^{MN_s-1} \Re\left\{\exp\left(j\omega_d T_s p\right)\right\} \left(MN_s - p\right) = \left| \frac{\sin \frac{\omega_d T_s MN_s}{2}}{\sin \frac{\omega_d T_s}{2}} \right|^2 - MN_s \, . \tag{B.26}$$

We can solve for the second summation in Equation (B.24) in a similar fashion. From Equation (3.22) we have[†]:

$$E_{\boldsymbol{d}}[D_k \mid M \leq D] \approx 1 - \frac{M}{D} \left(\frac{\cot \beta}{\beta} - \cot^2 \beta \right) , \tag{B.27}$$

where $\beta \triangleq MN_s T_s/2$. Finally, inserting Equation (B.26) into Equation (B.24) and comparing the result with Equation (B.27) we find:

$$2 \sum_{p=1}^{MN_s-1} \Re\left\{\exp\left(j\omega_d T_s p\right)\right\} p \left(MN_s - p\right) \approx MN_s \left| \frac{\sin \frac{\omega_d T_s MN_s}{2}}{\sin \frac{\omega_d T_s}{2}} \right|^2 \left[\frac{\cot\left(\frac{\omega_d T_s MN_s}{2}\right)}{\frac{\omega_d T_s MN_s}{2}} - \cot^2\left(\frac{\omega_d T_s MN_s}{2}\right) \right] . \tag{B.28}$$

We are now in a position to solve Equation (B.23) under the assumption that

[†]This is an approximation, the true expression is found by replacing the factor $1/\beta$ with $\frac{1}{MN_s} \cot\left(\frac{\beta}{MN_s}\right)$.

$M > D$. Re-writing Equation (B.23) we obtain:

$$E_{\boldsymbol{d}}[D_k \mid M > D] = 0.5P_k \left[MN_s + 2\frac{M}{D} \sum_{p=1}^{DN_s-1} \Re\left\{\exp\left(j\omega_d T_s p\right)\right\}\left(DN_s - p\right) - \frac{2}{DN_s} \sum_{p=1}^{DN_s-1} \Re\left\{\exp\left(j\omega_d T_s p\right)\right\} p\left(DN_s - p\right) \right] . \quad \text{(B.29)}$$

Now, the two summation terms above can be identified with Equations (B.26) and (B.28) respectively, under the substitution $M \to D$. Thus, after some algebraic manipulation, we obtain:

$$E_{\boldsymbol{d}}[D_k \mid M > D] = 0.5P_k \left(MN_s\right)^2 \alpha_D(\omega_d) \frac{\sin^2\left(\frac{\omega_d T_s DN_s}{2}\right)}{\sin^2\left(\frac{\omega_d T_s MN_s}{2}\right)} \times \left[\frac{M}{D} - \frac{\cot\left(\frac{\omega_d T_s DN_s}{2}\right)}{\frac{\omega_d T_s DN_s}{2}} + \cot^2\left(\frac{\omega_d T_s DN_s}{2}\right) \right] , \quad \text{(B.30)}$$

where $\alpha_D(\omega_d)$ is the effective power attenuation due to carrier Doppler effects only. Comparing Equations (3.6) and (B.30) above gives us the desired expression for $\overline{\alpha}_m$:

$$\overline{\alpha}_m(\delta\omega_d) = \left| \frac{\sin\frac{\beta D}{M}}{\sin\beta} \right|^2 \left(\frac{M}{D} - \frac{M\cot\left(\beta\frac{D}{M}\right)}{\beta D} + \cot^2\frac{\beta D}{M} \right) . \quad \text{(B.31)}$$

B.2 Derivations from Chapter 4

B.2.1 Z_I is the Difference of Two Non-Central χ^2 Variates for the Pair Wise Form

We wish to show that the real part of the differentially coherent sum, Z_I, in the pair wise form of the DCCD can be expressed as the difference of two non-central χ^2 rvs. An expression for the CHF of Z_I has already been specified in Equation (4.92). We now demonstrate that this is equivalent to the CHF of the difference of two χ^2 rvs.

Letting $X_i : \ i = 1, 2$ be independent non-central χ^2 distributed rvs:

$$X_i \sim \chi'^2\left(N, \lambda_i, \sigma_X^2\right) , \quad \text{(B.32)}$$

then the CHF of X_i is given by [102]:

$$\Phi_{X_i}(j\omega) = \frac{\exp\left(\frac{j\omega\lambda_i}{1-2j\omega\sigma_X^2}\right)}{(1-2j\omega\sigma_X^2)^{\frac{N}{2}}}. \tag{B.33}$$

Denoting by Y the rv:

$$Y = X_1 - X_2 = X_1 + (-X_2), \tag{B.34}$$

then the CHF of Y is given by:

$$\Phi_Y(j\omega) = \Phi_{X_1}(j\omega)\,\Phi_{-X_2}(j\omega). \tag{B.35}$$

The CHF of X_1 is given directly by Equation (B.33). The CHF of $-X_2$ can be found as follows:

$$\begin{aligned}\Phi_{-X_2}(j\omega) &\triangleq E_{X_2}[\exp(-j\omega X_2)]\\ &= E_{X_2}[\exp(j(-\omega)X_2)]\\ &= \Phi_{X_2}(-j\omega)\\ &= \frac{\exp\left(\frac{-j\omega\lambda_2}{1+2j\omega\sigma_X^2}\right)}{(1+2j\omega\sigma_X^2)^{\frac{N}{2}}}.\end{aligned} \tag{B.36}$$

Inserting Equations (B.33) and (B.36) into Equation (B.35) and simplifying, yields:

$$\Phi_Y(j\omega) = \frac{\exp\left(-\frac{\omega}{1+4\omega^2\sigma_X^4}\left[\omega\sigma_X^2(\lambda_1+\lambda_2) - j(\lambda_1-\lambda_2)\right]\right)}{(1+4\omega^2\sigma_X^4)^{\frac{N}{2}}}. \tag{B.37}$$

Comparing Equations (B.37) and (4.92) we find that:

$$\Phi_{Z_I}(j\omega) = \Phi_Y(j\omega), \tag{B.38}$$

under the following conditions:

$$\sigma_X^2 = \frac{1}{2}\sigma^2 \tag{B.39}$$

$$\lambda_1 + \lambda_2 = \lambda = \boldsymbol{\mu}^{\mathrm{H}}\boldsymbol{\mu} \tag{B.40}$$

$$\lambda_1 - \lambda_2 = \Re\{\kappa\} = \boldsymbol{\mu}^{\mathrm{H}} \boldsymbol{Q_I} \boldsymbol{\mu}. \tag{B.41}$$

Solving for λ_1 and λ_2 we obtain:

$$\lambda_1 = \frac{1}{2} \boldsymbol{\mu}^{\mathrm{H}} \left(\boldsymbol{I} + \boldsymbol{Q_I} \right) \boldsymbol{\mu} \tag{B.42}$$

$$\lambda_2 = \frac{1}{2} \boldsymbol{\mu}^{\mathrm{H}} \left(\boldsymbol{I} - \boldsymbol{Q_I} \right) \boldsymbol{\mu}, \tag{B.43}$$

which is the desired result.

B.2.2 An Integral Involving the Exponential Function with Trigonometric Functions in the Exponent

We wish to evaluate the integral:

$$I = \int_{-\pi}^{\pi} \exp\left(jx \left(a \cos\phi + b \sin\phi \right) \right) d\,\phi \quad a, b \in \mathbb{R}. \tag{B.44}$$

Making the substitutions:

$$a = p \cos\theta \qquad\qquad b = p \sin\theta, \tag{B.45}$$

yields:

$$I = \int_{-\pi}^{\pi} \exp\left(jxp \left(\cos\theta \cos\phi + \sin\theta \sin\phi \right) \right) d\,\phi \tag{B.46}$$

$$= \int_{-\pi}^{\pi} \exp\left(jxp \cos\left(\phi - \theta \right) \right) d\,\phi \tag{B.47}$$

$$= \int_{-\pi}^{\pi} \exp\left(jxp \cos\phi \right) d\,\phi \tag{B.48}$$

$$= 2\pi J_0\left(xp \right). \tag{B.49}$$

where, in the first step we have used a trigonometric identity, in the second step we make the observation that the value of the integrand is invariant to a phase shift in the cosine term, and in the third step we have used the well-known identity

[48, Equation 8.411.1]:

$$J_0(z) = \frac{1}{2\pi}\int_{-\pi}^{\pi} \exp(jz\cos\theta)\, d\theta. \tag{B.50}$$

Inserting the identity $p = \sqrt{a^2+b^2}$, yields:

$$\int_{-\pi}^{\pi} \exp(jx(a\cos\phi + b\sin\phi))\, d\phi = 2\pi J_0\left(x\sqrt{a^2+b^2}\right) \quad a, b \in \mathbb{R}. \tag{B.51}$$

B.2.3 Derivation of Equation (4.102)

We wish to prove Equation (4.102). The case $N = 1$ is trivial. Taking the case $N = 2$, then, by Equation (4.101), we have:

$$P_N(\rho,\phi) = \begin{vmatrix} 1 & -j\rho\sigma^2 e^{-j\phi} \\ -j\rho\sigma^2 e^{j\phi} & 1 \end{vmatrix} \tag{B.52}$$

$$= 1 + (\rho\sigma^2)^2. \tag{B.53}$$

Thus, we have the first two cases. This can be expanded to $N > 2$ as follows. Firstly, we denote by $\boldsymbol{P}_N$ the matrix $\boldsymbol{P}$ for the case of N observations. Next, we make the observation that, for $N > 2$, we can partition the matrix $\boldsymbol{P}_N$ as follows:

$$\boldsymbol{P}_N = \left(\begin{array}{c|cc} 1 & -j\rho\sigma^2 e^{-j\phi} & \mathbf{0}_{1,N-2} \\ -j\rho\sigma^2 e^{j\phi} & \multicolumn{2}{c}{\multirow{2}{*}{$\boldsymbol{P}_{N-1}$}} \\ \mathbf{0}_{N-2,1} & & \end{array}\right) \tag{B.54}$$

$$= \left(\begin{array}{c|cc|c} 1 & -j\rho\sigma^2 e^{-j\phi} & \mathbf{0}_{1,N-2} & \\ -j\rho\sigma^2 e^{j\phi} & 1 & -j\rho\sigma^2 e^{-j\phi} \quad \mathbf{0}_{1,N-3} & \\ & -j\rho\sigma^2 e^{j\phi} & & \multirow{2}{*}{$\boldsymbol{P}_{N-2}$} \\ \mathbf{0}_{N-2,1} & \mathbf{0}_{N-3,1} & & \end{array}\right), \tag{B.55}$$

where $\mathbf{0}_{i,j}$ is the $i \times j$ matrix of zeros. Thus, we have:

$$P_N(\rho,\phi) = |\boldsymbol{P}_N|$$

$$= 1 \times |\boldsymbol{P}_{N-1}| - (-j\rho\sigma^2 e^{-j\phi}) \times \begin{vmatrix} -j\rho\sigma^2 e^{j\phi} & -j\rho\sigma^2 e^{-j\phi} & \mathbf{0}_{1,N-3} \\ \mathbf{0}_{N-2,1} & \boldsymbol{P}_{N-2} & \end{vmatrix} \tag{B.56}$$

$$= P_{N-1}(\rho,\phi) + (\rho\sigma^2)^2 P_{N-2}(\rho,\phi)\,, \tag{B.57}$$

which is the desired result.

B.2.4 Derivation of Equation (4.103)

Letting $x = \rho\sigma^2$, we wish to show that:

$$P_N(x) = \sum_{i=0}^{\lfloor \frac{N}{2} \rfloor} \binom{N-i}{i} x^{2i}. \tag{B.58}$$

We use an inductive approach. Firstly, it is easy to see that Equation (B.58) holds for $N = 1$ and $N = 2$ (see Section B.2.3). Thus, it remains to be shown that, given that Equation (B.58) holds for $N = n-2$ and $N = n-1$, it also holds for $N = n$. Thus, we must show:

$$P_n(x) = P_{n-1}(x) + x^2 P_{n-2}(x) = \sum_{i=0}^{\lfloor \frac{N}{2} \rfloor} \binom{N-i}{i} x^{2i} \tag{B.59}$$

$$= \sum_{i=0}^{\lfloor \frac{n-1}{2} \rfloor} \binom{n-1-i}{i} x^{2i} + \sum_{i=0}^{\lfloor \frac{n-2}{2} \rfloor} \binom{n-2-i}{i} x^{2(i+1)}\,. \tag{B.60}$$

Considering initially the case of even n, this becomes:

$$P_n(x) = \sum_{i=0}^{\frac{n}{2}-1} \binom{n-1-i}{i} x^{2i} + \sum_{i=1}^{\frac{n}{2}} \binom{n-1-i}{i-1} x^{2i} \tag{B.61}$$

$$= \sum_{i=0}^{\frac{n}{2}-1} x^{2i} \left[\binom{n-1-i}{i} + \binom{n-1-i}{i-1} \right] + \binom{n-1-\frac{n}{2}}{\frac{n}{2}-1} x^n\,. \tag{B.62}$$

Taking the sum of binomials in the first summand of the expression above yields:

$$\binom{n-1-i}{i} + \binom{n-1-i}{i-1} = \frac{(n-1-i)!}{i!(n-1-2i)!} + \frac{(n-1-i)!}{(i-1)!(n-2i)!} \tag{B.63}$$

$$= \frac{(n-1-i)!(n-2i+i)}{i!(n-2i)!} \tag{B.64}$$

$$= \binom{n-i}{i}. \tag{B.65}$$

Taking the x^n term in Equation (B.62) we have:

$$\binom{n-1-\frac{n}{2}}{\frac{n}{2}-1} = \binom{\frac{n}{2}-1}{\frac{n}{2}-1} \tag{B.66}$$

$$= 1 \tag{B.67}$$

$$= \binom{n-\frac{n}{2}}{\frac{n}{2}}. \tag{B.68}$$

Thus, inserting Equations (B.65) and (B.68) into Equation (B.62), yields:

$$P_n(x) = \sum_{i=0}^{\frac{n}{2}} \binom{n-i}{i} x^{2n} \quad n \text{ even}. \tag{B.69}$$

The case when n is odd is easily shown in a similar manner.

B.2.5 Derivation of $P_{J,N}(\rho)$ by Gaussian Elimination

A useful mechanism for the determination of matrix determinants is the procedure known as *Gaussian elimination* [76, Chapter 6]. This process consists of the sequential application of row operations to a matrix (say $\boldsymbol{M}$) to yield a triangular matrix (say $\boldsymbol{D}$). It can be shown that the determinant of the matrix $\boldsymbol{D}$ is equal to the determinant of $\boldsymbol{M}$. In addition, for any triangular matrix, the determinant is simply equal to product of its diagonal elements.

Consider first of all the case $J = 1$, the matrix $\boldsymbol{P}$ is then given by:

$$\boldsymbol{P}_{1,N} = \begin{pmatrix} 1 & -j\rho\sigma^2 e^{-j\phi} & 0 & \cdots & 0 \\ -j\rho\sigma^2 e^{+j\phi} & 1 & -j\rho\sigma^2 e^{-j\phi} & \ddots & \vdots \\ 0 & -j\rho\sigma^2 e^{+j\phi} & 1 & \ddots & 0 \\ \vdots & \ddots & \ddots & \ddots & -j\rho\sigma^2 e^{-j\phi} \\ 0 & \cdots & 0 & -j\rho\sigma^2 e^{+j\phi} & 1 \end{pmatrix} \tag{B.70}$$

We wish to triangularise this matrix in order to enable the calculation of $|\boldsymbol{P}|$

with ease. The first step in the triangularisation procedure is to eliminate the sub-diagonal term on the second row of $\boldsymbol{P}$. To do this, simply add $j\rho\sigma^2 e^{j\phi}$ times row 1 to row 2, yielding the following matrix:

$$\begin{pmatrix} 1 & -j\rho\sigma^2 e^{-j\phi} & 0 & \cdots & 0 \\ 0 & 1+\sigma^4\rho^2 & -j\rho\sigma^2 e^{-j\phi} & \ddots & \vdots \\ 0 & -j\rho\sigma^2 e^{+j\phi} & 1 & \ddots & 0 \\ \vdots & \ddots & \ddots & \ddots & -j\rho\sigma^2 e^{-j\phi} \\ 0 & \cdots & 0 & -j\rho\sigma^2 e^{+j\phi} & 1 \end{pmatrix}.$$

To eliminate the third row, we repeat the procedure and add $(j\rho\sigma^2 e^{j\phi})/(1+\sigma^4\rho^2)$ times the second row of the matrix above to yield:

$$\begin{pmatrix} 1 & -j\rho\sigma^2 e^{-j\phi} & 0 & \cdots & 0 \\ 0 & 1+\sigma^4\rho^2 & -j\rho\sigma^2 e^{-j\phi} & \ddots & \vdots \\ 0 & 0 & 1+\frac{\sigma^4\rho^2}{1+\sigma^4\rho^2} & \ddots & 0 \\ \vdots & \ddots & \ddots & \ddots & -j\rho\sigma^2 e^{-j\phi} \\ 0 & \cdots & 0 & -j\rho\sigma^2 e^{+j\phi} & 1 \end{pmatrix}. \tag{B.71}$$

Repeating this procedure for all the rows of $\boldsymbol{P}$ will finally bring us to the triangular form. If we denote by $d_{J,n}$ the diagonal entry on row n, after the first n rows have been triangularised, then the diagonal term on row $n+1$ will be given by:

$$d_{1,n+1} = 1 + \frac{\sigma^4\rho^2}{d_{1,n}}, \tag{B.72}$$

when $J = 1$. The determinant of $\boldsymbol{P}$ is then given by:

$$|\boldsymbol{P}| = P_{1,N} = \prod_{n=1}^{N} d_{1,n}. \tag{B.73}$$

This is equivalent to Equation (4.103) on page 168.

The real advantage of the Gaussian elimination approach is that it allows us to express the determinant for general J, $P_{J,N}(\rho)$, in terms of the determinant for $J = 1$, for which we already have an expression.

Consider the case $J = 2$. Now, since we require $N > J$ we initially consider

$N = 3$, in which case we have:

$$\boldsymbol{P} = \begin{pmatrix} 1 & 0 & -j\rho\sigma^2 e^{-j\phi} \\ 0 & 1 & 0 \\ -j\rho\sigma^2 e^{j\phi} & 0 & 1 \end{pmatrix}.$$

Note that, in this case, the first 2 rows are already in a suitable form. In general, we will find that the first J rows are already in upper-triangular form, with 1's in the diagonal entries. We can eliminate the sub-diagonal entry in row 3 by adding $j\rho\sigma^2 e^{j\phi}$ times row 1, which gives:

$$\begin{pmatrix} 1 & 0 & -j\rho\sigma^2 e^{-j\phi} \\ 0 & 1 & 0 \\ 0 & 0 & 1 + \sigma^4\rho^2 \end{pmatrix}.$$

The procedure continues in this manner, and is almost identical to the procedure for the case $J = 1$ except that, instead of using the previous row to eliminate the sub-diagonal elements of the current row, the row before that is used. In general we will find that, to eliminate the sub-diagonal elements of row n requires the use of row $n - J$. Thus, the recursion on the diagonal element $d_{J,n}$ can be generalised to:

$$d_{J,n} = 1 + \frac{\sigma^4\rho^2}{d_{J,n-J}} \tag{B.74}$$

$$= d_{1,\lfloor \frac{n}{J} \rfloor + 1}. \tag{B.75}$$

The determinant can then be found from:

$$P_{J,N}(\rho) = \prod_{n=1}^{N} d_{J,n} \tag{B.76}$$

$$= \prod_{n=1}^{N} d_{1,\lfloor \frac{n}{J} \rfloor + 1}. \tag{B.77}$$

Making the substitution $a = \lfloor N/J \rfloor$ and $b = N - aJ$ yields:

$$P_{J,N}(\rho) = \left(\prod_{i=1}^{a} d_{1,i} \right)^{J-b} \left(\prod_{i=1}^{a+1} d_{1,i} \right)^{b} \tag{B.78}$$

$$= P_{1,a}^{J-b}(\rho) P_{1,a+1}^{b}(\rho), \tag{B.79}$$

which is the desired result.

B.2.6 Derivation of the CDF of R for the Standard Form of Differentially Coherent Processing

We wish to derive Equation (4.118). We begin with Equation (4.116):

$$f_R(r) = r \int_0^\infty \frac{\rho J_0(r\rho)}{P_N(\rho)} d\rho \ .$$

Integrating over r and interchanging the order of the integrals gives us:

$$F_R(r) = \int_0^\infty \frac{\rho}{P_N(\rho)} \int_0^r x J_0(x\rho)\, d\rho\, dx \tag{B.80}$$

$$= \int_0^\infty \frac{r J_1(r\rho)}{P_N(\rho)} d\rho\,, \tag{B.81}$$

where we have applied the identity:

$$\int z J_0(z)\, dz = z J_1(z)\,. \tag{B.82}$$

Applying the partial fraction expansion of Equation (4.110) to Equation (B.81) yields:

$$F_R(r) = \sum_{k=1}^{\lfloor \frac{N}{2} \rfloor} A_{N,k} \int_0^\infty \frac{r J_1(r\rho)}{\rho^2 + \gamma_k} d\rho \tag{B.83}$$

$$= \sum_{k=1}^{\lfloor \frac{N}{2} \rfloor} A_{N,k} \left[\frac{1}{\gamma_k} - \frac{r}{\sqrt{\gamma_k}} K_1(r\sqrt{\gamma_k}) \right] , \tag{B.84}$$

where $K_1(x)$ is the modified Bessel function of the second kind of order 1, defined in Equation (2.76). Now, from Equation (4.110) we have:

$$\frac{1}{P_N(\rho)} = \sum_{k=1}^{\lfloor \frac{N}{2} \rfloor} \frac{A_{N,k}}{\rho^2 + \gamma_k} \tag{B.85}$$

$$\therefore \frac{1}{P_N(0)} = \sum_{k=1}^{\lfloor \frac{N}{2} \rfloor} \frac{A_{N,k}}{\gamma_k}\,. \tag{B.86}$$

But, from Equation (4.103) we have:

$$P_N(0) = 1. \tag{B.87}$$

Thus, Equation (B.84) reduces to our desired result:

$$F_R(r) = 1 - \sum_{k=1}^{\lfloor \frac{N}{2} \rfloor} \frac{A_{N,k}}{\sqrt{\gamma_k}} r K_1\left(r\sqrt{\gamma_k}\right)\,. \tag{B.88}$$

B.2.7 Derivation of Equation (4.140)

We wish to prove that:

$$\boldsymbol{Q}_{\boldsymbol{I},J}\boldsymbol{Q}_{\boldsymbol{Q},J} + \boldsymbol{Q}_{\boldsymbol{Q},J}\boldsymbol{Q}_{\boldsymbol{I},J} = \boldsymbol{Q}_{\boldsymbol{Q},2J}, \tag{B.89}$$

for the standard form of the differentially coherent combining detector. We begin with the observations:

$$\boldsymbol{Q}_{\boldsymbol{I},J} = \frac{1}{2}\begin{pmatrix} \mathbf{0}_{J,J} & \boldsymbol{I}_{J,J} & \mathbf{0}_{J,J} & \cdots & \mathbf{0}_{J,J} \\ \boldsymbol{I}_{J,J} & \mathbf{0}_{J,J} & \boldsymbol{I}_{J,J} & \ddots & \vdots \\ \mathbf{0}_{J,J} & \boldsymbol{I}_{J,J} & \mathbf{0}_{J,J} & \ddots & \mathbf{0}_{J,J} \\ \vdots & \ddots & \ddots & \ddots & \boldsymbol{I}_{J,J} \\ \mathbf{0}_{J,J} & \cdots & \mathbf{0}_{J,J} & \boldsymbol{I}_{J,J} & \mathbf{0}_{J,J} \end{pmatrix} \tag{B.90}$$

$$\boldsymbol{Q}_{\boldsymbol{Q},J} = \frac{j}{2}\begin{pmatrix} \boldsymbol{0}_{J,J} & -\boldsymbol{I}_{J,J} & \boldsymbol{0}_{J,J} & \cdots & \boldsymbol{0}_{J,J} \\ \boldsymbol{I}_{J,J} & \boldsymbol{0}_{J,J} & -\boldsymbol{I}_{J,J} & \ddots & \vdots \\ \boldsymbol{0}_{J,J} & \boldsymbol{I}_{J,J} & \boldsymbol{0}_{J,J} & \ddots & \boldsymbol{0}_{J,J} \\ \vdots & \ddots & \ddots & \ddots & -\boldsymbol{I}_{J,J} \\ \boldsymbol{0}_{J,J} & \cdots & \boldsymbol{0}_{J,J} & \boldsymbol{I}_{J,J} & \boldsymbol{0}_{J,J} \end{pmatrix}. \tag{B.91}$$

Thus:

$$\boldsymbol{Q}_{\boldsymbol{I},J}\boldsymbol{Q}_{\boldsymbol{Q},J} = \frac{j}{4}\begin{pmatrix} \boldsymbol{I}_{J,J} & \boldsymbol{0}_{J,J} & -\boldsymbol{I}_{J,J} & \boldsymbol{0}_{J,J} & \cdots & \boldsymbol{0}_{J,J} \\ \boldsymbol{0}_{J,J} & \boldsymbol{0}_{J,J} & \boldsymbol{0}_{J,J} & -\boldsymbol{I}_{J,J} & \ddots & \vdots \\ \boldsymbol{I}_{J,J} & \boldsymbol{0}_{J,J} & \boldsymbol{0}_{J,J} & \boldsymbol{0}_{J,J} & \ddots & \boldsymbol{0}_{J,J} \\ \boldsymbol{0}_{J,J} & \boldsymbol{I}_{J,J} & \boldsymbol{0}_{J,J} & \boldsymbol{0}_{J,J} & \ddots & -\boldsymbol{I}_{J,J} \\ \vdots & \ddots & \ddots & \ddots & \ddots & \boldsymbol{0}_{J,J} \\ \boldsymbol{0}_{J,J} & \cdots & \boldsymbol{0}_{J,J} & \boldsymbol{I}_{J,J} & \boldsymbol{0}_{J,J} & -\boldsymbol{I}_{J,J} \end{pmatrix} \tag{B.92}$$

$$\boldsymbol{Q}_{\boldsymbol{Q},J}\boldsymbol{Q}_{\boldsymbol{I},J} = \frac{j}{4}\begin{pmatrix} -\boldsymbol{I}_{J,J} & \boldsymbol{0}_{J,J} & -\boldsymbol{I}_{J,J} & \boldsymbol{0}_{J,J} & \cdots & \boldsymbol{0}_{J,J} \\ \boldsymbol{0}_{J,J} & \boldsymbol{0}_{J,J} & \boldsymbol{0}_{J,J} & -\boldsymbol{I}_{J,J} & \ddots & \vdots \\ \boldsymbol{I}_{J,J} & \boldsymbol{0}_{J,J} & \boldsymbol{0}_{J,J} & \boldsymbol{0}_{J,J} & \ddots & \boldsymbol{0}_{J,J} \\ \boldsymbol{0}_{J,J} & \boldsymbol{I}_{J,J} & \boldsymbol{0}_{J,J} & \boldsymbol{0}_{J,J} & \ddots & -\boldsymbol{I}_{J,J} \\ \vdots & \ddots & \ddots & \ddots & \ddots & \boldsymbol{0}_{J,J} \\ \boldsymbol{0}_{J,J} & \cdots & \boldsymbol{0}_{J,J} & \boldsymbol{I}_{J,J} & \boldsymbol{0}_{J,J} & \boldsymbol{I}_{J,J} \end{pmatrix}. \tag{B.93}$$

Therefore, we have:

$$\boldsymbol{Q}_{\boldsymbol{I},J}\boldsymbol{Q}_{\boldsymbol{Q},J} + \boldsymbol{Q}_{\boldsymbol{Q},J}\boldsymbol{Q}_{\boldsymbol{I},J} = \frac{j}{2}\begin{pmatrix} \boldsymbol{0}_{J,J} & \boldsymbol{0}_{J,J} & -\boldsymbol{I}_{J,J} & \boldsymbol{0}_{J,J} & \cdots & \boldsymbol{0}_{J,J} \\ \boldsymbol{0}_{J,J} & \boldsymbol{0}_{J,J} & \boldsymbol{0}_{J,J} & -\boldsymbol{I}_{J,J} & \ddots & \vdots \\ \boldsymbol{I}_{J,J} & \boldsymbol{0}_{J,J} & \boldsymbol{0}_{J,J} & \boldsymbol{0}_{J,J} & \ddots & \boldsymbol{0}_{J,J} \\ \boldsymbol{0}_{J,J} & \boldsymbol{I}_{J,J} & \boldsymbol{0}_{J,J} & \boldsymbol{0}_{J,J} & \ddots & -\boldsymbol{I}_{J,J} \\ \vdots & \ddots & \ddots & \ddots & \ddots & \boldsymbol{0}_{J,J} \\ \boldsymbol{0}_{J,J} & \cdots & \boldsymbol{0}_{J,J} & \boldsymbol{I}_{J,J} & \boldsymbol{0}_{J,J} & \boldsymbol{0}_{J,J} \end{pmatrix} \tag{B.94}$$

$$= \frac{j}{2} \begin{pmatrix} \mathbf{0}_{2J,2J} & -\boldsymbol{I}_{2J,2J} & \mathbf{0}_{2J,2J} & \cdots & \mathbf{0}_{2J,2J} \\ \boldsymbol{I}_{2J,2J} & \mathbf{0}_{2J,2J} & -\boldsymbol{I}_{2J,2J} & \ddots & \vdots \\ \mathbf{0}_{2J,2J} & \boldsymbol{I}_{2J,2J} & \mathbf{0}_{2J,2J} & \ddots & \mathbf{0}_{2J,2J} \\ \vdots & \ddots & \ddots & \ddots & -\boldsymbol{I}_{2J,2J} \\ \mathbf{0}_{2J,2J} & \cdots & \mathbf{0}_{2J,2J} & \boldsymbol{I}_{2J,2J} & \mathbf{0}_{2J,2J} \end{pmatrix} \tag{B.95}$$

$$= \boldsymbol{Q}_{\boldsymbol{Q},2J} \,. \tag{B.96}$$

B.2.8 An Expression for the Probability that one χ^2 Distributed RV Exceeds Another

The following results have been accepted for publication in the IEEE Transactions on Communications [89].

Given two χ^2 distributed rvs X_1 and X_2 we wish to derive an expression for the probability that $X_2 > X_1$, denoted P_g:

$$P_g \triangleq \Pr\{X_2 > X_1\}, \tag{B.97}$$

where:

$$X_1 \sim \chi'^2(n = 2K, \lambda_1 = a_1^2, \sigma^2 = \sigma_1^2) \tag{B.98}$$

$$X_2 \sim \chi'^2(n = 2K, \lambda_2 = a_2^2, \sigma^2 = \sigma_2^2). \tag{B.99}$$

Our approach is based on that of Stein [131] and Simon and Alouini [122], but requires some preliminary results on the Marcum Q-function.

The Marcum Q-function is defined by the integral in Equation (2.43), but it can also be represented by a contour integral in the complex plane [102, 135]:

$$Q_K(a, b) = \frac{\exp\left(-\frac{a^2+b^2}{2}\right)}{2\pi j} \oint_{\Gamma_0} \frac{\exp\left(\frac{1}{2}\left(a^2\frac{1}{z} + b^2 z\right)\right)}{(1-z)z^K} dz, \tag{B.100}$$

where Γ_0 is any closed contour in the z-plane enclosing the point $z = 0$ (in a counter-clockwise direction), and no other singularities of the integrand.

For the sake of notational simplicity we define the function $f(a, b; z)$:

$$f(a, b; z) = \exp\left(-\frac{1}{2}\left[a^2\left(1 - \frac{1}{z}\right) + b^2(1 - z)\right]\right) \tag{B.101}$$

from which we re-write Equation (B.100) as:

$$Q_K(a, b) = \frac{1}{2\pi j}\oint_{\Gamma_0} \frac{f(a, b; z)}{z^K(1 - z)} dz. \tag{B.102}$$

The integrand in Equation (B.102) has three singularities, namely: a simple pole at $z = 1$ and essential singularities at both the origin and the point at infinity. For integer K the integrand is a single-valued function of z, and so its Riemann surface is the Riemann sphere [86]. This structure is illustrated in Figure B.1. From Equation (B.102), $Q_K(a, b)$ is given by the residue of the

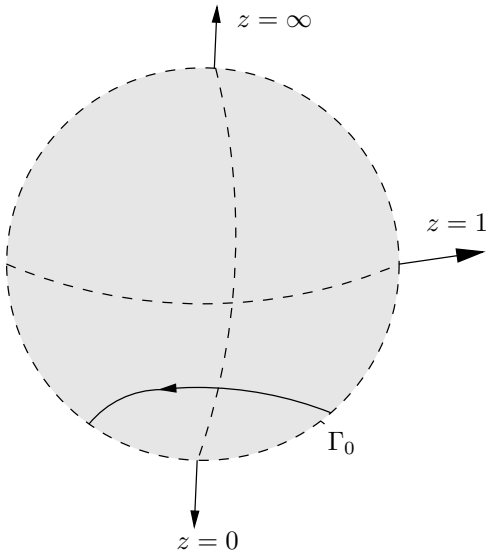


Figure B.1: The Marcum Q-function as a contour integral on the Riemann sphere, the arrows represent the three singularities of the integrand. The complex contour Γ_0 is also indicated.

function $f(a, b; z)(1 - z)^{-1}z^{-K}$ at the point $z = 0$:

$$Q_K(a, b) = \operatorname*{Res}_{z=0}\left\{\frac{f(a, b; z)}{(1 - z)z^K}\right\}. \tag{B.103}$$

Cauchy's theorem [79, eq. (4-10)], in conjunction with the residue theorem [79, eq. (5-83)], implies that the sum of the residues at all the singular points on the

Riemann surface of a function is zero. For the integrand of Equation (B.102), the residue at the point $z = 1$ is easily seen to be -1, so the residue at the point at infinity is, therefore, given by $1 - Q_K(a, b)$, *i.e.*:

$$1 - Q_K(a,b) = \frac{1}{2\pi j} \oint_{\Gamma_\infty} \frac{f(a,b;z)}{z^K(1-z)} dz. \tag{B.104}$$

Making the substitution $u = 1/z$ yields:

$$1 - Q_K(a,b) = \frac{1}{2\pi j} \oint_{\Gamma_0} \frac{f(b,a;u)\, u^{K-1}}{1-u} du. \tag{B.105}$$

It is easily seen that:

$$\operatorname*{Res}_{z=0} \left\{ \frac{f(a,b;z)}{(1-z)z^K} \right\} = \begin{cases} Q_K(a,b) & K > 0 \\ \\ 1 - Q_{1-K}(b,a) & K \leq 0 \end{cases} \tag{B.106}$$

$$\operatorname*{Res}_{z=\infty} \left\{ \frac{f(a,b;z)}{(1-z)z^K} \right\} = \begin{cases} 1 - Q_K(a,b) & K > 0 \\ \\ Q_{1-K}(b,a) & K \leq 0 \end{cases} \tag{B.107}$$

Equations (B.106) and (B.107) lead naturally to the definition of the Marcum Q-function for $K \leq 0$, by the identity:

$$Q_K(a,b) = 1 - Q_{1-K}(b,a). \tag{B.108}$$

Thus, we can re-write Equation (B.106) and Equation (B.107) as follows:

$$\operatorname*{Res}_{z=0} \left\{ \frac{f(a,b;z)}{(1-z)z^K} \right\} = Q_K(a,b) = 1 - Q_{1-K}(b,a) \tag{B.109}$$

$$\operatorname*{Res}_{z=\infty} \left\{ \frac{f(a,b;z)}{(1-z)z^K} \right\} = 1 - Q_K(a,b) = Q_{1-K}(b,a), \tag{B.110}$$

where $K \in \mathbb{Z}$.

The Marcum Q-function is related to the CDF of a χ^2 distributed rv with $2K$ degrees of freedom [102], and so the concept of negative order does not make physical sense. However, there is another interpretation that can be attributed to this function. In [67], Johnson showed, in effect, that the function $Q_K(a,b)$ is the CDF of the difference of two Poisson distributed rvs. Given $X_1 \sim \text{Poisson}(b^2/2)$ and $X_2 \sim \text{Poisson}(a^2/2)$ then:

$$Q_K(a,b) = \Pr\{X_1 - X_2 < K\}. \tag{B.111}$$

Clearly, in this context, K can take on any integer value. In addition, it is interesting to note that Siegel [118] also considered the concept of a non-central χ^2 distribution with zero degrees of freedom, in a different context. Both of these previous observations are consistent with our definition in Equation (B.108).

Returning now to the derivation of an expression for P_g, following Stein's technique we can write:

$$\Pr\{X_2 > X_1\} = \int_0^\infty f_{X_1}(x)[1 - F_{X_2}(x)]dx, \tag{B.112}$$

where:

$$f_{X_i}(x) = \frac{1}{2\sigma_i^2}\left(\frac{x}{a_i}\right)^{\frac{K_i-1}{2}} \exp\left(-\frac{1}{2}\{a_i + x\}\right) I_{K_i-1}\left(\frac{\sqrt{xa_i}}{\sigma_i^2}\right) \tag{B.113}$$

$$F_{X_i}(x) = 1 - Q_K\left(\frac{\sqrt{a_i}}{\sigma_i}, \frac{\sqrt{x}}{\sigma_i}\right). \tag{B.114}$$

Inserting Equations (B.113) and (B.114) into Equation (B.112) and making the change of variable $v = \sqrt{r}$ we obtain:

$$P_g = \int_0^\infty \frac{v}{\sigma_1^2}\left(\frac{v}{a_1}\right)^{K-1} e^{-\frac{1}{2}\left(a_1^2+v^2\right)} I_{K-1}\left(\frac{a_1 v}{\sigma_1^2}\right) Q_K\left(\frac{a_2}{\sigma_2}, \frac{v}{\sigma_2}\right) dv. \tag{B.115}$$

Now, substituting the integral on the right hand side of Equation (B.100) for the Marcum Q-function and interchanging the order of integration yields:

$$P_g = \frac{\exp\left(-\frac{1}{2}\left(\frac{a_1^2}{\sigma_1^2} + \frac{a_2^2}{\sigma_2^2}\right)\right)}{2\pi j} \oint_{\Gamma_0} \frac{\exp\left(\frac{a_2^2}{2\sigma_2^2}\frac{1}{z}\right)}{z^K(1-z)} \int_0^\infty \frac{v}{\sigma_1^2}\left(\frac{v}{a_1}\right)^{K-1}$$

$$\times \exp\left(-\frac{v^2}{2\sigma_1^2}\left[1+\frac{\sigma_1^2}{\sigma_2^2}(1-z)\right]\right) I_{K-1}\left(\frac{a_1 v}{\sigma_1^2}\right) dv\, dz\,. \tag{B.116}$$

Making the substitutions $y = v\left[1+\frac{\sigma_1^2}{\sigma_2^2}(1-z)\right]^{1/2}$ and $\alpha = a_1\left[1+\frac{\sigma_1^2}{\sigma_2^2}(1-z)\right]^{-1/2}$, the integral over v can be written as:

$$\mathcal{I} = \frac{\exp\left(\frac{\alpha^2}{2\sigma_1^2}\right)}{\left(1+\frac{\sigma_1^2}{\sigma_2^2}(1-z)\right)^K}\int_0^\infty \frac{y}{\sigma_1^2}\left(\frac{y}{\alpha}\right)^{K-1}\exp\left(-\frac{\alpha^2+y^2}{2\sigma_1^2}\right) I_{K-1}\left(\frac{\alpha y}{\sigma_1^2}\right) dy \tag{B.117}$$

where the integral over y is clearly the Marcum Q-function, as defined in Equation (2.43). Care must be taken regarding the convergence of this integral, as both y and α are complex quantities. For convergence of this integral we require $\Re\{\alpha^2+y^2\} \geq 0 \Rightarrow \Re\left\{1+\frac{\sigma_1^2}{\sigma_2^2}(1-z)\right\} \geq 0 \Rightarrow \Re\{z\} \leq 1+\frac{\sigma_2^2}{\sigma_1^2}$. But the position of the pole at $z=1$ implies that, on the contour Γ_0, $\Re\{z\} < 1$ and so the convergence requirement is met on this contour. This gives us:

$$\mathcal{I} = \frac{\exp\left(\frac{\alpha^2}{2\sigma_1^2}\right)}{\left(1+\frac{\sigma_1^2}{\sigma_2^2}(1-z)\right)^K} Q_K\left(\frac{\alpha}{\sigma_1}, 0\right) \tag{B.118}$$

$$= \frac{\exp\left(\frac{a_1^2}{2\sigma_1^2}\frac{1}{1+\frac{\sigma_1^2}{\sigma_2^2}(1-z)}\right)}{\left(1+\frac{\sigma_1^2}{\sigma_2^2}(1-z)\right)^K}\,. \tag{B.119}$$

Inserting Equation (B.119) into Equation (B.116) gives:

$$P_g = \frac{\exp\left(-\frac{1}{2}\left(\frac{a_1^2}{\sigma_1^2}+\frac{a_2^2}{\sigma_2^2}\right)\right)}{2\pi j}\oint_{\Gamma_0}\frac{\exp\left(\frac{a_2^2}{2\sigma_2^2}\frac{1}{z}\right)}{z^K(1-z)}\frac{\exp\left(\frac{a_1^2}{2\sigma_1^2}\frac{1}{1+\frac{\sigma_1^2}{\sigma_2^2}(1-z)}\right)}{\left(1+\frac{\sigma_1^2}{\sigma_2^2}(1-z)\right)^K}dz. \tag{B.120}$$

Letting $\Sigma^2 = \sigma_1^2+\sigma_2^2$ and making the substitution $p = \frac{\Sigma^2-\sigma_1^2 z}{\sigma_2^2 z}$ gives:

$$P_g = \frac{\exp\left(-\frac{a_1^2+a_2^2}{2\Sigma^2}\right)}{2\pi j}\oint_{\Gamma_\infty}\left(\frac{\sigma_2^2 p+\sigma_1^2}{\Sigma^2}\right)^{2K-1}\frac{\exp\left(\frac{1}{2(\Sigma^2)}\left[\frac{a_1^2}{p}+a_2^2 p\right]\right)}{p^K(1-p)}dp \tag{B.121}$$

$$= \frac{1}{2\pi j} \oint_{\Gamma_\infty} \left(\frac{\sigma_2^2 p + \sigma_1^2}{\Sigma^2} \right)^{2K-1} p^{-K} f\left(\frac{a_1}{\Sigma}, \frac{a_2}{\Sigma}; p \right) dp. \tag{B.122}$$

Expanding the power term by the binomial theorem we have:

$$P = \left(\frac{1}{\Sigma^2} \right)^{2K-1} \sum_{k=0}^{2K-1} \binom{2K-1}{k} (\sigma_2^2)^{2K-1-k} (\sigma_1^2)^k \\ \frac{1}{2\pi j} \oint_{\Gamma_\infty} p^{K-k-1} f\left(\frac{a_1}{\Sigma}, \frac{a_2}{\Sigma}; p \right) dp \tag{B.123}$$

Noting that the contour integral above is identical to the residue of Equation (B.110) with $K \to 1 + k - K$, we finally obtain the desired form of Equation (B.124):

$$P_g = \left(\frac{\sigma_2^2}{\Sigma^2} \right)^{2K-1} \sum_{k=0}^{2K-1} \binom{2K-1}{k} \left(\frac{\sigma_1^2}{\sigma_2^2} \right)^k Q_{K-k}\left(\frac{a_2}{\Sigma}, \frac{a_1}{\Sigma} \right) \tag{B.124}$$

B.3 Derivations from Chapter 5

B.3.1 The Fundamental Matrix

Since here we have two possible state diagrams, there are two transition matrices describing the search process, given by Equation (B.125) and Equation (B.126), where Equation (B.125) is associated with Figure 5.6 a) and Equation (B.126) is associated with Figure 5.6 b).

$$\boldsymbol{P} = \left(\begin{array}{cc|ccccc} 1 & 0 & 0 & 0 & \dots & \dots & 0 \\ 0 & 1 & 0 & 0 & \dots & \dots & 0 \\ \hline 0 & P_{fa_0} & 0 & P_{r_0} & 0 & \dots & 0 \\ 0 & P_{fa_0} & 0 & 0 & P_{r_0} & \dots & 0 \\ \vdots & \vdots & \vdots & \vdots & \ddots & \ddots & \vdots \\ P_{d_{10}} & P_{fa_{10}} & 0 & 0 & \dots & 0 & P_{r_{10}} \\ P_{d_{11}} & P_{fa_{11}} & P_{r_{11}} & 0 & 0 & \dots & 0 \end{array} \right) \tag{B.125}$$

$$\boldsymbol{P} = \left(\begin{array}{cc|ccccc} 1 & 0 & 0 & 0 & \dots & \dots & 0 \\ 0 & 1 & 0 & 0 & \dots & \dots & 0 \\ \hline 0 & P_{fa_0} & 0 & P_{r_0} & 0 & \dots & 0 \\ 0 & P_{fa_0} & 0 & 0 & P_{r_0} & \dots & 0 \\ \vdots & \vdots & \vdots & \vdots & \ddots & \ddots & \vdots \\ P_{d_{11}} & P_{fa_{11}} & 0 & 0 & \dots & 0 & P_{r_{11}} \\ P_{d_{10}} & P_{fa_{10}} & P_{r_{10}} & 0 & 0 & \dots & 0 \end{array}\right) \tag{B.126}$$

The only difference between these two matrices is the interchange of the transition probabilities associated with the H_{11} tile ($P_{d_{11}}$, $P_{r_{11}}$ and $P_{fa_{11}}$) with those of the H_{10} tile ($P_{d_{10}}$, $P_{r_{10}}$ and $P_{fa_{10}}$). Assuming both cases occur with equal probability, we can write the average transition matrix as:

$$\overline{\boldsymbol{P}} = \left(\begin{array}{cc|ccccc} 1 & 0 & 0 & 0 & \dots & \dots & 0 \\ 0 & 1 & 0 & 0 & \dots & \dots & 0 \\ \hline 0 & P_{fa_0} & 0 & P_{r_0} & 0 & \dots & 0 \\ 0 & P_{fa_0} & 0 & 0 & P_{r_0} & \dots & 0 \\ \vdots & \vdots & \vdots & \vdots & \ddots & \ddots & \vdots \\ \overline{P}_{d_1} & \overline{P}_{fa_1} & 0 & 0 & \dots & 0 & \overline{P}_{r_1} \\ \overline{P}_{d_1} & \overline{P}_{fa_1} & \overline{P}_{r_1} & 0 & 0 & \dots & 0 \end{array}\right) \tag{B.127}$$

where $\overline{P}_{d_1} = 0.5(P_{d_{11}} + P_{d_{10}})$, $\overline{P}_{r_1} = 0.5(P_{r_{11}} + P_{r_{10}})$ and $\overline{P}_{fa_1} = 0.5(P_{fa_{11}} + P_{fa_{10}})$. In the sequel we will consider the state diagram of Figure 5.6 a), with the understanding that we must average over both cases to yield a true representation of the search process.

Returning to the case a) state diagram of Figure 5.6 and following the same

procedure as for the one H_1 tile approximation we have, for $0 < n < N_{\mathrm{T}}$:

$$\boldsymbol{T}^n = \begin{pmatrix} 0 & 0 & \dots & 0 & P_{r_0}^n & 0 & \dots & 0 \\ 0 & 0 & \dots & 0 & 0 & P_{r_0}^n & \dots & 0 \\ \vdots & \vdots & \vdots & \vdots & \vdots & \ddots & \ddots & \vdots \\ 0 & 0 & \dots & 0 & 0 & 0 & \dots & P_{r_{10}} P_{r_0}^{n-1} \\ P_m P_{r_0}^{n-2} & 0 & \dots & 0 & 0 & 0 & \dots & 0 \\ 0 & P_m P_{r_0}^{n-2} & \ddots & 0 & 0 & 0 & \dots & 0 \\ \vdots & \ddots & \ddots & \ddots & \vdots & \vdots & \dots & \dots \\ 0 & 0 & \dots & P_{r_{11}} P_{r_0}^{n-1} & 0 & 0 & \dots & 0 \end{pmatrix} \tag{B.128}$$

where $P_m = P_{r_{11}} P_{r_{10}}$ is the total probability of missing the signal in both the H_{11} and H_{10} tiles. From Equation (5.16) and Equation (5.17) we have the following expression for the fundamental matrix:

$$\boldsymbol{N} = \frac{1}{1 - P_L} \begin{pmatrix} 1 & P_{r_0} & P_{r_0}^2 & \dots & P_{r_{11}} P_{r_0}^{N_{\mathrm{T}}-2} \\ P_m P_{r_0}^{N_{\mathrm{T}}-3} & 1 & P_{r_0} & \dots & P_{r_{11}} P_{r_0}^{N_{\mathrm{T}}-3} \\ P_m P_{r_0}^{N_{\mathrm{T}}-4} & P_m P_{r_0}^{N_{\mathrm{T}}-3} & 1 & \dots & P_{r_{11}} P_{r_0}^{N_{\mathrm{T}}-4} \\ \vdots & \vdots & \ddots & \ddots & \vdots \\ P_{r_{11}} & P_{r_{11}} P_{r_0} & \dots & P_{r_{11}} P_{r_0}^{N_{\mathrm{T}}-2} & 1 \end{pmatrix} \tag{B.129}$$

where, in this case, $P_L = P_m P_{r_0}^{N_{\mathrm{T}}-2} = P_{r_{11}} P_{r_{10}} P_{r_0}^{N_{\mathrm{T}}-2}$. Again, averaging over both possible state diagrams yields:

$$\overline{\boldsymbol{N}} = \frac{1}{1 - P_L} \begin{pmatrix} 1 & P_{r_0} & P_{r_0}^2 & \dots & \overline{P}_{r_1} P_{r_0}^{N_{\mathrm{T}}-2} \\ P_m P_{r_0}^{N_{\mathrm{T}}-3} & 1 & P_{r_0} & \dots & \overline{P}_{r_1} P_{r_0}^{N_{\mathrm{T}}-3} \\ P_m P_{r_0}^{N_{\mathrm{T}}-4} & P_m P_{r_0}^{N_{\mathrm{T}}-3} & 1 & \dots & \overline{P}_{r_1} P_{r_0}^{N_{\mathrm{T}}-4} \\ \vdots & \vdots & \ddots & \ddots & \vdots \\ \overline{P}_{r_1} & \overline{P}_{r_1} P_{r_0} & \dots & \overline{P}_{r_1} P_{r_0}^{N_{\mathrm{T}}-2} & 1 \end{pmatrix}. \tag{B.130}$$

Returning to the form of Equation (B.129), it is useful to divide the fundamental

matrix into subcomponents as follows:

$$\boldsymbol{N} = \frac{1}{1-P_L}\begin{pmatrix} \widetilde{\boldsymbol{N}} & \widetilde{\boldsymbol{c}} \\ \widetilde{\boldsymbol{r}} & 1 \end{pmatrix} \tag{B.131}$$

where:

$$\widetilde{\boldsymbol{N}}_{i,j} = \begin{cases} P_{r_0}^{j-i} & i \leq j \\ P_m P_{r_0}^{N_\mathrm{T}-2-(i-j)} & i > j \end{cases} \tag{B.132}$$

$$\widetilde{\boldsymbol{c}}_i = P_{r_{10}} P_{r_0}^{N_\mathrm{T}-2-i} \tag{B.133}$$

$$\widetilde{\boldsymbol{r}}_j = P_{r_{11}} P_{r_0}^{j} \,. \tag{B.134}$$

In this way, the submatrix $\widetilde{\boldsymbol{N}}$ is independent of the form of the state diagram, whereas the row vector $\widetilde{\boldsymbol{r}}$ and column vector $\widetilde{\boldsymbol{c}}$ incorporate all the information regarding the order of the H_{11} and H_{10} tiles.

$\widetilde{\boldsymbol{N}}$ has the same form as the fundamental matrix under the one H_1 tile approximation with $N_\mathrm{T}-1$ tiles in the search space (rather than N_T) and rejection probability P_m (rather than P_{r_1}).

B.3.2 Probabilities of Detection and False Alarm

Substituting the new fundamental matrix of Equation (B.129) into Equation (5.20), we obtain the following expression for $\boldsymbol{A}$:

$$\boldsymbol{A} = \frac{1}{1-P_L}\begin{pmatrix} 1 & P_{r_0} & \dots & P_{r_{10}} P_{r_0}^{N_\mathrm{T}-2} \\ P_m P_{r_0}^{N_\mathrm{T}-3} & 1 & \dots & P_{r_{10}} P_{r_0}^{N_\mathrm{T}-3} \\ \vdots & \vdots & \ddots & \vdots \\ P_{r_{11}} & P_{r_{11}} P_{r_0}^2 & \dots & 1 \end{pmatrix} \begin{pmatrix} 0 & P_{fa_0} \\ 0 & P_{fa_0} \\ \vdots & \vdots \\ P_{d_{10}} & P_{fa_{10}} \\ P_{d_{11}} & P_{fa_{11}} \end{pmatrix} . \tag{B.135}$$

Now, $P_{D,i}$, the probability of detection given starting state i, is given by:

$$P_{D,i} = \frac{1}{1-P_L} \begin{cases} P_{d_{10}} P_{r_0}^{N_\mathrm{T}-2-i} + P_{d_{11}} P_{r_{10}} P_{r_0}^{N_\mathrm{T}-2-i} & i < N_\mathrm{T}-1 \\ \\ P_{r_{11}} P_{d_{10}} P_{r_0}^{N_\mathrm{T}-2} + P_{d_{11}} & i = N_\mathrm{T}-1 \end{cases}$$

Once again averaging over the two possible forms of $\boldsymbol{N}$ we obtain:

$$\overline{P}_{D,i} = \frac{1}{1-P_L} \begin{cases} \overline{P}_{d_1} P_{r_0}^{N_\mathrm{T}-2-i} + \overline{P}_{rd_1} P_{r_0}^{N_\mathrm{T}-2-i} & i < N_\mathrm{T}-1 \\ \\ \overline{P}_{rd_1} P_{r_0}^{N_\mathrm{T}-2} + \overline{P}_{d_1} & i = N_\mathrm{T}-1 \end{cases}$$

where $\overline{P}_{rd_1} = 0.5(P_{r_{11}} P_{d_{10}} + P_{r_{10}} P_{d_{11}})$. Finally, averaging over the starting state i, yields:

$$P_D = \frac{1}{N_\mathrm{T}(1-P_L)} \left\{ \left(\overline{P}_{d_1} + \overline{P}_{rd_1}\right) \frac{1-P_{r_0}^{N_\mathrm{T}-1}}{1-P_{r_0}} + \overline{P}_{d_1} + \overline{P}_{rd_1} P_{r_0}^{N_\mathrm{T}-2} \right\} \tag{B.136}$$

and, once again, $P_{FA} = 1 - P_D$. Note the term $\overline{P}_{d_1} + \overline{P}_{rd_1}$ is the overall probability of detection in either of the H_1 cells.

B.3.3 First Order Statistics

Here, we follow the same procedure as for the one H_1 tile approximation to determine the mean number of dwells. We begin with $m_{1,i}$:

$$m_{1,i} = \sum_{j=0}^{N_\mathrm{T}-1} \boldsymbol{N}_{i,j} \tag{B.137}$$

$$= \frac{1}{1-P_L} \begin{cases} \sum_{j=0}^{N_\mathrm{T}-2} \widetilde{\boldsymbol{N}}_{i,j} + \widetilde{\boldsymbol{c}}_i & i < N_\mathrm{T}-1 \\ \\ \sum_{j=0}^{N_\mathrm{T}-2} \widetilde{\boldsymbol{r}}_j + 1 & i = N_\mathrm{T}-1 \end{cases} \tag{B.138}$$

$$= \begin{cases} \dfrac{1}{1-P_{r_0}} + \dfrac{P_m - P_{r_0}}{1-P_L}\dfrac{P_{r_0}^{N_\mathrm{T}-2-i}}{1-P_{r_0}} + \dfrac{\overline{P}_{r_1}P_{r_0}^{N_\mathrm{T}-2-i}}{1-P_L} & i < N_\mathrm{T}-1 \\ \dfrac{\overline{P}_{r_1}}{1-P_L}\dfrac{1-P_{r_0}^{N_\mathrm{T}-1}}{1-P_{r_0}} + \dfrac{1}{1-P_L} & i = N_\mathrm{T}-1. \end{cases} \tag{B.139}$$

Note that here we have averaged over the two possible forms of $\widetilde{\boldsymbol{r}}$ and $\widetilde{\boldsymbol{c}}$. Equation (B.139) is independent of the distribution of the starting state i. Once again, assuming a uniform *a priori* distribution on i we obtain:

$$\begin{aligned} m_1 =& \frac{N_\mathrm{T}-1}{N_\mathrm{T}P_{fa_0}} + \frac{1}{N_\mathrm{T}(1-P_L)} + \frac{(P_m - P_{r_0})(1-P_{r_0}^{N_\mathrm{T}-1})}{N_\mathrm{T}(1-P_L)P_{fa_0}^2} \\ &+ \frac{(P_{r_{11}} + P_{r_{10}})(1-P_{r_0}^{N_\mathrm{T}-1})}{N_\mathrm{T}(1-P_L)P_{fa_0}} \end{aligned} \tag{B.140}$$

B.3.4 Second Order Statistics

Following a similar procedure to that of Section 5.1.5 we define the matrix $\boldsymbol{M} = \boldsymbol{N}^2$ and inserting Equation (B.131) gives:

$$\boldsymbol{M} = \frac{1}{(1-P_L)^2}\begin{pmatrix} \widetilde{\boldsymbol{N}} & \widetilde{\boldsymbol{c}} \\ \widetilde{\boldsymbol{r}} & 1 \end{pmatrix}\begin{pmatrix} \widetilde{\boldsymbol{N}} & \widetilde{\boldsymbol{c}} \\ \widetilde{\boldsymbol{r}} & 1 \end{pmatrix} \tag{B.141}$$

$$= \frac{1}{(1-P_L)^2}\begin{pmatrix} \widetilde{\boldsymbol{M}} & \widetilde{\boldsymbol{\gamma}} \\ \widetilde{\boldsymbol{\rho}} & \widetilde{\boldsymbol{r}}\widetilde{\boldsymbol{c}}+1 \end{pmatrix} \tag{B.142}$$

where $\widetilde{\boldsymbol{M}} = \widetilde{\boldsymbol{N}}^2 + \widetilde{\boldsymbol{c}}\widetilde{\boldsymbol{r}}$, $\widetilde{\boldsymbol{\rho}} = \widetilde{\boldsymbol{r}}\widetilde{\boldsymbol{N}} + \widetilde{\boldsymbol{r}}$ and $\widetilde{\boldsymbol{\gamma}} = \widetilde{\boldsymbol{N}}\widetilde{\boldsymbol{c}} + \widetilde{\boldsymbol{c}}$.

Now, the matrix $\widetilde{\boldsymbol{N}}$ is identical in form to the fundamental matrix in the one H_1 case, but with $N_\mathrm{T} \rightarrow N_\mathrm{T}-1$ and $P_{r_1} \rightarrow P_m$. Thus we can re-write Equation (5.29) and Equation (5.30) directly as:

$$\left(\widetilde{\boldsymbol{N}}^2\right)_{i,j} = \begin{cases} P_m P_{r_0}^{N_\mathrm{T}-2-(i-j)}\left[N_\mathrm{T}-1+(j+1-i)(1-P_L)\right] & i > j \\ P_{r_0}^{j-i}\left[(N_\mathrm{T}-1)P_L + (j+1-i)(1-P_L)\right] & i \leq j\,. \end{cases} \tag{B.143}$$

From Equation (B.133) and Equation (B.134) we have:

$$(\widetilde{\boldsymbol{cr}})_{i,j} = P_m P_{r_0}^{N_{\mathrm{T}}-2-(i-j)}. \tag{B.144}$$

Combining these last two equations gives:

$$\widetilde{\boldsymbol{M}}_{i,j} = \begin{cases} P_m P_{r_0}^{N_{\mathrm{T}}-2-(i-j)} \left[N_{\mathrm{T}} + (j+1-i)(1-P_L)\right] & i > j \\ \\ P_{r_0}^{j-i} \left[N_{\mathrm{T}} P_L + (j+1-i)(1-P_L)\right] & i \leq j\,. \end{cases} \tag{B.145}$$

From Equation (B.132) and Equation (B.134) we obtain:

$$\widetilde{\boldsymbol{\rho}}_j = \overline{P}_{r_1} P_{r_0}^j \left(N_{\mathrm{T}} P_L + (j+2)(1-P_L)\right). \tag{B.146}$$

Similarly, using Equation (B.133) we have:

$$\widetilde{\boldsymbol{\gamma}}_i = \overline{P}_{r_1} P_{r_0}^{N_{\mathrm{T}}-2-i} \left(N_{\mathrm{T}} - i(1-P_L)\right) \tag{B.147}$$

and, finally:

$$\widetilde{\boldsymbol{r}}\widetilde{\boldsymbol{c}} = (N_{\mathrm{T}} - 1)P_L. \tag{B.148}$$

Now, from Equation (5.28), and assuming a uniform distribution on the starting state, we have:

$$\begin{aligned} m_2 &= 2\boldsymbol{\pi}^{\mathrm{T}}\boldsymbol{M}\boldsymbol{e} - m_1 \\ &= \frac{2}{N_{\mathrm{T}}(1-P_L)^2}\left\{\boldsymbol{e}^{\mathrm{T}}\widetilde{\boldsymbol{M}}\boldsymbol{e} + \boldsymbol{e}^{\mathrm{T}}\widetilde{\boldsymbol{\gamma}} + \widetilde{\boldsymbol{\rho}}\boldsymbol{e} + \widetilde{\boldsymbol{r}}\widetilde{\boldsymbol{c}} + 1\right\} - m_1. \end{aligned} \tag{B.149}$$

where:

$$\begin{aligned} \frac{\boldsymbol{e}^{\mathrm{T}}\widetilde{\boldsymbol{M}}\boldsymbol{e}}{N_{\mathrm{T}}(1-P_L)^2} &= \frac{N_{\mathrm{T}}-1}{N_{\mathrm{T}}P_{fa_0}^2} + \frac{(N_{\mathrm{T}}-1)(P_m - P_{r_0})^2 P_{r_0}^{N_{\mathrm{T}}-2}}{N_{\mathrm{T}}(1-P_L)^2 P_{fa_0}^2} \\ &\quad + \frac{2(P_m - P_{r_0})(1-P_{r_0}^{N_{\mathrm{T}}-1})}{N_{\mathrm{T}}(1-P_L)P_{fa_0}^3} + \frac{P_m(1-P_{r_0}^{N_{\mathrm{T}}-1})^2}{N_{\mathrm{T}}(1-P_L)^2 P_{fa_0}^2} \end{aligned} \tag{B.150}$$

$$\begin{aligned} \frac{\boldsymbol{e}^{\mathrm{T}}\widetilde{\boldsymbol{\gamma}} + \widetilde{\boldsymbol{\rho}}\boldsymbol{e}}{N_{\mathrm{T}}(1-P_L)^2} &= \frac{P_{r_{11}} + P_{r_{10}}}{(1-P_L)(1-P_{r_0})}\left\{\frac{N_{\mathrm{T}}P_{r_0}^{N_{\mathrm{T}}-2}(P_m - P_{r_0})}{(1-P_L)}\right. \\ &\quad \left. + \frac{(2-P_{r_0})(1-P_{r_0}^{N_{\mathrm{T}}-1})}{N_{\mathrm{T}}(1-P_{r_0})}\right\} \end{aligned} \tag{B.151}$$

$$\frac{\widetilde{\boldsymbol{r}}\widetilde{\boldsymbol{c}}+1}{N_{\mathrm{T}}(1-P_L)^2} = \frac{P_L}{(1-P_L)^2}+\frac{1}{N_{\mathrm{T}}(1-P_L)}\,. \tag{B.152}$$

After simplifying, we obtain the following expression for the mean square number of dwells under the two H_1 tile approximation:

$$\begin{aligned} m_2 = {} & \frac{(N_{\mathrm{T}}-1)(1+P_{r_0})}{N_{\mathrm{T}}P_{fa_0}^2}+\frac{2P_L}{(1-P_L)^2}+\frac{1}{N_{\mathrm{T}}(1-P_L)}+\frac{2P_m(1-P_{r_0}^{N_{\mathrm{T}}-1})^2}{N_{\mathrm{T}}(1-P_L)^2P_{fa_0}^2} \\ & +\frac{2(N_{\mathrm{T}}-1)(P_m-P_{r_0})^2P_{r_0}^{N_{\mathrm{T}}-2}}{N_{\mathrm{T}}(1-P_L)^2P_{fa_0}^2}+\frac{(3+P_{r_0})(P_m-P_{r_0})(1-P_{r_0}^{N_{\mathrm{T}}-1})}{N_{\mathrm{T}}(1-P_L)P_{fa_0}^3} \\ & +\frac{P_{r_{11}}+P_{r_{10}}}{(1-P_L)P_{fa_0}}\left\{\frac{2(P_m-P_{r_0})P_{r_0}^{N_{\mathrm{T}}-2}}{1-P_L}+\frac{(3-P_{r_0})}{N_{\mathrm{T}}P_{fa_0}}-\frac{P_{r_0}^{N_{\mathrm{T}}-1}}{N_{\mathrm{T}}}\right\} \end{aligned} \tag{B.153}$$

B.4 Derivations from Chapter 6

B.4.1 Mean and Variance of the Power Level Detector

We wish to derive the mean and variance of the power level detector for the detection of MAI in the parallel form of the ML detector. We assume that one full Doppler bin is covered by the detector tile and that this tile contains C_{T} cells. We also assume a complex signal representation, such that the rv X at the input to the correlators has a C_{T}-dimensional complex Gaussian distribution with mean $\boldsymbol{\mu}_X$ and covariance $\boldsymbol{C}_X$ given by:

$$\boldsymbol{C}_X = 2\sigma_X^2\boldsymbol{I}. \tag{B.154}$$

Note that σ_X^2 is the variance in either the in-phase or quadrature component of X and that the elements of X are statistically independent. Thus, from Equation (6.6), we have:

$$\boldsymbol{C}_Y = 2\sigma_X^2\boldsymbol{S}_k\boldsymbol{S}_k^{\mathrm{H}}. \tag{B.155}$$

Now, $\boldsymbol{S}_k\boldsymbol{S}_k^{\mathrm{H}}$ is the product of two circulant matrices and, hence, is itself a circulant matrix [50]. In fact, letting:

$$\boldsymbol{\Theta}_k \triangleq \boldsymbol{S}_k\boldsymbol{S}_k^{\mathrm{H}}, \tag{B.156}$$

then $\boldsymbol{\Theta}_k$ is the circulant matrix formed from the auto-correlation vector $\boldsymbol{\theta}_k$ of the spreading code from satellite k.

Appendix B. Mathematical Derivations

Our approach is similar that used in the derivation of the Gaussian approximations for the differentially coherent forms of detector/estimator. We begin with the characteristic function of ν and use Equation (6.10) to obtain its first two moments. Firstly, however, we require an expression for the determinant of the matrix $\boldsymbol{P}$ defined in Equation (6.9). For this we require the following useful property of circulant matrices [50]:

Property B.1 *Let $\boldsymbol{A}$ be an $N \times N$ circulant matrix whose first row is the vector $\boldsymbol{a}$, then the eigenvalues of $\boldsymbol{A}$ are given by the DFT of $\boldsymbol{a}$. Thus, letting λ_i be the i^{th} eigenvalue of $\boldsymbol{A}$ and $\boldsymbol{\lambda} = [\lambda_0, \lambda_1, \ldots, \lambda_{N-1}]$, then:*

$$\begin{aligned} \boldsymbol{\lambda} &= \text{DFT}\left\{\boldsymbol{a}\right\} \\ \therefore \lambda_i &= \sum_{n=0}^{N-1} a_i e^{-\frac{2\pi j}{N} ni}\,. \end{aligned}$$

Thus, letting λ_i denote the i^{th} eigenvalue of $\boldsymbol{C}_Y$, then the λ_i's are the roots of the characteristic equation of $\boldsymbol{C}_Y$:

$$|s\boldsymbol{I} - \boldsymbol{C}_Y| = 0. \tag{B.157}$$

We can use Equation (B.157) to derive an expression for the determinant of $\boldsymbol{P}$, as follows:

$$|s\boldsymbol{I} - \boldsymbol{C}_Y| = \prod_{i=0}^{C_{\text{T}}-1} (s - \lambda_i)\,. \tag{B.158}$$

Letting $s \to \frac{1}{j\omega}$, yields:

$$\left|\frac{1}{j\omega}\boldsymbol{I} - \boldsymbol{C}_Y\right| = \prod_{i=0}^{C_{\text{T}}-1} \left(\frac{1}{j\omega} - \lambda_i\right) \tag{B.159}$$

$$= \left(\frac{1}{j\omega}\right)^{C_{\text{T}}} \prod_{i=0}^{C_{\text{T}}-1} (1 - j\omega\lambda_i) \tag{B.160}$$

$$\therefore (j\omega)^{C_{\text{T}}} |s\boldsymbol{I} - \boldsymbol{C}_Y| = \prod_{i=0}^{C_{\text{T}}-1} (1 - j\omega\lambda_i)\,. \tag{B.161}$$

But, for any $N \times N$ matrix $\boldsymbol{A}$, $|c\boldsymbol{A}| = c^N |\boldsymbol{A}|$, so:

$$|\boldsymbol{I} - j\omega \boldsymbol{C}_Y| = \prod_{i=0}^{C_\mathrm{T}-1} (1 - j\omega\lambda_i) \tag{B.162}$$

$$= |\boldsymbol{P}|\,. \tag{B.163}$$

The Mean of ν

Inserting Equation (6.8) into Equation (6.10) yields:

$$E[\nu] = \frac{1}{j}\left(e^{-\boldsymbol{\mu}_Y^\mathrm{H} \boldsymbol{C}_Y^{-1}[\boldsymbol{I}-\boldsymbol{P}^{-1}]\boldsymbol{\mu}_Y} \frac{d\,|\boldsymbol{P}|^{-1}}{d\omega} + |\boldsymbol{P}|^{-1} \frac{d}{d\omega} e^{-\boldsymbol{\mu}_Y^\mathrm{H} \boldsymbol{C}_Y^{-1}[\boldsymbol{I}-\boldsymbol{P}^{-1}]\boldsymbol{\mu}_Y} \right)\Bigg|_{\omega=0}. \tag{B.164}$$

Taking each component in turn, we find:

$$e^{-\boldsymbol{\mu}_Y^\mathrm{H} \boldsymbol{C}_Y^{-1}[\boldsymbol{I}-\boldsymbol{P}^{-1}]\boldsymbol{\mu}_Y}\Big|_{\omega=0} = 1 \tag{B.165}$$

$$\frac{d\,|\boldsymbol{P}|^{-1}}{d\omega} = -\,|\boldsymbol{P}|^{-2} \frac{d\,|\boldsymbol{P}|}{d\omega} \tag{B.166}$$

$$|\boldsymbol{P}||_{\omega=0} = 1. \tag{B.167}$$

The derivative of $|\boldsymbol{P}|$ is obtained from Equation (B.162):

$$\frac{d\,|\boldsymbol{P}|}{d\omega} = \sum_{k=0}^{C_\mathrm{T}-1} (-j\lambda_k) \prod_{\substack{i=0 \\ i\neq k}}^{C_\mathrm{T}-1} (1 - j\omega\lambda_i) \tag{B.168}$$

$$\therefore \frac{d\,|\boldsymbol{P}|}{d\omega}\Big|_{\omega=0} = -j \sum_{k=0}^{C_\mathrm{T}-1} \lambda_k. \tag{B.169}$$

But λ_k is given by the k^{th} component of the DFT of the auto-correlation vector:

$$\therefore \frac{d\,|\boldsymbol{P}|}{d\omega}\Big|_{\omega=0} = -j2\sigma_X^2 \sum_{k=0}^{C_\mathrm{T}-1} \sum_{n=0}^{C_\mathrm{T}-1} e^{-\frac{2\pi j}{C_\mathrm{T}} nk} \boldsymbol{\theta}_n. \tag{B.170}$$

Now, by the orthogonality of the complex exponentials, we have:

$$\sum_{k=0}^{C_\mathrm{T}-1} e^{-\frac{2\pi j}{C_\mathrm{T}} nk} = \begin{cases} C_\mathrm{T} & n \equiv 0 \mod C_\mathrm{T} \\ 0 & \text{otherwise.} \end{cases} \tag{B.171}$$

Thus, inserting Equation (B.171) into Equation (B.170) yields:

$$\left.\frac{d\,|\boldsymbol{P}|}{d\omega}\right|_{\omega=0} = -j2\sigma_X^2 C_{\mathrm{T}}\boldsymbol{\theta}_0. \tag{B.172}$$

But $\boldsymbol{\theta}_0 = C_{\mathrm{T}}$ and hence:

$$\left.\frac{d\,|\boldsymbol{P}|}{d\omega}\right|_{\omega=0} = -j2{C_{\mathrm{T}}}^2\sigma_X^2. \tag{B.173}$$

Using the matrix identity:

$$\frac{d\boldsymbol{A}^{-1}}{dx} = -\boldsymbol{A}^{-1}\frac{d\boldsymbol{A}}{dx}\boldsymbol{A}^{-1}, \tag{B.174}$$

we find:

$$\frac{d}{d\omega}e^{-\boldsymbol{\mu}_Y^{\mathrm{H}}\boldsymbol{C}_Y^{-1}\left[\boldsymbol{I}-\boldsymbol{P}^{-1}\right]\boldsymbol{\mu}_Y} = -e^{-\boldsymbol{\mu}_Y^{\mathrm{H}}\boldsymbol{C}_Y^{-1}\left[\boldsymbol{I}-\boldsymbol{P}^{-1}\right]\boldsymbol{\mu}_Y}\boldsymbol{\mu}_Y^{\mathrm{H}}\boldsymbol{C}_Y^{-1}\boldsymbol{P}^{-1}\frac{d\boldsymbol{P}}{d\omega}\boldsymbol{P}^{-1}\boldsymbol{\mu}_Y \tag{B.175}$$

$$= je^{-\boldsymbol{\mu}_Y^{\mathrm{H}}\boldsymbol{C}_Y^{-1}\left[\boldsymbol{I}-\boldsymbol{P}^{-1}\right]\boldsymbol{\mu}_Y}\boldsymbol{\mu}_Y^{\mathrm{H}}\boldsymbol{C}_Y^{-1}\boldsymbol{P}^{-1}\boldsymbol{C}_Y\boldsymbol{P}^{-1}\boldsymbol{\mu} \tag{B.176}$$

Now, $\boldsymbol{P}|_{\omega=0} = \boldsymbol{I}$ and, hence:

$$\left.\frac{d}{d\omega}e^{-\boldsymbol{\mu}_Y^{\mathrm{H}}\boldsymbol{C}_Y^{-1}\left[\boldsymbol{I}-\boldsymbol{P}^{-1}\right]\boldsymbol{\mu}_Y}\right|_{\omega=0} = j\boldsymbol{\mu}_Y^{\mathrm{H}}\boldsymbol{\mu}_Y. \tag{B.177}$$

Finally, inserting Equations (B.165), (B.166) (B.167), (B.173) and (B.177) into Equation (B.164) and simplifying, yields:

$$E[\nu] = 2{C_{\mathrm{T}}}^2\sigma_X^2 + \boldsymbol{\mu}_Y^{\mathrm{H}}\boldsymbol{\mu}_Y. \tag{B.178}$$

Letting σ^2 denote the noise variance of the in-phase or quadrature component of the received signal at the input to the coherent accumulator, then:

$$\sigma_X^2 = M\sigma^2.$$

Recall, from Equation (2.31), that σ_Y^2 is given by:

$$\sigma_Y^2 = N_s M\sigma^2,$$

where N_s is the number of samples per code period. In the FFT-based detector/ estimator $N_s = C_{\mathrm{T}}$ (*i.e.* the number of samples per code period is equal to the number of cells per tile), and so we have:

$$E[\nu] = 2C_{\mathrm{T}}\sigma_Y^2 + \boldsymbol{\mu}_Y^{\mathrm{H}}\boldsymbol{\mu}_Y. \tag{B.179}$$

The Variance of ν

The variance of ν can be derived using the same approach as was demonstrated above for the mean. The only difficulty arises in the determination of the second order derivative of the determinant of $\boldsymbol{P}$, so we consider this in some detail here.

Taking the derivative of Equation (B.168) yields:

$$\frac{d^2\left|\boldsymbol{P}\right|}{d\omega^2} = \sum_{k=0}^{C_{\mathrm{T}}-1}(-j\lambda_k)\sum_{\substack{l=0\\l\neq k}}^{C_{\mathrm{T}}-1}(-j\lambda_l)\prod_{\substack{i=0\\i\notin\{k,l\}}}^{C_{\mathrm{T}}-1}(1-j\omega\lambda_i) \tag{B.180}$$

$$\therefore \left.\frac{d^2\left|\boldsymbol{P}\right|}{d\omega^2}\right|_{\omega=0} = -\sum_{k=0}^{C_{\mathrm{T}}-1}\sum_{\substack{l=0\\l\neq k}}^{C_{\mathrm{T}}-1}\lambda_k\lambda_l \tag{B.181}$$

$$= \sum_{k=0}^{C_{\mathrm{T}}-1}\lambda_k^2 - \left(\sum_{k=0}^{C_{\mathrm{T}}-1}\lambda_k\right)^2. \tag{B.182}$$

The second summation term in Equation (B.182) above can be identified as the negative of the square of Equation (B.173). The first summand can be simplified using Parseval's theorem for the DFT [21]:

Theorem B.1 (Parseval) *Given a length N vector $\boldsymbol{x}$ and its DFT $\boldsymbol{X}$, then*

$$\sum_{n=0}^{N-1}|x_n|^2 = \frac{1}{N}\sum_{k=0}^{N-1}|X_k|^2.$$

Recalling that λ_i is given by $2\sigma_X^2$ times the i^{th} coefficient of the DFT of the auto-correlation vector, $\boldsymbol{\theta}$, then Parseval's theorem yields:

$$\sum_{k=0}^{C_{\mathrm{T}}-1}\lambda_k^2 = 4\sigma_X^4 C_{\mathrm{T}}\sum_{k=0}^{C_{\mathrm{T}}-1}|\boldsymbol{\theta}_k|^2. \tag{B.183}$$

Thus, inserting Equations (B.183) and (B.173) into Equation (B.182) yields:

$$\left.\frac{d^2\left|\boldsymbol{P}\right|}{d\omega^2}\right|_{\omega=0} = 4\sigma_X^4 C_{\mathrm{T}} \sum_{k=0}^{C_{\mathrm{T}}-1} \left|\boldsymbol{\theta}_k\right|^2 - 4\sigma_X^4 {C_{\mathrm{T}}}^2 \tag{B.184}$$

$$= \frac{4\sigma_Y^4}{C_{\mathrm{T}}} \sum_{k=0}^{C_{\mathrm{T}}-1} \left|\boldsymbol{\theta}_k\right|^2 - 4\sigma_Y^4. \tag{B.185}$$

Again, applying the matrix identity of Equation (B.174), it can be shown that:

$$\left.\frac{d^2}{d\omega^2} e^{-\boldsymbol{\mu}_Y^{\mathrm{H}} \boldsymbol{C}_Y^{-1}\left[\boldsymbol{I}-\boldsymbol{P}^{-1}\right]\boldsymbol{\mu}_Y}\right|_{\omega=0} = \left(\boldsymbol{\mu}_Y^{\mathrm{H}}\boldsymbol{\mu}_Y\right)^2 + 2\boldsymbol{\mu}_Y^{\mathrm{H}}\boldsymbol{C}_Y\boldsymbol{\mu}_Y. \tag{B.186}$$

Using Equations (B.184) and (B.186) in conjunction with Equation (6.10) yields the following expression for the variance of ν:

$$\mathrm{Var}\left[\nu\right] = \frac{4\sigma_Y^4}{C_{\mathrm{T}}} \sum_{k=0}^{C_{\mathrm{T}}-1} \left|\boldsymbol{\theta}_k\right|^2 + 2\boldsymbol{\mu}_Y^{\mathrm{H}}\boldsymbol{C}_Y\boldsymbol{\mu}_Y. \tag{B.187}$$

Appendix C

Probability Theory

In this appendix we give a brief overview of probability theory as it applies in this thesis. It could be used as a quick reference for the notations and conventions maintained throughout the thesis. An excellent overview of probability theory, going into much greater detail than we do here, can be found in Papoulis' book [92].

C.1 Random Events and Random Variables

Probability theory concerns itself with randomness. We shall assume that the object of interest is an *experiment*, **E**. We denote by $\mathcal{S}$ the set of possible outcomes of **E**, which we call the *sample space* of the experiment. An *event* is defined as any subset of $\mathcal{S}$, containing any number of points from within $\mathcal{S}$. Assuming the experiment is random, then any event A is associated with a probability $\Pr\{A\}$, for which the following two properties hold:

Property C.1

$$\Pr\{A\} \geq 0$$

and

Property C.2

$$\Pr\{S\} = 1.$$

Given a sample space $\mathcal{S}$ and an event $s \in \mathcal{S}$, then a *random variable* $X(s)$ is defined as a mapping from $\mathcal{S}$ to a subset of the real numbers:

$$X(s) \ : \ \mathcal{S} \rightarrow \mathbb{R}.$$

In general we will consider only the random variable (rv) X, so that the dependence on s is implicit.

Consider the random event $X \leq x$ for some x such that $-\infty \leq x \leq \infty$, then the probability of such an event is denoted $F_X(x)$. This probability can be viewed as a continuous function of the variable x, and is called the cumulative distribution function (CDF):

$$F_X(x) = \Pr\{X \leq x\}. \tag{C.1}$$

The derivative of the CDF with respect to x is called the probability density function (PDF) denoted $f_X(x)$:

$$f_X(x) = \frac{\partial F_X(x)}{\partial x}. \tag{C.2}$$

The probability of the random event $x_1 \leq X \leq x_2$ is then given by:

$$\Pr\{x_1 \leq X \leq x_2\} = F_X(x_2) - F_X(x_1) \tag{C.3}$$

$$= \int_{x_1}^{x_2} f_X(x) dx. \tag{C.4}$$

If the mapping $X(s)$ maps elements of $\mathcal{S}$ to a discrete subset of the real numbers, then the rv X is called a discrete rv. In general we associate all discrete rvs with mappings to a subset of the set of integers $\mathbb{Z}$. We define the discrete rv $\mathrm{X}(s)$ as:

$$\mathrm{X}(s) \ : \ \mathcal{S} \to \mathbb{Z}.$$

In place of the probability *density* function of continuous rvs, we define the probability *mass* function (PMF) of discrete rvs. The PMF of the discrete rv X at the point $\mathrm{X} = n$ is given by:

$$\mathrm{p_X}(n) = \Pr\{\mathrm{X} = n\}. \tag{C.5}$$

The CDF of X is thus given by:

$$F_{\mathrm{X}}(n) = \sum_{i=-\infty}^{n} \mathrm{p_X}(i). \tag{C.6}$$

C.2 Expectation and Moments

The expected value — or *mean* — of an rv X is defined as:

$$\mu \triangleq E_X[x] = \int_{-\infty}^{\infty} x f_X(x) d\, x. \tag{C.7}$$

Note that if X is a discrete rv taking on values $n \in \mathbb{Z}$, then we have:

$$E_X[n] = \sum_{n=-\infty}^{\infty} n \mathrm{p}_X(n). \tag{C.8}$$

We define by m_n the n^{th} *moment* of the rv X:

$$m_n \triangleq E_X[x^n] = \int_{-\infty}^{\infty} x^n f_X(x) d\, x. \tag{C.9}$$

Of more general interest are the *central moments*:

$$E_X[(x-\mu)^n] = \int_{-\infty}^{\infty} (x-\mu)^n f_X(x) d\, x. \tag{C.10}$$

The first central moment is simply zero. The second central moment is called the *variance* and is denoted $\mathrm{Var}[X]$:

$$\mathrm{Var}[X] \triangleq E_X\left[(x-\mu)^2\right]. \tag{C.11}$$

C.3 Transform Domain Techniques

Transform domain methods often prove useful in the analysis of random variables, particularly when dealing the rvs which can be expressed as the sum of many other rvs.

C.3.1 The Moment Generating Function

The MGF of an rv X is defined by:

$$\Psi_X(s) \triangleq E_X[\exp(sx)], \tag{C.12}$$

assuming that the expected value exists for all values of s in some range $-h < s < h$. For a continuous rv we therefore have:

$$\Psi_X(s) = \int_{-\infty}^{\infty} f_X(x) \exp(sx)\, dx. \tag{C.13}$$

It is interesting to note at this point that Equation (C.13) above is essentially the equation of the two-sided Laplace transform of $f_X(x)$. In fact the only difference is in the sign of the transform variable, s.

The MGF takes its name from the following:

Property C.3

$$m_n = \left. \frac{\partial^n \Psi_X(s)}{\partial s^n} \right|_{s=0}.$$

Thus, given the MGF of the rv X, we can easily determine all the moments of X. Other useful properties include:

Property C.4 *Given two independent rvs X and Y, with MGFs $\Psi_X(s)$ and $\Psi_Y(s)$, then the MGF of the rv $Z = X + Y$ is given by:*

$$\Psi_Z(s) = \Psi_X(s)\, \Psi_Y(s).$$

Property C.5 *Given the rv X with MGF $\Psi_X(s)$, and another rv Y such that $Y = g(X)$, then the MGF of Y is given by:*

$$\Psi_Y(s) = E_X[\exp(sg(X))].$$

Property C.6 *Given that the rv X has MGF $\Psi_X(s)$ then the PDF of X can be determined using the Laplace inversion integral (Bromwich integral):*

$$f_X(x) = \frac{1}{2\pi j} \int_{c-j\infty}^{c+j\infty} \Psi_X(s) \exp(-sx)\, ds.$$

These last two properties prove useful in determining the PDF of a function of an rv.

C.3.2 The Characteristic Function

The characteristic function of the rv X is defined by:

$$\Phi_X(j\omega) = E_X[\exp(j\omega x)]. \tag{C.14}$$

By comparison with Equation (C.12) above, we see that the CHF is simply the MGF evaluated at $s = j\omega$. The properties of the CHF are very similar to the properties of the MGF.

Property C.7

$$m_n = \frac{1}{j^n} \left. \frac{\partial^n \Phi_X(j\omega)}{\partial \omega^n} \right|_{s=0}.$$

Property C.8 *Given two independent rvs X and Y, with CHFs $\Phi_X(j\omega)$ and $\Phi_Y(j\omega)$, then the CHF of the rv $Z = X + Y$ is given by:*

$$\Phi_Z(j\omega) = \Phi_X(j\omega)\,\Phi_Y(j\omega).$$

Property C.9 *Given the rv X with CHF $\Phi_X(j\omega)$, and another rv Y such that $Y = g(X)$, then the CHF of Y is given by:*

$$\Phi_Y(j\omega) = E_X[\exp(j\omega g(X))].$$

Property C.10 *Given that the rv X has CHF $\Phi_X(j\omega)$ then the PDF of X can be determined using the Fourier inversion integral:*

$$f_X(x) = \frac{1}{2\pi} \int_{-\infty}^{\infty} \Phi_X(j\omega) \exp(-j\omega x)\, d\omega.$$

So, in effect the MGF represents the two-sided Laplace transform of the PDF, and the CHF represents the Fourier transform of the PDF. It is important to note that the two functions are directly inter-changeable by the simple substitution $s \leftrightarrow j\omega$. Tables of Fourier transforms may be used to determine the CHF from the PDF and vice versa.

C.3.3 The Probability Generating Function

Whereas the MGF and CHF are useful tools in the analysis of continuous rvs, we now introduce the probability generating function (PGF), which is the equivalent function for the analysis of discrete rvs taking on non-negative integer values. The PGF is essentially a sequence generating function, an excellent introduction to which can be found in [149].

Given the discrete rv X, the PGF $\mathrm{P_X}(z)$ is defined by:

$$\mathrm{P_X}(z) \triangleq E_{\mathrm{X}}\left[z^k\right] \tag{C.15}$$

$$= \sum_{i=0}^{\infty} \mathrm{p}_X(i)\, z^i. \tag{C.16}$$

Some useful properties include:

Property C.11

$$\left.\frac{\partial^n \mathrm{P_X}(z)}{\partial\, z^n}\right|_{z=1} = E_{\mathrm{X}}\left[\prod_{i=0}^{n-1}(\mathrm{X}-i)\right].$$

Property C.12 *Given two independent discrete rvs* X *and* Y*, with PGFs* $\mathrm{P_X}(z)$ *and* $\mathrm{P_Y}(z)$*, then the PGF of the discrete rv* $\mathrm{Z} = \mathrm{X} + \mathrm{Y}$ *is given by:*

$$\mathrm{P_Z}(z) = \mathrm{P_X}(z)\,\mathrm{P_Y}(z).$$

Property C.13 *Given that the discrete rv* X *has PGF* $\mathrm{P_X}(z)$ *then the PMF of* X *can be determined using the inversion formula:*

$$\mathrm{p_X}(n) = \frac{1}{2\pi j}\oint_{\Gamma_0} \mathrm{P_X}(z)\, z^{-(n+1)} d\, z,$$

where Γ_0 *is a complex contour in the* z*-domain enclosing the origin.*

References

[1] *Proceedings of the IEEE: Special Issue on GPS*, vol. 87, Jan. 1999.

[2] *GPS Interface Control Document ICD-200c.* United States Coast Guard, 2000.

[3] Digital cellular telecommunications system (Phase 2+); Location Services (LCS); Broadcast network assistance for Enhanced Observed Time Difference (E-OTD) and Global Positioning System (GPS) positioning methods. ETSI Std. ETSI TS 101 527, Rev. 8.4.0, Dec. 2001.

[4] Co-ordination group on access to location information by emergency services (CGALIES) final report. Available at: `http://cgalies.telefiles.de/cgalies_final.pdf`, 28th Jan. 2002. Accessed 16th Oct. 2006.

[5] European Commission recommendation 2003/558/EC: On the processing of caller location information in electronic communication networks for the purpose of location-enhanced emergency call services. Available at: `http://eur-lex.europa.eu/`, 25th Jul. 2003.

[6] *GPS Interface Control Document ICD-200c.* United States Coast Guard, 2003.

[7] Digital cellular telecommunications system (Phase 2+); Location Services (LCS); Mobile Station (MS) - Serving Mobile Location Centre (SMLC) Radio Resource LCS Protocol (RRLP). ETSI Std. ETSI TS 144 031, Rev. 6.8.0, Jul. 2005.

[8] ABI-Research. Mobile cellular industry as set for the year of the 3G phone. Available at

http://www.abiresearch.com/abiprdisplay.jsp?pressid=595, Feb. 2006. Accessed 16th Oct. 2006.

[9] M. Abramowitz and I. A. Stegun (eds.). *Handbook of mathematical functions, with formulas, graphs, and mathematical tables*. National Bureau of Standards, U.S.A., 1965. ISBN 0-471-80007-4.

[10] D. Akopian. A fast satellite acquisition method. In *Proceedings of the 14th International Technical Meeting of the Satellite Division of the Institute of Navigation ION GPS 2001*, pp. 2871–2881. Institute of Navigation, Salt Lake City, Utah, Sep. 2001.

[11] D. Akopian. Fast FFT based GPS satellite acquisition methods. *IEE Proceedings - Radar, Sonar and Navigation*, vol. 152, no. 4, pp. 277–286, Aug. 2005.

[12] A. Alaqeeli, J. Starzyk and F. van Graas. Real-time acquisition and tracking for GPS receivers. In *Proceedings of the IEEE International Symposium on Circuits and Systems (ISCAS 2003)*, vol. IV, pp. 500–503. Bangkok, Thailand, May 26–29 2003.

[13] L. C. Andrews and R. L. Phillips. *Mathematical Techniques for Engineers and Scientists*. SPIE Press, Washington, USA, 2003. ISBN 0-8194-4506-1.

[14] V. Ashe. Detector analysis. Confidential report, ParthusCeva Ltd., 2003.

[15] J. A. Ávila Rodríguez, V. Heiries, T. Pany et al. Theory on acquisition algorithms for indoor positioning. In *Proceedings of the 12th Saint Petersburg International Conference on Integrated Navigation Systems*. Saint Petersburg, Russia, May 23–25 2005.

[16] J. A. Ávila Rodríguez, T. Pany and B. Eissfeller. A theoretical analysis of acquisition algorithms for indoor positioning. In *Proceedings of the 2nd ESA Workshop on Satellite Navigation User Equipment Technologies (NAVITEC 2004)*. Noordwijk, The Netherlands, Dec. 8–10 2004.

[17] P. Axelrad and R. G. Brown. GPS navigation algorithms. In *Global Positioning System: Theory and Applications*, vol. 1, chap. 9, pp. 409–433. American Institute of Aeronautics and Astronautics, 1996.

[18] M. J. Barrett. Error probability for optimal and suboptimal quadratic receivers in rapid Rayleigh fading channels. *IEEE Journal on Selected Areas in Communications*, vol. SAC-5, no. 2, pp. 302–304, Feb. 1987.

[19] P. Bezucha. Mean acquisition time of serial spread spectrum PN acquisition system in the presence of code doppler. In *Proceedings of the IEEE Seventh International Symposium on Spread Spectrum Techniques and Applications (ISSSTA)*, vol. 3, pp. 751–755. Prague, Czech Republic, 2–5 Sep. 2002.

[20] M. S. Braasch and A. J. Van Dierendonck. GPS receiver architectures and measurements. *Proceedings of the IEEE*, vol. 87, no. 1, pp. 48–64, Jan. 1999.

[21] R. N. Bracewell. *The Fourier Transform and Its Applications*. McGraw-Hill, 1999. ISBN 0-07-303938-1.

[22] W. R. Braun. Performance analysis for the expanding search PN acquisition algorithm. *IEEE Transactions on Communications*, vol. 30, no. 3, pp. 424–435, Mar. 1982.

[23] P. E. Cantrell and A. K. Ojha. Comparison of generalized Q-function algorithms. *IEEE Transactions on Information Theory*, vol. IT-33, no. 4, pp. 591–596, Jul. 1987.

[24] D. E. Cartier. Partial correlation properties of pseudonoise (PN) code in noncoherent synchronization/detection schemes. *IEEE Transactions on Communications*, vol. 24, no. 8, pp. 898–903, Aug. 1976.

[25] K. K. Chawla and D. V. Sarwate. Parallel acquisition of PN sequences in DS/SS systems. *IEEE Transactions on Communications*, vol. 42, no. 5, pp. 2155–2164, May 1994.

[26] U. Cheng. Performance of a class of parallel spread-spectrum code acquisition schemes in the presence of data modulation. *IEEE Transactions on Communications*, vol. 36, no. 5, pp. 596–604, May 1988.

[27] U. Cheng, W. J. Hurd and J. I. Statman. Spread-spectrum code acquisition in the presence of Doppler shift and data modulation. *IEEE Transactions on Communications*, vol. 38, no. 2, pp. 241–250, Feb. 1990.

[28] C.-D. Chung. Differentially coherent detection technique for direct-sequence code acquisition in a Rayleigh fading mobile channel. *IEEE Transactions on Communications*, vol. 43, no. 2/3/4, pp. 1116–1126, February/March/April 1995.

[29] A. J. R. M. Coenen and D. J. R. van Nee. Novel fast GPS/GLONASS code-acquisition technique using low update rate FFT. *Electronics Letters*, vol. 28, no. 9, pp. 863–865, 1992.

[30] M. Cohn and A. Lempel. On fast m-sequence transforms. *IEEE Transactions on Information Theory*, vol. 23, no. 1, pp. 135–137, Jan. 1977.

[31] G. E. Corazza. On the MAX/TC criterion for code acquisition and its applications to DS-SSMA systems. *IEEE Transactions on Communications*, vol. 44, no. 9, pp. 1173–1182, Sep. 1996.

[32] G. E. Corazza, C. Caini, A. Vanelli-Coralli et al. DS-CDMA code acquisition in the presence of correlated fading — part I: Theoretical aspects. *IEEE Transactions on Communications*, vol. 52, no. 7, pp. 1160–1168, Jun. 2004.

[33] P. A. Dafesh and J. K. Holmes. Practical and theoretical tradeoffs of active parallel correlator and passive matched filter acquisition implementations. In *Proceedings of the Institute of Navigation Annual Meeting, ION AM 2000*, pp. 352–367. San Diego, CA, Jun. 26–28 2000.

[34] R. G. Davenport. FFT processing of direct sequence spreading codes using modern DSP microprocessors. In *Proceedings of the IEEE 1991 National Aerospace and Electronics Conference NAECON*, pp. 98–105. IEEE, Dayton, OH, May 1991.

[35] R. B. Davies. Numerical inversion of a characteristic function. *Biometrika*, vol. 60, no. 2, pp. 415–417, Aug. 1973.

[36] R. B. Davies. Algorithm AS 155: The distribution of a linear combination of χ^2 random variables. *Applied Statistics*, vol. 29, no. 3, pp. 323–333, 1980.

[37] L. D. Davisson and P. G. Flikkema. Fast single-element PN acquisition for the TDRSS MA system. *IEEE Transactions on Communications*, vol. 36, no. 11, pp. 1226–1235, Nov. 1988.

[38] D. M. DiCarlo and C. L. Weber. Statistical performance of single dwell serial synchronization systems. *IEEE Transactions on Communications*, vol. 28, no. 8, pp. 1382–1388, Aug. 1980.

[39] D. M. DiCarlo and C. L. Weber. Multiple dwell serial search: Performance and application to direct sequence code acquisition. *IEEE Transactions on Communications*, vol. 31, no. 5, pp. 650–659, May 1983.

[40] H. Elders-Boll and U. Dettmar. Efficient differentially coherent code/Doppler acquisition of weak GPS signals. In *Proceedings of the International Symposium on Spread Spectrum Techniques and Applications (ISSSTA)*, pp. 731–735. Sydney, Australia, 30th Aug. – 2nd Sep. 2004.

[41] P. Enge and P. Misra. Scanning the issue. *Proceedings of the IEEE*, vol. 87, no. 1, pp. 3–15, Jan. 1999.

[42] C. C. Fan and Z. Tsai. A differentially coherent delay-locked loop for spread-spectrum tracking receivers. *IEEE Communications Letters*, vol. 3, no. 10, pp. 282–284, Oct. 1999.

[43] FCC. Fact sheet: FCC wireless 911 requirements. Available at: `http://www.fcc.gov/911/enhanced`, Jan. 2001.

[44] J. Gil-Pelaez. Note on the inversion theorem. *Biometrika*, vol. 38, no. 3/4, pp. 481–482, Dec. 1951.

[45] R. Gold. Optimal binary sequences for spread spectrum multiplexing. *IEEE Transactions on Information Theory*, vol. 13, pp. 619–621, Oct. 1967.

[46] S. W. Golomb. *Shift Register Sequences*. Holden Day Series In Information Systems. Holden-Day Inc., San Francisco, CA, USA, 1967. ISBN 0-89412-048-4.

[47] S. D. Gordon and J. A. Ritcey. Calculating the K-distribution by saddle-point integration. *IEE Proceedings – Radar, Sonar and Navigation*, vol. 142, no. 4, pp. 162–166, Aug. 1995.

[48] I. S. Gradshteyn and I. M. Ryzhik. *Table of Integrals, Series, and Products*. Academic Press, New York, 4th edn., 1965. ISBN 0-12-294757-6.

[49] R. L. Graham, D. E. Knuth and O. Patashnik. *Concrete Mathematics*. Addison-Wesley, 1989. ISBN 0-201-55802-5.

[50] R. M. Gray. Toeplitz and circulant matrices: A review. *Foundations and Trends in Communications and Information Theory*, vol. 2, no. 3, pp. 155–239, 2006. URL `http://ee.stanford.edu/~gray/toeplitz.pdf`.

[51] T. Haddrell and A. R. Pratt. Understanding the indoor GPS signal. In *Proceedings of the 14th International Technical Meeting of the Satellite Division of the Institute of Navigation ION GPS 2001*, pp. 1487–1500. Institute of Navigation, Salt Lake City, Utah, Sep. 2001.

[52] C. W. Helstrom. *Probability and Stochastic Processes for Engineers*. Prentice Hall, Englewood Cliffs, NJ, USA, 1991. ISBN 0-02-353571-7.

[53] C. W. Helstrom. Computing the generalized Marcum Q-function. *IEEE Transactions on Information Theory*, vol. 38, no. 4, pp. 1422–1428, Jul. 1992.

[54] C. W. Helstrom. *Elements of Signal Detection and Estimation*. PTR Prentice Hall, Englewood Cliffs, NJ, USA, 1995. ISBN 0-13-808940-X.

[55] J. K. Holmes and L. Biederman. Delay-lock-loop mean time to lose lock. *IEEE Transactions on Communications*, vol. 26, no. 11, pp. 1549–1556, Nov. 1978.

[56] J. K. Holmes and C. C. Chen. Acquisition time performance of PN spread-spectrum systems. *IEEE Transactions on Communications*, vol. 25, no. 8, pp. 778–783, Aug. 1977.

[57] P. M. Hopkins. A unified analysis of pseudonoise synchronization by envelope correlation. *IEEE Transactions on Communications*, vol. 25, no. 8, pp. 770–778, Aug. 1977.

[58] W. J. Hurd, J. I. Statman and V. A. Vilnrotter. High dynamic GPS receiver using Maximum-Likelihood estimation and frequency tracking. *IEEE Transactions on Aerospace and Electronics Systems*, vol. 23, no. 4, pp. 425–437, Sep. 1987.

[59] J. Iinatti and A. Pouttu. Differentially coherent code acquisition in Doppler. In *Proceedings of the IEEE Vehicular Technology Conference (VTC Fall 1999)*, vol. 2, pp. 703–707. Amsterdam, Sept. 19–22 1999.

[60] J. Iinatti and A. Pouttu. Differentially coherent code acquisition in jamming and data modulation. In *Proceedings of the IEEE Military Communications Conference (MILCOM'99)*, pp. 579–573. Atlantic City, NJ, Oct. 31 – Nov. 3 1999.

[61] M. Iosifescu. *Finite Markov Processes and their Applications*. Wiley Series in Probability and Mathematical Sciences. John Wiley & Sons, 1980. ISBN 0-471-27677-4.

[62] D. R. Iskander. The characteristic function of the K-distributed interference. In *Proceedings of the 12th European Signal Processing Conference (EUSIPCO 04)*, pp. 1429–1432. Vienna, Austria, Sep. 2004.

[63] E. Jakeman and P. N. Pusey. A model for non-Rayleigh sea echo. *IEEE Transactions on Antennas and Propagation*, vol. AP-24, no. 6, pp. 806–814, Nov. 1976.

[64] D. R. Jensen and H. Solomon. A Gaussian approximation to the distribution of a definite quadratic form. *Journal of the American Statistical Association*, vol. 67, no. 340, pp. 898–902, Dec. 1972.

[65] Y. K. Jeong, O.-S. Shin and K. B. Lee. Fast slot synchronization for intercell asynchronous DS/CDMA systems. *IEEE Transactions on Wireless Communications*, vol. 1, no. 2, pp. 353–360, Apr. 2002.

[66] D. H. Johnson. Notes for ELEC 531: Estimation and detection theory. `http://www.ece.rice.edu/~dhj/courses/elec531/`. Accessed 16 February 2006.

[67] N. L. Johnson. On an extension of the connexion between Poisson and χ^2 distributions. *Biometrika*, vol. 46, no. 3/4, pp. 352–363, Dec. 1959.

[68] V. M. Jovanović. Analysis of strategies for serial-search spread-spectrum code acquisition – direct approach. *IEEE Transactions on Communications*, vol. 36, no. 11, pp. 1208–1220, Nov. 1988.

[69] V. M. Jovanović. On the distribution function of the spread-spectrum code acquisition time. *IEEE Journal on Selected Areas in Communications*, vol. 10, no. 4, pp. 760–769, May 1992.

[70] E. D. Kaplan (ed.). *Understanding GPS: Principles and Applications*. Artech House Publishers, 1996. ISBN 0-89006-793-7.

[71] M. D. Karunanayake, M. E. Cannon and G. Lachapelle. Evaluation of assisted GPS (AGPS) in weak signal environments using a hardware simulator. In *Proceedings of the Institute of Navigation GNSS Conference*. Long Beach, CA, Sep. 21–24 2004.

[72] M. Kendall, A. Stuart and J. K. Ord. *Kendall's Advanced Theory of Statistics*, vol. 1. Charles Griffin & Company Ltd, 5th edn., 1987. ISBN 0-85264-285-7.

[73] S. Kotz, N. L. Johnson and D. W. Boyd. Series representations of distributions of quadratic forms in normal variables. I. Central case. *The Annals of Mathematical Statistics*, vol. 38, no. 3, pp. 823–837, Jun. 1967.

[74] S. Kotz, N. L. Johnson and D. W. Boyd. Series representations of distributions of quadratic forms in normal variables. II. Non-central case. *The Annals of Mathematical Statistics*, vol. 38, no. 3, pp. 838–848, Jun. 1967.

[75] N. F. Krasner. GPS receiver and method for processing GPS signals. US Patent, Jul. 1998. No. 5,781,156.

[76] E. Kreyszig. *Advanced Engineering Mathematics*. Wiley, 8th edn., 1999. ISBN 0-471-33328-X.

[77] D. Kubrak, C. Macabiau and M. Monnerat. Analysis of a software-based A-GPS acquisition performance using statistical processes. In *Proceedings of the Institute of Navigation National Technical Meeting (ION NTM 2005)*, pp. 1082–1092. Institute of Navigation, San Diego, California, 24–26 Jan. 2005.

[78] G. Lachapelle. GNSS indoor location technologies. *Journal of Global Positioning Systems*, vol. 3, no. 1–2, pp. 2–11, 2004.

[79] W. R. LePage. *Complex Variables and the Laplace Transform for Engineers*. McGraw-Hill, 1961. ISBN 0-07-037206-3.

[80] J. Li and S. Tantaratana. Optimal and suboptimal coherent acquisition schemes for PN sequences with data modulation. *IEEE Transactions on Communications*, vol. 43, no. 2/3/4, pp. 554–564, Feb.–Apr. 1995.

[81] D. M. Lin and J. B. Y. Tsui. Acquisition schemes for software GPS receivers. In *Proceedings of the 11th International Technical Meeting of the Satellite Division of the Institute of Navigation ION GPS 1998*, pp. 317–325. Nashville, Tennessee, Sep. 15–18 1998.

[82] D. M. Lin and J. B. Y. Tsui. Comparison of acquisition methods for software GPS receiver. In *Proceedings of the 13th International Technical Meeting of the Satellite Division of the Institute of Navigation ION GPS 2000*, pp. 2385–2390. Salt Lake City, Utah, Sep. 19–22 2000.

[83] J. I. Marcum. A statistical theory of target detection by pulsed radar. *IRE Transactions on Information Theory*, vol. 6, pp. 59–267, Apr. 1960.

[84] H. Meyr and G. Polzer. Performance analysis for general PN-spread-spectrum acquisition techniques. *IEEE Transactions on Communications*, vol. 31, no. 12, pp. 1317–1319, Dec. 1983.

[85] L. B. Milstein, J. Gevargiz and P. K. Das. Rapid acquisition for direct sequence spread-spectrum communications using parallel SAW convolvers. *IEEE Transactions on Communications*, vol. COM-33, no. 7, pp. 593–600, Jul. 1985.

[86] T. Needham. *Visual Complex Analysis*. Oxford University Press, 1997. ISBN 0-19-853446-9.

[87] F. Oberhettinger. *Tables of Bessel Transforms*. Springer Verlag, 1972. ISBN 0-387-05997-0.

[88] C. O'Driscoll and C. C. Murphy. Performance analysis of an FFT based fast acquisition GPS receiver. In *Proceedings of the Institute of Navigation National Technical Meeting, ION NTM 2005*, pp. 1014–1025. San Diego, CA, Jan. 24–26 2005.

[89] C. O'Driscoll and C. C. Murphy. A simplified expression for the probability of error for binary multichannel communications. *IEEE Transactions on Communications*, 2006. Accepted for publication.

[90] S. M. Pan, D. E. Dodds and S. Kumar. Acquisition time distribution for spread-spectrum receivers. *IEEE Journal on Selected Areas in Communications*, vol. 8, no. 5, pp. 800–808, Jun. 1990.

[91] S.-M. Pan, D. H. Madill and D. E. Dodds. Unified time-domain analysis of serial search with application to spread spectrum receivers. *IEEE Transactions on Communications*, vol. 43, pp. 3046–3054, Dec. 1995.

[92] A. Papoulis. *Probability, Random Variables, and Stochastic Processes*. McGraw-Hill, 1st edn., 1965. ISBN 0-07-048448-1.

[93] B. W. Parkinson and J. J. Spilker Jr. (eds.). *Global Positioning System: Theory and Applications*, vol. 1. American Institute of Aeronautics and Astronautics, Washington DC, 1996. ISBN 1-56347-106-X.

[94] P. B. Patnaik. The non-central χ^2- and F-distributions and their applications. *Biometrika*, vol. 36, no. 1/2, pp. 202–232, Jun. 1949.

[95] B. Peterson, R. J. Hartnett, R. Fiedler et al. Frequency domain techniques for fast GPS acquisition and interference detection/rejection. *NAVIGATION: Journal of The Institute of Navigation*, vol. 43, no. 3, pp. 237–255, Fall 1996.

[96] R. L. Peterson, R. E. Ziemer and D. E. Borth. *Introduction to Spread Spectrum Communications*. Prentice Hall, Upper Saddle River, NJ., 1995.

[97] L. A. Pipes and L. R. Harvill. *Applied Mathematics for Engineers and Physicists*. McGraw-Hill, Inc., 3rd edn., 1971. ISBN 0-07-Y85577-3.

[98] A. Polydoros and M. K. Simon. Generalized serial search code acquisition: The equivalent circular state diagram approach. *IEEE Transactions on Communications*, vol. 32, no. 12, pp. 1260–1268, Dec. 1984.

[99] A. Polydoros and C. L. Weber. A unified approach to serial search spread-spectrum code acquisition—part I: General theory. *IEEE Transactions on Communications*, vol. 32, no. 5, pp. 542–549, May 1984.

[100] A. Polydoros and C. L. Weber. A unified approach to serial search spread-spectrum code acquisition—part II: A matched filter receiver. *IEEE Transactions on Communications*, vol. 32, no. 5, pp. 550–560, May 1984.

[101] J. G. Proakis. On the probability of error for multichannel reception of binary signals. *IEEE Transactions on Communication Technology*, vol. 16, no. 1, pp. 68–71, Feb. 1968.

[102] J. G. Proakis. *Digital Communications*. McGraw Hill, 4th edn., 2001. ISBN 0-07-232111-3.

[103] M. L. Psiaki. Block acquisition of weak GPS signals in a software receiver. In *Proceedings of the 14th International Technical Meeting of the Satellite Division of the Institute of Navigation ION GPS 2001*, pp. 2838–2870. Institute of Navigation, Salt Lake City, Utah, Sep. 2001.

[104] S. S. Rappaport. Computing approximations for the generalized Q function and its complement. *IEEE Transactions on Information Theory*, vol. 17, no. 4, pp. 497–498, Jul. 1971.

[105] S. S. Rappaport and D. M. Grieco. Spread-spectrum signal acquisition: Methods and technology. *IEEE Communications Magazine*, vol. 22, no. 6, pp. 6–21, Jun. 1984.

[106] J. G. Reid and M. F. Driscoll. An accessible proof of Craig's theorem in the noncentral case. *The American Statistician*, vol. 42, no. 2, pp. 139–142, May 1988.

[107] R. R. Rick. *Parallel Acquisition in Code Division Mupliple Access Spread Spectrum Systems*. Ph.D. thesis, University of California San Diego, 1995.

[108] R. R. Rick and L. B. Milstein. Noncoherent parallel acquisition in CDMA spread spectrum systems. In *Proceedings of the 1994 International Conference on Communications*, pp. 1422–1426. May 1994.

[109] S. M. Ross. *Simulation*. Academic Press, 2nd edn., 1997.

[110] M. Sankaran. On the non-central chi-square distribution. *Biometrika*, vol. 46, no. 1/2, pp. 235–237, Jun. 1959.

[111] L. L. Scharf. *Statistical Signal Processing: Detection, Estimation, and Time Series Analysis*. Addison–Wesley, 1991. ISBN 0-201-19038-9.

[112] A. Schmid and A. Neubauer. Performance evaluation of differential correlation for single shot measurement positioning. In *Proceedings of the 17th International Technical Meeting of the Satetllite Division of the Institute of Navigation, (ION GNSS 2004)*, pp. 1998–2009. Long Beach, CA, Sep. 21–24 2004.

[113] S. K. Shanmugam, R. Watson, J. Nielson et al. Differential signal processing schemes for enhanced GPS acquisition. In *Proceedings of the 18th International Technical Meeting of the Satetllite Division of the Institute of Navigation, (ION GNSS 2005)*. Long Beach, CA, Sep. 13–16 2005.

[114] J. Sheil and I. O'Muircheartaigh. The distribution of non-negative quadratic forms in normal variables. *Applied Statistics*, vol. 26, no. 1, pp. 92–98, 1977.

[115] J. L. Shewfelt, R. Nishikawa, C. Norman et al. Enhanced sensitivity for acquisition in weak signal environments through the use of extended dwell times. In *Proceedings of the 14th International Technical Meeting of the Satellite Division of the Institute of Navigation ION GPS 2001*, pp. 155–162. Institute of Navigation, Salt Lake City, Utah, Sep. 2001.

[116] O.-S. Shin and K. B. Lee. Differentially coherent combining for double-dwell code acquisition in DS-CDMA systems. *IEEE Transacations on Communications*, vol. 7, no. 51, pp. 1046–1050, Jul. 2003.

[117] D. A. Shnidman. The calculation of the probability of detection and the generalized Marcum Q-Function. *IEEE Transactions on Information Theory*, vol. 35, no. 2, pp. 389–400, Mar. 1989.

[118] A. F. Siegel. The noncentral chi-squared distribution with zero degrees of freedom and testing for uniformity. *Biometrika*, vol. 66, no. 2, pp. 381–386, Aug. 1979.

[119] E. W. Siess and C. L. Weber. Acquisition of direct sequence signals with modulation and jamming. *IEEE Journal on Selected Areas in Communications*, vol. 4, no. 2, pp. 254–272, Mar. 1986.

[120] M. K. Simon and M.-S. Alouini. A unified approach to the probability of error for noncoherent and differentially coherent modulations over generalized fading channels. *IEEE Transactions on Communications*, vol. 46, no. 12, pp. 1625–1638, Dec. 1998.

[121] M. K. Simon and M.-S. Alouini. Exponential-type bounds on the generalized Marcum Q-Function with application to error probability analysis over fading channels. *IEEE Transactions on Communications*, vol. 48, no. 3, pp. 359–366, Mar. 2000.

[122] M. K. Simon and M.-S. Alouini. On the difference of two chi-square variates with application to outage probability computation. *IEEE Transactions on Communications*, vol. 49, no. 11, pp. 1946–1954, Nov. 2001.

[123] M. K. Simon, J. K. Omura, R. A. Scholtz et al. *Spread Spectrum Communications Handbook*. McGraw-Hill, electronic edn., 2002. ISBN 0-07-138215-1.

[124] N. J. A. Sloane. The online encylopedia of integer sequences. URL `http://www.research.att.com/~njas/sequences/`.

[125] A. M. Slonneger and D. V. Sarwate. Noncoherent parallel acquisition of PN sequences in direct-sequence spread-spectrum systems. In *Proceedings of the IEEE Second International Symposium on Spread Spectrum Techniques and Applications (ISSTA)*, pp. 31–34. Yokohama, Japan, November 29 – December 2 1992.

[126] E. Sourour and S. C. Gupta. Direct-sequence spread-spectrum parallel acquisition in nonselective and frequency-selective rician fading channels. *IEEE Journal on Selected Areas in Communications*, vol. 10, no. 3, pp. 535–544, Apr. 1992.

[127] E. A. Sourour and S. C. Gupta. Direct-sequence spread-spectrum parallel acquisition in a fading mobile channel. *IEEE Transactions on Communications*, vol. 38, no. 7, pp. 992–998, Jul. 1990.

[128] J. J. Spilker Jr. GPS signal structure and theoretical performance. In *Global Positioning System: Theory and Applications*, vol. 1, chap. 3, pp. 57–120. American Institute of Aeronautics and Astronautics, 1996.

[129] M. Srinivasan and D. V. Sarwate. Simple schemes for parallel acquisition of spreading sequences in DS/SS systems. *IEEE Transactions on Vehicular Technology*, vol. 45, no. 3, pp. 593–598, Aug. 1996.

[130] J. A. Starzyk and Z. Zhu. Averaging correlation for C/A code acquisition and tracking in frequency domain. In *Proceedings of the Midwestern Symposium on Circuits and Systems*. Dayton, OH, Aug. 2001.

[131] S. Stein. Unified analysis of certain coherent and noncoherent binary communications systems. *IEEE Transactions on Information Theory*, vol. 10, no. 1, pp. 43–51, Jan. 1964.

[132] J. Stewart. *Calculus*. Brooks/Cole Publishing Company, 3rd edn., 1994. ISBN 534-21798-2.

[133] R. A. Stirling-Gallacher, A. P. Hulbert and G. J. R. Povey. A fast acquisition technique for a direct sequence spread spectrum signal in the presence of a large Doppler shift. In *Proceedings of the International Symposium on Spread Spectrum Techniques and Applications ISSTA*, pp. 156–160. IEEE, Sep. 1996.

[134] Y. T. Su. Rapid code acquisition algorithms employing PN matched filters. *IEEE Transactions on Communications*, vol. 36, no. 6, pp. 724–733, Jun. 1988.

[135] C. Tellambura, A. Annamalai and V. K. Bhargava. Closed form and infinite series solutions for the MGF of a dual-diversity selection combiner output in bivariate Nakagami fading. *IEEE Transactions on Communications*, vol. 51, no. 4, pp. 539–542, Apr. 2003.

[136] The MathWorks, Inc. Communications toolbox. `http://www.mathworks.com/products/communications/`. Accessed on Nov. 1st 2006.

[137] J. B.-Y. Tsui. *Fundamentals of Global Positioning System Receivers: A Software Approach*. Wiley, 2000. ISBN 0-471-38154-3.

[138] G. L. Turin. The characteristic function of Hermitian quadratic forms in complex normal variables. *Biometrika*, vol. 47, no. 1/2, pp. 199–201, Jun. 1960.

[139] H. Urkowitz. Energy detection of unknown deterministic signals. *Proceedings of the IEEE*, vol. 55, no. 4, pp. 523–531, Apr. 1967.

[140] A. J. van Dierendonck. GPS receivers. In *Global Positioning System: Theory and Applications*, vol. 1, chap. 8, pp. 329–407. American Institute of Aeronautics and Astronautics, 1996.

[141] D. J. R. van Nee and A. J. R. M. Coenen. New fast GPS code-acquisition technique using FFT. *Electronics Letters*, vol. 27, no. 2, pp. 158–160, 1991.

[142] H. L. Van Trees. *Detection, Estimation, and Modulation Theory. Part 1.* Wiley, 2001. ISBN 0-471-09517-6.

[143] A. J. Viterbi. *CDMA: Principles of Spread Spectrum Communication.* Addison-Wesley, 1995.

[144] A. Wald. *Sequential Analysis.* Wiley Series in Probability and Mathematical Statistics. Wiley, 1947.

[145] A. Wald and J. Wolfowitz. Optimum character of the sequential probability ratio test. *The Annals of Mathematical Statistics*, vol. 19, no. 3, pp. 326–339, Sep. 1948.

[146] G. N. Watson. *A Treatise on the Theory of Bessel Functions.* Cambridge University Press, 2nd edn., 1995. ISBN 0-521-48391-3.

[147] A. Weinberg. Generalized analysis for the evaluation of search strategy effects on PN acquisition performance. *IEEE Transactions on Communications*, vol. 31, no. 1, pp. 37–49, Jan. 1983.

[148] E. W. Weisstein. Fibonacci polynomial. From Mathworld – a Wolfram web resource. URL `http://mathworld.wolfram.com/FibonacciPolynomial.html`.

[149] H. S. Wilf. *Generatingfunctionology.* Academic Press, 2nd edn., 1994. ISBN 1-56881-279-5. URL `http://www.math.upenn.edu/~wilf/DownldGF.html`.

[150] Wolfram Research Inc. The Wolfram functions site. URL `http://functions.wolfram.com`.

[151] R. A. Wooding. Multivariate distribution of complex normal variables. *Biometrika*, vol. 43, no. 1/2, pp. 212–215, Jun. 1956.

[152] R.-C. Wu, Y. T. Su and W.-C. Lin. Noncoherent detectors for PN code acquisition in the presence of data modulation. *IEICE Transactions on Communications*, vol. E83-B, no. 11, pp. 2455–2463, Nov. 2000.

[153] C. Yang. Fast code acquisition with FFT and its sampling schemes. In *Proceedings of the 1996 9th International Technical Meeting of the Satellite Division of the Institute of Navigation, ION GPS-96*, pp. 1729–1734. Institute of Navigation, Sep. 17–20 1996.

[154] C. Yang. Frequency-domain GPS baseband processor. In *Proceedings of the 14th International Technical Meeting of the Satellite Division of the Institute of Navigation ION GPS 2001*, pp. 2859–2870. Institute of Navigation, Salt Lake City, Utah, Sep. 2001.

[155] S. Yoon, I. Song, S. Y. Kim et al. A DS-CDMA code acquisition scheme robust to residual code phase offset variation. *IEEE Transactions on Vehicular Technology*, vol. 49, no. 6, pp. 2405–2418, Nov. 2000.

[156] M. H. Zarrabizadeh and E. S. Sousa. A differentially coherent PN code acquisition receiver for CDMA systems. *IEEE Transactions on Communications*, vol. 45, no. 11, pp. 1456–1465, 1997.